UNIVERSITY OF CALIFORNIA, SAN DIEGO

Vibration-Based Damage Identification and Health Monitoring of Civil Structures

A dissertation submitted in partial satisfaction of

the requirements for the degree Doctor of Philosophy

in

Structural Engineering

by

Xianfei He

Committee in Charge

Professor Joel P. Conte, Chair
Professor Ahmed Elgamal, Co-Chair
Professor Raymond A. de Callafon
Professor Bhaskar Rao
Professor Michael D. Todd

2008

The Dissertation of Xianfei He is approved, and it is acceptable in quality and form for publication on microfilm:

_____

_____

_____

_____
Co-Chair

_____
Chair

University of California, San Diego

2008

To my family for their support

TABLE OF CONTENTS

ACKNOWLEDGEMENTS

I would like to express my deepest appreciation and most sincere gratitude to my advisors Professor Joel P. Conte and Professor Ahmed Elgamal for giving me the opportunity to pursue my Ph.D. at the University of California, San Diego. They have been for me rigorous and insightful teachers as well as reliable and enlightening guides in my research. Their guidance and support has been the key to my academic growth over the past five years. I will forever be grateful to them.

I would also like to thank my committee members, Professor Raymond A. de Callafon, Professor Bhaskar Rao, and Professor Michael D. Todd, who have always been willing to dedicate their time to help me with my research.

I am grateful to Dr. Babak Moaveni for his collaboration on system and damage identification of civil structures during my Ph.D. studies. I am also grateful to Dr. Michael Fraser for his help in developing and implementing the long-term structural monitoring system on the Voigt Bridge. Assistance from Dr. Babak Moaveni, Dr. Linjun Yan, Mr. Andre Barbosa, Mr. Maurizio Gobbato, Mr. Ozgur Ozcelik, Mr. Ian Prowell, Mr. Guocheng Zhang, Mr. Scott Calman, Mr. Daryl Rysdyk, Mr. Andrew Gunthardt, and Mr. Robert Parks, for deploying this monitoring system is highly appreciated.

Special thanks are given to all my colleagues and friends who helped me make the completion of this dissertation possible.

Chapter 3 of this dissertation contains the material from the following two papers submitted to the Journal of Structural Engineering, ASCE (2007): (1) “Dynamic Testing of Alfred Zampa Memorial Bridge” with authors Joel P. Conte, Xianfei He, Babak Moaveni, Sami F. Masri, John P. Caffrey, Mazen Wahbeh, Farzad Tasbihgoo, Daniel H. Whang, and

Ahmed Elgamal; and (2) “System Identification of Alfred Zampa Memorial Bridge Using Dynamic Field Test Data” with authors Xianfei He, Babak Moaveni, Joel P. Conte, Ahmed Elgamal, and Sami F. Masri. The first paper has been in press (with permission from ASCE) and the second one is under review for possible publication. The dissertation author is the primary investigator of these two papers.

Chapter 4 of this dissertation is based on the manuscript submitted for possible publication (tentatively approved) in the Journal of Computer-Aided Civil and Infrastructure Engineering (2007) under the title “Modal Identification Study of Vincent Thomas Bridge Using Simulated Wind-Induced Ambient Vibration Data” with authors Xianfei He, Babak Moaveni, Joel P. Conte, Ahmed Elgamal, and Sami F. Masri. The dissertation author is the primary investigator of this paper.

Chapter 5 of this dissertation is an extended version of the paper published in the proceedings of the 4th Word Conference on Structural Control and Monitoring (2006) under the title “Damage Identification of a Seven-Story Reinforced Concrete Shear Wall Building Tested on the UCSD-NEES Shake Table” with authors Xianfei He, Babak Moaveni, Joel P. Conte, Jose I Restrepo, and Ahmed Elgamal. This chapter is also an extended version of the manuscript in final stage of preparation for possible publication in the Journal of Structural Engineering, ASCE (2008) under the title “Damage Identification of a Seven-Story Reinforced Concrete Shear Wall Building Sliced Tested on the UCSD-NEES Shake Table” with authors Babak Moaveni, Xianfei He, and Joel P. Conte. The dissertation author is primary investigator of these two papers.

Chapter 6 of this dissertation is an extended version of the manuscript published in the proceedings of the International Conference on Experimental Vibration Analysis for Civil Engineering Structures (2007) under the title “Structural monitoring of the I-5 / Voigt Drive

Bridge, San Diego County, California" with authors Michael Fraser, Xianfei He, Ahmed Elgamal, and Joel P. Conte. The dissertation author is the primary investigator of this paper.

Support of this research was provided by the U.S. National Science Foundation under NSF ITR Grant No. 0205720 and a fellowship from the California Institute for Telecommunications and Information Technology. This support is gratefully acknowledged.

VITA

1998	B.E., Tongji University, Shanghai, P.R. China
2001	M.S., Tongji University, Shanghai, P.R. China
2003-2007	Research Assistant, University of California, San Diego
2008	Ph.D., University of California, San Diego

PUBLICATIONS

Journal Publications

He, X., Moaveni, B., Conte, J. P., Elgamal, A., and Masri, S. F. (2007). "System identification of Alfred Zampa Memorial Bridge using dynamic field test data." *Journal of Structural Engineering, ASCE*, under review.

de Callafon, R. A., Moaveni, B., Conte, J. P., **He, X.,** and Udd, E. (2007). "General realization algorithm for modal identification of linear dynamic systems." *Journal of Engineering Mechanics, ASCE*, under review.

He, X., Moaveni, B., Conte, J. P., Elgamal, A., and Masri, S. F. (2007). "Modal identification study of Vincent Thomas Bridge using simulated stochastic wind response data." *Journal of Computed-Aided Civil and Infrastructure Engineering, tentatively accepted.*

Conte, J. P., **He, X.,** Moaveni, B., Masri, S. F., Caffrey, J. P., Wahbeh, M., Tasbihgoo, F., Whang, D. H., and Elgamal, A. (2007). "Dynamic testing of Alfred Zampa Memorial Bridge." *Journal of Structural Engineering, ASCE*, in press.

Moaveni, B., **He, X.,** Conte, J. P., and de Callafon, R. (2007). "Damage identification of a composite beam based on changes of modal parameters." *Journal of Computed-Aided Civil and Infrastructure Engineering*, in press.

Chen, A., **He, X.,** and Xiang, H. (2002). "Identification of 18 flutter derivatives of bridge decks." *Journal of Wind Engineering and Industrial Aerodynamics*, 90, 2007-2022.

Liu, Z., **He, X.,** and Chen A. (2002). "Flutter stability analysis of long-span suspension bridge during the erection." *Journal of Tongji University (Chinese).*

Chen, A., Xiang, H., **He, X.,** and Ding, Q. (2002). "Identification of 18 flutter derivatives of bridge decks using free vibration data." *Journal of Tongji University (Chinese).*

Conference Publications

He, X., Fraser, M., Conte J. P., and Elgamal, A. (2007). "Investigation of environmental effects on identified modal parameters of the Voigt Bridge." *Proceedings of the 18th Engineering Mechanics Division Conference of the ASCE*, Blacksburg, VA.

Fraser, M., **He, X**., Elgamal, A., and Conte J. P. (2007). "Structural monitoring of the I-5 / Voigt Drive Bridge, San Diego County, California." *Proceedings of the International Conference on Experimental Vibration Analysis for Civil Engineering Structures*, Porto, Portugal.

Conte J. P., Moaveni, B., **He, X.,** and Barbosa, A. R. (2007). "System and damage identification of a seven-story reinforced concrete building structure tested on the UCSD-NEES shake table." *Proceedings of the International Conference on Experimental Vibration Analysis for Civil Engineering Structures*, Porto, Portugal.

He, X., Moaveni, B., Conte, J. P., Restrepo, J. I., and Elgamal, A. (2006). "Damage identification of a seven-story reinforced concrete shear wall building tested on the UCSD-NEES shake table." *Proceedings of the 4th Word Conference on Structural Control and Monitoring*, San Diego, USA.

He, X., Moaveni, B., Conte, J. P., and Elgamal, A. (2006). "Comparative study of system identification techniques applied to New Carquinez Bridge." *Proceedings of the 3rd International Conference on Bridge Maintenance, Safety, and Management*, Porto, Portugal.

Moaveni, B., **He, X.,** Conte, J. P., and Restrepo, J. I. (2006). "System identification of a seven-story reinforced concrete shear wall building tested on the UCSD-NEES shake table." *Proceedings of the 4th Word Conference on Structural Control and Monitoring*, San Diego, USA.

Moaveni, B., **He, X.,** Conte, J. P., and Udd, E. (2006). "Effect of damage on modal parameters using full-scale test data." *Proceedings of International Conference on Modal Analysis* (IMAC-XXIV), St. Louis, USA.

He, X., Moaveni, B., Conte, J. P., Elgamal, A., Masri, S. F., Caffrey, J. P., Wahbeh, M., Tasbihgoo, F., and Whang, D. H. (2005). "System identification of New Carquinez Bridge using ambient vibration data." *Proceedings of International Conference on Experimental Vibration Analysis for Civil Engineering Structures*, Bordeaux, France.

He, X., Moaveni, B., Conte, J. P., Elgamal, A., and Masri, S. F. (2004). "System identification of Vincent Thomas Bridge using simulated wind response data." *Proceedings of 2nd International Conference on Bridge Maintenance, Safety, and Management*, Kyoto, Japan.

Fraser, M., Yan, L., **He, X.,** Elgamal, A., Conte, J. P., and Fountain, T. (2004). "Simple neural network application for traffic monitoring." *Proceedings of the International Conference on Computational & Experimental Engineering and Sciences* (ICCES'04), Madeira, Portugal.

Chen, A., **He, X.,** and Xiang, H. (2001). “Identification of flutter derivatives of bridge decks.” *Proceedings of The 5th Aisa-Pacific Conference on Wind Engineering*, Japan

He, X., Chen, A., and Xiang, H. (1998). “Fatigue Analysis of cables of multi-span cable-stayed bridges.” *Proceedings of the 13th Symposium of Chinese Civil Engineering Association*, Shanghai. (Chinese)

ABSTRACT OF THE DISSERTATION

Vibration-Based Damage Identification and Health Monitoring of Civil Structures

by

Xianfei He

Doctor of Philosophy in Structural Engineering

University of California, San Diego, 2008

Professor Joel P. Conte, Chair

Professor Ahmed Elgamal, Co-Chair

Civil structures undergo progressive deterioration due to ageing under the effects of environmental conditions. This deterioration has become a worldwide concern. In addition, natural and man-made hazards such as earthquakes, hurricanes, and explosions can also cause structural damages or exacerbate existing damage. Vibration-based structural damage identification and health monitoring has been the subject of significant research in structural engineering over the past decade.

The research work presented in this dissertation consists of: (1) a comparative study of output-only system identification techniques as applied to the Alfred Zampa Memorial Bridge based on dynamic field test data, through which the performance of different output-only system identification methods applied to the bridge vibration data and corresponding to

different excitation sources is investigated; (2) development of a simulation framework for wind-induced ambient vibration response of Vincent Thomas Bridge using a detailed three-dimensional finite element model of the bridge and a state-of-the-art stochastic wind excitation model, which provides a validated framework to study the effects of realistic damage scenarios in long-span cable-supported bridges on their identified modal parameters; (3) damage identification of a full-scale seven-story reinforced concrete building slice tested on the UCSD-NEES shake table using a sensitivity-based finite element model updating strategy based on the modal parameters identified from ambient vibration data; (4) development and implementation of a state-of-the-art long-term continuous monitoring system on the Voigt Bridge Testbed, which will serve as a live laboratory for structural health monitoring technologies; (5) development of an automated system identification procedure for extracting modal parameters of the Voigt Bridge as a function of time; and (6) investigation of the environmental effects on the identified modal parameters of the Voigt Bridge and objective criterion for damage detection under varying environmental conditions.

The research work presented and the results obtained in this dissertation contribute significantly to the development of robust and reliable vibration-based structural health monitoring systems for large and complex real-world structures.

Chapter 1

Introduction

1.1 Introduction of Vibration-Based Structural Damage Identification and Health Monitoring

Civil structures undergo progressive deterioration due to ageing under the effects of environmental conditions. This deterioration has become a worldwide concern. In the United States, over 50% of all bridges were built before the 1940's and approximately 27.5% of these structures are structurally deficient (Stalling et al., 2000; Fraser, 2006; Yan, 2006). In addition, natural and man-made hazards such as earthquakes, hurricanes, and explosions could also cause structural damages or exacerbate the existing damage.

As a traditional method, visual inspection has been widely applied for damage detection. However, this method has some inherent drawbacks: (1) Only the observable damage can be detected by visual inspection. It is very difficult (if not impossible) to detect some hidden damages inside a structure. However, these hidden damages may cause sudden collapse of the structure. (2) Structural condition assessment is based on subjective criteria by using the visual inspection method. For a structure, different inspectors could make different judgments as to the extent and significance of damage. (3) The visual inspection is a very time inefficient and expensive method. The depth visual inspection carried out on the Brooklyn Bridge in New York consumed three months of time at a cost of over one-million dollars (Aktan et al., 2001; Fraser, 2006). (4) It is impossible to perform continuous monitoring of a

structure using the visual inspection method. Even though the inspection can be repeated over a period, it is possible that some serious damages could happen between two inspections.

Thus the vibration-based structural damage identification and health monitoring has been the subject of significant research in structural engineering in recent years (Doebling et al., 1996; Farrar and Jauregui, 1998; Sohn et al., 2003; Guan, 2006). The basic premise of vibration-based structural damage identification is that changes in structural characteristics such as mass, stiffness, and energy dissipation mechanisms, will influence the vibration response of structures. Therefore, changes in structural dynamic properties / modal properties (i.e., natural frequencies, damping ratios, mode shapes, and quantities derived thereof) are often used as damage indicators in damage identification of civil structures. In order to identify structural damage / deterioration at an early stage and to enable maintenance and repair works at the initial damage phase, to maximize the lifespan of the structure at minimum life-cycle costs, while guaranteeing structural safety and reliability, it is necessary to perform long-term continuous health monitoring of the structure during its service life. With recent development in the PC-data based data acquisition systems, wireless technologies, and the broadband data transmission, there is the potential to acquire different types of data such as acceleration response measurements and environmental condition measurements from a large number of channels and stream the data in real-time or near real-time over the Internet to various remote locations (Fraser, 2006; Guan, 2006). Long-term continuous health monitoring of a structure makes it possible not only to allow for the early identification of possible damages existing in the structure using real-time data to ensure structural and operational safety, but also to (1) evaluate the health condition of the structure shortly after a major catastrophic event such as earthquake, hurricane, and terrorism attack; and (2) study the

effects of varying environmental conditions such as temperature and humidity on the modal properties.

In this chapter, the vibration-based damage identification techniques are first reviewed. Then the objectives and scope of this research are addressed. Finally the organization of this dissertation is presented.

1.2 Literature Review of Vibration-Based Structural Damage Identification

Salawu (1997) presented a review on the use of natural frequency changes for damage detection. It is however challenging if not impossible to localize the detected damage (e.g., to obtain spatial information on the damage) from changes in natural frequencies only. Pandey et al. (1991) introduced the concept of mode shape curvature for damage localization. In their study, both a cantilever and a simply supported beam model were used to demonstrate the effectiveness of using changes in modal curvature as damage indicator to detect and localize damage. As an extension of this work, Abdel Wahab and De Roeck (1999) introduced the concept of curvature damage factor, which was defined as the average of difference in modal curvature through overall modes. In their study, a simply supported and a continuous beam model containing damaged parts at different locations were used to demonstrate the presented method. It was found that the modal curvature of lower vibration modes was in general more accurate than those of the higher vibration modes and when more than one fault existed in the structure, it was not possible to localize damages in all locations from the modal curvature of only one vibration mode. The technique proposed in their study was further applied to a real structure, namely Bridge Z24. It should be noted that the mode shape curvatures are sensitive to damage, but the differentiation process enhances the experimental errors inherent in mode shapes, yielding a large statistical uncertainty. To overcome this difficulty, Ho and Ewins

(2000) proposed changes in the mode shape slope squared as damage indicating features. To compute the derivative of the mode shape, a local polynomial was fit through every four consecutive measurement points and the resulting polynomial was differentiated. They noted that this way of computing mode shape derivatives was subjected to smaller variations than those with a finite difference approximation, which is typically used to calculate the derivatives.

As another mode shape based damage indicator, Pandey and Biswas (1994) proposed the use of changes in the dynamically measured flexibility matrix to detect and localize damage. They showed that the flexibility matrix of a structure can be easily and accurately estimated from a few low frequency vibration modes of the structure. Toksoy and Aktan (1994) performed modal testing on a continuous three-span reinforced concrete slab bridge which was loaded up to failure. The authors reported that the location and severity of the damage could be reliably identified by using natural frequencies, modal damping ratios and mode shapes. Better damage identification results were obtained by using the modal flexibility matrix. Catbas et al. (1997) performed damage identification of a three-span continuous steel stringer bridge. The removal of bearing plates was successfully localized by using the modal flexibility of the bridge. The amount of damage was estimated by evaluating measured deflections of truck loading tests. Zhao and DeWolf (1999) presented a sensitivity study to determine the best candidates of damage signatures for the purpose of health monitoring of bridges. They reviewed and analyzed different diagnostic parameters, including natural frequencies, mode shapes, and modal flexibility. The comparison approach was based on a perturbation coefficient in the stiffness matrix determined from a finite element model. A spring-mass system with five degrees of freedom was used to demonstrate the application of the sensitivity analysis. The results presented in their study indicated that the modal flexibility

was more likely to indicate damage than either the natural frequencies or mode shapes separately. Recently, Bernal and Gunes (2002; 2004) have incorporated changes in modal flexibility matrices (or flexibility proportional matrices) into the damage locating vector technique to localize damage.

Methods based on changes in identified modal properties to detect and localize damage in structures have also been further developed for the purpose of damage quantification (i.e., estimation of the extent of damage). Among these methods are (1) damage index methods, (2) the direct stiffness calculation method, (3) elemental modal strain energy methods, and (4) sensitivity-based finite element model updating methods.

1.2.1 Damage Index Methods

The damage index method was developed by Stubbs et al. (1992, 1995; Kim and Stubbs 1995; and Stubbs and Kim 1996) to identify the damage in structures using a ratio of strain energy in discrete structural element before and after the damage. Mode shapes measured before and after damage are required in this method but they do not need to be mass normalized. Considering a linear, undamaged structure, its i^{th} modal stiffness can be expressed as

$$K_i^m = \mathbf{\Phi}_i^T \mathbf{K} \mathbf{\Phi}_i \tag{1.1}$$

where $\mathbf{\Phi}_i$ = i^{th} mode shape vector and $\mathbf{K}$ = system stiffness matrix. The superscript T represents the transpose of the mode shape vector. The contribution of the j^{th} member to the i^{th} modal stiffness is given by

$$K_{ij}^m = \mathbf{\Phi}_i^T \mathbf{K}_j \mathbf{\Phi}_i \tag{1.2}$$

where $\mathbf{K}_j$ = contribution of the j^{th} member to the system stiffness. The fraction of modal energy of the i^{th} mode and the j^{th} member (also called modal sensitivity) is defined as

$$F_{ij} = K_{ij}^{m} / K_{i}^{m} \tag{1.3}$$

Similarly, the fraction of modal energy of a damaged structure can be defined as

$$F_{ij}^{*} = K_{ij}^{m*} / K_{i}^{m*} \tag{1.4}$$

in which the superscript * represents that those quantities are derived from the damaged structure and

$$K_{i}^{m*} = \boldsymbol{\Phi}_{i}^{*T} \mathbf{K}^{*} \boldsymbol{\Phi}_{i}^{*}; \quad K_{ij}^{m*} = \boldsymbol{\Phi}_{i}^{*T} \mathbf{K}_{j}^{*} \boldsymbol{\Phi}_{i}^{*} \tag{1.5}$$

The contributions of the j^{th} member to the system stiffness $\mathbf{K}_j$ and $\mathbf{K}_j^*$ can be rewritten as

$$\mathbf{K}_{j} = E_{j} \mathbf{K}_{j0}; \quad \mathbf{K}_{j}^{*} = E_{j}^{*} \mathbf{K}_{j0} \tag{1.6}$$

where the scalars E_j and E_j^* = parameters representing material stiffness properties related to the undamaged and damaged structure, respectively. The matrix $\mathbf{K}_{j0}$ contains only the geometric quantities, which is assumed to be the same between the undamaged and damaged structure.

Under the assumption that the modal sensitivities for the i^{th} mode and the j^{th} member are the same for both undamaged and damaged structure states, the following equation can be derived

$$F_{ij} / F_{ij}^{*} = (K_{ij}^{m} K_{i}^{m*}) / (K_{ij}^{m*} K_{i}^{m}) = 1 \tag{1.7}$$

Substituting equations (1.1), (1.2), (1.5), and (1.6) into equation (1.7), a damage index β_j for the j^{th} member can be derived as

$$\beta_{j} = \frac{E_{j}}{E_{i}^{*}} = \frac{\gamma_{ij}^{*} K_{i}^{m}}{\gamma_{ij} K_{i}^{m*}} = \frac{\boldsymbol{\Phi}_{i}^{*T} \mathbf{K}_{j0} \boldsymbol{\Phi}_{i}^{*} K_{i}^{m}}{\boldsymbol{\Phi}_{i}^{T} \mathbf{K}_{j0} \boldsymbol{\Phi}_{i} K_{i}^{m*}} \tag{1.8}$$

where

$$\gamma_{ij} = \boldsymbol{\Phi}_i^T \mathbf{K}_{j0} \boldsymbol{\Phi}_i; \quad \gamma_{ij}^* = \boldsymbol{\Phi}_i^{*T} \mathbf{K}_{j0} \boldsymbol{\Phi}_i^* \tag{1.9}$$

In order to avoid the numerical problems when the denominator of equation (1.8) becomes near zeros (e.g., the j^{th} member is at or near a node of the i^{th} mode) the equation (1.7) is rewritten by adding unity to both the numerator and the denominator,

$$(F_{ij}+1)/(F_{ij}^*+1) = [(K_{ij}^m + K_i^m)K_i^{m*}]/[(K_{ij}^{m*} + K_i^{m*})K_i^m] = 1 \tag{1.10}$$

Similarly substituting equations (1.1), (1.2), (1.5), and (1.6) into equation (1.10), the damage index β_j can be estimated by

$$\beta_j \approx \frac{(\gamma_{ij}^* + \sum_{k=1}^{NE} \gamma_{ij}^*)K_i^m}{(\gamma_{ij} + \sum_{k=1}^{NE} \gamma_{ij})K_i^{m*}} = \frac{(\boldsymbol{\Phi}_i^{*T} \mathbf{K}_{j0} \boldsymbol{\Phi}_i^* + \sum_{k=1}^{NE} \boldsymbol{\Phi}_i^{*T} \mathbf{K}_{k0} \boldsymbol{\Phi}_i^*)K_i^m}{(\boldsymbol{\Phi}_i^T \mathbf{K}_{j0} \boldsymbol{\Phi}_i + \sum_{k=1}^{NE} \boldsymbol{\Phi}_i^T \mathbf{K}_{k0} \boldsymbol{\Phi}_i)K_i^{m*}} \tag{1.11}$$

in which *NE* = number of elements. It should be noted that the stiffness of undamaged and damaged structure are both assumed to be approximately uniform in deriving above equation. In the case that several measured modes (*NM*) are available to localize a potential damage, the equation (1.11) can be rewritten as

$$\beta_j \approx \frac{\sum_{i=1}^{NM}(\gamma_{ij}^* + \sum_{k=1}^{NE} \gamma_{ij}^*)K_i^m}{\sum_{i=1}^{NM}(\gamma_{ij} + \sum_{k=1}^{NE} \gamma_{ij})K_i^{m*}} = \frac{\sum_{i=1}^{NM}(\boldsymbol{\Phi}_i^{*T} \mathbf{K}_{j0} \boldsymbol{\Phi}_i^* + \sum_{k=1}^{NE} \boldsymbol{\Phi}_i^{*T} \mathbf{K}_{k0} \boldsymbol{\Phi}_i^*)K_i^m}{\sum_{i=1}^{NM}(\boldsymbol{\Phi}_i^T \mathbf{K}_{j0} \boldsymbol{\Phi}_i + \sum_{k=1}^{NE} \boldsymbol{\Phi}_i^T \mathbf{K}_{k0} \boldsymbol{\Phi}_i)K_i^{m*}} \tag{1.12}$$

Assuming that the collection of damage indices β_j represents a sample population of a normally distributed random variable β (i.e., the damage index β_j associated with each member is treated as a realization of the random variable β), a normalized damage indicator is defined as

$$z_j = (\beta_j - \bar{\beta})/\sigma_\beta \tag{1.13}$$

where $\bar{\beta}$, σ_β = mean value and standard deviation of β. Then the damage location can be identified by setting a damage threshold value based on the hypothesis testing theory.

Once damage is localized at the j^{th} member, the severity of damage can be estimated as

$$\alpha_j = \frac{dE_j}{E_j} = \frac{E_j + dE_j}{E_j} - 1 = \frac{E_j^*}{E_j} - 1 = \frac{1}{\beta_j} - 1 \tag{1.14}$$

in which α_j = severity estimator, representing the fractional change in the stiffness of the j^{th} member, which can be obtained as

$$\alpha_j = \frac{\sum_{i=1}^{NM} (\boldsymbol{\Phi}_i^T \mathbf{K}_{j0} \boldsymbol{\Phi}_i + \sum_{k=1}^{NE} \boldsymbol{\Phi}_i^T \mathbf{K}_{k0} \boldsymbol{\Phi}_i) K_i^{m*}}{\sum_{i=1}^{NM} (\boldsymbol{\Phi}_i^{*T} \mathbf{K}_{j0} \boldsymbol{\Phi}_i^* + \sum_{k=1}^{NE} \boldsymbol{\Phi}_i^{*T} \mathbf{K}_{k0} \boldsymbol{\Phi}_i^*) K_i^m} - 1 \tag{1.15}$$

The value of α_j is bounded between 0 and -1. The case that $\alpha_j = 0$ indicates no damage occurred, while $\alpha_j = -1$ indicates total loss of the stiffness for that element.

Stubbs and Kim (1996) applied this method to a finite element model of two-span continuous beam, where the fraction of modal strain energy for an Euler-Bernouli beam model [(i.e., the equivalent expression for the right-hand side of equation (1.3)] of element *k* and mode *i* between two locations (x_k , $x_k + \Delta x_k$) was expressed as

$$F_{ij} = \frac{K_{ij}^m}{K_i^m} = \frac{\int_{x_k}^{x_k + \Delta x_k} EI_z \{\phi_i''(x)\}^2 dx}{\int_0^L EI_z \{\phi_i''(x)\}^2 dx} \tag{1.16}$$

where E = elastic modulus and I_z = second moment of moment area about the z axis. The method was shown to be able to localize damage with reasonable accuracy (locations of the false-positive predictions were always adjacent to the real damaged element). However, the severity estimation using this method was not very satisfactory.

Cornwell et al. (1999a) extended the damage index method based on equation (1.8) to plate-like structures that are characterized by two-dimensional curvature. For a two

dimensional (2D) plate structure, the modal strain energy associate with the i^{th} mode is defined as

$$U_i^m = \frac{D}{2}\iint_A [(\frac{\partial^2 \phi_i}{\partial x^2})^2 + (\frac{\partial^2 \phi_i}{\partial y^2})^2 + 2\nu \frac{\partial^2 \phi_i}{\partial x^2}\frac{\partial^2 \phi_i}{\partial y^2} + 2(1-\nu)\frac{\partial^2 \phi_i}{\partial x \partial y}]dxdy \tag{1.17}$$

where A = area of the plate surface; D = flexural rigidity of the plate, $D = Eh^3/12(1-v^2)$, E, h, and v = elastic modulus, thickness, and Poisson ratio of the plates, respectively. Similarly, the modal strain energy for the j^{th} sub-region is derived as

$$U_{ij}^m = \frac{D_j}{2}\iint_{A_j} [(\frac{\partial^2 \phi_i}{\partial x^2})^2 + (\frac{\partial^2 \phi_i}{\partial y^2})^2 + 2\nu \frac{\partial^2 \phi_i}{\partial x^2}\frac{\partial^2 \phi_i}{\partial y^2} + 2(1-\nu)\frac{\partial^2 \phi_i}{\partial x \partial y}]dxdy \tag{1.18}$$

Following the assumptions $F_{ij} = U_{ij}^m / U_i^m = F_{ij}^* = U_{ij}^{m*} / U_i^{m*}$ and $D = Eh^3/12(1-v^2)$ is essentially constant over the area of the plate for both undamaged and damaged modes, the damage index for the j^{th} sub-region can be derived

$$\beta_j = \frac{D_j}{D_j^*} = \frac{\sum_{i=1}^{NM} f_{ij}^*}{\sum_{i=1}^{NM} f_{ij}} \tag{1.19}$$

where

$$f_{ij} = \frac{\iint_{A_j} [(\frac{\partial^2 \phi_i}{\partial x^2})^2 + (\frac{\partial^2 \phi_i}{\partial y^2})^2 + 2\nu \frac{\partial^2 \phi_i}{\partial x^2}\frac{\partial^2 \phi_i}{\partial y^2} + 2(1-\nu)\frac{\partial^2 \phi_i}{\partial x \partial y}]dxdy}{\iint_A [(\frac{\partial^2 \phi_i}{\partial x^2})^2 + (\frac{\partial^2 \phi_i}{\partial y^2})^2 + 2\nu \frac{\partial^2 \phi_i}{\partial x^2}\frac{\partial^2 \phi_i}{\partial y^2} + 2(1-\nu)\frac{\partial^2 \phi_i}{\partial x \partial y}]dxdy} \tag{1.20}$$

Once again, a normalized damage index can be defined using equation (1.13) based on the collection of damage indices β_j for localization of damage.

Duffey et al. (2001) extended the damage index method based on equation (1.8) to be applicable to structures undergoing vibrations predominantly in axial or torsional modes. The damage index for the case of axial vibration was derived as

$$\beta_j = \frac{(EA)_j}{(EA)_j^*} = \frac{\int_{a_k}^{a_{k+1}} (\frac{d\psi_i^*}{dx})^2 dx / \int_{a_k}^{L} (\frac{d\psi_i^*}{dx})^2 dx}{\int_{a_k}^{a_{k+1}} (\frac{d\psi_i}{dx})^2 dx / \int_{a_k}^{L} (\frac{d\psi_i}{dx})^2 dx} \tag{1.21}$$

where EA = axial rigidity; ψ_i = i^{th} axial mode shape; $a_k \le x \le a_{k+1}$ = interval of the j^{th} region along the span of length L. An analogous damage index for the case of torsional vibration was derived as

$$\beta_j = \frac{(GJ)_j}{(GJ)_j^*} = \frac{\int_{a_k}^{a_{k+1}} (\frac{d\vartheta_i^*}{dx})^2 dx / \int_{a_k}^{L} (\frac{d\vartheta_i^*}{dx})^2 dx}{\int_{a_k}^{a_{k+1}} (\frac{d\vartheta_i}{dx})^2 dx / \int_{a_k}^{L} (\frac{d\vartheta_i}{dx})^2 dx} \tag{1.22}$$

where GJ = torsional rigidity; ϑ_i = i^{th} torsional mode shape. In their studies, the method was compared to the flexibility-change method presented by Pandey and Biswas (1994). Two methods were applied to both simulated and experimental spring-mass systems undergoing axial response. Both the flexibility-change method and the damage index method were successful in detecting and localizing damaged elements for 10-percent reductions in element stiffnesses in a simulated spring-mass system. However, the flexibility change method requires the mass-normalized mode shapes and natural frequencies whereas the damage index method requires only arbitrary normalized mode shapes. For the experimental damage cases, the damage index method performed well to detect and localize the damage. However, results were not favorable with the flexibility-change method. Based on the cases presented, it was found that results using this method were somehow unreliable, depending strongly on damage location, damage level, and number of modes included.

Kim and Stubbs (2002) presented an improved version of their previous work on the damage index methods (Kim and Stubbs, 1995, 1996) to overcome the limits of the existing damage index algorithms. It is assumed that the structure is damaged at a single location, thus

$$\frac{dK_{ij}^{m}}{K_i^m}=\frac{dK_i^m}{K_i^m}=\frac{d\lambda_i}{\lambda_i}+\frac{dM_i}{M_i}(1+\frac{d\lambda_i}{\lambda_i}) \tag{1.23}$$

where dK_{ij}^{m} = change of the j^{th} element modal stiffness; λ_i, M_i, K_i^m = i^{th} eigenvalue, i^{th} modal mass, and i^{th} modal stiffness of the undamaged structure, respectively; $d\lambda_i$, dM_i dK_i^m = change in the i^{th} eigenvalue, change in the i^{th} modal mass, and change in the i^{th} modal stiffness, respectively. Following the definition of equations (1.2), (1.5), and (1.14)

$$dK_{ij}^{m}=K_{ij}^{m*}-K_{ij}^{m}=\gamma_{ij}^{*}(E_j+dE_j)-\gamma_{ij}E_j \tag{1.24}$$

where $\gamma_{ij}=\boldsymbol{\Phi}_i^T\mathbf{K}_{j0}\boldsymbol{\Phi}_i$ and $\gamma_{ij}^{*}=\boldsymbol{\Phi}_i^{*T}\mathbf{K}_{j0}^{*}\boldsymbol{\Phi}_i^{*}$. Dividing both sides of equation (1.24) by K_i^m and assuming that the structure has uniform stiffness in the undamaged state [i.e., $K_i^m=\boldsymbol{\Phi}_i^T\mathbf{K}\boldsymbol{\Phi}_i=E_j\boldsymbol{\Phi}_i^T\mathbf{K}_0\boldsymbol{\Phi}_i$ follow the concept introduced in equation (1.6)], the following expression can be obtained

$$\frac{E_j}{E_j^{*}}=\frac{E_j}{E_j+dE_j}=\frac{\gamma_{ij}^{*}/\gamma_i}{\frac{dK_{ij}^{m}}{K_i^m}+\frac{\gamma_{ij}}{\gamma_i}} \tag{1.25}$$

where $\gamma_i=\boldsymbol{\Phi}_i^T\mathbf{K}_0\boldsymbol{\Phi}_i$. Substituting equation (1.23) into the above equation, the damage index β_j can be derived as (*NM* measured vibration modes are involved)

$$\beta_j=\frac{E_j}{E_j^{*}}=\frac{\sum_{i=1}^{NM}\gamma_{ij}^{*}}{\sum_{i=1}^{NM}\{\gamma_i[\frac{d\lambda_i}{\lambda_i}+\frac{dM_i}{M_i}(1+\frac{d\lambda_i}{\lambda_i})]+\gamma_{ij}\}} \tag{1.26}$$

Consequently, the severity of damage can be estimated as

$$\alpha_j=1/\beta_j-1 \tag{1.27}$$

The updated version of the damage index algorithm based on equation (1.26) and algorithms based on equations (1.8) and (1.12) were evaluated by predicting damage location

and severity estimation in a numerical model of a two-span continuous beam (Kim and Stubbs, 2002). The equivalent expression for γ_{ij} , γ_{ij}^{*} , and γ_i in the damage index equations [equations (1.8), (1.12),and (1.26)] were computed as

$$\gamma_{ij} = \int_{x_k}^{x_k+\Delta x_k} \{\phi_i''(x)\}^2 dx \tag{1.28}$$

$$\gamma_{ij}^{*} = \int_{x_k}^{x_k+\Delta x_k} \{\phi''^{*}(x)\}^2 dx \tag{1.29}$$

$$\gamma_i = \int_0^L \{\phi_i''(x)\}^2 dx \tag{1.30}$$

where locations x_k and $x_k + \Delta x_k$ = two nodal locations of an element *j* for the beam model; *L* = length of the beam model. The following relationships between the algorithms and their accuracy in damage prediction were obtained. First, the use of damage index algorithm based on equation (1.8) for the damage prediction exercises resulted in (1) relatively small Type I error (false detection of true damage locations); (2) small localization error; (3) relatively high Type II error (prediction of locations that are not damaged); and (4) high severity estimation error. It consistently overestimated severities of damage. Second, the use of damage index algorithm based on equation (1.12) resulted in no error related to damage localization but high severity estimation error. It consistently underestimated severities of damage. Finally, the use of improved damage index algorithm based on equation (1.26) resulted in no error related to damage localization and very small severity estimation error.

1.2.2 Direct Stiffness Calculation Method

The direct stiffness calculation technique was developed by Maeck and De Roeck (1999; Maeck et al., 2000) to predict the damage location and severity from measured modal displacement derivatives for a free-free set-up experimental reinforced concrete beam. The

advantage of this method is that no numerical model is needed to obtain the dynamic stiffness distribution for statically determined systems. As for hyperstatic systems, the reaction forces and internal forces are depended on the stiffness of the structure. It was pointed out that an iterative procedure is needed to find the stiffness distribution of the structure. The method makes use of the basic relation that the dynamic bending stiffness *EI* at each section is equal to the bending moment *M* in that section divided by the corresponding curvature (i.e., second derivative of the bending mode shape ϕ^b)

$$EI = \frac{M}{d^2\phi^b / dx^2} \tag{1.31}$$

In the same manner, the dynamic torsion stiffness *GJ* in each section can be calculated from torsional moment *T* in that section and the corresponding torsion rate (or torsion angle per unit length, i.e., first derivative of torsional mode shape ϕ^t)

$$GJ = \frac{T}{d\phi^t / dx} \tag{1.32}$$

In order to apply equations (1.31) and (1.32) for damage detection and localization, the modal internal forces (i.e., *M* and *T*) and the modal curvature as well as the torsional angle per unit length need to be calculated.

The eigenvalue problem of an undamped system can be written as

$$\mathbf{K}\boldsymbol{\Phi}_m = \omega_m^2 \mathbf{M}\boldsymbol{\Phi}_m \tag{1.33}$$

in which **K** = stiffness matrix; **M** = analytical mass matrix; ω_m = m^{th} measured circular eigenfrequency; and $\boldsymbol{\Phi}_m$ = m^{th} measured mode shape. The above equation can be seen as a pseudo-static system: for each mode internal (section) forces are due to the inertial load $\omega_m^2 \mathbf{M}\boldsymbol{\Phi}_m$. In such way, the mass distribution of the system has to be assumed known. In

addition, when this method was applied for the damage identification (Maeck and De Roeck, 1999; Maeck et al., 2000), a lumped mass matrix was used in equation (1.33), which is acceptable in the case that measurement mesh is rather dense. For the m^{th} bending mode, $\mathbf{\Phi}_m$ in equation (1.33) can be replaced by $\mathbf{\Phi}_m^b$, i.e. the modal deflections that are directly available from measurements. In the calculation of the modal internal forces, the contribution of rotational inertia turned out to be negligible for the lower modes when a reasonably dense measurement grid is used. For the m^{th} torsional modes, $\mathbf{\Phi}_m$ in equation (1.33) can be replaced by $\mathbf{\Phi}_m^t$, i.e. the rotation angles which are normally not directly measured. However, from the modal deflections at two different points of the same cross section of the beam, the torsion angles are directly obtained. If in equation (1.33), $\mathbf{\Phi}_m$ contains only the modal displacements at the measurement points, one obtains a discrete pattern of the inertia load. A correction can be made by linearly interpolating the measurements and obtaining in this way a distributed load. Once the inertial loads are obtained from the measured mode shapes and rotation angles, the modal internal forces can be derived based on the internal force equilibrium assuming that the beam is only subjected to the inertial loads

$$M_{i+1} = M_i + V_i(x_{i+1} - x_i) - \int_{x_i}^{x_{i+1}} \omega_m^2 \rho A \phi_m^b(x)(x_{i+1} - x)dx \tag{1.34}$$

$$V_{i+1} = V_i - \int_{x_i}^{x_{i+1}} \omega_m^2 \rho A \phi_m^b(x)dx \tag{1.35}$$

$$T_{i+1} = T_i - \int_{x_i}^{x_{i+1}} \omega_m^2 i_a \phi_m^t(x)dx \tag{1.36}$$

where M_i, V_i, T_i = modal bending moment, modal shear forces and modal torsional moment respectively; ρ, A, and i_a = density, cross area and polar moment of inertia of the structure, respectively. In the recursive formula shown in equations (1.34), (1.35), and (1.36), the values of M_0, V_0, T_0 are zero for the special case of free-free set-up beam.

The next step in deriving the dynamic bending and torsion stiffness consists of the calculation of curvatures along the beam for the bending modes and torsion rates for the torsional modes. Direct calculation of the first and second derivatives from measured mode shapes using the central difference approximation, results in oscillating and inaccurate values. Two smoothing procedures accounting for the inherent inaccuracies of the measured mode shapes can be applied (Maeck and De Roeck,1999), namely global smoothing procedure and Mindlin smoothing method, a weighted residual penalty-based technique.

It should be noted that even though the damage identification results using this method showed generally good agreement with observations from the experiment (Maeck and De Roeck, 1999; Maeck et al., 2000). The method appeared to suffer from numerical difficulties when the modal curvature is close to zero. In this case, the approximation for the stiffness is no longer accurate. In addition, the method was only shown to work for the statically determinate structure and it was not explained explicitly how such a method could be applied to the statically indeterminate structure.

1.2.3 Element Modal Strain Energy Methods

Shi et al. (1998; 2000) proposed a method of using change of modal strain energy in each structural element before and after occurrence of damage to localize and quantify the damage. The damage is assumed to affect only the stiffness matrix of the system. When damage occurs in a structure, the stiffness matrix $\mathbf{K}^d$, the i^{th} modal eigenvalue λ_i^d, and the i^{th} mode shape $\mathbf{\Phi}_i^d$ of the damaged system can be expressed as

$$\mathbf{K}_d = \mathbf{K} + \sum_{i=1}^{L} \Delta \mathbf{K}_j = \mathbf{K} + \sum_{i=1}^{L} \alpha_j \mathbf{K}_j \quad (-1 \le \alpha_j \le 0) \tag{1.37}$$

$$\lambda_d = \lambda_i + \Delta \lambda_i \tag{1.38}$$

$$\mathbf{\Phi}_i^d = \mathbf{\Phi}_i + \Delta\mathbf{\Phi}_i \tag{1.39}$$

where the damage in an element is expressed as a fractional change of the element stiffness matrix; the superscript *d* indicates the damage case; α_j = coefficient defining a fractional reduction of the j^{th} element stiffness matrix; and *L* = total number of the elements in the system.

The element modal strain energy method (Shi et al. 1998; 2000) can be divided into two steps: first, the damage is localized using the change of element modal strain energy, and then the severity of damage at potential damage locations is determined using an iterative procedure. The element modal strain energy is defined as the product of the elemental stiffness matrix and the second power of the mode shape component. For the j^{th} element and the i^{th} mode, the modal strain energy before and after the occurrence of damage is defined as

$$MSE_{ij} = \mathbf{\Phi}_i^T \mathbf{K}_j \mathbf{\Phi}_i \tag{1.40}$$

$$MSE_{ij}^d = \mathbf{\Phi}_i^{d^T} \mathbf{K}_j \mathbf{\Phi}_i^d \tag{1.41}$$

where MSE_{ij}, MSE_{ij}^d = undamaged and damaged modal strain energy of the j^{th} element for the i^{th} mode; $\mathbf{\Phi}_i$ $\mathbf{\Phi}_i^d$ = i^{th} mode shape of undamaged and damaged structure, respectively; $\mathbf{K}_j$ = element stiffness of the j^{th} element. Because the damage elements are not known, the undamaged element stiffness matrix $\mathbf{K}_j$ is used instead of the damaged one in equation (1.41). In this method, the modal strain energy change ratio, is defined for damage localization (Shi et al., 1998)

$$MSECR_{ij} = \frac{\left| MSE_{ij}^d - MSE_{ij} \right|}{MSE_{ij}} \tag{1.42}$$

in which *i*, *j* = mode number and element number, respectively. Shi et al. (1998; 2000) claimed that the modal strain energy change of a damaged element is larger that that of any

other undamaged element. Elements which are linked with the damaged one have smaller values of modal strain energy change. If an element is far away from the damage element, the modal strain energy change of this element will be much smaller. Therefore, the modal strain energy change ratio could be a meaningful indicator for damage localization.

The modal strain energy change of the j^{th} element for the i^{th} mode could be obtained from the experimental mode shape as

$$MSEC_{ij} = \mathbf{\Phi}_i^{d^T} \mathbf{K}_j \mathbf{\Phi}_i^d - \mathbf{\Phi}_i^T \mathbf{K}_j \mathbf{\Phi}_i \tag{1.43}$$

Substituting equation (1.39) into equation (1.43) and neglecting second-order terms, the modal strain energy change $MSEC_{ij}$ can be expressed in terms of the small changes in the experimental mode shapes $\Delta\mathbf{\Phi}_i$

$$MSEC_{ij} = 2\mathbf{\Phi}_i^T \mathbf{K}_j \Delta\mathbf{\Phi}_i \tag{1.44}$$

For a small perturbation in an un-damped dynamic system, the equation of motion can be described as

$$[(\mathbf{K} + \Delta\mathbf{K}) - (\lambda_i + \Delta\lambda_i)\mathbf{M}](\mathbf{\Phi}_i + \Delta\mathbf{\Phi}_i) = 0 \tag{1.45}$$

The equation (1.45) can be rewritten as neglecting the second-order terms

$$(\mathbf{K} - \lambda_i\mathbf{M})\Delta\mathbf{\Phi}_i = \Delta\lambda_i\mathbf{M}\mathbf{\Phi}_i - \Delta\mathbf{K}\mathbf{\Phi}_i \tag{1.46}$$

The term $\Delta\mathbf{\Phi}_i$ can be expressed as a linear combination of mode shapes of the original system

$$\Delta\mathbf{\Phi}_i = \sum_{k=1}^{n} d_{ik}\mathbf{\Phi}_k \tag{1.47}$$

in which d_{ik} = scalar factors; and n = total number of modes of the original system. Inserting equation (1.47) into equation (1.46), and after some manipulation, d_{ik} can be obtained

$$d_{ik} = -\frac{\boldsymbol{\Phi}_r^T \Delta \mathbf{K} \boldsymbol{\Phi}_i}{\lambda_r - \lambda_i} \quad (r \neq i) \tag{1.48}$$

For the case of $r = i$, it is easy to know that $d_{rr} = 0$. Substituting equations (1.48), (1.47) into equation (1.44) and neglecting higher-order terms, the modal strain energy change can be expressed as

$$MSEC_{ij} = 2\boldsymbol{\Phi}_i^T \mathbf{K}_j \left(\sum\nolimits_{r=1}^{n} -\frac{\boldsymbol{\Phi}_r^T \Delta \mathbf{K} \boldsymbol{\Phi}_i}{\lambda_r - \lambda_i} \boldsymbol{\Phi}_r\right) \quad (r \neq i) \tag{1.49}$$

Substituting equation (1.37) into above equation, the modal strain energy change can be rewritten

$$MSEC_{ij} = \sum\nolimits_{p=1}^{L} -2\alpha_p \boldsymbol{\Phi}_i^T \mathbf{K}_j \sum\nolimits_{r=1}^{n} \frac{\boldsymbol{\Phi}_r^T \mathbf{K}_p \boldsymbol{\Phi}_i}{\lambda_r - \lambda_i} \boldsymbol{\Phi}_r \quad (r \neq i) \tag{1.50}$$

It can be seen from above equation, the term on the left-hand side is the element modal strain energy change of the j^{th} element for the i^{th} mode, which can be obtained from equation (1.43) by using the experimental mode shape of the undamaged and damaged states. All the terms on the right-hand side are all known information of the undamaged system except α_p. Thus the severity of damage can be obtained by solving the equation (1.50).

After determining the damage sites using the localization approach, i.e., using equation (1.42), the damage severity of the suspected damage elements can then be evaluated for the i^{th} mode

$$\begin{Bmatrix} MSEC_{i1} \\ MSEC_{i2} \\ \vdots \\ MSEC_{iJ} \end{Bmatrix} = \begin{bmatrix} \beta_{11} & \beta_{12} & \cdots & \beta_{1q} \\ \beta_{21} & \beta_{22} & \cdots & \beta_{2q} \\ \vdots & \vdots & \ddots & \vdots \\ \beta_{J1} & \beta_{J2} & \cdots & \beta_{Jq} \end{bmatrix} \begin{Bmatrix} \alpha_1 \\ \alpha_1 \\ \vdots \\ \alpha_q \end{Bmatrix} \tag{1.51}$$

where q = number of suspected damage elements; J = number of the selected element for the computation of the modal strain energy change; β_{st} ($s = 1, 2, \cdots, J$; $t = 1, 2, \cdots, q$) =

sensitivity coefficient of modal strain energy to damage, which is obtained from equation (1.50) as

$$\beta_{st} = -2\sum_{r=1}^{n} \boldsymbol{\Phi}_i^T \mathbf{K}_s \frac{\boldsymbol{\Phi}_r^T \mathbf{K}_t \boldsymbol{\Phi}_i}{\lambda_r - \lambda_i} \boldsymbol{\Phi}_r \quad (r \neq i) \tag{1.52}$$

and n = number of analytical modes that theoretically should be equal to the total number of degrees of freedom of the structure. In practice, only n^* number lowest modes ($n^* < n$) are used in the equation (1.52). The number of suspected damaged elements q would be much smaller than the total number of elements L in the system. The group of selected elements for modal strain energy change computation may or may not include the suspected damage elements with $J \geq q$. When there are m modes used in the identification, the equation (1.51) becomes an overdetermined set of equations of size $m \times J$. An iterative process was introduced by Shi et al. (2000) in order to find the damage coefficients in (1.51). Once the coefficients α_p are estimated by solving the equation (1.51), these coefficients are then used to update the related elements to obtain the corrected elemental stiffness matrix and the global stiffness matrix. The updated system is considered as a new undamaged state of the structure. Then a new set of damage coefficients α_p can be obtained using the modal strain energy change and the coefficients β_{st} in the sensitivity matrix calculated based on the updated undamaged state. This process is repeated until convergence in the estimated α_p. It is worth noting that this process determines the damage coefficients α_p with updating of the elemental stiffness matrix from the undamaged state to the damaged state.

The method discussed above was illustrated and verified by a numerical example with a fixed-end beam and an experiment with a single-bay, two-story portal steel frame structure Shi et al. (2000). Results indicated that the presented method was effective in localizing

damage, but it was noise sensitive in the damage quantification. Shi et al. (2002) further proposed an improved version of this method in which the change of the i^{th} mode shape before and after the occurrence of damage in the structure is rewritten as (Sutter et al., 1988)

$$\Delta\boldsymbol{\Phi}_i = \mathbf{K}^{-1}\mathbf{b}_w\mathbf{b} + \sum_{k=1}^{n^*} d_{ik}^w \boldsymbol{\Phi}_k \tag{1.53}$$

where

$$\mathbf{b}_w = \mathbf{I} + \lambda_i\mathbf{M}\mathbf{K}^{-1} + (\lambda_i\mathbf{M}\mathbf{K}^{-1})^2 + \cdots + (\lambda_i\mathbf{M}\mathbf{K}^{-1})^{w-1} \tag{1.54}$$

$$\mathbf{b} = \Delta\lambda_i\mathbf{M}\boldsymbol{\Phi}_i - \Delta\mathbf{K}\boldsymbol{\Phi}_i \tag{1.55}$$

in which w = a weighting factor. Substituting equations (1.53), (1.54), and (1.55) into equation (1.46), and after some manipulation, d_{ik}^w can be obtained

$$d_{ik}^w = -\frac{(\frac{\lambda_i}{\lambda_r})^w \boldsymbol{\Phi}_r^T \Delta\mathbf{K}\boldsymbol{\Phi}_i}{\lambda_r - \lambda_i} \quad (r \neq i) \tag{1.56}$$

Thus the change of the i^{th} mode shape can be written as

$$\Delta\boldsymbol{\Phi}_i = \mathbf{K}^{-1}\mathbf{b}_w\mathbf{b} + \sum_{r=1}^{n^*} -\frac{(\frac{\lambda_i}{\lambda_r})^w \boldsymbol{\Phi}_r^T \Delta\mathbf{K}\boldsymbol{\Phi}_i}{\lambda_r - \lambda_i}\boldsymbol{\Phi}_r \quad (r \neq i) \tag{1.57}$$

Inserting equations (1.37) and (1.57) into (1.44), the modal strain energy change of the j^{th} element for the i^{th} mode becomes

$$\begin{aligned} MSEC_{ij} = \sum_{p=1}^{L} -2\alpha_p \boldsymbol{\Phi}_i^T \mathbf{K}_j [\mathbf{K}^{-1}\mathbf{b}_w(\boldsymbol{\Phi}_i^T \mathbf{K}_p \boldsymbol{\Phi}_i^T \mathbf{M}\boldsymbol{\Phi}_i - \mathbf{K}_p\boldsymbol{\Phi}_i) \\ + (\sum_{r=1}^{n^*} -\frac{(\frac{\lambda_i}{\lambda_r})^w \boldsymbol{\Phi}_r^T \mathbf{K}_p \boldsymbol{\Phi}_i}{\lambda_r - \lambda_i}\boldsymbol{\Phi}_r)] \quad (r \neq i) \end{aligned} \tag{1.58}$$

The corresponding sensitivity coefficient of modal strain energy to damage β_{st} is now becoming

$$\beta_{st} = 2\boldsymbol{\Phi}_i^T \mathbf{K}_s [\mathbf{K}^{-1} \mathbf{b}_w (\boldsymbol{\Phi}_i^T \mathbf{K}_t \boldsymbol{\Phi}_i^T \mathbf{M} \boldsymbol{\Phi}_i - \mathbf{K}_t \boldsymbol{\Phi}_i) + (\sum_{r=1}^{n^*} - \frac{(\frac{\lambda_i}{\lambda_r})^w \boldsymbol{\Phi}_r^T \mathbf{K}_t \boldsymbol{\Phi}_i}{\lambda_r - \lambda_i} \boldsymbol{\Phi}_r)] \quad (r \neq i) \tag{1.59}$$

Comparing between equations (1.48) and (1.56) gives the following relationship

$$\frac{d_{ir}^{(w)}}{d_{ir}} = (\frac{\lambda_i}{\lambda_r})^w \tag{1.60}$$

when $\lambda_r > \lambda_i$, $d_{ir}^{(w)} \ll d_{ir}$. This means the contribution from using higher modes in the computation of $\Delta\boldsymbol{\Phi}_i$ in equation (1.53) for the improved version of modal strain energy method will be less than that in equation (1.47) for the original version of the method. Therefore a smaller number of analytical modes are required in improved version of the method to achieve the same degree of accuracy as in the original method, which needs a large number of modes in the computation. Again, the improved algorithm was illustrated and verified by a numerical example with a fixed-end beam and an experiment with a single-bay, two-story portal steel frame structure. It was demonstrated that the improved algorithm (1) reduced the truncation error in computation; (2) avoided the finite element modeling errors in higher modes; and (3) improved the rate of convergence in the computation.

The measured mode shapes and elemental stiffness matrix are required in the above identification algorithms (both original and improved algorithms). As well known, the measured modes are usually incomplete in practice because of the limited number of sensors. In order to apply this method for damage identification, the mode shape expansion technique is needed to expand the measured mode shape to the full dimension of the finite element model.

1.2.4 Sensitivity-Based Finite Element Model Updating

Another class of vibration-based damage identification methods consists of applying sensitivity-based finite element (FE) model updating for damage identification (Friswell and Mottershead, 1995). This class of methods updates the physical parameters of a FE model of the structure by minimizing an objective function expressing the discrepancy between analytically predicted and experimentally identified modal parameters and quantities derived thereof that are sensitive to damage. Optimum solutions of the problem are reached through sensitivity-based optimization algorithms.

The FE model updating can be described as to find a solution for the following generic nonlinear least squares problem

$$\min_{\boldsymbol{\theta}} f(\boldsymbol{\theta}) = \frac{1}{2}\mathbf{r}(\boldsymbol{\theta})^T \mathbf{r}(\boldsymbol{\theta}) = \frac{1}{2}\sum_{j=1}^{m}[r_j(\boldsymbol{\theta})]^2 \tag{1.61}$$

in which where $\mathbf{r}(\boldsymbol{\theta})$ = residual vector containing the differences between the numerical predicted and experimental determined modal data; $\boldsymbol{\theta} \in \mathbb{R}^n$ = a set of physical parameters, also called updating parameters, which will be adjusted in order to minimize the objective functions. The updating parameters are the uncertain physical properties of the numerical model. Instead of the absolute value of each uncertain variable θ, a dimensionless correction factor p_i can be defined to represent the variation of θ_i relative to its reference values θ_i^{ref}

$$\mathbf{p} = [p_i] = \left[-(\theta_i - \theta_i^{ref})/\theta_i^{ref}\right] \quad \rightarrow \quad \theta_i = \theta_i^{ref}(1 - p_i) \tag{1.62}$$

The correction factor p_i can be assigned to a single element or a group of elements. Then the FE model updating problem defined in equation (1.61) can be rewritten as

$$\min_{\mathbf{p}} f(\mathbf{p}) = \frac{1}{2}\mathbf{r}(\mathbf{p})^T \mathbf{r}(\mathbf{p}) = \frac{1}{2}\sum_{j=1}^{m}[r_j(\mathbf{p})]^2 \tag{1.63}$$

Considering the importance and the identification accuracy of the different modal parameters (i.e., statistical uncertainty of identified parameters), the weighted nonlinear least squares problem can be used in the FE model updating instead of the normal least squares problem given in equation (1.63), i.e.,

$$\min_{\mathbf{p}} f(\mathbf{p}) = \frac{1}{2}\mathbf{r}(\mathbf{p})^T \mathbf{W}\mathbf{r}(\mathbf{p}) = \frac{1}{2}\sum_{j=1}^{m}[w_j r_j(\mathbf{p})]^2 \tag{1.64}$$

where $\mathbf{W}$ = a diagonal matrix whose component is w_j^2 and w_j = weight factor for the residual $r_j(\mathbf{p})$. Depending on each particular FE model updating problem, the weight factors w_j applied to the various modal residuals can be selected so as to account for the different levels of identification accuracy of the different modal parameters. In practice, the weight factors are usually obtained as the reciprocals of the standard deviation or coefficient-of-variation of the corresponding measured modal parameters.

In the application of the sensitivity-based FE model updating techniques, the fundamental properties of the original model such as the symmetry, positivity and sparse pattern in the stiffness and mass matrices are retained because the updating is carried out at the element level. In addition, there is a physical explanation for each updating parameter. Therefore the sensitivity-based model updating techniques have attracted more and more attention in the civil engineering research community.

Teughels and De Roeck (2004) applied the FE model updating techniques to a pre-stressed concrete highway bridge Z24 in Switzerland for damage identification. The damage pattern was identified using eigen-frequencies and un-scaled mode shapes obtained from ambient vibrations. For the undamaged as well as the damaged state of the bridge, the modal properties computed from the updated model correspond well with their experimentally identified counterparts. Jaishi and Ren (2005) demonstrated a comparative study of the

influence of different possible residuals in objective function through a simulated simply supported beam. Frequency residual only, mode shape related function only, modal flexibility (uniform load surface) residual only, and their combinations were studied independently. It was found that the objective function which consisted of all three residuals was the best for FE model updating in view of model tuning as well as damage localization. This objective function was then implemented in a second case study of a concrete-filled steel tubular arch bridge. The FE model mass matrix obtained from Guyan reduction technique was used to obtain the mass-normalized mode shapes in order to calculate the modal flexibility. The updated FE model of the bridge was able to produce a sufficient improvement on modal parameters of the concerned modes which were in close agreement with the experimental results. In stead of using uniform load surface residual obtained from the modal flexibility matrix, Jaishi and Ren (2006) presented the objective function consisting of the modal flexibility matrix component residual (through the Frobenius matrix norm) in the FE model updating for damage detection. The proposed damage identification procedure was illustrated with a simulated example of simply supported beam and afterwards was applied for damage identification of a laboratory tested reinforced concrete beam. It was verified that the modal flexibility was sensitive to damage and the proposed procedure of FE model updating using the modal flexibility residual was promising for the detection of damaged elements.

The difference between various sensitivity-based FE model updating algorithms can be found in: objective functions to be minimized, numerical schemes used to implement the optimization, and algorithms to obtain the sensitivity matrix. The sensitivity-based FE model updating strategy applied in this study for damage identification of a real-world structure will be explained in detail in Chapter 5.

1.3 Objectives and Scope

As reviewed in the above section, vibration-based structural damage identification has received increasing attention and has progressed significantly in the civil engineering community over the past decade. Most of these damage identification techniques are typically investigated, verified and validated by using numerically simulated data and/or laboratory experimental data. Sensitivity-based FE model updating has been shown to be a good candidate methodology for damage identification of real-world structures. However, the application of FE model updating for identifying damage in large and complex structures using modal parameters identified based on field response measurements is still very limited. In addition, among these limited applications, real structures are usually represented by beam-type or truss-type models to simplify the identification problem.

In vibration-based structural damage identification, it is very crucial to extract modal parameters accurately based on structural response measurements. The accuracy of the identified modal parameters directly influences the structural damage identification results. Experimental modal analysis has been widely used in the civil engineering research community to extract structural modal parameters from vibration measurements. In classical experimental modal analysis, the frequency response functions (FRFs) in the frequency domain or impulse response functions (IRFs) in the time domain usually provide the basic input of system identification algorithms, which produce accurate estimates of modal parameters provided that the signal-to-noise ratio of the dynamic measurement data is high enough. However, it is very difficult to obtain FRFs or IRFs in dynamic field tests of civil structures, since typically only the structure dynamic response (output) can be measured in such tests. Thus, most often, modal parameters have to be extracted based on structural response measurements only. It is worth noting that output-only system identification

techniques are necessary and essential for developing long-term continuous vibration-based structural health monitoring systems. For the continuous monitoring of a structure during its service life, it is impossible to measure its sources of excitation and only its response to ambient/natural excitation sources such as traffic, wind, micro-tremors and combinations thereof can be measured. Several output-only system identification techniques have been developed and applied to civil engineering structures. However, the performance of these techniques applied to real-world large and complex structures based on low-amplitude dynamic response measurements still needs further investigation.

As discussed earlier, the basic premise of vibration-based structural damage identification and health monitoring is that changes in structural characteristics such as mass, stiffness, and energy dissipation mechanisms, will influence the vibration response of the structure. Therefore, changes in modal parameters can be used as damage indicators in structural damage identification and health monitoring. However, varying environmental conditions (e.g., temperature, wind characteristics, and humidity) may also cause changes in these modal parameters. Variations in modal parameters due to changes in environmental conditions have been shown to be very significant in previous limited studies; they may be even larger than those caused by structural damage (Abdel Wahab and De Roeck, 1997; Cornwell et al., 1999b; Peeters and De Roeck, 2001; Xia et al., 2006; He et al., 2007). Therefore, in order to develop a robust and reliable vibration-based structural health monitoring system, it is of significant importance to study the correlation between the identified modal parameters and the varying environmental conditions.

In view of the issues in the area of vibration-based damage identification and health monitoring of civil structures addressed above, the objectives of the research work presented in this dissertation are as follows.

1. Perform a comparative study of output-only system identification techniques applied to the Alfred Zampa Memorial Bridge (AZMB) based on dynamic field test data. The modal parameters of the AZMB identified using different methods and data from different types of test are compared for cross-validation purposes and also to investigate the performance of these output-only system identification methods when applied to bridge vibration data corresponding to different excitation sources.

2. Improve / extend the existing sensitivity-based finite element (FE) model updating techniques for damage identification of real-world structures. A FE model updating strategy is applied for damage identification of a full-scale seven-story reinforced concrete building slice tested on the UCSD-NEES shake table based on the modal parameters identified from the ambient vibration data.

3. Develop and deploy a state-of-the-art long-term continuous monitoring system on the Voigt Bridge. This instrumented bridge testbed will serve as a live laboratory in developing structural health monitoring technologies.

4. Investigate the effects of changing environmental conditions on the identified modal parameters of the Voigt Bridge and provide an objective criterion for damage detection under varying environmental conditions.

In order to overcome the scarcity of actual ambient vibration test data for studying the effects of various damage scenarios on system identification results for large and complex bridge structures, a simulation platform to simulate wind-induced vibration response of long-span suspension bridges is also developed in this study. The simulation is performed using a detailed three-dimensional FE model of the bridge and a state-of-the-art stochastic wind excitation model including both buffeting and self-excited forces. High fidelity model-based simulation provides an excellent framework for developing and validating system and damage

identification methods (for realistic damage scenarios) as well as for determining the optimum number, type and location of sensors to be deployed in order to maximize the information related to potential damage gathered in the form of dynamic signatures of the bridge.

The research work outlined above is essential for the development of robust and reliable health monitoring systems for large and complex real-world civil structures.

1.4 Organization of Dissertation

The content and structure of this dissertation is arranged as follows:

Chapter 2 presents a literature review of output-only system identification techniques including both time domain methods and frequency domain methods. These methods includes: (1) the natural excitation technique (NExT) combined with eigensystem realization algorithm (ERA); (2) the random decrement technique combined with ERA; (3) the covariance-driven stochastic subspace identification method; (4) the data-driven stochastic subspace identification method, (5) the Fourier spectra analysis method and (6) the enhanced frequency domain decomposition method. In order to improve the reliability and accuracy of identified modal parameters using NExT-ERA, the multiple-reference NExT-ERA (MNExT-ERA) is developed as an extension of the NExT-ERA in this study.

Chapter 3 provides a comparative study of system identification techniques applied to the Alfred Zampa Memorial Bridge (AZMB) based on the dynamic field test data. The modal parameters of the AZMB identified using different methods and data from different types of test are compared for cross-validation purposes and also to investigate the performance of these output-only system identification methods applied to bridge vibration data corresponding to different excitation sources. Finally, the identified natural frequencies and

mode shapes are compared with their analytical counterparts obtained from a three-dimensional (3D) finite element (FE) model used in the design phase of the AZMB.

Chapter 4 describes the simulation framework developed for wind-induced ambient vibration response of the Vincent Thomas Bridge (VTB) using a detailed 3D FE model of the bridge and a state-of-the-art stochastic wind excitation model. Based on simulated wind-induced ambient vibration data, modal parameters of the VTB are identified using the data-driven stochastic subspace identification method. The system identification results are verified by the computed eigenproperties of the bridge FE model, which allows to assess the performance of the above output-only system identification method when applied to wind-excited long-span suspension bridges.

Chapter 5 describes the sensitivity-based FE model updating techniques for vibration-based structural damage identification. A linear flat shell element is implemented in the element library of the MATLAB-based structural analysis software FEDEASLab, which is then integrated with the FE model updating algorithms used/developed in order to perform structural damage identification. A comparative study of the influence of different objective functions on the damage identification results is performed by using simulated data for a simply supported plate. Finally a sensitivity-based FE model updating strategy is applied for damage identification of a full-scale seven-story reinforced concrete building slice tested on the UCSD-NEES shake table based on the modal parameters identified from the ambient vibration data.

Chapter 6 develops and implements a state-of-the-art long-term continuous monitoring system on the Voigt Bridge Testbed. This monitoring system makes it possible to: (1) study the effects of varying environmental conditions such as temperature, wind characteristics, and humidity on the identified modal properties of the bridge; (2) allow for the

early identification of possible damages in the bridge structure and enable maintenance and repair works at the initial damage phase; and (3) evaluate the health condition of this structure shortly after a major catastrophic event such as an earthquake.

Chapter 7 develops an automated system identification procedure based on the data-driven stochastic subspace identification method. This automated system identification procedure is applied to identify the modal parameters of the Voigt Bridge as a function of time based on the data collected over a period of 50 days from the deployed structural monitoring system. Different environmental parameters are investigated during the monitoring period and then ARX models are used to correlate the identified natural frequencies with these measured environmental parameters. Finally an objective criterion is provided for damage detection under varying environmental conditions.

Chapter 8 summarizes and concludes this dissertation.

1.5 Summary

The vibration-based structural damage identification and health monitoring has been the subject of significant research in structural engineering in recent years. The basic premise of vibration-based structural damage identification is that changes in structural characteristics such as mass, stiffness, and energy dissipation mechanisms influence the vibration response characteristics of structures. Therefore, changes in modal parameters and quantities derived thereof are often used as damage indicators in structural damage identification and health monitoring.

A comprehensive literature review on the vibration-based structural damage identification methods are first presented in this chapter. Then the objectives and scope of this research and the organization of this dissertation are provided.

1.6 References

Abdel Wahab, M. and De Roeck, G. (1997). "Effect of temperature on dynamic system parameters of a highway bridge," *Structural Engineering International*, 7(4), 266-270.

Abdel Wahab, M., and De Roeck, G. (1999). "Damage detection in bridges using modal curvatures: Application to a real damage scenario." *Journal of Sound and Vibration*, 226(2), 217-235.

Aktan, E., Chase, S., Inman, D., and Pines, D. (2001). "Monitoring and Managing the Health of Infrastructure Systems," *Proceedings of the 2001 SPIE Conference on Health Monitoring of Highway Transportation Infrastructure*, Irvine, CA, March 6-8.

Bernal, D., and Gunes, B. (2002). "Damage localization in output-only systems: a flexibility based approach." *Proceedings of the 20th Modal Analysis Conference*, Los Angeles, 1185-1191.

Bernal, D., and Gunes, B. (2004). "Flexibility based approach for damage characterization: Benchmark application." *Journal of Engineering Mechanics*, ASCE, 130(1), 61-70.

Catabas, F., Lenett, M., Brown, D., Doebling, S., Farrar, C., and Turer, A. (1997). "Modal analysis of multi-reference impact test data for steel stringer bridges." *Proceedings of 15th International Modal Analysis Conference*, Orlando, Fl.

Cornwell, P., Doebling, S. W. and Farrar, C. R., (1999a). "Application of the strain energy damage detection method to plate-like structures." *Journal of Sound and Vibration*, 224(2), 359-374.

Cornwell, P., Farrar, C. R., Doebling, S.W, and Sohn, H. (1999b). "Environmental variability of modal properties," *Experimental Techniques*, 23(6), 45-48.

Doebling, S. W., Farrar, C. R., Prime, M. B., and Shevitz, D. W. (1996). "Damage identification and health monitoring of structural mechanical systems from changes in their vibration characteristics: A literature review." *Report No. LA-13070-MS*, Los Alamos National Laboratory, Los Alamos, New Mexico.

Duffey, T. A., Doebling, S. W., Farrar, C. R., Baker, W. E., and Rhee, W. H. (2001). "Vibration-Based Damage Identification in Structures Exhibiting Axial and Torsional Response." *Journal of Vibration and Acoustics*, 123(1): 84-91.

Farrar, C. R., and Jauregui, D. A. (1998). "Comparative study of damage identification algorithms applied to a bridge: I. experiment," *Smart Materials and Structures*, 7(5), 704-719.

Fraser, M. (2006). "Development and implementation of an integrated framework for structural health monitoring." *PhD Dissertation*, Department of Structural Engineering, University of California, San Diego, La Jolla, CA.

Friswell, M. I., and Mottershead, J. E. (1995). *Finite Element Model Updating in Structural Dynamics*, Kluwer Academic Publisher, Dordrecht, Boston, MA.

Guan, H. (2006). "Vibration-based structural health monitoring og highway bridges." *PhD Dissertation*, Department of Structural Engineering, University of California, San Diego, La Jolla, CA.

Guan, H., Karbhari, V. M., and Sikorsky, C. S. (2006). "Web-based structural health monitoring of a FRP composite bridge." *Computed-Aided Civil and Infrastructure Engineering*, 21(1), 39-56.

He, X., Fraser, M., Conte J. P., and Elgamal, A. (2007). "Investigation of environmental effects on identified modal parameters of the Voigt Bridge." *Proceedings of 18th Engineering Mechanics Division Conference of the ASCE*, Blacksburg, VA.

Ho, Y. K., and Ewins, D. J. (2000). "On structural damage identification with mode shapes." *Proceedings of COST F3 Conference on System Identification and Structural Health Monitoring*, Madrid, Spain, 677-686.

Jaishi, B., and Ren, W. X. (2005). "Structural finite element model updating using ambient vibration test results." *Journal of Structural Engineering*, ASCE, 131(4), 617-628.

Jaishi, B., and Ren, W. X. (2006). "Damage detection by finite element model updating using modal flexibility residual." *Journal of Sound and Vibration*, 290 (1-2), 369-387.

Kim, J. T., and Stubbs, N., (1995). "Model-uncertainty impact and damage-detection accuracy in plate girder." *Journal of Structural Engineering*, ASCE, 121, 1409-1417.

Kim, J. T., and Stubbs, N., (2002). "Improved damage identification method based on modal information." *Journal of Sound and Vibration*, 252(2), 223-238.

Maeck, J., and De Roeck, G. (1999). "Dynamic bending and torsion stiffness derivation from modal curvatures and torsion rates." *Journal of Sound and Vibration*, 225(1), 153-170.

Maeck, J., Abdel Wahab, M., Peeters, B., De Roeck, G., De Visscher, J., De Wilde, W. P., Ndambi, J. M., and Vantomme, J. (2000). "Damage identification in reinforced structures by dynamic stiffness determination." *Engineering Structures*, 22(10), 1339-1349.

Maeck, J. (2003). "Damage assessment of civil engineering structures by vibration monitoring." *PhD Dissertation*, K.U., Leuven, Belgium.

Mottershead J. E., and Friswell M. I. (1993). "Model updating in structural dynamics: A Survey." *Journal of Sound and Vibration*, 167(2), 347-375.

Pandey, A. K., Biswas, M., and Samman, M. M. (1991). "Damage detection from changes in curvature mode shapes." *Journal of Sound and Vibration*, 145(2), 321-332.

Pandey, A. K., and Biswas, M. (1994). "Damage detection in structures using changes in flexibility." *Journal of Sound and Vibration*, 169 (1), 3-17.

Peeters, B. and De Roeck, G. (2001). "One-year monitoring of the Z24-Bridge: environmental effects versus damage events," *Earthquake Engineering and Structural Dynamics*, 30(2), 149-171.

Salawu, O. S. (1997). "Detection of structural damage through changes in frequency: A review." *Engineering Structures*, 19(9), 718-723.

Shi, Z. Y., Law, S. S., and Zhang, L. M. (1998). "Structural damage localization from modal strain energy change." *Journal of Sound and Vibration*, 218(5), 825-844.

Shi, Z. Y., Law, S. S., and Zhang, L. M. (2000). "Structural damage detection from modal strain energy change." *Journal of engineering mechanics*, 126(12), 1216-1223.

Shi, Z.Y., Law, S. S., and Zhang, L.M. (2002). "Improved damage quantification from elemental modal strain energy change." *Journal of Engineering Mechanics*, ASCE, 128(5), 521-529.

Sohn, H., Farrar, C. R., Hemez, F. M., Shunk, D. D., Stinemates, D. W., and Nadler, B. R. (2003). "A review of structural health monitoring literature: 1996-2001." *Report No. LA-13976-MS*, Los Alamos National Laboratory, Los Alamos, New Mexico.

Stalling, J. M., Tedesco, J. W., El-Mihilmy, M., and McCauley, M. (2000). "Field performance of FRP bridge repair." *Journal of Bridge Engineering*, ASCE, 5(2), 107-113.

Stubbs, N. and Kim, J. T. (1996). "Damage localization in structures without baseline modal parameters." *AIAA Journal*, 34(8), 1644-1649.

Stubbs, N., Kim, J. T., and Farrar, C. (1995). "Field verification of a nondestructive damage localization and sensitivity estimator algorithm." *Proceedings of the 13th International Modal Analysis Conference*, Nashville, TN.

Stubbs, N., Kim, J. T., and Tapole, K. (1992). ''An efficient and robust algorithm for damage localization in offshore platforms.'' *ASCE 10th Structures Congress*, Reston, VA.

Sutter, R., Charles, C. J., Joanne, W., and Howard, M. A. (1988). "Comparison of several methods for calculating vibration mode shapes." *AIAA Journal*, 26(12),1506-1511.

Toksoy, T., and Aktan, A. E. (1994). "Bridge-condition assessment by modal flexibility." *Experimental Mechanics*, 34(3), 271-278.

Teughels, A., and De Roeck, G. (2004). "Structural damage identification of the highway bridge Z24 by FE model updating." *Journal of Sound and Vibration*, 278(3), 589-610.

Teughels, A., De Roeck, G., and Suykens, J. A. K. (2003). "Global optimization by coupled local minimizers and its application to FE model updating." *Computers & Structures*, 81(24-25) 2337-2351.

Teughels, A., Maeck, J., and De Roeck, G. (2002). "Damage assessment by FE model updating using damage functions." *Computers & Structures*, 80(25), 1869-1879.

Xia, Y., Hao, H., Zanardo, G., and Deeks, A. (2006). "Long term vibration monitoring of an RC slab: Temperature and humidity effect," *Engineering Structures*, 28(3), 441-452.

Yan, L. (2006). "Sensor Data Analysis and Information Extraction for Structural Health Monitoring." PhD Dissertation, Department of Structural Engineering, University of California, San Diego, La Jolla, CA.

Zhao, J., DeWolf, J. T. (1999). "Sensitivity study for vibration parameters used in damage detection." *Journal of Structural Engineering*, ASCE, 125(4), 410-417.

Chapter 2

Output-Only System Identification

2.1 Introduction

Experimental modal analysis has been widely used in the civil engineering research community to extract structural modal parameters (e.g., natural frequencies, damping ratios and mode shapes) from vibration measurements. These modal parameters are essential for structural damage identification and health monitoring.

In classical experimental modal analysis, the frequency response functions (FRFs) in the frequency domain or impulse response functions (IRFs) in the time domain are usually the basis of system identification algorithms, which produce accurate estimates of modal parameters provided that the signal-to-noise ratio of the dynamic measurement data is high enough. However, it is very difficult to obtain FRFs or IRFs in dynamic field tests of civil structures, since typically only the structure dynamic response (output) can be measured in such tests. Especially in the case of large and flexible bridges (such as suspension and cable-stayed bridges) with natural frequencies of the predominant vibration modes in the range 0-1 Hz, it is extremely challenging and costly to provide controlled excitation for significant level of response. Thus, system identification methods based on response-only measurements (output-only) have received increasing attention and obtained substantial progress in the civil engineering community in recent years. It is worth noting that these output-only system identification techniques are necessary and essential for developing a long-term continuous vibration-based structural health monitoring system. For continuously monitoring a structure

during its service life, it is impossible to measure the input signals and only structural response subjected to ambient/natural excitation sources such as traffic, wind, micro-tremors and combinations thereof can be measured. The experimental modal analysis techniques, which utilize only response measurements of a structure under operational or ambient conditions to identify the modal parameters, are also named as operational modal analysis (OMA).

Output-only system identification methods can be classified into two main groups, namely (1) frequency domain methods, and (2) time domain methods. The major frequency domain methods, such as the peak picking (PP) method, the frequency domain decomposition (FDD) technique (Brincker et al., 2000) and the enhanced FDD (EFDD) technique (Brincker et al., 2001), are developed based on response auto / cross-spectral densities. Time domain output-only system identification methods can be subdivided into two categories, namely (1) two-stage methods, and (2) one-stage methods. In the two-stage approaches, free vibration response estimates, including random decrement functions and response correlation functions, are obtained in the first stage from response measurements, and then modal parameters are identified in the second stage using any classical system identification algorithm based on impulse / free response function estimates. These classical system identification algorithms include the Ibrahim time domain (ITD) method (Ibrahim and Mikulcik, 1977), the multiple-reference Ibrahim time domain (MITD) method (Fukuzono, 1986), the least-squares complex exponential (LSCE) method (Brown et al., 1979), the polyreference complex exponential (PRCE) method (Vold et al., 1982), and the eigensystem realization algorithm (ERA) (Juang and Pappa, 1985). In contrast to two-stage approaches, one-stage system identification methods such as the data-driven stochastic subspace identification (SSI-DATA) method (Van Overschee and De Moor, 1996) can be used to identify modal parameters based on output-only measurements directly.

Brief review of different output-only system identification techniques is provided in following sections. These methods include: (1) the natural excitation technique (James et al., 1993) combined with ERA (NExT-ERA), (2) the random decrement technique (Cole, 1968) combined with ERA (RDT-ERA), (3) the covariance-driven stochastic subspace identification method (Van Overschee and De Moor, 1996), (4) SSI-DATA, (5) the Fourier spectra analysis (FSA) method (He et al., 2005) and (6) EFDD method. The first three methods belong to two-stage time domain system identification methods whereas the SSI-DATA is a one-stage system identification method, and the last two methods are frequency domain non-parametric methods. It should be noted that in order to improve the reliability and accuracy of identified modal parameters using NExT-ERA, the Multiple-reference NExT-ERA (MNExT-ERA) is developed as an extension of the NExT-ERA in this study.

2.2 Eigensystem Realization Algorithm

The eigensystem realization algorithm (ERA) was developed by Juang and Pappa (1985) for modal parameter identification and model reduction of linear systems. The discrete-time state-space representation of a finite dimensional, linear time invariant system of order *n* is given by

$$\begin{aligned} \mathbf{z}(k+1) &= \mathbf{A}\mathbf{z}(k) + \mathbf{B}\mathbf{u}(k) \\ \mathbf{x}(k) &= \mathbf{C}\mathbf{z}(k) + \mathbf{D}\mathbf{u}(k) \end{aligned} \tag{2.1}$$

where $\mathbf{A} \in \mathbb{R}^{n\times n}$, $\mathbf{B} \in \mathbb{R}^{n\times l}$, $\mathbf{C} \in \mathbb{R}^{m\times n}$, $\mathbf{D} \in \mathbb{R}^{m\times l}$ = state space matrices in discrete form; $\mathbf{z}(k) \in \mathbb{R}^{n}$ = state vector; $\mathbf{u}(k) \in \mathbb{R}^{l}$ = load vector (vector of loading functions); and $\mathbf{x}(k) \in \mathbb{R}^{m} = \begin{bmatrix} x_1(k) & x_2(k) & \cdots & x_m(k) \end{bmatrix}^T$, a column vector of size *m* (= number of measured / output channels) which represents the system response at discrete time $t = k(\Delta t)$ along the m

measured degrees of freedom (DOFs). Free vibration response (i.e., $\mathbf{u}(k)=0$) of the system can be obtained as

$$\mathbf{x}(0)=\mathbf{C}\mathbf{z}(0);\ \mathbf{x}(1)=\mathbf{C}\mathbf{A}\mathbf{z}(0);\ \mathbf{x}(2)=\mathbf{C}\mathbf{A}^2\mathbf{z}(0);\ \cdots\ \mathbf{x}(k)=\mathbf{C}\mathbf{A}^k\mathbf{z}(0) \tag{2.2}$$

Based on the free response vector, the following two $(m\times s)\times s$ Hankel matrices are formed

$$\mathbf{H}^s(0)=\begin{bmatrix}\mathbf{x}(1) & \mathbf{x}(2) & \cdots & \mathbf{x}(s)\\ \mathbf{x}(2) & \mathbf{x}(3) & \cdots & \mathbf{x}(s+1)\\ \vdots & \vdots & \ddots & \vdots\\ \mathbf{x}(s) & \mathbf{x}(s+1) & \cdots & \mathbf{x}(2s-1)\end{bmatrix}_{(m\times s\times s)} \tag{2.3}$$

$$\mathbf{H}^s(1)=\begin{bmatrix}\mathbf{x}(2) & \mathbf{x}(3) & \cdots & \mathbf{x}(s+1)\\ \mathbf{x}(3) & \mathbf{x}(4) & \cdots & \mathbf{x}(s+2)\\ \vdots & \vdots & \ddots & \vdots\\ \mathbf{x}(s+1) & \mathbf{x}(s+2) & \cdots & \mathbf{x}(2s)\end{bmatrix}_{(m\times s\times s)} \tag{2.4}$$

where s = an integer that determines the Hankel matrix size. Substituting equation (2.2) into equation (2.3), the Hankel matrix $\mathbf{H}^s(0)$ can be written

$$\mathbf{H}^s(0)=\begin{bmatrix}\mathbf{C}\mathbf{A}\mathbf{z}(0) & \mathbf{C}\mathbf{A}^2\mathbf{z}(0) & \cdots & \mathbf{C}\mathbf{A}^s\mathbf{z}(0)\\ \mathbf{C}\mathbf{A}^2\mathbf{z}(0) & \mathbf{C}\mathbf{A}^3\mathbf{z}(0) & \cdots & \mathbf{C}\mathbf{A}^{s+1}\mathbf{z}(0)\\ \vdots & \vdots & \ddots & \vdots\\ \mathbf{C}\mathbf{A}^s\mathbf{z}(0) & \mathbf{C}\mathbf{A}^{s+1}\mathbf{z}(0) & \cdots & \mathbf{C}\mathbf{A}^{2s-1}\mathbf{z}(0))\end{bmatrix}=\mathbf{H}_1\mathbf{H}_2 \tag{2.5}$$

in which

$$\mathbf{H}_1=\begin{bmatrix}\mathbf{C}\\ \mathbf{C}\mathbf{A}\\ \vdots\\ \mathbf{C}\mathbf{A}^{s-1}\end{bmatrix} \tag{2.6}$$

$$\mathbf{H}_2=\begin{bmatrix}\mathbf{A}\mathbf{z}(0) & \mathbf{A}^2\mathbf{z}(0) & \cdots & \mathbf{A}^s\mathbf{z}(0)\end{bmatrix}$$

Similarly substitute equation (2.2) into equation (2.4), the Hankel matrix $\mathbf{H}^s(1)$ can be written

$$\mathbf{H}^s(1) = \mathbf{H}_1 \mathbf{A} \mathbf{H}_2 \tag{2.7}$$

Therefore the state space system matrices **A** and **C** can be obtained

$$\begin{aligned} \mathbf{A} &= \mathbf{H}_1^{\dagger} \mathbf{H}^s(1) \mathbf{H}_2^{\dagger} \\ \mathbf{C} &= \mathbf{E}_m^T \mathbf{H}_1 \end{aligned} \tag{2.8}$$

where $\mathbf{H}_1^{\dagger}$ and $\mathbf{H}_2^{\dagger}$ = Moore-Penrose pseudo-inverse matrices of $\mathbf{H}_1$ and $\mathbf{H}_2$ respectively; $\mathbf{E}_m^T = [\mathbf{I}_m \quad \mathbf{0}]$, and $\mathbf{I}_m$ is the $m \times m$ unit matrix.

A singular value decomposition of Hankel matrix $\mathbf{H}^s(0)$ is performed as

$$\mathbf{H}^s(0) = \mathbf{U} \boldsymbol{\Sigma} \mathbf{V}^T = \begin{bmatrix} \mathbf{U}_n & \mathbf{U}_p \end{bmatrix} \begin{bmatrix} \boldsymbol{\Sigma}_n & \mathbf{0} \\ \mathbf{0} & \boldsymbol{\Sigma}_p \end{bmatrix} \begin{bmatrix} \mathbf{V}_n^T \\ \mathbf{V}_p^T \end{bmatrix} \tag{2.9}$$

The singular value decomposition is partitioned according to the selected number *n* of largest singular values as shown in the above equation in which the diagonal matrix $\boldsymbol{\Sigma}$ is split up in two diagonal matrices: $\boldsymbol{\Sigma}_n$ and $\boldsymbol{\Sigma}_p$ which contain the *n* largest (corresponding to the order of the realized system) and the remaining *p* relatively small singular values (corresponding to computational error or noise), respectively. Then the matrices of $\mathbf{H}_1$ and $\mathbf{H}_2$ can be obtained

$$\mathbf{H}_1 = \mathbf{U}_n \boldsymbol{\Sigma}_n^{1/2}; \quad \mathbf{H}_2 = \boldsymbol{\Sigma}_n^{1/2} \mathbf{V}_n^T \tag{2.10}$$

The state-space matrices **A** and **C** [see equation (2.8)] can be estimated by

$$\begin{aligned} \mathbf{A} &= \boldsymbol{\Sigma}_n^{-1/2} \mathbf{U}_n^T \mathbf{H}^s(1) \mathbf{V}_n \boldsymbol{\Sigma}_n^{-1/2} \\ \mathbf{C} &= \mathbf{E}_m^T \mathbf{U}_n \boldsymbol{\Sigma}_n^{1/2} \end{aligned} \tag{2.11}$$

Based on matrices **A** and **C**, the modal parameters (natural frequencies and damping ratios) of $N = n/2$ vibration modes can be obtained as

$$\omega_i = \left|\ln(\lambda_{2i-1})/\Delta t\right|$$
$$\zeta_i = -\cos(angle(\ln(\lambda_{2i-1}))); \quad i = 1,\ 2,\ \ldots,\ N \tag{2.12}$$

where $\lambda_i = i^{th}$ eigenvalue of matrix **A** and Δt = sampling time. It should be noted that λ_{2i-1} and λ_{2i} (i = 1, 2, …, N) are complex conjugate pairs of eigenvalues, each pair corresponding to a vibration mode, i.e., the natural frequency and damping ratio obtained from λ_{2i-1} are the same as those obtained from λ_{2i}. The vibration mode shapes are obtained as

$$\phi_i = \mathbf{C} \cdot \mathbf{T}_{2i-1} \tag{2.13}$$

where $\mathbf{T}_i$ denotes the i^{th} eigenvector of matrix **A**. Similarly, $\mathbf{T}_{2i-1}$ and $\mathbf{T}_{2i}$ (i = 1, 2, …, N) are complex conjugate pairs of eigenvectors, each pair corresponding to a vibration mode.

Based on the realized state-space model and the identified modal parameters, the contribution of the i^{th} mode to free vibration response can be derived as

$$\mathbf{x}_i(k) = \phi_i \lambda_{2i-1}{}^k \hat{\mathbf{z}}_{2i-1}(0) + \phi_i^* \lambda_{2i}{}^k \hat{\mathbf{z}}_{2i}(0) \tag{2.14}$$

in which the superscript * denotes the complex conjugate, and $\hat{\mathbf{z}}_i(0)$ = initial condition for the i^{th} modal response, which is easily to be obtained

$$\hat{\mathbf{z}}(0) = \mathbf{T}^{-1}\mathbf{z}(0) = \mathbf{T}^{-1}\mathbf{A}^{-1}\boldsymbol{\Sigma}_n^{1/2}\mathbf{V}_n^T\mathbf{E}_n^T \tag{2.15}$$

where $\mathbf{E}_n = [1\ \ \mathbf{0}]$, $\mathbf{z}(0)$ = initial conditions of state vector in equation (2.1) in the case of free vibration.

2.3 Natural Excitation Technique

The basic principle behind the natural excitation technique (NExT) is that the theoretical cross-correlation function of the response processes along two different DOFs of an ambient (broad-band) excited structure has the same analytical form as the impulse

response function (or, more generally, the free vibration response) of the structure (James et al., 1993; Farrar and James, 1997; Caicedo et al., 2004). Consider the differential equation of motion of an *N* DOF, linear time-invariant system

$$\mathbf{M}\ddot{\mathbf{x}}(t)+\mathbf{C}\dot{\mathbf{x}}(t)+\mathbf{K}\mathbf{x}(t)=\mathbf{P}\mathbf{f}(t) \tag{2.16}$$

with initial conditions $\mathbf{x}(0)=\mathbf{x}_0$ and $\dot{\mathbf{x}}(0)=\dot{\mathbf{x}}_0$, where $\mathbf{x}(t)$, $\dot{\mathbf{x}}(t)$, and $\ddot{\mathbf{x}}(t)$ = nodal displacement, velocity, and acceleration vectors, respectively; $\mathbf{M}, \mathbf{C}$, and $\mathbf{K}$ = mass, damping, and stiffness matrices, respectively; $\mathbf{P}$ = load distribution matrix; and $\mathbf{f}(t)$ = load vector function. Assuming that the ambient excitation function and structural responses are each stationary stochastic processes, equation (2.16) can be rewritten as

$$\mathbf{M}\ddot{\mathbf{X}}(t)+\mathbf{C}\dot{\mathbf{X}}(t)+\mathbf{K}\mathbf{X}(t)=\mathbf{P}\mathbf{F}(t) \tag{2.17}$$

where $\mathbf{X}(t)$, $\dot{\mathbf{X}}(t)$, and $\ddot{\mathbf{X}}(t)$ = displacement, velocity, and acceleration stochastic vector processes, respectively; $\mathbf{F}(t)$ = stochastic excitation vector process. Multiplying each term of equation (2.17) expressed at time $t=t+\tau$ with the scalar reference response quantity $\mathrm{X}_r(t)$ and taking the mathematical expectation (*E*) yields

$$\mathbf{M}E[X_r(t)\ddot{\mathbf{X}}(t+\tau)]+\mathbf{C}E[X_r(t)\dot{\mathbf{X}}(t+\tau)]+\mathbf{K}E[X_r(t)\mathbf{X}(t+\tau)]=\mathbf{P}E[X_r(t)\mathbf{F}(t+\tau)] \tag{2.18}$$

Under the condition that future input forces are uncorrelated with the current structural response in the reference channel *r*, equation (2.18) reduces to

$$\mathbf{M}E[X_r(t)\ddot{\mathbf{X}}(t+\tau)]+\mathbf{C}E[X_r(t)\dot{\mathbf{X}}(t+\tau)]+\mathbf{K}E[X_r(t)\mathbf{X}(t+\tau)]=\mathbf{0} \tag{2.19}$$

which is equivalent to (Lutes and Sarkani, 1997)

$$\mathbf{M}\ddot{\mathbf{R}}_{X_r\mathbf{X}}(\tau)+\mathbf{C}\dot{\mathbf{R}}_{X_r\mathbf{X}}(\tau)+\mathbf{K}\mathbf{R}_{X_r\mathbf{X}}(\tau)=\mathbf{0} \tag{2.20}$$

in which $\mathbf{R}_{X_r\mathbf{X}}(\tau)$ is the cross-correlation vector between $\mathrm{X}_r(t)$ and $\mathbf{X}(t)$. It is observed that the above differential equation governing the cross-correlation vector function $\mathbf{R}_{X_r\mathbf{X}}(\tau)$ is

identical to the equation of motion (2.16) under free vibration condition. It can also be shown that the correlation functions of the velocity and acceleration processes also satisfy equation (2.20) for positive values of the time lag τ (Beck et al. 1994). Once an estimation of the cross-correlation vector $\mathbf{R}_{X_r\mathbf{X}}(\tau)$ is obtained for a given reference channel, the ERA method reviewed above can be used to estimate the modal parameters.

In order to improve the reliability and accuracy of identified modal parameters, the multiple-reference NExT-ERA (MNExT-ERA) can be applied as an extension of NExT-ERA. In MNExT-ERA, instead of using a single (scalar) reference response channel as in NExT-ERA, a vector of reference channels (multiple reference channels) is used to obtain an output cross-correlation matrix. The correlation matrix between an *N*-DOF response vector $\mathbf{X}(t)$ (e.g., nodal displacements, velocities, or accelerations) and a subset of this response vector, $\mathbf{X}^r(t)$ (with N_r reference channels), is defined as

$$\mathbf{R}_{\mathbf{X}^r\mathbf{X}}(\tau)=\left[\mathbf{R}_{X_1^r\mathbf{X}}(\tau) \quad \mathbf{R}_{X_2^r\mathbf{X}}(\tau) \quad \cdots \quad \mathbf{R}_{X_{N_r}^r\mathbf{X}}(\tau)\right]_{N\times N_r} \tag{2.21}$$

It can be seen that each column of the cross-correlation matrix $\mathbf{R}_{\mathbf{X}^r\mathbf{X}}(\tau)$ is a cross-correlation vector between the system response vector and a single (scalar) reference response. The cross- correlation matrix $\mathbf{R}_{\mathbf{X}^r\mathbf{X}}(\tau)$ is then used to form Hankel matrices for application of ERA and identifying modal parameters

$$\mathbf{H}^s(0)=\begin{bmatrix}\mathbf{R}(1) & \mathbf{R}(2) & \cdots & \mathbf{R}(s)\\ \mathbf{R}(2) & \mathbf{R}(3) & \cdots & \mathbf{R}(s+1)\\ \vdots & \vdots & \ddots & \vdots\\ \mathbf{R}(s) & \mathbf{R}(s+1) & \cdots & \mathbf{R}(2s-1)\end{bmatrix}_{(m\times s)\times(N_r\times s)} \tag{2.22}$$

$$\mathbf{H}^{s}(1)=\begin{bmatrix} \mathbf{R}(2) & \mathbf{R}(3) & \cdots & \mathbf{R}(s+1) \\ \mathbf{R}(3) & \mathbf{R}(4) & \cdots & \mathbf{R}(s+2) \\ \vdots & \vdots & \ddots & \vdots \\ \mathbf{R}(s+1) & \mathbf{R}(s+2) & \cdots & \mathbf{R}(2s) \end{bmatrix}_{(m\times s)\times(N_r\times s)} \tag{2.23}$$

The basic idea behind the use of multiple reference channels (as opposed to the classical approach of using a single reference channel) is to avoid missing modes in the NExT-ERA identification process due to the proximity of the reference channel to nodes of these modes. In the case that a single cross-correlation vector does not contain significant information about a given vibration mode, the latter can still be identified accurately in MNExT-ERA through output cross-correlation functions based on other reference channels. In MNExT-ERA, the ERA is applied in its multiple-input, multiple-output formulation, but instead of forming the Hankel matrix based on the free vibration response of a truly multiple-input system, the block Hankel matrix is formed by including N_r cross-correlation vectors with different reference channels.

2.4 Random Decrement Technique

The random decrement technique (RDT) was developed by Cole and co-workers during the late 1960s and early 1970s at NASA (Cole, 1968, 1971, 1973; Chang, 1975). The basic idea behind this technique is to estimate random decrement (RD) functions by averaging time segments of the measurement data selected under certain triggering conditions. Considering two stationary processes $\mathbf{X}(t)$ and $\mathbf{Y}(t)$, the auto- $\mathbf{D}_{\mathbf{XX}}(\tau)$ and cross- $\mathbf{D}_{\mathbf{YX}}(\tau)$ RD functions are defined as conditional mean values

$$\begin{aligned} \mathbf{D}_{\mathbf{XX}}(\tau) &= E[\mathbf{X}(t+\tau)\,|\,C_{\mathbf{X}(t)}] \\ \mathbf{D}_{\mathbf{YX}}(\tau) &= E[\mathbf{Y}(t+\tau)\,|\,C_{\mathbf{X}(t)}] \end{aligned} \tag{2.24}$$

The first subscript refers to the process for which the mean value is calculated and the second subscript refers to the process for which the condition is fulfilled. The condition $C_{\mathbf{x}(t)}$ represents the triggering conditions. Under the assumption that the processes are not only stationary but also ergodic, the RD functions can be estimated as

$$\begin{aligned}\hat{\mathbf{D}}_{\mathbf{XX}}(\tau) &= \frac{1}{N}\sum_{i=1}^{N}\mathbf{x}(t_i+\tau)\,|\,C_{\mathbf{x}(t_i)} \\ \hat{\mathbf{D}}_{\mathbf{YX}}(\tau) &= \frac{1}{N}\sum_{i=1}^{N}\mathbf{y}(t_i+\tau)\,|\,C_{\mathbf{x}(t_i)}\end{aligned} \tag{2.25}$$

where *N* denotes the number of triggering points. From equations (2.24) and (2.25), it can be seen that the triggering condition simply describes a requirement for the initial condition of the time segments in the averaging process at time lag $\tau = 0$. Level crossing triggering condition $C^{L}_{X(t)}$, zero crossing triggering condition $C^{Z}_{X(t)}$, positive point triggering condition $C^{P}_{X(t)}$, and local extreme triggering condition $C^{E}_{X(t)}$ are the most often used triggering conditions in the application of RDT, which are defined as

$$\begin{aligned}C^{L}_{X(t)} &= \{X(t) = a\} \\ C^{Z}_{X(t)} &= \{X(t) = 0, \dot{X}(t) > 0\} \\ C^{P}_{X(t)} &= \{a_1 \le X(t) < a_2\} \\ C^{E}_{X(t)} &= \{a_1 \le X(t) < a_2, \dot{X}(t) = 0\}\end{aligned} \tag{2.26}$$

Asmussen (1997) introduced a generalized triggering condition $C^{G_A}_{X(t)}$ defined as

$$C^{G_A}_{X(t)} = \{a_1 \le X(t) < a_2, b_1 \le \dot{X}(t) < b_2\} \tag{2.27}$$

All different triggering conditions defined as equations (2.26) can be considered as specific formulation of this general triggering condition $C^{G_A}_{X(t)}$.

RD functions have been traditionally interpreted as free decays (Cole 1968, 1971, 1973). For example, if the triggering condition is $X(t)=a$ only, the RD free decay represents a step response and if the triggering condition is $\dot{X}(t)=v$ only, the free decay corresponds to an impulse response. In both of these cases, the modal parameters can be extracted using the RD functions by classical system identification algorithm such as ERA.

The relation between RD functions and correlation functions have been investigated by several studies (e.g., Vandiver et al., 1982; Brincker et al., 1990, 1991; Asmussen, 1997). Based on the assumption that the stochastic processes are stationary zero-mean Gaussian processes, the RD functions subject to the general triggering condition $C_{X(t)}^{G_A}$ can be derived (Asmussen, 1997)

$$\begin{aligned} D_{XX}(\tau) &= \frac{R_{XX}(\tau)}{\sigma_X^2}\tilde{a} - \frac{R'_{XX}(\tau)}{\sigma_{\dot{X}}^2}\tilde{b} \\ D_{YX}(\tau) &= \frac{R_{YX}(\tau)}{\sigma_X^2}\tilde{a} - \frac{R'_{YX}(\tau)}{\sigma_{\dot{X}}^2}\tilde{b} \end{aligned} \tag{2.28}$$

where $R_{XX}(\tau)$ and $R_{YX}(\tau)$ = auto and cross correlation functions of stationary processes; $R'_{XX}(\tau)$ and $R'_{YX}(\tau)$ = time derivative of the auto and cross correlation functions; σ_X^2 and $\sigma_{\dot{X}}^2$ = variance of process $X(t)$ and derivative process $\dot{X}(t)$, respectively; $\tilde{a}$ and $\tilde{b}$ are defined as

$$\tilde{a} = \frac{\int_{a_1}^{a_2} x f_X(x)dx}{\int_{a_1}^{a_2} f_X(x)dx}; \quad \tilde{b} = \frac{\int_{b_1}^{b_2} \dot{x} f_{\dot{X}}(\dot{x})d\dot{x}}{\int_{b_1}^{b_2} f_{\dot{X}}(\dot{x})d\dot{x}} \tag{2.29}$$

where $f_X(x)$ and $f_{\dot{X}}(\dot{x})$ are the probability density distribution functions of stochastic variables $X(t)$ and $\dot{X}(t)$, respectively. It is worth noting that the relation between RD functions subjected to any particular triggering condition and the correlation functions can be

determined directly from equations (2.28) and (2.29). Among the four trigger conditions defined in equation (2.26), the positive point triggering condition is perhaps the simplest triggering condition. Under this triggering condition, the RD functions are proportional to response correlation functions.

2.5 Covariance-Driven Stochastic Subspace Identification

Covariance-driven stochastic subspace identification (SSI-COV) is developed based on the stochastic system realization theory which is closely related to deterministic realization and was developed in 1970's (Akaike, 1974). Instead of the impulse response function (IRF) used in deterministic realization theory to identify the modal parameters such as ERA method, the stochastic realization theory uses the covariance of output-only response in the modal identification. Based on the previous works by Van Overschee and de Moor (1996), Peeters and de Roeck (2001), and Zhang (2005), the SSI-COV is briefly reviewed in this section. Equation (2.1) is rewritten here

$$\begin{aligned} \mathbf{z}(k+1) &= \mathbf{A}\mathbf{z}(k) + \mathbf{B}\mathbf{u}(k) \\ \mathbf{x}(k) &= \mathbf{C}\mathbf{z}(k) + \mathbf{D}\mathbf{u}(k) \end{aligned} \tag{2.30}$$

In practice, the input function $\mathbf{u}$ is often unknown / unmeasured and only the response of the structure is measured. Thus, the discrete-time state-space model in equations (2.30) can be extended to the following stochastic version thereof

$$\begin{aligned} \mathbf{z}(k+1) &= \mathbf{A}\mathbf{z}(k) + \mathbf{w}(k) \\ \mathbf{x}(k) &= \mathbf{C}\mathbf{z}(k) + \mathbf{v}(k) \end{aligned} \tag{2.31}$$

where state-space matrices **A** and **C** are the same as in equations (2.1) and (2.30): **A** = state transition matrix, which completely characterizes the dynamics of the system through its eigenproperties, and **C** = output matrix that specifies how the inner states are transformed into

the measured system response/output; $\mathbf{w}(k) \in \mathbb{R}^n$ = process noise due to external disturbances and modeling inaccuracies (i.e, missing high-frequency dynamics) and unknown input excitation (undistinguishable from the external disturbances); and $\mathbf{v}(k) \in \mathbb{R}^m$ = measurement noise due to sensor inaccuracies and also unknown input excitation (feed-through term). Both noise terms $\mathbf{w}(k)$ and $\mathbf{v}(k)$ are assumed to be zero-mean, white vector sequences with the following covariance matrix:

$$E\left[\begin{pmatrix}\mathbf{w}(i)\\ \mathbf{v}(i)\end{pmatrix}\begin{pmatrix}\mathbf{w}(j)^T & \mathbf{v}(j)^T\end{pmatrix}\right]=\begin{bmatrix}\mathbf{Q} & \mathbf{S}\\ \mathbf{S}^T & \mathbf{R}\end{bmatrix}\delta_{ij} \tag{2.32}$$

where E[…] is the mathematical expectation operator; δ_{ij} = Kronecker delta; and **Q, R, S** = process and measurement noise auto / cross-covariance matrices.

The stochastic process is assumed to be stationary with zero-mean, i.e.,

$$E\left[\mathbf{z}(k)\right]=0; \quad E\left[\mathbf{z}(k)\mathbf{z}^T(k)\right]=\boldsymbol{\Sigma}^z \tag{2.33}$$

where the state covariance matrix is independent of the time k. Both noise terms $\mathbf{w}(k)$ and $\mathbf{v}(k)$ are independent of state process $\mathbf{z}(k)$

$$E\left[\mathbf{z}(k)\mathbf{w}^T(k)\right]=0; \quad E\left[\mathbf{z}(k)\mathbf{v}^T(k)\right]=0 \tag{2.34}$$

The output covariance matrix is defined as

$$\boldsymbol{\Lambda}_i = E\left[\mathbf{x}(k+i)\mathbf{x}^T(k)\right] \tag{2.35}$$

then we can find

$$\boldsymbol{\Lambda}_0 = E\left[\mathbf{x}(k)\mathbf{x}^T(k)\right]=E\left[(\mathbf{C}\mathbf{z}(k)+\mathbf{v}(k))(\mathbf{C}\mathbf{z}(k)+\mathbf{v}(k))^T\right]=\mathbf{C}\boldsymbol{\Sigma}^z\mathbf{C}^T+\mathbf{R} \tag{2.36}$$

The state and output covariance matrix $\mathbf{G}$ is defined as

$$\mathbf{G} = E\left[\mathbf{z}(k+1)\mathbf{x}^T(k)\right]=E\left[(\mathbf{A}\mathbf{z}(k)+\mathbf{w}(k))(\mathbf{C}\mathbf{z}(k)+\mathbf{v}(k))^T\right]=\mathbf{A}\boldsymbol{\Sigma}^{\mathbf{z}}\mathbf{C}^T+\mathbf{S} \tag{2.37}$$

Based on these definitions, the following properties are readily be derived

$$\begin{aligned} \mathbf{\Sigma}^z &= \mathbf{A}\Sigma^z\mathbf{A}^T + \mathbf{Q}; \quad \mathbf{\Lambda}_0 = \mathbf{C}\mathbf{\Sigma}^z\mathbf{C}^T + \mathbf{R} \\ \mathbf{G} &= \mathbf{A}\mathbf{\Sigma}^z\mathbf{C}^T + \mathbf{S}; \quad \mathbf{\Lambda}_i = \mathbf{C}\mathbf{A}^{i-1}\mathbf{G} \end{aligned} \tag{2.38}$$

The property $\mathbf{\Lambda}_i = \mathbf{C}\mathbf{A}^{i-1}\mathbf{G}$ in the above equation indicates that the output covariance can be considered as Markov parameters (impulse responses) of a deterministic linear time invariant system $\mathbf{A}$, $\mathbf{G}$, $\mathbf{C}$, and $\mathbf{\Lambda}_0$. Thus the classical deterministic realization theory can be extended to stochastic systems. In practice, the covariance $\mathbf{\Lambda}_i$ can be estimated form measurement data

$$\mathbf{\Lambda}_i = E\left[\mathbf{x}(k+i)\mathbf{x}^T(k)\right] = \lim \frac{1}{N}\sum_{k=0}^{N-1}\mathbf{x}(k+i)\mathbf{x}^T(k) \tag{2.39}$$

where the second equation follows the ergodicity assumption.

In order to estimate $\mathbf{A}$, $\mathbf{C}$, and $\mathbf{G}$ though decomposition of the covariance matrix, two block Toeplitz matrices $\mathbf{T}(0)$ and $\mathbf{T}(1)$ are defined

$$\mathbf{T}(0) = \begin{bmatrix} \Lambda_i & \Lambda_{i-1} & \cdots & \Lambda_1 \\ \Lambda_{i+1} & \Lambda_i & \cdots & \Lambda_2 \\ \vdots & \vdots & \ddots & \vdots \\ \Lambda_{2i-1} & \Lambda_{2i-2} & \cdots & \Lambda_i \end{bmatrix} = \mathbf{O}_i\mathbf{\Gamma}_i = \begin{bmatrix} \mathbf{C} \\ \mathbf{C}\mathbf{A} \\ \vdots \\ \mathbf{C}\mathbf{A}^{i-1} \end{bmatrix} \begin{bmatrix} \mathbf{A}^{i-1}\mathbf{G} & \mathbf{A}^{i-2}\mathbf{G} & \cdots & \mathbf{G} \end{bmatrix} \tag{2.40}$$

$$\mathbf{T}(1) = \begin{bmatrix} \Lambda_{i+1} & \Lambda_i & \cdots & \Lambda_2 \\ \Lambda_{i+2} & \Lambda_{i+1} & \cdots & \Lambda_3 \\ \vdots & \vdots & \ddots & \vdots \\ \Lambda_{2i} & \Lambda_{2i-1} & \cdots & \Lambda_{i+1} \end{bmatrix} = \mathbf{O}_i\mathbf{A}\mathbf{\Gamma}_i \tag{2.41}$$

where the matrices $\mathbf{O}_i$ and $\mathbf{\Gamma}_i$ are called the extended observability matrix and the reversed extended stochastic controllability matrix, respectively. Following the same procedure as described in the ERA section, both matrices $\mathbf{O}_i$ and $\mathbf{\Gamma}_i$ can be obtained through the singular value decomposition of the block Toeplitz matrix $\mathbf{T}(0)$. Then the system matrices **A** and **C** as well as modal parameters are ready to be identified.

2.6 Data-Driven Stochastic Subspace Identification

The data-driven stochastic subspace identification (SSI-DATA) extracts a linear state-space model of the system considered using output-only measurement data directly (Van Overschee and De Moor, 1996; Peeters and De Roeck, 2001). Compared to two-stage time-domain system identification methods such as SSI-COV and NExT-ERA, SSI-DATA does not require any pre-processing of the data to calculate auto / cross-correlation functions or auto / cross-spectra of output data (i.e., SSI-DATA is a one-stage system identification method). In addition, robust numerical techniques such as QR factorization, singular value decomposition and least squares are involved in this method. A brief review of this method is presented next.

Considering the discrete-time stochastic state-space model in equations (2.30), the output block Hankel matrix is defined as

$$\mathbf{X}_{0|2i-1} = \frac{1}{\sqrt{j}} \left[\begin{array}{cccc} \mathbf{x}(0) & \mathbf{x}(1) & \cdots & \mathbf{x}(j-1) \\ \vdots & \vdots & \vdots & \vdots \\ \mathbf{x}(i-2) & \mathbf{x}(i-1) & \cdots & \mathbf{x}(i+j-3) \\ \mathbf{x}(i-1) & \mathbf{x}(i) & \cdots & \mathbf{x}(i+j-2) \\ \hline \mathbf{x}(i) & \mathbf{x}(i+1) & \cdots & \mathbf{x}(i+j-1) \\ \mathbf{x}(i+1) & \mathbf{x}(i+2) & \cdots & \mathbf{x}(i+j) \\ \vdots & \vdots & \cdots & \vdots \\ \mathbf{x}(2i-1) & \mathbf{x}(2i) & \cdots & \mathbf{x}(2i+j-2) \end{array}\right] = \begin{bmatrix} \mathbf{X}_{0|i-1} \\ \mathbf{X}_{i|2i-1} \end{bmatrix} = \begin{bmatrix} \mathbf{X}_p \\ \mathbf{X}_f \end{bmatrix} = \left[\begin{array}{c} (\text{'past'}) \updownarrow \\ \hline (\text{'future'}) \updownarrow \end{array}\right] \tag{2.42}$$

where the first subscript 0 and i denotes the time index of the first element of the first column and the second subscript i-1 and 2i-1 denotes the time index of the last element of the first column. The columns j is typically set to be n_x -2i-1 (n_x is sampling points of the response), implying all the measured data are used (It is assumed that $j \to \infty$ for all theoretical derivations). The subscript p and f represent the past and future. The matrices $\mathbf{X}_p$ and $\mathbf{X}_f$ are defined by splitting the output Hankel matrix $\mathbf{X}_{0|2i-1}$ into two sub-matrices of i block rows.

Another division is obtained by shifting the first block row of the future matrix $\mathbf{X}_f$ to the past matrix $\mathbf{X}_p$

$$\mathbf{X}_{0|2i-1} = \begin{bmatrix} \mathbf{X}_{0|i} \\ \mathbf{X}_{i+1|2i-1} \end{bmatrix} = \begin{bmatrix} \mathbf{X}_p^+ \\ \mathbf{X}_f^- \end{bmatrix} = \begin{bmatrix} ('\text{past}') \updownarrow (m+1)i \\ ('\text{future}') \updownarrow (m-1)i \end{bmatrix} \tag{2.43}$$

The SSI-Data algorithm starts by the orthogonal projection of the row space of future output, $\mathbf{X}_{i|2i-1}$ into the row space of past output, $\mathbf{X}_{0|i-1}$ which is defined (Van Overschee and De Moor, 1996)

$$\mathbf{Y}_i = \mathbf{X}_f \Big/ \mathbf{X}_p = \mathbf{X}_{i|2i-1} \Big/ \mathbf{X}_{0|i-1} = \mathbf{X}_{i|2i-1}\mathbf{X}_{0|i-1}{}^T(\mathbf{X}_{0|i-1}\mathbf{X}_{0|i-1}{}^T)^\dagger \mathbf{X}_{0|i-1} \tag{2.44}$$

where the symbol '†' denotes the Moore-Penrose pseudo-inverse operator. The projection of equation (2.44) can be computed by the numerically robust QR factorization. All the useful past information to predict the future are kept by this projection and the (uncorrelated) noise is canceled out. A singular value decomposition of the projection $\mathbf{Y}_i$ is performed as

$$\mathbf{Y}_i = \mathbf{U}\mathbf{\Sigma}\mathbf{V}^T = \begin{bmatrix} \mathbf{U}_n & \mathbf{U}_p \end{bmatrix} \begin{bmatrix} \mathbf{\Sigma}_n & \mathbf{0} \\ \mathbf{0} & \mathbf{0} \end{bmatrix} \begin{bmatrix} \mathbf{V}_n^T \\ \mathbf{V}_p^T \end{bmatrix} = \mathbf{U}_n \mathbf{\Sigma}_n \mathbf{V}_n^T \tag{2.45}$$

It has been proved that the projection $\mathbf{Y}_i$ can be written as the product of extended observability matrix $\mathbf{O}_i$ and the Kalman filter state sequence $\hat{\mathbf{Z}}_i$

$$\mathbf{Y}_i = \mathbf{O}_i \hat{\mathbf{Z}}_i \tag{2.46}$$

where $\mathbf{O}_i = \begin{bmatrix} \mathbf{C}^T & (\mathbf{CA})^T & \cdots & (\mathbf{CA}^{i-1})^T \end{bmatrix}^T$ and $\hat{\mathbf{Z}}_i = \begin{bmatrix} \hat{\mathbf{z}}(i) & \hat{\mathbf{z}}(i+1) & \cdots & \hat{\mathbf{z}}(i+j-1) \end{bmatrix}$. Based equations (2.45) and (2.46) , matrices $\mathbf{O}_i$ and $\hat{\mathbf{Z}}_i$ can be determined by

$$\begin{aligned} \mathbf{O}_i &= \mathbf{U}_n \mathbf{\Sigma}_n^{1/2} \\ \hat{\mathbf{Z}}_i &= \mathbf{O}_i^\dagger \mathbf{Y}_i \end{aligned} \tag{2.47}$$

Another projection similar to projection $\mathbf{Y}_i$ is defined as

$$\mathbf{Y}_{i-1} = \mathbf{X}_f^- \Big/ \mathbf{X}_p^+ = \mathbf{X}_{i+1|2i-1} \Big/ \mathbf{X}_{0|i} \tag{2.48}$$

Similar to equation (2.46), projection $\mathbf{Y}_{i-1}$ can be written as

$$\mathbf{Y}_{i-1} = \mathbf{O}_{i-1}\hat{\mathbf{Z}}_{i+1} \tag{2.49}$$

The extended observaility matrix $\mathbf{O}_{i-1}$ is easily obtained by removing the last block of the matrix $\mathbf{O}_i$ (the last *m* rows) and then the state sequence

$$\hat{\mathbf{Z}}_{i+1} = \mathbf{O}_{i-1}{}^{\dagger}\mathbf{Y}_{i-1} \tag{2.50}$$

Once the Kalman filter state estimate sequences $\hat{\mathbf{Z}}_i$ and $\hat{\mathbf{Z}}_{i+1}$ are obtained from the output-only data, the system matrices **A** and **C** can be estimated using the following linear functions

$$\begin{pmatrix} \hat{\mathbf{Z}}_{i+1} \\ \mathbf{X}_{i|i} \end{pmatrix} = \begin{pmatrix} \mathbf{A} \\ \mathbf{C} \end{pmatrix} \hat{\mathbf{Z}}_i + \begin{pmatrix} \boldsymbol{\rho}_w \\ \boldsymbol{\rho}_v \end{pmatrix} \tag{2.51}$$

where $\boldsymbol{\rho}_w$ and $\boldsymbol{\rho}_v$ are the residuals uncorrelated with the Kalman state sequences and outputs. The equation (2.51) can be solved in a least squares sense

$$\begin{pmatrix} \tilde{\mathbf{A}} \\ \tilde{\mathbf{C}} \end{pmatrix} = \begin{pmatrix} \hat{\mathbf{Z}}_{i+1} \\ \mathbf{X}_{i|i} \end{pmatrix} \hat{\mathbf{Z}}_i{}^{+} \tag{2.52}$$

Modal parameters can be identified based on equations (2.12) and (2.13) using the estimated system matrices $\tilde{\mathbf{A}}$ and $\tilde{\mathbf{C}}$.

2.7 Non-Parametric Frequency Domain Methods

2.7.1 Fourier Spectral Analysis Technique

This method might be the simplest method to estimate the natural frequency and mode shapes using only response measurements subjected to ambient excitations. In this method, the natural frequencies and vibration mode shapes are determined based on the Fourier amplitude spectra (FAS) and Fourier phase spectra (FPS) of the multi-channel response data. Each output channel is subjected to a Fast Fourier Transform (FFT). The natural frequencies of the system are identified as the frequencies corresponding to FAS peaks presented in a significant number of channels. The mode shape associated with an identified natural frequency is obtained as the ratios of the magnitudes of the FAS peaks at the various channels to the magnitude of the FAS peak at a reference channel making use of the FPS's to obtain the phase (i.e., in-phase or 180 degrees out-of-phase) information. A few drawbacks of the FSA method applied to measured ambient vibration data are: (1) modal damping ratios cannot be estimated with reasonable accuracy; (2) the accuracy of modal frequency estimation is limited to the frequency resolution of response Fourier spectra; (3) closely spaced modes cannot be identified separately, and (4) FSA is not suitable for non-classically damped structures. Therefore, this method is usually applied for the preliminary signal analysis.

2.7.2 Frequency Domain Decomposition Technique

The frequency domain decomposition (FDD) method, a non-parametric frequency-domain approach, is an extension of the basic frequency domain (BFD) approach referred to as peak picking technique. According to the FDD technique, the modal parameters are estimated through SVD of the power spectral density (PSD) matrix performed at all discrete frequencies. Considering a lightly damped system, the number of vibration modes

contributing significantly to a given cross-spectral density (CSD) function at a particular frequency is limited to a small number (usually 1 or 2). Through the above mentioned SVD, CSD functions are decomposed into single-degree-of-freedom (SDOF) CSD functions, each corresponding to a single vibration mode of the dynamic system. In the EFDD method (Brincker et al. 2001), the natural frequency and damping ratio of a vibration mode are identified from the SDOF CSD function corresponding to that mode. For this purpose, the SDOF CSD function is taken back to the time domain by inverse Fourier transformation, and the frequency and damping ratio of the mode considered are estimated from the zero-crossing times and the logarithmic decrement, respectively, of the corresponding SDOF auto-correlation function.

It is worth noting that since only the data near the peak of the singular values plot are used to estimate correlation function of the corresponding SDOF system, it may cause the bias error in the damping estimation. Most recently, frequency-spatial domain decomposition has been developed to solve this problem making use of the property of the unitary singular matrix to obtain the enhanced output PSD by pre- and post- multiplying a singular vector corresponding to a certain natural frequency (Zhang et al., 2005). In this way the output PSD is enhanced around the modal frequency and is attenuated when the frequency beyond this region. Therefore, the singular vector corresponding to this modal frequency works like a modal filter. More details about the EFDD method can be found in Brincker et al. (2000, 2001a, b), Gade et al. (2005), and Zhang et al. (2005).

2.8 Summary

Output-only system identification techniques are briefly reviewed in this chapter. These methods are: (1) the natural excitation technique combined with eigensystem realization

algorithm (NExT-ERA) and the multiple-reference NExT-ERA (MNExT-ERA); (2) the random decrement technique combined with ERA (RDT-ERA), (3) the covariance-driven stochastic subspace identification (SSI-COV) method, (4) the data-driven stochastic subspace identification (SSI-DATA) method, (5) the Fourier spectra analysis (FSA) method and (6) the enhanced frequency domain decomposition (EFDD) method. NExT-ERA / MNExT-ERA, RDT-ERA, and SSI-COV belong to two-stage time domain system identification methods whereas the SSI-DATA is a one-stage time domain system identification method. The last two methods are frequency domain non-parametric methods. These output-only system identification techniques are necessary and essential for developing a long-term continuous vibration-based structural health monitoring system.

2.9 References

Akaike, H. (1974). "Stochastic theory of minimal realization." *IEEE Trans. Automatic Control*, AC-19.

Allemang, R. J., and Brown, D. L. (1982). "A correlation coefficient for modal vector analysis." *Proceedings of 1st International Modal analysis Conference, Society of Experimental mechanics*, Bethel, Conn., 110-116.

Asmussen, J. C. (1997). "Modal analysis based on the random decrement technique—application to civil engineering structures." *Ph. D dissertation*, University of Aalborg, Denmark.

Beck, J. L., May, B. S., and Polidori, D. C. (1994). "Determination of modal parameters from ambient vibration data for structural health monitoring." Proceedings of 1st World Conference on structural Control, Los Angeles, California, TA3: 3-12

Brincker, R., Krenk, S. and Jensen, J. L. (1990). "Estimation of correlation functions by random decrement technique." *Proceedings of Skandinavisk Forum for Stokastisk Mechanik*, Lund, Sweden.

Brincker, R., Krenk, S. and Jensen, J. L. (1991). "Estimation of correlation functions by random decrement technique." *Proceedings of the 9th International Modal Analysis Conference and Exhibit*, Firenze, Italy.

Brincker, R., Zhang, L., and Andersen, P. (2000). "Modal identification from ambient responses using frequency domain decomposition." *Proceedings of the 18th IMAC*, San Antonio, Texas.

Brincker, R., Ventura, C., and Andersen, P. (2001). "Damping estimation by frequency domain decomposition." *Proceedings of IMAC XIX*, Kissimmee, USA.

Brincker, R., Zhang, L. M., and Andersen, P. (2001). "Modal identification of output-only systems using frequency domain decomposition." *Smart Materials and Structures*, 10(3), 441-445.

Brown, D. L., Allemang, R. J., Zimmerman, R., and Mergeay, M. (1979). "Parameters estimation techniques for modal analysis." *Society of Automotive Engineers*, Technique Paper 790221.

Caicedo, J. M., Dyke, S. J., and Johnson, E. A. (2004). "Natural excitation technique and eigensystem realization algorithm for phase I of the IASC-ASCE benchmark problem: simulated data." Journal of Engineering Mechanics, ASCE, 130(1), 49-60.

Chang, C. S. (1975). "Study of dynamic characteristics of aerodynamic systems utilizing random decrement signature." NASA CR-132563.

Cole, H. A. (1968). "On-the-line analysis of random vibrations." *AIAA paper* No. 68-288.

Cole, H. A. (1971). "Failure detection of a space shuttle wing by random decrement." NASA TMX-62,041.

Cunha, A. and Caetano, E. (2005). "From input-output to output-only modal identification of civil engineering structures." Proceedings of the 1st International Operational Modal Analysis Conference, Copenhagen, Denmark.

Cole, H. A. (1973). "On-line failure detection and damping measurements of aerospace structure by random decrement signature." NASA CR-2205.

Farrar, C. R., and James III, G. H. (1997). "System identification from ambient vibration measurements on a bridge." Journal of Sound and Vibration, 205 (1), 1-18.

Fukuzono, K. (1986). "Investigation of multiple-reference Ibrahim time domain modal parameter estimation technique." *M.S. thesis*, University of Cincinnati.

Gade, S., Moller, B.N., Herlufsen, H., and Konstantin-Hansen, H. (2005). "Frequency domain techniques for operational modal analysis." *Proceedings of the 1st International Operational Modal Analysis Conference*, Copenhagen, Denmark.

Ibrahim, S. R., and Mikulcik, E. C. (1977). "A method for the direct identification of vibration parameters from the free response." *The Shock and Vibration Bulletin*, 47(4), 183-198.

James, G. H., Carne, T. G., and Lauffer, J. P. (1993). "The natural excitation technique for modal parameters extraction from operating wind turbines." *Report No. SAND92-1666, UC-261*, Sandia National Laboratories, Sandia, NM, USA.

Juang, J. N., and Pappa, R. S. (1985). "An eigensystem realization Algorithm for modal parameters identification and model reduction." *Journal of Guidance, Control and Dynamics*, 8(5), 620-627.

Lutes, L. D., and Sarkani, S. (1997). *Stochastic Analysis of Structural and Mechanical Vibrations*. Prentice Hall.

Peeters, B., and De Roeck, G. (2001). "Stochastic system identification for operational modal analysis: A review." *Journal of Dynamic Systems, Measurement, and Control*, 123(4), 659-667.

Van Overschee, P., and De Moor, B. (1996). *Subspace Identification for Linear Systems: Theory-Implementation-Applications*, Kluwer Academic Publishers, Norwell, Massachusetts, USA.

Vandiver, J. K., Dunwoody, A. B., Campbell, R. B., and Cook, M. F. (1982). "A mathematical basis for the random decrement vibration signature analysis technique." *Journal of Mechanical Design*, 104, 307-313.

Vold, H., Kundrat, J., Rocklin, G. T., and Russel, R. (1982). "A Multi-input modal estimation algorithm for mini-computers." *SAE Technical Paper Series*, No. 820194.

Zhang, L., Wang, T., and Tamura, Y. (2005). "Frequency-spatial domain decomposition technique with application to operational modal analysis of civil engineering structures." *Proceedings of the 1st International Operational Modal Analysis Conference*, Copenhagen, Denmark.

Chapter 3

Dynamic Testing and System Identification of Alfred Zampa Memorial Bridge

3.1 Introduction

Dynamic tests of bridges are usually subdivided into two types: forced and ambient vibration tests. Forced vibration tests are directly related to the application of classical experimental modal analysis (Ewins, 2003), in which the bridge is usually excited by artificial means such as eccentric or linear inertial shakers (Halling et al., 2001; Brownjohn et al., 2003) or drop weights (Abdel Wahab and De Roeck, 1998). A sudden impact on the bridge induces a condition of free vibration. In previous experimental studies, some creative methods have been employed to generate impact loads in dynamic testing of bridges. For example, in a study by Delaunay et al. (1999), the horizontal impulsive force was generated by the sudden release of a tension cable that connected the bridge to a tug-boat. In another study by Huang et al. (1999), impact forces in the longitudinal and transverse directions were generated by the sudden braking of a truck at a specified location on the bridge, whereas vertical impact forces were generated by simply letting the rear wheels of the truck drop from the top of a concrete block. Earthquake excitation (when measured) provides a natural source of forced vibration for bridge and other civil structures (Smyth et al., 2003).

In general, forced vibration tests provide more accurate modal identification results than ambient vibration tests, since (a) well-defined input excitations are used in the modal identification procedure, and (b) the excitations can be optimized to enhance the response of

the vibration modes of interest. However, in the case of large and flexible bridges (such as suspension and cable-stayed bridges) with natural frequencies of the predominant modes in the range 0-1Hz, it is challenging and costly to provide controlled excitation for significant level of response.

In contrast, ambient vibration tests take advantage of "free" or natural excitation sources such as traffic, wind, micro-tremors and combinations thereof. Moreover, since ambient vibration tests do not interrupt service of the test structure (e.g., shutting down traffic during bridge testing), they can be used readily for long term continuous structural health monitoring applications. Ambient vibration tests have been successfully applied to a variety of bridge structures such as the Vincent Thomas suspension bridge (Abdel-Ghaffar and Housner, 1978), Golden Gate suspension bridge (Abdel-Ghaffar and Scanlan, 1985), Roebling suspension bridge (Ren et al., 2004a), Safti Link curved cable-stayed bridge (Brownjohn et al., 1999), Vasco da Gama cable-stayed bridge (Cunha et al,. 2001), twin curved cable-stayed bridges on the north and south sides of Malpensa airport in Milan (Gentile and Martinez y Cabrera, 2004), Brent-Spence truss bridge (Harik et al., 1997) and Tennesse River steel arch bridge (Ren et al., 2004b). In these studies, system identification based on ambient vibration test data provided accurate estimates of natural frequencies and mode shapes despite the relatively low amplitude of the measured vibrations. Even though modal damping ratios / factors can be satisfactorily identified using ambient vibration data, they typically require the use of advanced system identification methods due to the low amplitude and relatively low signal-to-noise ratio of such data. Therefore, results on identification of modal damping ratios using ambient vibration data are scarce.

This chapter describes in detail a set of dynamic tests performed on the Alfred Zampa Memorial Bridge (AZMB). They include ambient vibration tests (mainly wind-induced) and

forced vibration tests based on controlled traffic loads and vehicle-induced impact loads. The vibration response of the bridge was measured using an array of 34 uni-axial and 10 tri-axial force-balanced accelerometers from the mobile field laboratory of the George E. Brown, Jr. Network for Earthquake Engineering Simulation (NEES) field testing site at the University of California at Los Angeles (NEES@UCLA). These accelerometers were installed at 25 selected stations along both sides of the bridge deck. Instead of roving accelerometers around to the different measurement stations with fixed accelerometers at one or more reference stations (as commonly done for dynamic testing of bridges), a total of 64 channels of acceleration response data were recorded simultaneously in the tests described here, including 25 vertical, 25 transversal, and 14 longitudinal motion components. These dynamic field tests are the first ones conducted on the AZMB, and they were performed just before the bridge opening to traffic. Therefore, these tests provided a unique opportunity to determine the dynamic properties of the bridge in its as-built (baseline) condition with no previous traffic loads or seismic excitation.

Three different output-only system identification algorithms were applied to dynamic field test data collected from the AZMB for modal identification. These methods consist of: (1) the multiple-reference natural excitation technique combined with eigensystem realization algorithm (MNExT-ERA) (Juang and Pappa, 1985; James et al., 1993, He et al., 2006), a two-stage time-domain system identification method; (2) the data-driven stochastic subspace identification (SSI-DATA) method (Van Overschee and De Moor, 1996), a one-stage time-domain system identification method; and (3) the enhanced frequency domain decomposition (EFDD) technique (Brincker et al., 2001), a non-parametric frequency domain system identification method which is a sophisticated extension of the well-known peak picking technique. The modal parameters of the AZMB identified using different methods and data

from different types of test are compared for cross-validation purposes and also to investigate the performance of these output-only system identification methods applied to bridge vibration data corresponding to different excitation sources. Finally, the identified natural frequencies and mode shapes are compared with their analytical counterparts obtained from a three-dimensional (3D) finite element model used in the design phase of the AZMB.

3.2 Alfred Zampa Memorial Bridge

The Carquinez Strait, located about 32 km northeast of San Francisco, carries the Sacramento River into San Francisco Bay. Before construction of the AZMB, the strait was spanned by two steel truss bridges built in 1927 and 1958, respectively, which provide a vital link on the interstate Highway I-80 corridor. The AZMB is the third bridge crossing the Carquinez Strait and will replace the original bridge that was built in 1927. With a main span of 728 m and side spans of 147 m and 181 m, the AZMB is the first major suspension bridge built in the United States (US) since the 1960s. The design and construction of the AZMB incorporates several innovative structural features that have never been used previously for a suspension bridge in the US, namely (1) orthotropic (aerodynamic) steel deck; (2) reinforced concrete towers; and (3) large-diameter drilled shaft foundations. The AZMB is also the first suspension bridge in the world with concrete towers in a high seismic zone.

The closed steel box girder with orthotropic deck provides a light weight, durable, and low-maintenance alternative to the stiffening trusses that have been used on previous suspension bridges in the US. It is continuous through the towers, with expansion joints located only at the far ends of the side spans. Its slender 3 m depth allows adequate navigation clearance without excess structure height. Its shape was developed in a wind tunnel to provide aerodynamic stability and low drag. Its rigidity against bending and torsion contributes to

superior bridge performance under wind, seismic, and traffic loads. Its closed form, with smooth outside surfaces and stiffening elements located inside, reduces maintenance costs.

The reinforced concrete towers rising about 125 m above the mean water level are the prominent architectural feature of the bridge. The ductile frames formed by the tower shafts and their connecting struts provide a “rectangle of air” above drivers. This is the first application of concrete towers on a suspension bridge in the US, and to any suspension bridge in the world in a high seismic risk zone. The cellular shafts incorporate spirally reinforced corner pilasters to improve ductility and provide architectural relief. The towers were designed to a seismic standard requiring essentially elastic behavior in the maximum credible earthquake (as defined in Caltrans’ seismic design procedures), with some limited inelastic behavior allowed in their lower sections. Drilled shaft foundations support pile caps on which the towers were built. Steel casings were driven through overlying sediments into the top of the rock. Then an uncased rock socket was drilled below the casing. The rock socket and casing were then reinforced and concreted. Each tower is supported by twelve such shafts, with a maximum length of about 90 m. These foundations are economical to build, have less impact on water flow than large sunken caissons, and were designed to the same seismic standard as the towers.

The south transition pier supports the end of the steel deck girder, houses tie-downs that divert the geometry of the cables to the south anchorage, and supports the end of the south viaduct. It is structurally and architecturally similar to the main towers, with cellular reinforced concrete shafts and pile foundations. The south cable anchorage transfers the thrust of the cables to the ground via massive concrete anchor blocks and a combination of batter piles and vertical piles. The splay chambers rise 18 m above ground, while the anchor blocks extend about 10 m beneath the ground surface. The north cable anchorage transfers the thrust

of the cables to the ground by direct bearing on the underlying rock, and also serves as a bridge abutment. The concrete anchor blocks and splay chambers are benched into the rock beneath the roadway and only the relatively small saddle housings are exposed. More details about this bridge such as the special engineering studies and structural quantities can be found elsewhere (Ketchum, 2006; Caltrans, 2006).

3.3 Description of Instrumentation and Data Acquisition System

3.3.1 NEES@UCLA Data Acquisition Equipment

Equipment from NEES@UCLA was used to perform the dynamic tests on the AZMB. The NEES@UCLA field mobile laboratory deployed for this study consisted of:

1. EpiSensor accelerometers from Kinemetrics Inc. including both EpiSensor ES-U (uni-axial) and EpiSensor ES-T (tri-axial). The EpiSensor force-balanced accelerometers have a wide frequency bandwidth from DC (i.e., 0Hz) to 200Hz, a large amplitude range (user selectable at $\pm 0.25\ g, \pm 0.5\ g, \pm 1\ g, \pm 2\ g, \pm 4\ g$) set at $\pm 2\ g$ for these experiments, and a broad dynamic range (140 dB+ for ES-U and 155 dB+ for ES-T). The significant bandwidth (from DC to 200 Hz) allows for the study of motions at higher frequencies while maintaining the very important low frequency and DC response needed in field calibration, in post-processing of the data (e.g., double integration of acceleration records) and in studying the low frequency predominant modes of the AZMB. Figure 3.1 shows both EpiSensors ES-U and ES-T used in the tests.

2. Quanterra Q330 data loggers from Kinemetrics, Inc., to provide signal conditioning (e.g., anti-aliasing filter), analog to digital (A/D) conversion, GPS (i.e., global positioning system) time stamping for synchronization across multiple nodes,

local memory buffer and IP-network (i.e., Internet Protocol network) communication capabilities via hardwire or wireless. The nominal performance specifications for the Q330 data loggers include 24-bit A/D resolution, 135 dB dynamic range, and a time stamp (time synchronization) accuracy of < 0.1 ms. Figure 3.2 shows a Q330 data logger used in the tests.

3. Antelope data acquisition software (Boulder Real Time Technologies, 2006) for real-time monitoring and recording of data. A data concentrator which consists of a field-ruggedized UNIX workstation running Antelope, networking switches and wireless communication radios, was used to centrally record the data from each of the Q330 data logger nodes.

4. Mobile command center containing computing facilities, satellite uplink (not used in these tests) and equipment storage.

Collectively, the NEES@UCLA field data acquisition system represents the state-of-the-art in seismic monitoring equipment. The accelerometers transmit analog signals to the Q330 data loggers in which they are digitized, time-stamped and stored in a local memory buffer as data packets. From there, the data packets are sent to the data concentration point using Transmission Control Protocol / Internet Protocol (TCP/IP) with either Ethernet cables or IEEE 802.11b, a standard for local area networks from the Institute of Electrical and Electronic Engineers (IEEE), long-range wireless radios. Ethernet cables were used for this experiment due to external radio frequency interference which limited drastically the transmission distance of the wireless equipment. The data concentration point contains a Sun Microsystems Netra 120 server (a high density, thin, ruggedized server designed to withstand extreme levels of temperatures, humidity, radiation and vibrations) running Antelope data acquisition software to centrally record data packets received from each of the various

Quanterra Q330 nodes. Finally, the Antelope server in the data concentration point transmits, using an orb2orb transfer protocol, all of the received data packets to a laptop computer inside the mobile command center also running Antelope software. The laptop computer was used to observe the experiment in real-time using the Antelope real-time monitoring (Antelope RTM) system. Figure 3.3 illustrates the network of the NEES@UCLA field mobile laboratory.

3.3.2 Accelerometer Layout

The mobile command center was located near midpoint of the bridge main span and the accelerometers were installed at selected locations (stations) along both sides of the bridge deck covering the whole length of the bridge. Along the west side of the bridge deck, 14 stations were instrumented with either a single EpiSensor ES-T (tri-axial) or three EpiSensors ES-U (uni-axial) at each station to measure the vertical, transversal and longitudinal motion components. The east side of the bridge deck was instrumented with 22 EpiSensors ES-U at 11 stations (i.e., two uni-axial accelerometers per station) measuring the vertical and transversal motion components. Figure 3.4 shows the sensor locations along the bridge deck. At each station, the accelerometers were mounted on a square aluminium plate of size $203 \times 203 \times 6$ (mm) . These plates were attached to the bridge deck using semi-permanent adhesive sheets providing the required stiffness between the plates and the deck. Each Q330 has two 3-channel ports (A and B) to connect sensors. A hub was used to connect up to three EpiSensors ES-U to each port. Due to a limited number of hubs available at the time of the experiments and the narrow time window available to perform the experiments, acceleration responses at stations 6SW (i.e., station 6 at southwest side of the bridge deck), 6SE, 7SE, 6NE and 7NE (see Figure 3.4) could not be recorded.

3.4 Dynamic Tests Performed on the Bridge

Three types of excitation sources were used for the dynamic field tests performed on the AZMB: controlled traffic loads, vehicle-induced impact loads and wind. The controlled traffic loads consisted of two heavy trucks weighing 405 kN (Truck A) and 409 kN (Truck B), respectively, traversing the bridge at specified velocities and the impact loads were generated using one or both of these trucks driving over triangular shaped steel ramps (60cm long and 10cm high) designed and constructed specifically for these tests. The vehicle-induced impact excitation was intended to induce a free vibration response significantly higher than the ambient vibration response (mainly wind-induced) and the response to the controlled traffic loads. Four controlled traffic load patterns were defined in the controlled traffic loads and vehicle-induced impact tests, namely: (I) two trucks crossing over the bridge in parallel (Figure 3.5a); (II) two trucks crossing over the bridge in opposite direction (Figure 3.5b); (III) one truck crossing over the bridge; and (IV) two trucks crossing over the bridge following each other in the same traffic lane. It should be mentioned that the trucks could only use the two middle traffic lanes (see Figure 3.5) during the tests.

3.4.1 Controlled Traffic Load Tests

The first three controlled traffic load patterns were used as the excitation sources in this set of tests. For each traffic load pattern, two specified truck velocities were used, namely 24 km/h and 48 km/h. Due to the end-of-construction field condition at the time of the tests, the trucks could be driven at the specified velocities only along the main span of the bridge (between the two towers). During the tests, the trucks were commanded through radio communication from the mobile command center, located near midpoint of the main span, where the data were monitored in real-time and recorded. Table 3.1 provides a detailed

description of the controlled traffic load tests. As an illustration, Figure 3.6 shows the vertical acceleration response at the midpoint, south quarter point and near the south end of main span on the west side of the bridge deck (i.e., stations 0W, 3SW, and 5SW) measured in Test No. 5, during which one truck crossed over the bridge from north to south on the west traffic lane. Notice that a peak vertical bridge deck acceleration of about 0.01g is observed during this test. The Fourier amplitude spectrum of the vertical response measured at station 3SW is shown in Figure 3.7. For a long-span suspension bridge such as the AZMB, the lower modes natural frequencies are below 1 Hz. It is observed from Figure 3.7 that during the controlled traffic load tests, the vibration modes with natural frequencies above 1 Hz (higher vibration modes) are more significantly excited than those with natural frequencies below 1 Hz (lower vibration modes).

3.4.2 Vehicle-Induced Impact Tests

Two pairs of triangular shaped steel ramps were used in the vehicle-induced impact tests. As an illustration, Figure 3.8 shows two pairs of steel ramps set up along the centerline of the bridge main span. In this set of tests, all of the four controlled traffic load patterns defined above were used in combination with seven different ramp configurations: (a) two pairs of ramps located at midpoint of main span; (b) a single pair of ramps located at midpoint of main span on the west traffic lane; (c) a pair of ramps located at the north quarter point of main span on the west traffic lane and the second pair located at midpoint of main span on the east traffic lane; (d) one pair of ramps located at the north quarter point of main span on the west traffic lane and the second pair located at the south quarter point of main span on the east traffic lane; (e) a single pair of ramps located at the north quarter point of main span on the west traffic lane; (f) a pair of ramps located at both the north and south quarter points of main span on the east traffic lane; and (g) a pair of ramps located at both the north quarter point and

midpoint of main span on the west traffic lane. The trucks approached the ramps at the specified velocity of 32 km/h, but traversed the ramps at the reduced velocity of 8 km/h. For safety reason, one of the trucks crossed over the ramps at very low velocity (less than 1 km/h). Details of these tests are provided Table 3.2.

As an illustration, Figure 3.9 shows the vertical bridge deck acceleration response at the midpoint, south quarter point and near the south end of main span on the west side of bridge deck (i.e., stations 0W, 3SW, and 5SW) measured in Test No. 10, during which both trucks crossed over the bridge in opposite direction with two pairs of ramps located at midpoint of main span. Notice that a peak vertical bridge deck acceleration of about 0.08g is observed during this test, which is significantly larger than that observed in Test No. 5 (peak acceleration of 0.01g). Figure 3.10 shows the Fourier amplitude spectra of the vertical acceleration response measured at station 3SW in Test No. 10 and Test No. 12, during which both trucks crossed over the bridge in opposite direction with two pairs of ramps located at the north quarter point of main span on the west traffic lane and the south quarter point of main span on the east traffic lane, respectively. It is clearly seen that the relative contributions of the bridge vibration modes to the measured response depends on the locations of the steel ramps (i.e., the locations of the impact loads). However, in both cases (Test No. 10 and Test No. 12) the higher vibration modes were excited much more significantly than the lower vibration modes.

At the end of the sequence of vehicle-induced impact tests, the response of the bridge was measured due to longitudinal forces applied on the bridge deck. These forces were generated through braking of the trucks while they were crossing over the bridge in parallel from south to north (Test No. 16). In this test, for safety consideration, the drivers applied normal and not hard breaks on the trucks to stop at midpoint of main span.

3.4.3 Ambient Vibration Tests

Ambient vibration tests were conducted after completion of all the tests based on the two trucks in traffic condition, just after midnight local time, while there were no construction activities on the bridge and thus bridge vibrations were induced mainly by wind. Two cases of ambient vibration tests were performed: the bridge response was measured (1) when both trucks were stationed at midpoint of main span (Test No. 17), and (2) after both trucks left the bridge (Test No. 18). As an illustration, Figure 3.11 shows the vertical acceleration response at the midpoint, south quarter point and near the south end of main span on the west side of the bridge deck (i.e., stations 0W, 3SW, and 5SW) measured in Test No. 18. Notice that a peak vertical bridge deck acceleration of about 0.003g is observed during this test, which is much smaller than that observed in Test No. 5 (controlled traffic load tests), see Figure 3.6. The Fourier amplitude spectrum of the vertical acceleration response measured at station 3SW is shown in Figure 3.12. During Test No. 18, the vibration modes below 1 Hz were excited as much as those above 1 Hz. Despite the fact that the amplitude of the measured ambient vibration response is much lower than that of the forced vibration response measured, the ambient vibration data was found to be very clean (i.e., high signal-to-noise ratio, see Figure 3.12), especially for identifying the lower vibration modes.

3.5 System Identification

System identification of the AZMB was performed based on both ambient and forced vibration test data. During the dynamic tests, the bridge acceleration response at various points (stations) was sampled at a rate of 200 Hz resulting in a Nyquist frequency of 100 Hz, which is much higher than the frequencies of interest in this study (< 4 Hz). The 20 minutes long ambient vibration test data used in this study were collected just after midnight local time,

while there were no construction activities on the bridge. Therefore, the bridge ambient vibrations were driven mainly by wind (Test No. 18).

As described in the previous section, two types of forced vibration tests were performed on the AZMB, namely (1) controlled traffic load tests, and (2) vehicle-induced impact tests. In the vehicle-induced impact tests, the load applied to the bridge departed from an ideal impulse load due to the continuous motion of the truck on the bridge before and after the impact, which causes errors in identifying the damping ratios (He et al., 2006). Therefore, the bridge vibration data from the vehicle-induced impact tests were not used to identify the bridge modal parameters in this study. Due to the limited duration of each controlled traffic load test (100 seconds for Tests No. 1, 2, 3 and 200 seconds for Tests No. 4, 5, 6) and the requirement of high frequency resolution (to resolve closely-spaced vibration modes) in the system identification, the bridge vibration measurements from the six different tests are concatenated back to back resulting in a total duration of 900 seconds (15 minutes). As an illustration, Figure 3.13 shows the bridge vertical acceleration response at the midpoint, south quarter point and near the south end of main span on the west side of the bridge deck (i.e., stations 0W, 3SW, and 5SW, respectively) measured during the six forced vibration tests. The amplitude of vibration of the bridge during the first 300 seconds (trucks moving at 48 km/h) is larger than during the last 600 seconds (trucks moving at 24 km/h).

In order to improve the computational efficiency and avoid missing modes in the system identification process, the lower vibration modes (with natural frequencies below 1 Hz) and higher vibration modes (with natural frequencies above 1 Hz) are identified separately by applying to the bridge vibration data a low-pass Butterworth infinite impulse response (IIR) filter of order 7 with a cut-off frequency of 1 Hz and a band-pass finite impulse response (FIR)

filter of order 1024 with lower and upper cut-off frequencies of 1 Hz and 4 Hz, respectively. Only vertical response measurements were used to identify the higher vibration modes.

3.5.1 System Identification Results Based on Ambient Vibration Data

In the implementation of MNExT-ERA, stations 1NE, 2SW, 3NW, and 4SE were used as reference stations and response correlation functions were estimated through inverse Fourier transformation of the corresponding PSD functions. Estimation of the PSD functions was based on Welch-Bartlett method using 300 second long (60,000 points) Hanning windows with 50 percent overlap, in order to reduce the effects of spectral leakage. In order to increase the computational efficiency of the system identification procedure, the estimated auto / cross-correlation functions were down-sampled to 10 Hz and 40 Hz for identifying lower and higher vibration modes, respectively. After down-sampling, the Nyquist frequency is still much higher than the frequency range of interest ($\leq$ 1 Hz for lower vibration modes and $\leq$ 4 Hz for higher vibration modes). The down-sampled estimated auto / cross-correlation functions were then used to form Hankel matrices for applying ERA in the second stage of the modal identification. Due to the fact that the accelerometer measuring the vertical response at station 5SE was not functioning properly, the Hankel matrix constructed using vertical vibration data for identifying lower vibration modes has dimensions $(21\times 200)\times(4\times 200)$ (21 stations, 4 reference stations), while the Hankel matrix based on horizontal vibration data has dimensions $(22\times 200)\times(4\times 200)$ (22 stations). For identifying the higher vibration modes, a Hankel matrix of dimensions $(21\times 400)\times(4\times 400)$ was constructed. The natural frequencies and damping ratios of the identified vibration modes are reported in Table 3.3 together with those identified using the other two methods. It should be noted that the modal parameters of some significant higher (vertical) vibration modes are not reported here, because the corresponding

mode shapes could not be classified due to insufficient spatial density of the sensor network deployed along the bridge deck.

In applying SSI-DATA to identify the modal parameters of the lower vibration modes, the filtered measured data were first down-sampled to 10 Hz and then used to form the output Hankel matrix composed of 100 block rows with either 21 rows in each block (21 vertical channels) for identifying vertical modes or 22 rows in each block (22 horizontal channels) for identifying horizontal modes. In identifying the higher vibration modes using SSI-DATA, the filtered measured data were first down-sampled to 40 Hz and then used to form the output Hankel matrix composed of 50 block rows with 21 rows in each block (21 vertical channels). The identified natural frequencies and damping ratios are reported in Table 3.3. In the application of MNExT-ERA and SSI-DATA in this study, a stabilization diagram was used to determine the "optimum" order of the realized system from which the modal parameters are extracted. For example, in identifying the modal parameters of the lower vibration modes (below 1 Hz) using SSI-DATA based on the ambient vibration data, the order of the realized system was determined as $n = 32$.

In the implementation of EFDD, the 20 minutes long filtered ambient vibration data were also down-sampled to 10 Hz and 40 Hz for identifying lower and higher vibration modes, respectively. Estimation of the PSD functions was based on Welch-Bartlett method using 300 seconds long Hanning windows with 50 percent overlap. The modal frequencies were estimated at peak locations (i.e., peak picking) in the first singular value versus frequency plot and the mode shapes were estimated by the first singular vector at the corresponding frequencies (Brincker et al., 2001). The SDOF CSD functions are estimated from the first singular value plot using a modal assurance criterion (MAC) (Allemang and Brown, 1982) higher than 0.95 between the estimated mode shape and the singular vectors at

discrete frequencies around the natural frequency. The modal parameters estimated using EFDD are given in Table 3.3.

From Table 3.3, it is observed that the natural frequencies identified using the three system identification methods considered here are in excellent agreement, except for a few modes which could not be identified by all three methods such as the first anti-symmetric vertical mode (1-AS-V) missed using EFDD and the 5-AS-V mode missed by the SSI-DATA method. It is also found that the modal damping ratios identified using the three different methods are in reasonable agreement for most identified vibration modes considering that the estimation uncertainty of damping ratios is inherently higher than that of natural frequencies. The modal damping ratios of some higher torsional modes (4-AS-T, 5-S-T, 5-AS-T) identified using EFDD are near zero. It is worth mentioning that the identified modal damping ratios might be influenced by the aerodynamic damping induced by the wind-structure interaction. The fact that certain modes (1-AS-V, 2-S-T, 5-AS-V, 4-S-T) could not be identified by all three methods is likely due to their low participation (relative to other modes) in the measured bridge vibration (i.e., these modes were not significantly excited).

The vibration mode shapes identified using MNExT-ERA, SSI-DATA, and EFDD are complex valued. Figure 3.14 represents in polar plots (i.e., rotating vectors in the complex plane) the mode shapes of the AZMB (main span only) identified using MNExT-ERA based on ambient vibration data. These polar plots have the advantage to show directly the extent of the non-proportional damping characteristics of a vibration mode. If all complex valued components of a mode shape vector are collinear (i.e., in phase or 180 degrees out of phase), this vibration mode is said to be classically (or proportionally) damped. On the other hand, the more these mode shape components are scattered in the complex plane, the more the vibration mode is non-classically (or non-proportionally) damped. However, measurement noise,

estimation errors, and modeling errors could also cause a “true” classically damped mode to be identified as non-classically damped. Figure 3.14 shows that most of the vibration modes identified in this study are either perfectly or nearly classically damped except for some higher vibration modes (5-AS-V, 2-AS-T, 3-AS-T, 4-S-T, 4-AS-T).

A 3D representation of the normalized mode shapes for these identified vibration modes is given in Figure 3.15. Normalization was performed by projecting all mode shape components onto their principal axis (in the complex plane) and then scaling this projected mode shape vector for a unit value of its largest component. The identified space-discrete mode shapes were interpolated between the sensor locations using cubic splines along both sides of the bridge deck and straight lines along the deck transverse direction. Since the accelerometers at stations 6SW, 6SE, 7SE, 6NE and 7NE could not be recorded, the vibration mode shapes are plotted over the bridge main span only and are based on the assumption that the motion of the bridge deck at the towers is restrained in both the horizontal and vertical direction. In addition, the vertical acceleration response at station 5SE was not recorded properly during the tests, and the mode shape components at stations 5NE and 5SW were used to estimate the component at station 5SE based on the symmetric or anti-symmetric property of vibration modes. From Figure 3.15 it is observed that: (1) the identified mode shapes with natural frequencies of 0.41 Hz and 0.56 Hz (observed only over the main span in this study) are neither symmetric nor anti-symmetric with respect to the centerline of the main span, and (2) the identified modes with natural frequencies of 0.96 Hz and 1.04 Hz have similar mode shapes (i.e., 4-AS-V). Additional measurement stations on the towers and approach spans (which have different lengths) are needed to identify the corresponding bridge global mode shapes.

MAC values were computed in order to compare corresponding mode shapes identified using different system identification methods and are reported in Table 3.4. The high MAC values obtained for most vibration modes indicate an excellent agreement between the mode shapes identified using different methods based on ambient vibration data. The low MAC values of higher torsional modes such as 4-S-T (i.e., fourth symmetric torsional mode) and 5-AS-T (i.e., fifth anti-symmetric torsional mode) indicate that the accuracy of these identified mode shapes is not as high as that for lower vibration modes, which could be due to the low participation (relative to other modes) of these modes to the measured bridge response.

3.5.2 System Identification Results Based on Forced Vibration Data

The system identification methods MNExT-ERA, SSI-DATA, and EFDD were also applied to identify the bridge modal parameters based on forced vibration test data. MNExT-ERA and EFDD were implemented in exactly the same way as for ambient vibration data. However, in applying SSI-DATA to identify the higher vibration modes, an output Hankel matrix was formed composed of 60 block rows instead of 50 (for ambient vibration data) due to the fact that the forced vibration tests are of shorter duration than the ambient vibration test. The modal parameters identified using these three methods based on the forced vibration data are reported in Table 3.5. The identified natural frequencies using different methods are found to be in excellent agreement. The modal damping ratios of some vibration modes such as 1-AS-V, 1-S-T, and 2-AS-T identified using EFDD are near zero. Excluding these modes, the modal damping ratios estimated using the different methods are in reasonable agreement, especially those identified using MNExT-ERA and SSI-DATA. The high MAC values (see Table 3.6) obtained for most vibration modes indicate an excellent agreement between the mode shapes identified using different methods based on forced vibration test data. The low MAC values obtained for a few modes, such as the 1-AS-V and the mode with a natural

frequency of 0.41 Hz, could be due to the low relative participation of these modes to the measured forced vibration response of the bridge.

By comparing the average values of the modal parameters (natural frequencies and modal damping ratios) identified using the three methods based on the ambient vibration data (see Table 3.3) with their counterparts identified based on the forced vibration data (see Table 3.5.), it is found that: (1) The natural frequencies identified using the two types of test data are in excellent agreement except for the 1-AS-V mode. The significant difference in the identified natural frequencies for this mode reflects the difficulty in identifying it due to its very low relative contribution to the bridge vibration response in both the ambient and forced vibration tests. Thus, this mode could not be reliably identified. (2) The order (in terms of natural frequency) of vibration modes 1-S-V and 1-AS-V identified based on ambient vibration data is swapped over when these modes are identified based on forced vibration data. (3) The identified modal damping ratios are response amplitude dependent. For most vibration modes, especially for the lower vibration modes, the modal damping ratios identified using forced vibration data are higher than those identified using ambient vibration data as clearly shown in Figure 3.16. The order of the vibration modes used in the figure corresponds to the sorted natural frequencies identified based on forced vibration data. Figure 3.17 shows the average (over the three methods) of the MAC values between the corresponding mode shapes identified based on ambient vibration and forced vibration data. The high average MAC values obtained for most vibration modes indicate an excellent agreement between the mode shapes identified using the two types of test data. The low average MAC values obtained for a few higher torsional modes is likely due to the large estimation errors of these modes due to their low relative contributions to the measured bridge vibration response.

3.6 Comparison between Experimental and Analytical Modal Parameters

A 3D finite element model of the AZMB developed in the structural analysis software ADINA (ADINA R&D Inc., 2002) was provided by Caltrans (Dr. Charles Sikorsky, personal communication, 2005). Figure 3.18 shows the 3D finite element model of the AZMB. This finite element model is composed mainly of: (1) linear elastic frame elements (with possible initial strain) to model the two main suspension cables, suspender cables, steel box girder (in both the longitudinal and transversal directions) and tower shafts (at some specific locations, the shafts are modeled using multilinear inelastic frame elements), (2) multilinear inelastic frame elements to model the pile foundations supporting the tower shafts, and (3) linear elastic shell elements to model the pile caps. The inertia properties of the bridge are modeled with element consistent mass matrices based on element shape functions and material density. Additional lumped masses, assigned to some translational DOFs, are also included in the model to represent various equivalent masses not accounted for by the element mass matrices. This finite element model of the AZMB is composed of 3281 elements and approximately 14,000 DOFs. It was used in the design process of this bridge.

In this section, the identified natural frequencies and mode shapes of the bridge vibration modes below or slightly above 1 Hz are compared with their analytical counterparts obtained from the finite element model of the bridge. The first 200 vibration modes of the finite element model of the AZMB were computed. In order to pair each identified vibration mode with the corresponding analytical vibration mode, MAC values were calculated between the identified mode shape and all 200 computed mode shapes truncated at accelerometer locations (i.e., measured DOFs) in order to have the same size as the identified mode shapes. For each identified vibration mode, the computed eigen-mode with the highest MAC value is considered as its analytical counterpart. In the case where several computed eigen-modes have

very close high MAC values with the identified mode considered, the one with natural frequency closest to the identified natural frequency is selected. The computed natural frequencies and mode shapes corresponding to the lowest 16 identified vibration modes are shown in Figure 3.19 together with the corresponding natural frequencies identified from ambient and forced vibration data, respectively, averaged over the three system identification methods used. Figure 3.20 shows in bar plot the comparison between natural frequencies identified from ambient and forced vibration data (averaged over the three methods used) and analytically predicted from the finite element model of the bridge. By comparing the corresponding identified and analytically predicted natural frequencies (given in Figure 3.19), the following observations can be made: (1) The identified and analytically predicted natural frequencies of the 1-S-V, 2-S-V, and 2-AS-V vibration modes are in excellent agreement. Their differences are less than 1 percent. The agreement between identified and analytical natural frequencies for the 2-AS-H, 1-S-T, and 1-AS-T modes is very good, with differences less than or slightly above 3 percent. (2) The discrepancies between identified and analytically predicted natural frequencies for the 1-S-H and 1-AS-V modes are significant. For the 1-S-H mode, the discrepancy is likely due to inaccuracies in the finite element model, since the system identification results using different methods based on different test data are found to be in very good agreement. However, for the 1-AS-V mode, the discrepancy could be caused by both inaccuracies in the finite element model and system identification errors, since the natural frequency of this mode identified using different test data are not in good agreement either. (3) The other identified and corresponding analytically predicted natural frequencies are found to be in reasonable agreement (less than 10 percent difference). Figure 3.21 shows in bar plot the MAC values (averaged over the three system identification methods used) between identified and analytically predicted mode shapes. For most vibration modes, there is

a very good to excellent agreement between identified and analytically predicted mode shapes. The low MAC values obtained for a few modes, such as the 1-AS-V and the mode with a natural frequency of 0.41 Hz, are caused by both system identification errors due to the low relative contributions of these modes to the measured bridge vibration and inaccuracies in the finite element model of the bridge.

3.7 Summary and Conclusions

A set of dynamic field tests were conducted on the Alfred Zampa Memorial Bridge (AZMB), located 32 km northeast of San Francisco on interstate Highway I-80, just before its opening to traffic in November 2003. These tests provided a unique opportunity to obtain the modal parameters of the bridge in its as-built condition with no previous traffic loads or seismic excitation.

The dynamic field tests included ambient vibration tests (mainly wind-induced) and forced vibration tests based on controlled traffic loads and vehicle-induced impact loads. The controlled traffic loads consisted of two heavy trucks traversing the bridge at specified velocities and the impact loads were generated using one or both of these trucks driving over small steel ramps designed and constructed specifically for these tests. During the vibration tests, the dynamic response of the bridge was measured using an array of 34 uni-axial and 10 tri-axial force-balanced accelerometers. These accelerometers were installed at 25 selected stations along both sides of the bridge deck, covering the whole length of the bridge main span. Instead of roving accelerometers around to the different measurement stations with fixed accelerometers at one or more reference stations (as typically done in the past), a total of 64 channels of acceleration response data were recorded simultaneously in the dynamic field tests described here, including 25 vertical, 25 transversal, and 14 longitudinal motion components.

During the forced vibration tests, the vibration modes with natural frequencies above 1 Hz were more significantly excited than those with natural frequencies below 1 Hz, which renders the lower vibration modes of the bridge (< 1 Hz) more difficult to identify. During the ambient vibration tests, the bridge was excited mainly by the wind which provided a broadband excitation. The lower vibration modes (< 1 Hz) and some higher modes (> 1 Hz) were excited almost at the same level. Therefore, the ambient vibration data was found to be more informative for identification of the lower vibration modes. In addition, even though the amplitude of the measured ambient vibration response is very low (0.003g peak acceleration), the recorded data was found to be very clean (i.e., data has high signal-to-noise ratio).

Two time domain system identification methods, namely the multiple-reference natural excitation technique combined with the eigensystem realization algorithm (MNExT-ERA) and the data-driven stochastic subspace identification (SSI-DATA) method, as well as a frequency domain method, namely enhanced frequency domain decomposition (EFDD), were applied to identify the modal parameters of the bridge based on bridge vibration data from two types of test: ambient vibration test and forced vibration tests based on controlled-traffic loads. From the modal identification results obtained, the following conclusions can be made: (1) The natural frequencies identified using the three different methods are in excellent agreement for each type of tests. (2) The natural frequencies identified based on data from the two different types of test are also in excellent agreement, except for the 1-AS-V (first anti-symmetric vertical) mode. The significant difference in the identified natural frequencies for this mode reflects the difficulty in identifying it due to its very low relative contribution to the measured bridge vibration in both the ambient and forced vibration tests. In addition, the order (in terms of natural frequency) of vibration modes 1-S-V and 1-AS-V identified based on ambient vibration data is swapped over when these modes are identified based on forced

vibration data. (3) Considering that the estimation (or statistical) uncertainty of modal damping ratios is inherently higher than that of natural frequencies, the modal damping ratios identified are in reasonable agreement across the different identification methods used. (4) The identified modal damping ratios are response amplitude dependent. For most vibration modes, especially for the lower vibration modes, the modal damping ratios identified using forced vibration data are higher than those identified using ambient vibration data. (5) For most vibration modes, the mode shapes identified using different methods and the different test data are in excellent agreement.

The system identification results obtained from this study provide benchmark modal properties of the AZMB, which can be used as a baseline in future health monitoring studies of this bridge. Overall, all three system identification methods applied in this study performed very well in both types of test. However, in order to avoid missing modes in the identification process, use of several system identification methods is recommended for cross-validation purposes, as different methods have different estimation variability with respect to input factors such as measurement noise level, frequency content of input excitation, and excitation amplitude. It should be noted that the performance of the EFDD method is not as robust as that of the other two methods, since it requires user intervention for peak picking in the identification process.

Finally, the identified natural frequencies and mode shapes are compared with their analytically predicted counterparts obtained from a 3D finite element model used in the design phase of the AZMB. The identified (experimental) and analytical modal properties are found to be in good agreement for the most contributing modes to the measured bridge vibration.

3.8 Acknowledgements

This Chapter contains the material from the following two papers submitted to the Journal of Structural Engineering, ASCE (2007): (1) “Dynamic Testing of Alfred Zampa Memorial Bridge” with authors Joel P. Conte, Xianfei He, Babak Moaveni, Sami F. Masri, John P. Caffrey, Mazen Wahbeh, Farzad Tasbihgoo, Daniel H. Whang, and Ahmed Elgamal; and (2) “System Identification of Alfred Zampa Memorial Bridge Using Dynamic Field Test Data” with authors Xianfei He, Babak Moaveni, Joel P. Conte, Ahmed Elgamal, and Sami F. Masri. The first paper has been in press (with permission from ASCE) and the second one is under review for possible publication. The dissertation author is the primary investigator of these two papers. The dynamic field tests on the Alfred Zampa Memorial Bridge used for this part of research was performed by a joint UCSD-USC-UCLA research team. I wish to acknowledge the USC and UCLA research team members: Sami F. Masri, John P. Caffrey, Mazen Wahbeh and Farazad Tasbihgoo (USC), Steve Kang and Daniel Whang (UCLA) for their cooperation and help during the tests. The dynamic tests were also assisted by several individuals and organizations: Brian Boal (Caltrans), Louis Bates (Caltrans Consultant Engineer), Joe Reyes (Caltrans), and Frank Daams (FCI/Cleveland Bridge). Their help is very much appreciated. I am thankful to Dr. Mark Ketchum (from OPAC Consulting Engineers) for very useful and interesting discussions about the conception and design of the Alfred Zampa Memorial Bridge. I am also grateful to the California Department of Transportation and Dr. Charles Sikorsky who provided the finite element model of this bridge.

3.9 References

Abdel-Ghaffar, A. M., and Housner, G. W. (1978). “Ambient vibration tests of suspension bridge.” *Journal of the Engineering Mechanics Division*, ASCE, 104(5), 983-999.

Abdel-Ghaffar, A. M., and Scanlan, R. H. (1985). "Ambient vibration studies of Golden Gate Bridge: I. suspended structure." *Journal of Engineering Mechanics*, ASCE, 111(4), 463-482.

Abdel Wahab, M. M., and De Roeck, G. (1998). "Dynamic testing of prestressed concrete bridges and numerical verification." *Journal of Bridge Engineering*, ASCE, 3(4), 159-169.

Allemang, R. J., and Brown, D. L. (1982). "A correlation coefficient for modal vector analysis." *Proceedings of 1st International Modal Analysis Conference*, Bethel, Connecticut, 110-116.

Boulder Real Time Technologies (2006). *Antelope Release 4.8 <http://www.brtt.com>*. Boulder Real Time Technologies, Inc, Boulder, Colorado.

Brincker, R., Ventura, C., and Andersen, P. (2001). "Damping estimation by frequency domain decomposition." *Proceedings of IMAC XIX*, Kissimmee, USA.

Brownjohn, J. M. W., Lee, J., and Cheong B. (1999). "Dynamic performance of a curved cable-stayed bridge." *Engineering Structures*, 21(11), 1015-1027.

Brownjohn, J. M. W., Moyo, P., Omenzetter, P., and Lu, Y. (2003). "Assessment of highway bridge upgrading by dynamic testing and finite- element model updating." *Journal of Bridge Engineering*, ASCE, 8(3), 162-172.

California Department of Transportation (Caltrans), (2006). "The New Carquinez Bridge." <http://www.dot.ca.gov/dist4/carquinez.htm> (August 15, 2006).

Cunha, A., Caetano, E., and Delgado, R. (2001). "Dynamic tests on large cable-stayed bridge." *Journal of Bridge Engineering*, ASCE, 6(1), 54-62.

Delaunay D., Grillaud, G., Bietry, J., and Sacre, C. (1999). "Wind response of long span bridges: in-situ measurements and modal analysis." *Proceedings of the 17th International Modal Analysis Conference*, Kissimmee, Florida, 719-725.

Doebling, S. W., Farrar, C. R., Prime, M. B., and Shevitz, D. W. (1996). "Damage identification and health monitoring of structural mechanical systems from changes in their vibration characteristics: A literature review." *Report No. LA-13070-MS*, Los Alamos National Laboratory, Los Alamos, New Mexico.

Ewins, D. J. (2003). *Modal Testing: Theory, Practice and Application*, Research Studies Press, Baldock, UK.

Gentile, C., and Martinez y Cabrera, F. (2004). "Dynamic performance of twin curved cable-stayed bridges." *Earthquake Engineering and Structural Dynamics*, 33(1), 15-34.

Halling, M. W., Muhammad, I., and Womack, K. C. (2001). "Dynamic testing for condition assessment of bridge bents." *Journal of Structural Engineering*, ASCE, 127(2), 161-167.

Harik, I. E., Allen, D. L., Street, R. L., Guo, M., Graves, R. C., Harison, J., and Gawry, M. J. (1997). "Free and ambient vibration of Brent-Spence Bridge." *Journal of Structural Engineering*, ASCE, 123(9), 1262-1268.

Huang, C. S., Yang, Y. B., Lu, L. Y., and Chen C. H. (1999). "Dynamic testing and system identification of a multi-span highway bridge." *Earthquake Engineering and Structural Dynamics*, 28(8), 857-878.

He, X., Moaveni, B., Conte, J. P., and Elgamal, A. (2006). "Comparative study of system identification techniques applied to New Carquinez Bridge." *Proceedings of the 3rd International Conference on Bridge Maintenance, Safety and Management*, Porto, Portugal.

James, G. H., Carne, T. G., and Lauffer, J. P. (1993). "The natural excitation technique for modal parameters extraction from operating wind turbines." *Report No. SAND92-1666, UC-261*, Sandia National Laboratories, Sandia, New Mexico.

Juang, J. N., and Pappa, R. S. (1985). "An eigensystem realization algorithm for modal parameter identification and model reduction." *Journal of Guidance, Control and Dynamics*, 8(5), 620-627.

Ketchum, M. (2006). "Carquinez Strait Bridge page." <http://www.ketchum.org/carquinez.html> (August 15, 2006).

Peeters, B., and De Roeck, G. (2001). "Stochastic system identification for operational modal analysis: A review." *Journal of Dynamic Systems, Measurement, and Control*, 123(4), 659-667.

Ren, W. X., Harik, I. E., Blandford, G. E., Lenett, M., and Baseheart, T. M. (2004a). "Roebling suspension bridge. II: Ambient testing and live-load response." *Journal of Bridge Engineering*, ASCE, 9(2), 119-126.

Ren, W. X., Zhao, T., and Harik, I. E. (2004b). "Experimental and analytical modal analysis of steel arch bridge." *Journal of Structural Engineering*, ASCE, 130(7), 1022-1031.

Smyth, A.W., Pei, J.-S., and Masri, S.F. (2003). "System identification of the Vincent Thomas suspension bridge using earthquake records," *Earthquake Engineering and Structural Dynamics*, 32(3), 339-367.

Sohn, H., Farrar, C. R., Hemez, F. M., Shunk, D. D., Stinemates, D. W., and Nadler, B. R. (2003). "A review of structural health monitoring literature: 1996-2001." *Report No. LA-13976-MS*, Los Alamos National Laboratory, Los Alamos, New Mexico.

Van Overschee, P., and De Moor, B. (1996). *Subspace Identification for Linear Systems: Theory-Implementation-Applications*, Kluwer Academic Publishers, Norwell, Massachusetts, USA.

Table Captions

Table 3.1. Controlled traffic load tests

Tests No. Time*	Traffic Pattern	Driving Direction	Velocity (km/h)	Test description
1 04:14:05	Pattern I	From North (N) to South (S)	48	Truck A driving on the west lane and truck B driving on the east lane.
2 04:24:10	Pattern III	From S to N	48	Truck A crossing over the bridge on the west lane.
3 04:30:13	Pattern II	Truck A from N to S; Truck B from S to N	48	Truck A driving on the west lane and truck B driving on the east lane.
4 04:48:41	Pattern II	Truck A from S to N; Truck B from N to S	24	Truck A driving on the east lane and truck B driving on the west lane.
5 04:56:55	Pattern III	From N to S	24	Truck A crossing over the bridge on the west lane.
6 05:04:15	Pattern I	From S to N	24	Truck A driving on the west lane and truck B driving on the east lane.

** The time shown here and in the next table is the Coordinated Universal Time (UTC) (also known as Greenwich Mean Time).*

Table 3.2. Vehicle-induced impact load tests

Tests No. Time	Traffic Pattern	Driving Direction	Impact Loads	Test description
7 05:55:05	Pattern I	From North (N) to South (S)	Configuration a	Truck A driving on the west lane and truck B driving on the east lane.
8 06:25:13	Pattern I	From S to N	Configuration a	Truck A driving on the west lane and truck B driving on the east lane.
9 06:39:40	Pattern III	From N to S	Configuration b	Truck A crossing over the bridge on the west lane.
10 06:47:32	Pattern II	Truck A from S to N; Truck B from N to S	Configuration a	Truck A driving on the east lane and truck B driving on the west lane.
11 07:12:13	Pattern II	Truck A from N to S; Truck B from S to N	Configuration c	Truck A driving on the west lane and truck B driving on the east lane.
12 07:30:27	Pattern II	Truck A from S to N; Truck B from N to S	Configuration d	Truck A driving on the east lane and truck B driving on the west lane.
13 07:36:10	Pattern III	From N to S	Configuration e	Truck A crossing over the bridge on the west lane.
14 07:54:25	Pattern IV	From S to N	Configuration f	Two trucks following each other to cross over the bridge on the east lane.
15 08:13:20	Pattern IV	From N to S.	Configuration g	Two trucks following each other to cross over the bridge on the west lane.

Table 3.3. System identification results based on the ambient vibration data

Modes	Natural frequencies [Hz]			Damping ratios [%]		
	MNEXT -ERA	SSI-DATA	EFDD	MNEXT -ERA	SSI-DATA	EFDD
1-S-H	0.159	0.158	0.161	1.29	0.50	2.47
1-S-V	0.194	0.193	0.193	0.27	0.21	0.89
1-AS-V	0.204	0.201		1.98	1.36	
2-S-V	0.258	0.258	0.259	0.21	0.23	1.00
2-AS-V	0.350	0.350	0.349	0.15	0.20	0.66
1-AS-H	0.361	0.365	0.361	1.68	0.49	0.92
	0.414	0.414	0.415	0.23	0.13	0.72
1-S-T	0.469	0.471	0.476	1.29	0.17	0.48
3-S-V	0.484	0.483	0.484	0.15	0.21	0.71
	0.561	0.561	0.562	0.16	0.15	0.34
3-AS-V	0.645	0.645	0.645	0.09	0.11	0.42
1-AS-T	0.738	0.741	0.737	0.18	0.34	0.28
4-S-V	0.799	0.799	0.799	0.16	0.23	0.34
4-AS-V	0.958	0.956	0.957	0.27	0.15	0.17
2-S-T	1.003	1.007		2.97	0.58	
4-AS-V	1.036	1.035	1.038	0.11	0.22	0.24
5-S-V	1.160	1.174	1.165	0.18	0.36	0.50
5-AS-V	1.345		1.343	0.46		0.11
2-AS-T	1.367	1.360	1.362	1.00	0.26	0.19
6-S-V	1.572	1.575	1.570	0.63	0.30	0.14
3-S-T	1.684	1.689	1.685	0.17	0.09	0.26
3-AS-T	2.029	2.025	2.034	0.34	0.13	0.14
4-S-T	2.331	2.340		0.21	0.32	
4-AS-T	2.671	2.673	2.676	0.40	0.45	0.00
5-S-T	2.949	2.948	2.947	0.27	0.13	0.08
5-AS-T	3.273	3.271	3.301	0.59	0.15	0.00

Notes: (1) In the first column, S = Symmetric; AS: = Anti-Symmetric; H, V, T = Horizontal, Vertical, and Torsional mode, respectively.

(2) An empty cell in the first column indicates that the corresponding mode is neither a symmetric nor an anti-symmetric mode.

(3) An empty cell in the second through sixth column indicates that the natural frequency and/or damping ratio is not available because the corresponding vibration mode was missed in the identification process.

Table 3.4. MAC values between mode shapes identified using different methods based on the ambient vibration data

Modes	MAC values		
	MNExT-ERA & SSI-DATA	MNExT-ERA & EFDD	SSI-DATA& EFDD
1-S-H	1.000	1.000	1.000
1-S-V	0.998	1.000	0.997
1-AS-V	0.991		
2-S-V	1.000	1.000	1.000
2-AS-V	1.000	1.000	1.000
1-AS-H	0.985	0.987	0.998
	1.000	1.000	1.000
1-S-T	0.976	0.994	0.991
3-S-V	0.996	0.997	0.999
	0.997	1.000	0.996
3-AS-V	1.000	1.000	1.000
1-AS-T	0.986	0.995	0.995
4-S-V	0.998	0.999	1.000
4-AS-V	0.994	0.973	0.986
2-S-T	0.980		
4-AS-V	0.994	0.997	0.987
5-S-V	0.991	1.000	0.992
5-AS-V		0.950	
2-AS-T	0.934	0.806	0.875
6-S-V	0.988	0.997	0.994
3-S-T	0.988	0.998	0.992
3-AS-T	0.647	0.940	0.781
4-S-T	0.318		
4-AS-T	0.673	0.881	0.740
5-S-T	0.682	0.996	0.706
5-AS-T	0.910	0.420	0.363

Table 3.5. System identification results based on the forced vibration test data

Modes	Natural frequencies [Hz]			Damping ratios [%]		
	MNEXT -ERA	SSI-DATA	EFDD	MNEXT -ERA	SSI-DATA	EFDD
1-S-H	0.160	0.165	0.161	3.56	1.53	0.89
1-AS-V	0.174	0.172	0.176	9.11	6.84	0.00
1-S-V	0.194	0.193	0.195	1.77	1.23	0.97
2-S-V	0.257	0.256	0.252	1.00	0.47	1.72
2-AS-V	0.349	0.348	0.349	0.59	0.39	1.07
1-AS-H	0.366	0.368	0.361	1.98	1.67	0.66
	0.407	0.408	0.405	2.02	2.52	0.82
1-S-T	0.473	0.469	0.479	0.81	0.36	0.00
3-S-V	0.478	0.484		1.76	1.51	
	0.561	0.559	0.564	1.30	0.97	0.39
3-AS-V	0.645	0.644	0.647	1.02	0.79	0.63
1-AS-T	0.736	0.736	0.733	0.30	0.25	0.50
4-S-V	0.794	0.795	0.794	0.36	0.21	0.53
4-AS-V	0.954	0.953	0.950	0.33	0.16	0.44
2-S-T		0.998			0.91	
4-AS-V	1.028	1.034	1.028	0.48	0.29	0.15
5-S-V	1.152	1.184	1.152	0.41	1.42	0.40
5-AS-V	1.334	1.360	1.333	1.00	1.44	0.07
2-AS-T	1.366		1.367	0.52		0.00
6-S-V	1.563	1.557	1.567	0.84	0.44	0.19
3-S-T	1.687	1.699	1.685	0.31	0.36	0.09
3-AS-T	2.019	2.021	2.022	0.27	0.22	0.20
4-S-T		2.334			0.41	
4-AS-T	2.656	2.657	2.654	0.23	0.13	0.25
5-S-T	2.951	2.943	2.957	0.11	0.23	0.11
5-AS-T		3.275			0.26	

Table 3.6. MAC values between mode shapes identified using different methods based on the forced vibration data

Modes	MAC values		
	MNExT-ERA & SSI-DATA	MNExT-ERA& EFDD	SSI-DATA& EFDD
1-S-H	0.998	0.998	0.999
1-AS-V	0.697	0.711	0.517
1-S-V	0.961	0.998	0.966
2-S-V	0.998	0.997	0.993
2-AS-V	0.996	1.000	0.996
1-AS-H	0.956	0.954	0.944
	0.842	0.916	0.788
1-S-T	0.989	0.998	0.988
3-S-V	0.902		
	0.974	0.956	0.983
3-AS-V	0.997	0.986	0.982
1-AS-T	0.996	0.998	0.996
4-S-V	0.994	0.997	0.997
4-AS-V	0.988	0.987	0.998
2-S-T			
4-AS-V	0.964	0.974	0.945
5-S-V	0.980	0.999	0.982
5-AS-V	0.941	0.996	0.945
2-AS-T		0.664	
6-S-V	0.998	0.999	0.998
3-S-T	0.843	0.932	0.965
3-AS-T	0.949	0.967	0.958
4-S-T			
4-AS-T	0.905	0.972	0.894
5-S-T	0.821	0.853	0.689
5-AS-T			

Figure Captions

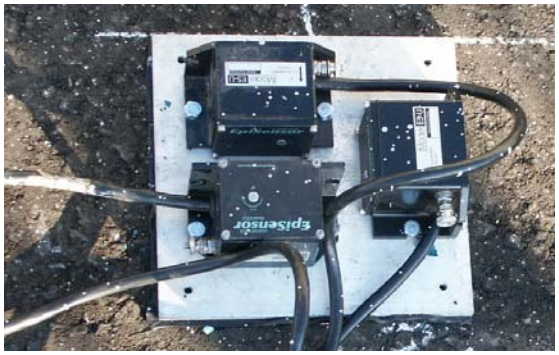

(a) EpiSensors ES-U

(b) EpiSensor ES-T

Figure 3.1. EpiSensor accelerometers

Figure 3.2. Quanterra Q330 instrumented in the tests

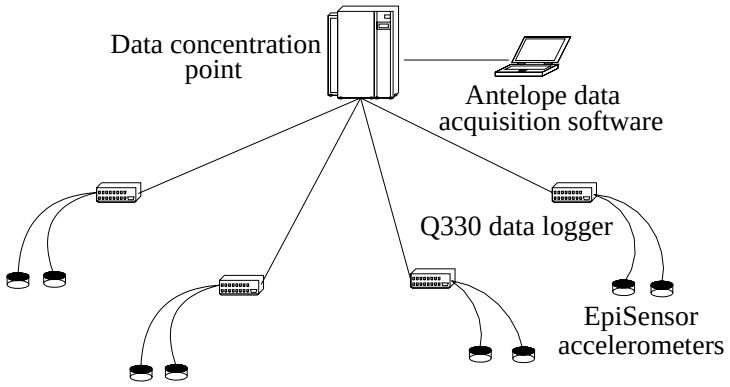

Figure 3.3. Network diagram of the NEES@UCLA seismic monitoring equipment

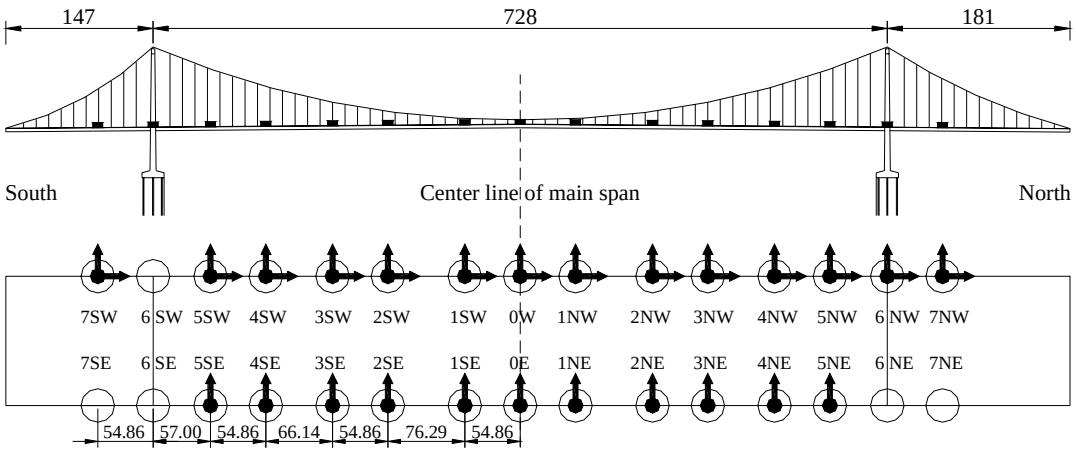

Figure 3.4. Layout of accelerometers along the bridge deck (unit: m)

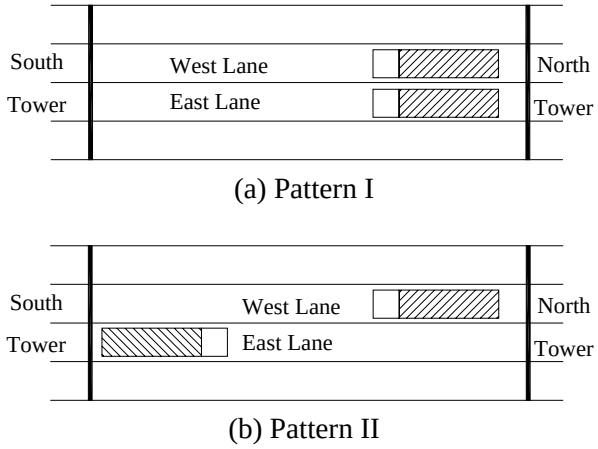

Figure 3.5. Controlled traffic load patterns

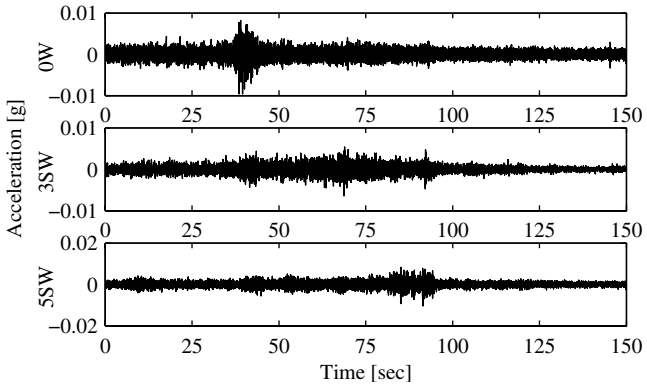

Figure 3.6. Vertical bridge deck acceleration response measured in Test No. 5

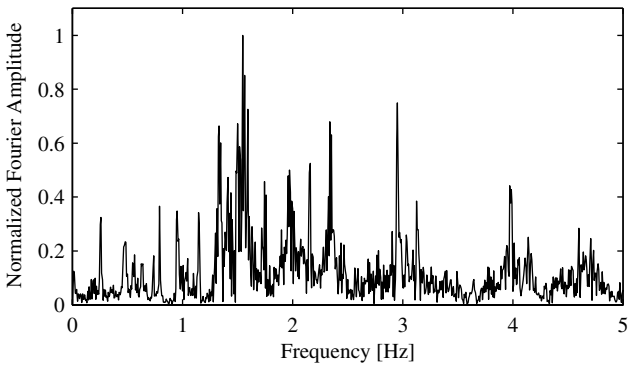

Figure 3.7. Fourier amplitude spectrum of vertical acceleration response at station 3SW measured in Test No. 5

Figure 3.8. Steel ramps used in the tests

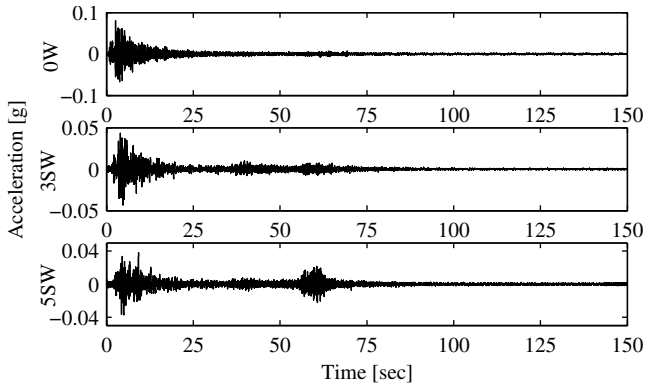

Figure 3.9. Vertical bridge deck acceleration response measured in Test No. 10

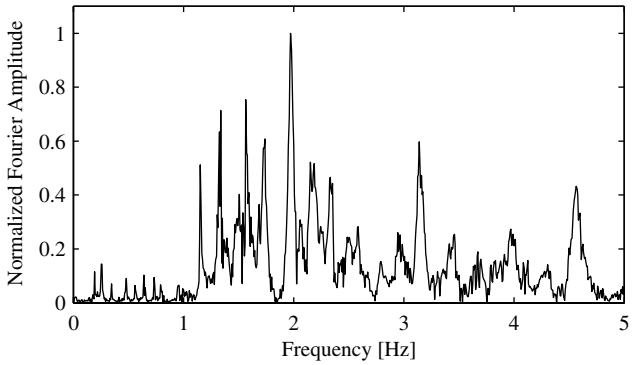

(a) Test No. 10

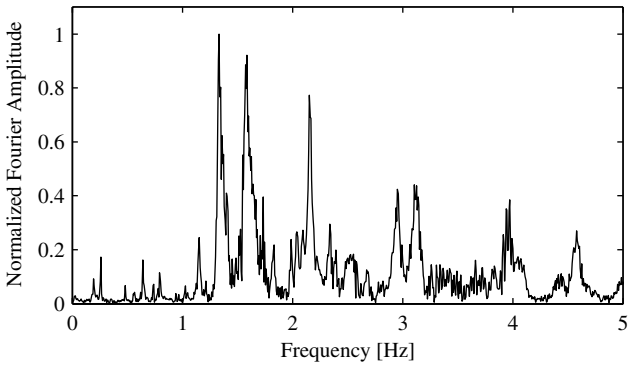

(b) Test No. 12

Figure 3.10. Fourier amplitude spectra of vertical acceleration response at station 3SW measured in Tests No. 10 and 12

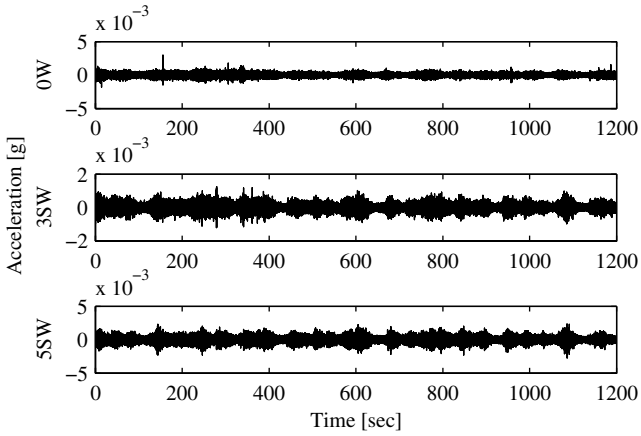

Figure 3.11. Vertical bridge deck acceleration response measured in Test No. 18

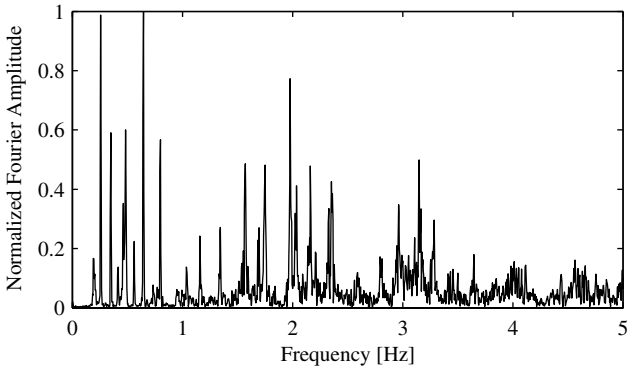

Figure 3.12. Fourier amplitude spectrum of vertical acceleration response at station 3SW measured in Test No. 18

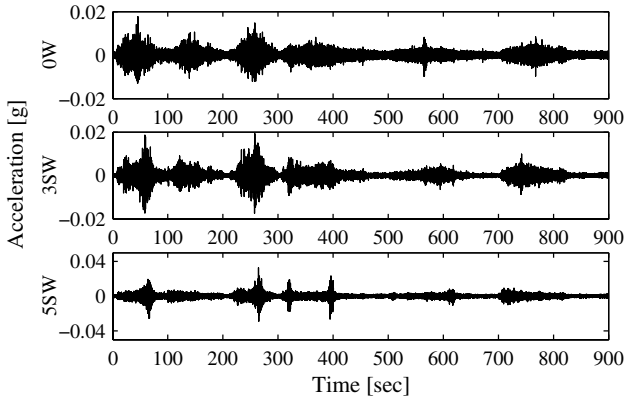

Figure 3.13. Vertical acceleration response measured during the six controlled traffic load tests

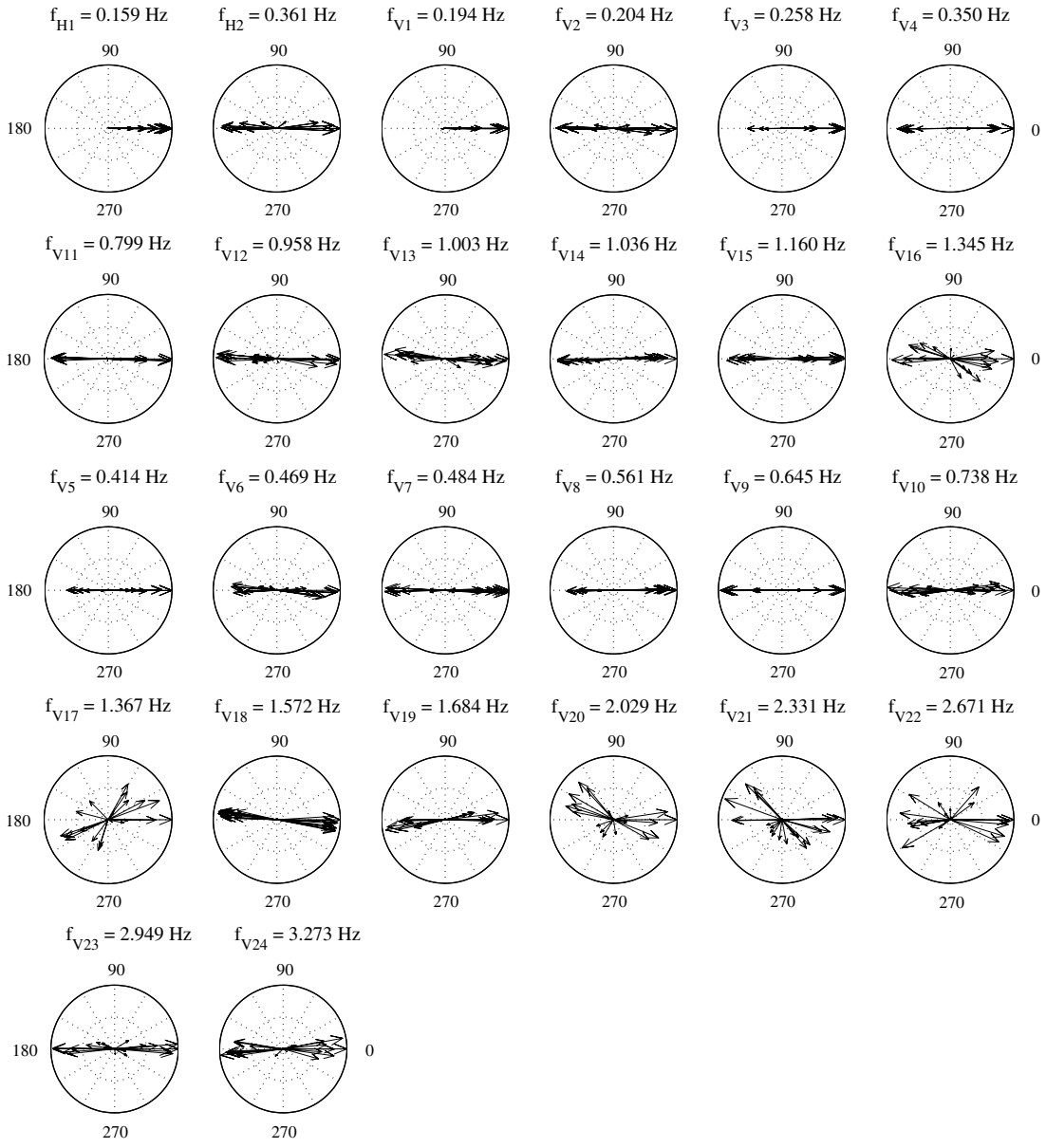

Figure 3.14. Polar plot representation of vibration mode shapes identified using MNExT-ERA based on ambient vibration data

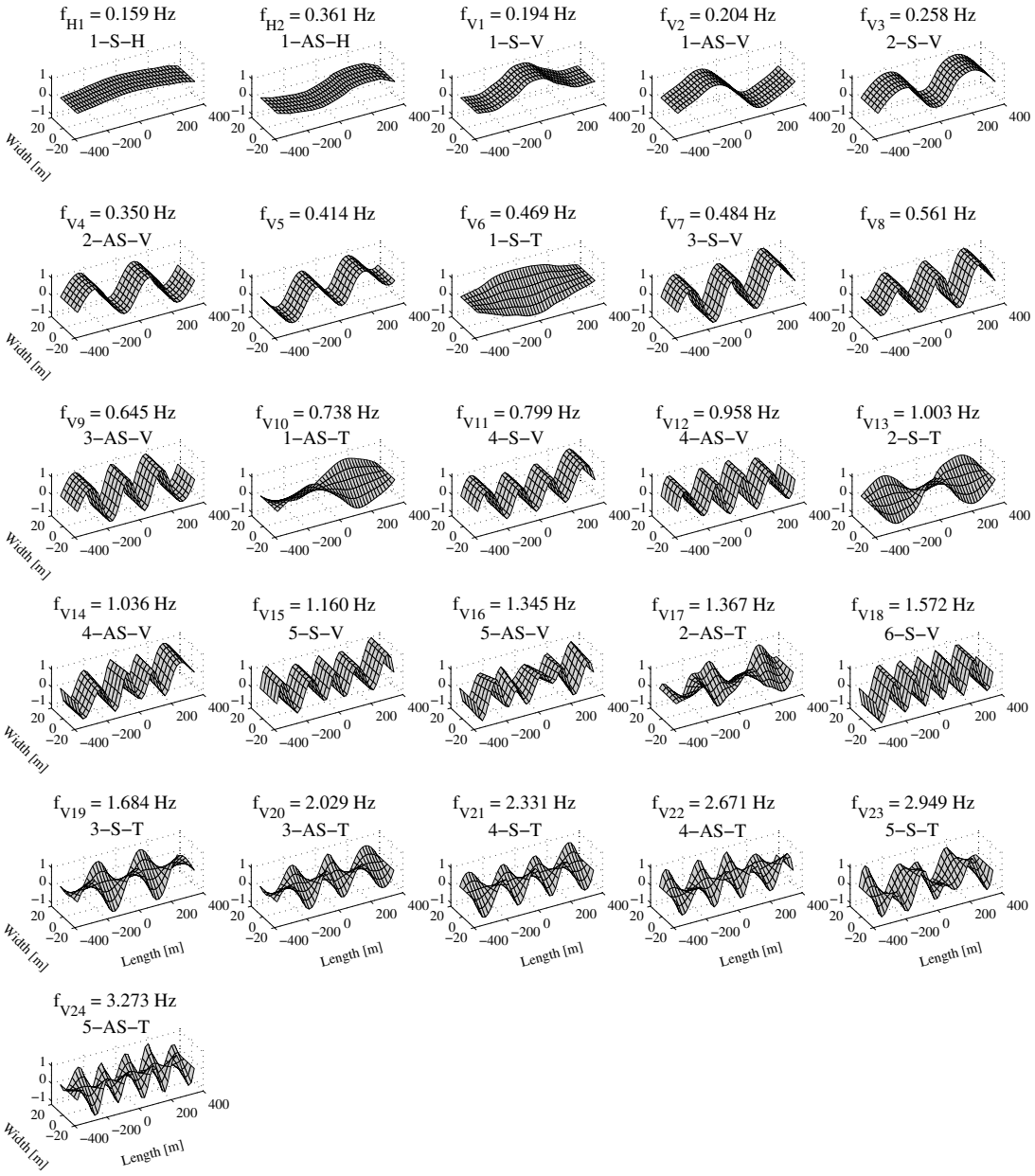

Figure 3.15. 3D representation of normalized vibration mode shapes identified using MNExT-ERA based on ambient vibration data

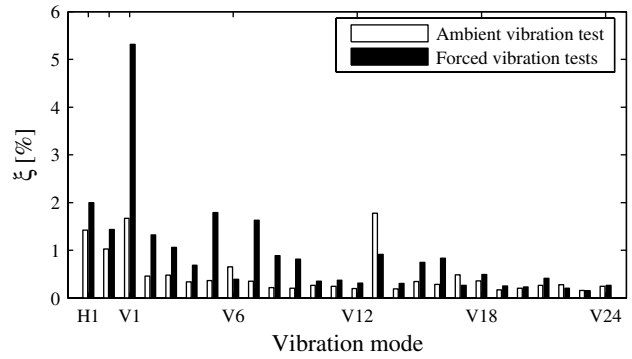

Figure 3.16. Comparison of damping ratios identified using ambient vibration and forced vibration test data (see Figure 3.14 or Figure 3.15 for abbreviation of vibration modes)

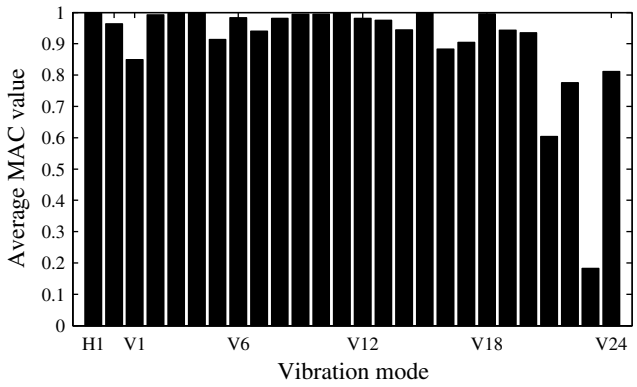

Figure 3.17. Averaged (over the three methods) MAC values between corresponding mode shapes identified based on ambient vibration and forced vibration test data

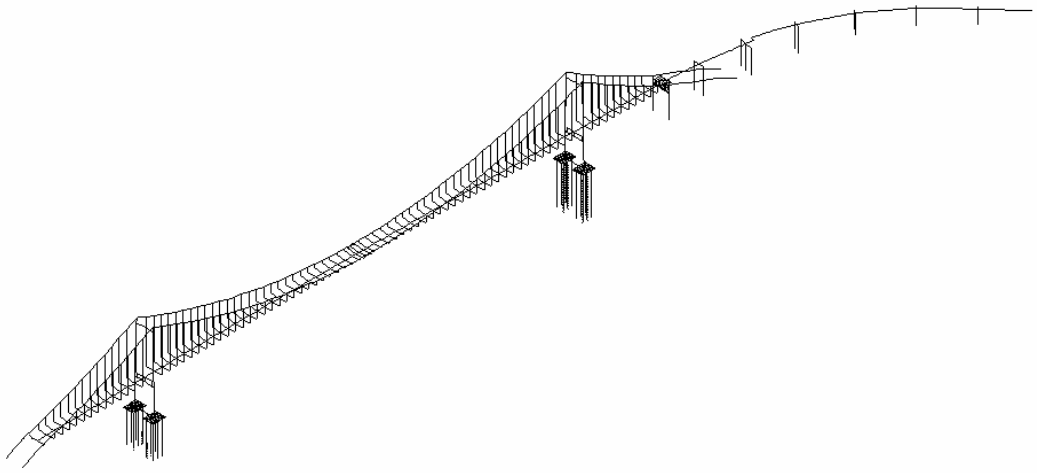

Figure 3.18. Finite element model of the AZMB

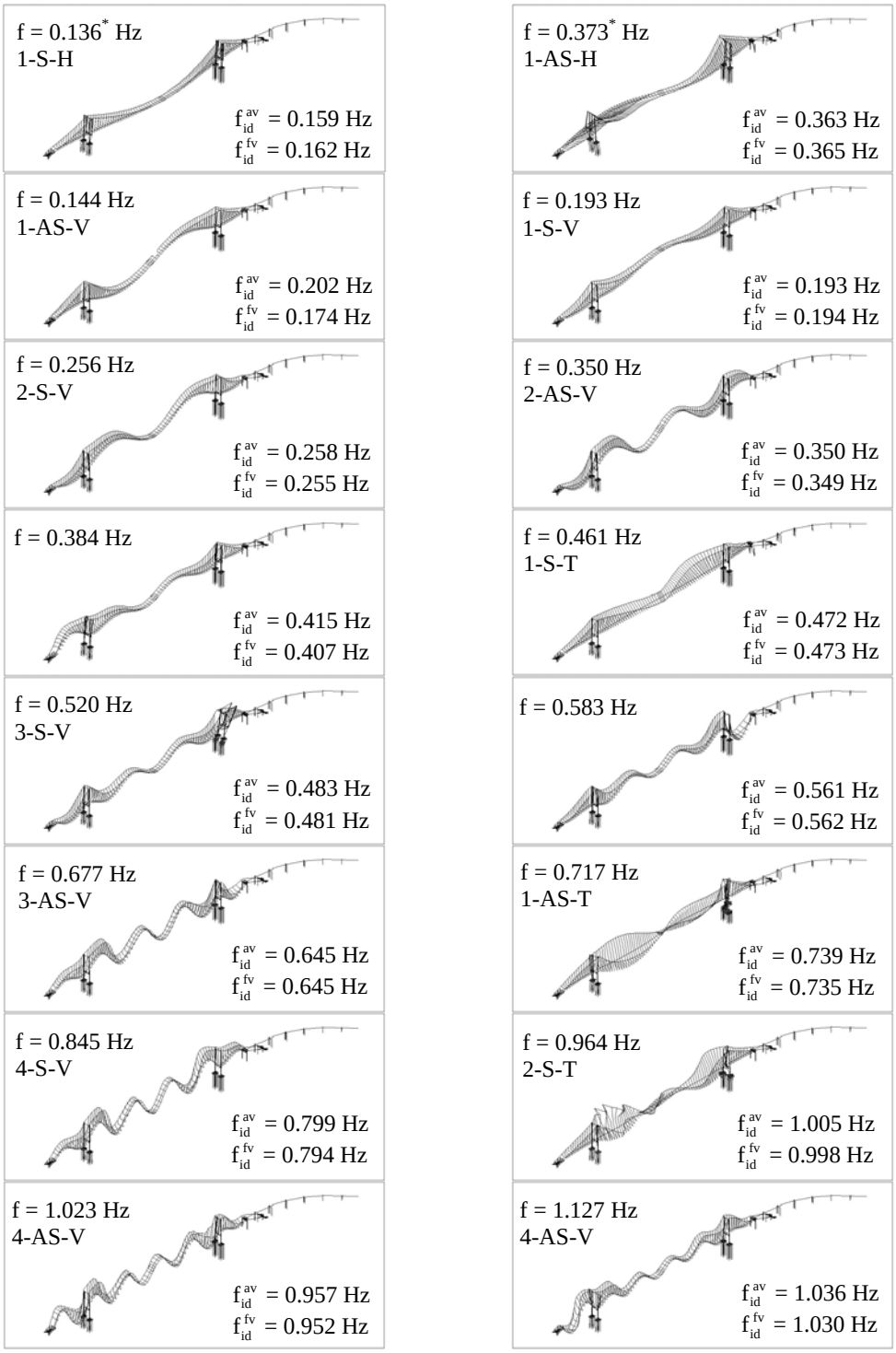

Figure 3.19. Vibration mode shapes of the AZMB computed from the bridge finite element model in ADINA* : horizontal vibration modes; f_{id}^{av}, f_{id}^{fv} = natural frequency identified based on ambient vibration and forced vibration data, respectively, averaged over the three system identification methods)

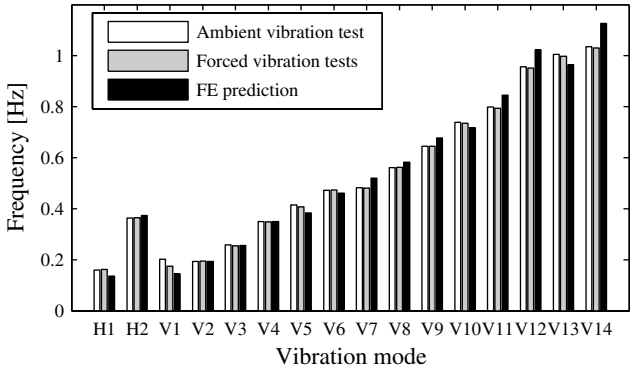

Figure 3.20. Comparison of identified (averaged over the three methods) and analytically predicted natural frequencies

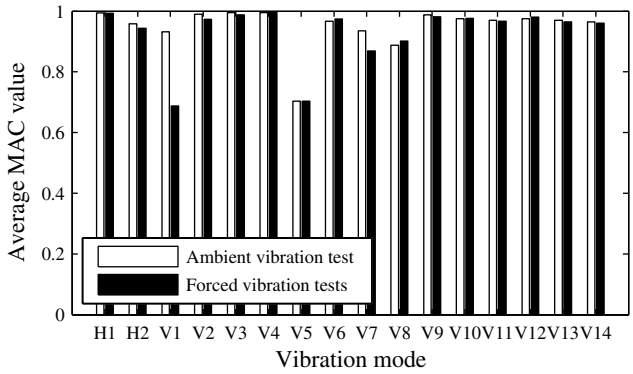

Figure 3.21. Averaged (over the three methods) MAC values between identified and analytically predicted mode shapes

Chapter 4

System Identification of Vincent Thomas Bridge Using Simulated Wind-Induced Ambient Vibration Data

4.1 Introduction

Vibration-based structural health monitoring has been the subject of significant research in structural engineering in recent years. The basic premise of vibration-based structural health monitoring is that changes in structural characteristics such as mass, stiffness, and energy dissipation mechanisms influence the vibration response characteristics of structures. Therefore, changes in dynamic features such as modal parameters and quantities derived thereof are often used as damage indicators in structural damage identification and health monitoring. Salawu (1997) presented a review on the use of natural frequency changes for damage detection. It is however challenging if not impossible to localize the detected damage (e.g., to obtain spatial information on the damage) from changes in natural frequencies only. Pandey et al. (1991) introduced the concept of mode shape curvature for damage localization. In their study, both a cantilever and a simply supported beam model were used to demonstrate the effectiveness of using changes in modal curvature as damage indicator to detect and localize damage. As another mode shape based damage indicator, Pandey and Biswas (1994) proposed the use of changes in the dynamically measured flexibility matrix to detect and localize damage. They showed that the flexibility matrix of a structure can be easily and accurately estimated from a few low frequency vibration modes of the structure. Methods based on changes in identified modal parameters to detect and localize damage in structures

have also been further developed for the purpose of damage quantification (i.e., estimation of the extent of damage). Among these methods are strain-energy based methods (Shi et al., 2002), the direct stiffness calculation method (Maeck and De Roeck, 1999), and sensitivity-based finite element (FE) model updating methods (Friswell and Mottershead, 1995; Teughels and De Roeck, 2004). A comprehensive literature survey on vibration-based structural health monitoring methods can be found in a number of recent publications (Doebling et al., 1996; Farrar and Jauregui, 1998; Sohn et al., 2003).

In order to develop a robust and reliable structural health monitoring methodology, it is essential to investigate the effects of realistic damage scenarios on structural modal properties. Since it is inconvenient or impossible to study the changes in structural modal parameters caused by various damage scenarios and damage levels through actual tests on a real structure during its service life, dynamic response simulation of the structure based on a well calibrated and validated FE model thereof provides an essential tool in structural health monitoring research. In this study, a simulation platform is presented to simulate the wind-induced (ambient) vibration response of Vincent Thomas Bridge (VTB) using a detailed three-dimensional (3D) FE model of the bridge and a state-of-the-art stochastic wind excitation model. The VTB is a suspension bridge that crosses over the main channel of Los Angeles Harbor in San Pedro, California. The bridge was constructed in the early 1960's with an overall length of approximately 1850 m, comprising the main span of 457 m and 154 m spans on either side. Generally, traffic, wind, micro-tremors and their combinations are the main sources of ambient excitation for bridges. This paper focuses on realistic simulation of the wind-induced response of VTB and system identification of the bridge based on its simulated wind response data.

Wind loads, including self-excited (caused by the interaction between wind and structural motion) and buffeting forces (caused by the fluctuating wind velocity field), are dependent on the geometric configuration of the bridge deck section, the reduced frequency of the bridge, and the incoming wind velocity fluctuations. In the simulation, the self-excited forces are represented in the time domain by means of convolution integrals involving aerodynamic impulse functions and structural motions. In order to simulate properly the stochastic characteristics of buffeting forces, the longitudinal (along-wind direction) and vertical spatially discrete wind velocity fields along the bridge axis are simulated as two independent stochastic vector processes according to their prescribed power spectral density matrices. The spectra of the longitudinal and vertical wind velocity fields are assumed to remain constant along the bridge axis and the coherence function of the wind velocity fluctuations at two different positions along the bridge is taken as the model proposed by Davenport (1968).

In the second part of the chapter, the dynamic properties of the bridge are identified using the data-driven stochastic subspace identification method (Van Overschee and De Moor, 1996) based on low-amplitude simulated wind-induced response of VTB. The system identification results are verified by the computed eigenproperties of the bridge FE model, which allows to assess the performance of the above output-only system identification method when applied to wind-excited long-span suspension bridges. In order to study the effects of measurement noise on the system identification results, zero-mean Gaussian white noise processes are added to the simulated output signals. Statistical properties (bias and coefficient-of-variation) of the identified modal parameters are investigated under increasing level of measurement noise.

The framework presented in this paper will allow to investigate systematically the effects of various realistic damage scenarios in long-span cable-supported bridges on changes in modal identification results obtained from ambient vibration data. Such studies are required in order to develop robust and reliable vibration-based structural health monitoring methods for this type of bridges, which is a long-term research objective of the authors.

4.2 Aerodynamic Forces

4.2.1 Self-Excited Forces

The differential equations of motion of a bridge subjected to aerodynamic forces with respect to the static equilibrium position can be expressed as

$$\mathbf{M}\ddot{\mathbf{x}}(t)+\mathbf{C}\dot{\mathbf{x}}(t)+\mathbf{K}\mathbf{x}(t)=\mathbf{F}=\mathbf{F}_{se}+\mathbf{F}_{b} \tag{4.1}$$

where $\mathbf{x}(t)$, $\dot{\mathbf{x}}(t)$, and $\ddot{\mathbf{x}}(t)$ = nodal displacement, velocity, and acceleration response vectors, respectively; **M**, **C**, and **K** = structural mass, damping, and stiffness matrices, respectively; and **F** = nodal load vector, where the subscripts *se* and *b* correspond to the self-excited and buffeting force components, respectively (see Figure 4.1).

For harmonic structural motion, the self-excited forces such as lift L_{se}, drag D_{se}, and pitching moment M_{se} per unit span of the bridge are typically expressed as (Scanlan, 1978a; Simiu and Scanlan, 1996; Chen et al., 2000a, b)

$$\begin{aligned}
L_{se}(t)&=\frac{1}{2}\rho U^2 B\left[KH_1^*\frac{\dot{h}}{U}+KH_2^*\frac{B\dot{\alpha}}{U}+K^2H_3^*\alpha+K^2H_4^*\frac{h}{B}+KH_5^*\frac{\dot{p}}{U}+K^2H_6^*\frac{p}{B}\right]\\
D_{se}(t)&=\frac{1}{2}\rho U^2 B\left[KP_1^*\frac{\dot{p}}{U}+KP_2^*\frac{B\dot{\alpha}}{U}+K^2P_3^*\alpha+K^2P_4^*\frac{p}{B}+KP_5^*\frac{\dot{h}}{U}+K^2P_6^*\frac{h}{B}\right]\\
M_{se}(t)&=\frac{1}{2}\rho U^2 B^2\left[KA_1^*\frac{\dot{h}}{U}+KA_2^*\frac{B\dot{\alpha}}{U}+K^2A_3^*\alpha+K^2A_4^*\frac{h}{B}+KA_5^*\frac{\dot{p}}{U}+K^2A_6^*\frac{p}{B}\right]
\end{aligned} \tag{4.2}$$

where ρ = air density; U = mean wind velocity; B = bridge deck width; ω = circular frequency of vibration; $K = \omega B/U$ = reduced frequency; H_i^*, A_i^* and P_i^* ($i = 1, \ldots, 6$) = flutter derivatives; and h, p, and α = vertical, lateral, and torsional displacement, respectively. It should be noted that the formulation of the self-excited forces in equation (4.2) cannot be applied directly in time domain simulation, since the flutter derivatives are frequency dependent. For arbitrary structural motion, the self-excited forces per unit span can be expressed in terms of impulse response functions as (Lin and Yang, 1983; Chen et al., 2000a, b)

$$\begin{aligned} L_{se}(t) &= \frac{1}{2}\rho U^2\left[\int_{-\infty}^{t} f_{Lh}(t-\tau)h(\tau)d\tau + \int_{-\infty}^{t} f_{Lp}(t-\tau)p(\tau)d\tau + \int_{-\infty}^{t} f_{L\alpha}(t-\tau)\alpha(\tau)d\tau\right] \\ D_{se}(t) &= \frac{1}{2}\rho U^2\left[\int_{-\infty}^{t} f_{Dh}(t-\tau)h(\tau)d\tau + \int_{-\infty}^{t} f_{Dp}(t-\tau)p(\tau)d\tau + \int_{-\infty}^{t} f_{D\alpha}(t-\tau)\alpha(\tau)d\tau\right] \\ M_{se}(t) &= \frac{1}{2}\rho U^2\left[\int_{-\infty}^{t} f_{Mh}(t-\tau)h(\tau)d\tau + \int_{-\infty}^{t} f_{Mp}(t-\tau)p(\tau)d\tau + \int_{-\infty}^{t} f_{M\alpha}(t-\tau)\alpha(\tau)d\tau\right] \end{aligned} \tag{4.3}$$

where the $f_{Xy}(\cdots)$ terms in the integrands are the impulse response functions of the self-excited forces, which are associated with the aerodynamic force component indicated by the subscript. In order to evaluate the self-excited forces in the time domain based on equation (4.3), it is necessary to determine the aerodynamic impulse response functions based on the experimentally determined flutter derivatives. For this purpose, the self-excited forces are taken to the frequency domain via Fourier transformation of equations (4.2) and (4.3) as

$$\begin{bmatrix} \mathscr{F}[L_{se}(t)] \\ \mathscr{F}[D_{se}(t)] \\ \mathscr{F}[M_{se}(t)] \end{bmatrix} = \frac{1}{2}\rho U^2 \begin{bmatrix} K^2(iH_1^* + H_4^*) & K^2(iH_5^* + H_6^*) & K^2B(iH_2^* + H_3^*) \\ K^2(iP_5^* + P_6^*) & K^2(iP_1^* + P_4^*) & K^2B(iP_2^* + P_3^*) \\ K^2B(iA_1^* + A_4^*) & K^2B(iA_5^* + A_6^*) & K^2B^2(iA_2^* + A_3^*) \end{bmatrix} \cdot \begin{bmatrix} \mathscr{F}[h(t)] \\ \mathscr{F}[p(t)] \\ \mathscr{F}[\alpha(t)] \end{bmatrix} \tag{4.4}$$

$$\begin{bmatrix} \mathscr{F}[L_{se}(t)] \\ \mathscr{F}[D_{se}(t)] \\ \mathscr{F}[M_{se}(t)] \end{bmatrix} = \frac{1}{2}\rho U^2 \begin{bmatrix} \mathscr{F}[f_{Lh}(t)] & \mathscr{F}[f_{Lp}(t)] & \mathscr{F}[f_{L\alpha}(t)] \\ \mathscr{F}[f_{Dh}(t)] & \mathscr{F}[f_{Dp}(t)] & \mathscr{F}[f_{D\alpha}(t)] \\ \mathscr{F}[f_{Mh}(t)] & \mathscr{F}[f_{Mp}(t)] & \mathscr{F}[f_{M\alpha}(t)] \end{bmatrix} \cdot \begin{bmatrix} \mathscr{F}[h(t)] \\ \mathscr{F}[p(t)] \\ \mathscr{F}[\alpha(t)] \end{bmatrix} \tag{4.5}$$

where $\mathscr{F}[\ldots]$ = Fourier transform operator. Thus, the relationship between aerodynamic impulse response functions and flutter derivatives can be obtained by comparing equations (4.4) and (4.5) term by term:

$$\begin{aligned} \mathscr{F}[f_{Lh}(t)] &= K^2(iH_1^* + H_4^*) \\ \mathscr{F}[f_{Lp}(t)] &= K^2(iH_5^* + H_6^*) \\ \mathscr{F}[f_{L\alpha}(t)] &= K^2B(iH_2^* + H_3^*) \end{aligned} \tag{4.6}$$

$$\begin{aligned} \mathscr{F}[f_{Dh}(t)] &= K^2(iP_5^* + P_6^*) \\ \mathscr{F}[f_{Dp}(t)] &= K^2(iP_1^* + P_4^*) \\ \mathscr{F}[f_{D\alpha}(t)] &= K^2B(iP_2^* + P_3^*) \end{aligned} \tag{4.7}$$

$$\begin{aligned} \mathscr{F}[f_{Mh}(t)] &= K^2B(iA_1^* + A_4^*) \\ \mathscr{F}[f_{Mp}(t)] &= K^2B(iA_5^* + A_6^*) \\ \mathscr{F}[f_{M\alpha}(t)] &= K^2B^2(iA_2^* + A_3^*) \end{aligned} \tag{4.8}$$

Using the above equations, the self-excited forces can be used in time domain analysis based on equation (4.3) once the flutter derivatives are obtained from wind-tunnel experiments. The experimental flutter derivatives in the above equations are usually obtained at a discrete set of reduced frequencies $K(\omega_k)$. Then, the rational function approximation method known as Roger's approximation is used to estimate the aerodynamic force coefficients defined in equations (4.6), (4.7), and (4.8), also known as aerodynamic transfer functions, as continuous

functions of the reduced frequency K (Roger, 1977; Chen et al., 2000a; Lazzari et al., 2004). For example, let

$$\mathscr{F}[f_{Lh}(t)] = K^2(iH_1^* + H_4^*) = \left[C_{Lh,1} + iC_{Lh,2}\frac{B\omega}{U} + C_{Lh,3}(\frac{iB\omega}{U})^2 + \sum_{k=4}^{n} C_{Lh,k}\frac{i\omega}{d_{Lh,k}\frac{U}{B} + i\omega}\right] \tag{4.9}$$

where $C_{Lh,i}$ and $d_{Lh,k}$ ($d_{Lh,k} \geq 0$; $i = 1, \ldots, n$ and $k = 4, \ldots, n$) = frequency independent coefficients. The first and second terms on the right-end side of equation (4.9) represent the non-circulatory static-aerodynamics and the aerodynamic damping, respectively; the third term denotes the additional aerodynamic mass which is usually negligible; and the rational terms represent the unsteady components which lag the velocity term and allow an approximation of the time delays through the positive values of parameters $d_{Lh,k}$. The value of n indicates the level of accuracy in this approximation. Based on equation (4.9), the following relations can be derived:

$$\begin{aligned} H_1^*(v) &= \frac{v}{2\pi}C_{Lh,2} + \sum_{k=4}^{n}\frac{v^3}{2\pi d_{Lh,k}^2 v^2 + 8\pi^3}C_{Lh,k}d_{Lh,k} \\ H_4^*(v) &= \frac{v^2}{4\pi^2}C_{Lh,1} - C_{Lh,3} + \sum_{k=4}^{n}\frac{v^2}{d_{Lh,k}^2 v^2 + 4\pi^2}C_{Lh,k} \end{aligned} \tag{4.10}$$

where $v = 2\pi / K$ = reduced velocity. Therefore, the frequency independent coefficients $C_{Lh,i}$ and $d_{Lh,k}$ can be determined through least squares fitting of flutter derivatives obtained experimentally at discrete reduced frequencies/velocities. The above rational function representation of the aerodynamic transfer function for the self-excited lift force component induced by the vertical structural motion [see equation (4.9)] can be extended into the Laplace domain by introducing the Laplace parameter $s = i\omega$. Then, the self-excited lift force

component induced by vertical structural motion can be derived by substituting the inverse Laplace transformation of $\mathscr{F}[f_{Lh}(t)]_{(i\omega=s)}$ into the corresponding component in equation (4.3) as

$$L_{se,h}(t)=\frac{1}{2}\rho U^2\left[C_{Lh,1}h(t)+C_{Lh,2}\frac{B}{U}\dot{h}(t)+C_{Lh,3}\frac{B^2}{U^2}\ddot{h}(t)+\sum_{k=4}^{n}C_{Lh,k}\int_{-\infty}^{t}e^{-\frac{d_{Lh,k}U}{B}(t-\tau)}\dot{h}(\tau)d\tau\right] \tag{4.11}$$

The self-excited lift force components induced by lateral and torsional structural motions can be obtained similarly. Thus, the total self-excited lift force can be expressed as

$$\begin{aligned}L_{se}(t)&=L_{se,h}(t)+L_{se,p}(t)+L_{se,\alpha}(t)=\\&\frac{1}{2}\rho U^2\left[C_{Lh,1}h(t)+C_{Lh,2}\frac{B}{U}\dot{h}(t)+C_{Lh,3}\frac{B^2}{U^2}\ddot{h}(t)+\sum_{k=4}^{n}C_{Lh,k}\int_{-\infty}^{t}e^{-\frac{d_{Lh,k}U}{B}(t-\tau)}\dot{h}(\tau)d\tau\right]\\&+\frac{1}{2}\rho U^2\left[C_{Lp,1}p(t)+C_{Lp,2}\frac{B}{U}\dot{p}(t)+C_{Lp,3}\frac{B^2}{U^2}\ddot{p}(t)+\sum_{k=4}^{n}C_{Lp,k}\int_{-\infty}^{t}e^{-\frac{d_{Lp,k}U}{B}(t-\tau)}\dot{p}(\tau)d\tau\right]\\&+\frac{1}{2}\rho U^2B\left[C_{L\alpha,1}\alpha(t)+C_{L\alpha,2}\frac{B}{U}\dot{\alpha}(t)+C_{L\alpha,3}\frac{B^2}{U^2}\ddot{\alpha}(t)+\sum_{k=4}^{n}C_{L\alpha,k}\int_{-\infty}^{t}e^{-\frac{d_{L\alpha,k}U}{B}(t-\tau)}\dot{\alpha}(\tau)d\tau\right]\end{aligned} \tag{4.12}$$

Formulations for the self-excited drag force $D_{se}(t)$ and self-excited moment $M_{se}(t)$ can be derived similarly. These derivations are not shown here for the sake of brevity.

4.2.2 Buffeting Forces

The buffeting forces per unit span of the bridge are commonly expressed as (Scanlan, 1978b; Simiu and Scanlan, 1996; Chen et al., 2000a, b)

$$L_b(t) = -\frac{1}{2}\rho U^2 B\left\{C_L \chi_{Lbu}\frac{2u(t)}{U} + [C_L' + C_D]\chi_{Lbw}\frac{w(t)}{U}\right\}$$

$$D_b(t) = \frac{1}{2}\rho U^2 B\left\{C_D \chi_{Dbu}\frac{2u(t)}{U} + C_D' \chi_{Dbw}\frac{w(t)}{U}\right\} \tag{4.13}$$

$$M_b(t) = \frac{1}{2}\rho U^2 B^2\left\{C_M \chi_{Mbu}\frac{2u(t)}{U} + C_M' \chi_{Mbw}\frac{w(t)}{U}\right\}$$

where C_L, C_D, C_M = mean lift, drag and moment coefficients, respectively; $C_L' = dC_L/d\alpha$, $C_D' = dC_D/d\alpha$ and $C_M' = dC_M/d\alpha$ (α = angle of attack of the wind); $u(t)$ and $w(t)$ = wind velocity fluctuations in the longitudinal and vertical directions, respectively; χ_{Lbu}, χ_{Lbw}, χ_{Dbu}, χ_{Dbw}, χ_{Mbu}, χ_{Mbw} = aerodynamic admittance transfer functions between wind velocity fluctuations and buffeting forces. Their squared magnitudes are known as aerodynamic admittance functions. Similar to the self-excited forces in equation (4.2), the buffeting forces in equation (4.13) cannot be used directly in time domain analysis, since the aerodynamic admittance transfer functions are frequency dependent. From equation (4.13), the buffeting force spectra can be derived as

$$S_{Lb}(\omega) = \frac{1}{4}\rho^2 U^2 B^2\left\{4C_L^2\left|\chi_{Lbu}\right|^2 S_{uu}(\omega) + [C_L' + C_D]^2\left|\chi_{Lbw}\right|^2 S_{ww}(\omega)\right\}$$

$$S_{Db}(\omega) = \frac{1}{4}\rho^2 U^2 B^2\left\{4C_D^2\left|\chi_{Dbu}\right|^2 S_{uu}(\omega) + C_D'^2\left|\chi_{Dbw}\right|^2 S_{ww}(\omega)\right\} \tag{4.14}$$

$$S_{Mb}(\omega) = \frac{1}{4}\rho^2 U^2 B^4\left\{4C_M^2\left|\chi_{Mbu}\right|^2 S_{uu}(\omega) + C_M'^2\left|\chi_{Mbw}\right|^2 S_{ww}(\omega)\right\}$$

where $S_{uu}(\omega)$, $S_{ww}(\omega)$ = power spectral density functions of longitudinal and vertical wind velocity fluctuations, respectively. It should be noted that the statistical correlation between longitudinal and vertical wind velocity fluctuations is neglected in deriving equation (4.14). The aerodynamic admittance functions are assumed to be identical and approximated by the Liepmann function (Liepmann, 1952) as

$$\left|\chi_r(\omega)\right|^2 = 1/(1+\frac{\pi\omega B}{U}) \tag{4.15}$$

where the subscript r refers to Lbu, Lbw, Dbu, Dbw, Mbu, and Mbw. Equivalent wind power spectral density functions are defined as

$$\begin{aligned} S_{uu}^{eq}(\omega) &= S_{uu}(\omega)/(1+\pi\omega B/U) \\ S_{ww}^{eq}(\omega) &= S_{ww}(\omega)/(1+\pi\omega B/U) \end{aligned} \tag{4.16}$$

Thus, the buffeting forces can be obtained from the equivalent wind velocity fluctuations simulated using the equivalent wind power spectral density functions as

$$\begin{aligned} L_b(t) &= -\frac{1}{2}\rho U^2 B\left\{C_L\frac{2u^{eq}(t)}{U}+[C_L'+C_D]\frac{w^{eq}(t)}{U}\right\} \\ D_b(t) &= \frac{1}{2}\rho U^2 B\left\{C_D\frac{2u^{eq}(t)}{U}+C_D'\frac{w^{eq}(t)}{U}\right\} \\ M_b(t) &= \frac{1}{2}\rho U^2 B^2\left\{C_M\frac{2u^{eq}(t)}{U}+C_M'\frac{w^{eq}(t)}{U}\right\} \end{aligned} \tag{4.17}$$

4.2.3 Rational Function Approximation of Flutter Derivatives

This section illustrates the rational function representation of self-excited force coefficients [see equations (4.6), (4.7), and (4.8)] through least squares fitting of flutter derivatives determined experimentally at discrete reduced frequencies/velocities [see equation (4.10)].

Since the aerodynamic coefficients of VTB are not available, the flutter derivatives H_1^* to H_4^* and A_1^* to A_4^*, determined experimentally for the William Preston Lane Bridge (WPLB) (J. D. Raggett, Personal communication, 2004) located in Baltimore, Maryland, are used for VTB which is similar in size and design. The remaining dimensionless aerodynamic

coefficients are taken as (J. D. Raggett, Personal communication, 2004): $H_5^* = H_6^* = 0$, $A_5^* = A_6^* = 0$ and $P_2^* = P_3^* = P_4^* = P_5^* = P_6^* = 0$; $C_L = 0$, $C_M = 0$, $C_D = 0.162$ (C_D is estimated as 2.5 times the projected frontal area per unit length of the bridge deck normalized by the deck's width); $C_L' \cong K(H_1^{*2} + H_4^{*2})^{1/2} = 1.415$, $C_M' \cong K(A_1^{*2} + A_4^{*2})^{1/2} = 0.238$ and $C_D' = 0$; and $P_1^* = -2C_D / K$.

In this study, two lag terms (i.e., n = 5) are used in the rational representations [e.g., equation (4.9)]. Figure 4.2 shows a comparison of the flutter derivatives estimated from the rational function representations [e.g., equation (4.10)] and those measured in wind tunnel tests for WPLB. The excellent agreement obtained indicates that the self-excited forces on the bridge deck section can be approximated by the rational functions considered with very good accuracy.

4.3 Simulation of Wind-Induced Response of Vincent Thomas Bridge

A detailed 3D FE model of VTB (see Figure 4.3) developed in the structural analysis software ADINA (ADINA R&D Inc., 2002) was used in this study for the simulation of wind-induced response of VTB. This FE model is composed of 3D linear elastic (tension-only) truss elements to represent the main suspension cables and suspender cables, 3D linear elastic membrane and shell elements to model the reinforced-concrete bridge deck and stringers supporting the deck on the floor trusses, and beam-column elements to model the stiffening trusses, the lateral braces between the stiffening trusses, and the tower shafts. The floor trusses were modeled with 3D elastic beam-column and trusses elements. This FE model consists of approximately 8,900 nodes and 9,400 elements, resulting in approximately 22,000 degrees of freedom (DOFs). The natural frequencies of the low frequency vibration modes computed

from this FE model of VTB are given in Table 4.1 where they are compared with the (1) corresponding natural frequencies previously identified from actual ambient vibration data and earthquake records (Abdel-Ghaffar et al., 1992), and (2) corresponding natural frequencies computed from other validated FE models of VTB (Abdel-Ghaffar et al., 1992). This comparison shows that the FE model of VTB used in this study captures reasonably well the dominant low frequency vibration modes of this bridge.

In simulating the wind-induced response of VTB, the aerodynamic forces are assumed to act along the bridge deck only. The aerodynamic parameters are assumed to be invariant along the bridge axis and the variation of the aerodynamic characteristics due to static rotation of the bridge deck (under gravity loads and aerostatic forces due to mean wind velocity) is neglected for simplicity. The aerodynamic parameters introduced in Section 4.2.3 are used in the simulation. The buffeting forces are simulated based on the simulated equivalent wind velocity fluctuation time histories according to equation (4.17). The statistical correlation between longitudinal and vertical wind velocity fluctuations is ignored so that the spatially discretized wind velocity field is simulated as the combination of two independent stochastic vector processes. The simulation of the wind velocity fluctuations, $u^{eq}(t)$ and $w^{eq}(t)$, is performed using the spectral representation method in conjunction with the fast Fourier transform technique (Deodatis, 1996; Cao et al., 2000). The wind spectra for the longitudinal and vertical wind velocity fields are taken as Kaimal's spectrum (Kaimal et al., 1972) and Panofsky's spectrum (Lumley and Panofsky, 1964), respectively, defined as

$$S_{uu}(\omega, z) = \frac{200 z u_*^2}{4\pi U(z)[1 + \frac{50\omega z}{2\pi U(z)}]^{5/3}} \tag{4.18}$$

$$S_{ww}(\omega, z) = \frac{3.36 z u_*^2}{4\pi U(z)[1+10(\frac{\omega z}{2\pi U(z)})^{5/3}]}$$

where $u_* = kU(z)/\ln(z/z_0)$ = shear velocity of the wind flow in m/s; z_0 = roughness length in m; $k \approx 0.4$; and $U(z)$ = mean wind velocity in m/s at height z above the ground level. In this study, $z_0 = 0.07$ m, and the height of the bridge deck above the ground is $z = 60$ m. The mean wind velocity, U, is taken as 10 m/s (36 km/h) to simulate wind-induced ambient vibrations under common low wind intensity. The coherence function of the wind velocity fluctuations at two different locations of abscissas x_1 and x_2 along the bridge deck is taken as (Davenport, 1968; Cao et al., 2000)

$$Coh_r(x_1, x_2, \omega) = \exp(-\frac{\lambda\omega|x_1 - x_2|}{2\pi U(z)}), \quad \omega > 0 \tag{4.19}$$

where subscript $r = u$ or w, $\lambda = 10$ for the longitudinal wind velocity fluctuation and $\lambda = 8$ for the vertical wind velocity fluctuation. The aerodynamic forces are discretized at 27 locations along the bridge axis as shown in Figure 4.4, implying that the longitudinal and vertical stochastic wind velocity fields are discretized into two independent vector processes of 27 components each. Two hour long wind velocity records are simulated with a sampling time of $\Delta t = 0.25$ s. As illustration, Figure 4.5 shows a sample of the simulated longitudinal and vertical wind velocity fluctuations at the center point of main span. The estimated (from simulated time histories) equivalent power spectral density function of the longitudinal wind velocity fluctuation is compared in Figure 4.6 to the theoretical wind spectrum [see equations (4.16) and (4.18)] used to simulate the stochastic wind velocity field. Similarly, Figure 4.7 shows a comparison between exact and estimated (from simulated time histories) coherence functions of the longitudinal wind velocity fluctuations at two stations located 28.4 m apart.

From Figure 4.6 and Figure 4.7, it is observed that the simulated wind velocity field along the bridge follows closely the assumed theoretical wind spectrum and coherence function.

It is assumed that the self-excited forces per unit span at different locations along an "aerodynamic" element of length L (corresponding to the tributary length of the "aerodynamic" node located at the center of the "aerodynamic" element) are fully correlated, while the random fluctuation of the buffeting forces per unit span along an "aerodynamic" element is accounted for. It is assumed that the buffeting force components induced by the longitudinal, u, and vertical, w, wind velocity fluctuations are uncorrelated, since the statistical correlation between u and w is neglected. Based on the above assumptions, for example, the self-excited and buffeting lift force components acting at an "aerodynamic" node with tributary length L can be expressed as (Chen et al., 2000a)

$$\begin{aligned} L_{se}^{e}(t) &= L_{se}^{c}(t)L \\ L_{b}^{e}(t) &= L\int_{0}^{t}[h_{Lbu}(t-\tau)L_{bu}^{c}(\tau)+h_{Lbw}(t-\tau)L_{bw}^{c}(\tau)]d\tau \end{aligned} \tag{4.20}$$

where the superscript c indicates the center location of the "aerodynamic" element e; $h_{Lbu}(t)$ and $h_{Lbw}(t)$ are the impulse response functions, the Fourier transforms of which, $H_{Lbu}(\omega)$ and $H_{Lbw}(\omega)$ (referred to as the joint acceptance functions), satisfy the following relation:

$$\left|H_{Lbr}(\omega)\right|^{2} = \frac{1}{L^{2}}\int_{0}^{L}\int_{0}^{L} coh_{Lbr}(x_{1,}x_{2},\omega)dx_{1}dx_{2} \tag{4.21}$$

in which $r = u$ or w; and $coh_{Lbr}(x_{1,}x_{2},\omega)$ denotes the coherence function of the lift buffeting force components per unit span at two different positions x_1 and x_2 along the "aerodynamic" element, which is assumed to be the same as that for the wind velocity fluctuations [see equation (4.19)]. The drag and moment buffeting force components can be expressed in a

similar way. The transfer functions $H_{L_{br}}(\omega)$ ($r = u, w$) in equation (4.21) are also approximated using rational functions for the purpose of time domain analysis, e.g.,

$$H_{L_{br}}(\omega) = [C_1 + \sum_{k=2}^{n} C_k \frac{i\omega}{d_k \frac{U}{B} + i\omega}] \tag{4.22}$$

where the coefficients C_k and d_k are determined through least squares fitting.

The dynamic response of a suspension bridge depends on the deformed bridge configuration and stress state under gravity loads. Therefore, first a geometric nonlinear static analysis is performed for the bridge under gravity loads only, using an incremental-iterative solution procedure. The aerodynamic wind forces (with buffeting forces based on the fluctuating wind velocity fields $u(t)$ and $w(t)$ and self-excited forces computed based on the displacement field of the bridge relative to its static equilibrium position under gravity loads only) are then applied with initial conditions given by the bridge state under gravity loads only. The dynamic equations of motion of the bridge under aerodynamic wind loads are linearized (geometrically) about the displacement and stress fields corresponding to gravity loads. Finally, these linearized equations of motion are solved using the constant average acceleration version of Newmark time stepping method with parameters $\delta = 0.5$ and $\alpha = 0.25$. As illustration, Figure 4.8 shows the simulated vertical dynamic response of the bridge at the center of main span.

4.4 System Identification of Vincent Thomas Bridge

4.4.1 Data-Driven Stochastic Subspace Identification

Data-driven stochastic subspace identification (SSI-DATA) is one of the most advanced state-of-the-art output-only system identification method, which has already been successfully applied for modal parameter identification of long-span bridges based on ambient

vibration data. The SSI-DATA algorithm extracts a linear state-space model of the system considered using output-only measurement data directly (Van Overschee and De Moor, 1996; Peeters and De Roeck, 2001). Compared to two-stage time-domain system identification methods such as covariance-driven stochastic subspace identification (SSI-COV) (Van Overschee and De Moor, 1996) and the natural excitation technique (NExT) (James et al., 1993) combined with the eigensystem realization algorithm (ERA) (Juang and Pappa, 1985), SSI-DATA does not require any pre-processing of the data to calculate auto/cross-correlation functions or auto/cross-spectra of output data (i.e., SSI-DATA is a one-stage system identification method). In addition, robust numerical techniques such as QR factorization, singular value decomposition (SVD) and least squares are involved in this method. A brief review of this method is presented next.

The discrete-time state-space representation of a linear time-invariant system of order n is defined as

$$\begin{aligned} \mathbf{z}(k+1) &= \mathbf{A}\mathbf{z}(k) + \mathbf{B}\mathbf{u}(k) \\ \mathbf{x}(k) &= \mathbf{C}\mathbf{z}(k) + \mathbf{D}\mathbf{u}(k) \end{aligned} \tag{4.23}$$

where $\mathbf{A} \in \mathbb{R}^{n \times n}$, $\mathbf{B} \in \mathbb{R}^{n \times l}$, $\mathbf{C} \in \mathbb{R}^{m \times n}$, $\mathbf{D} \in \mathbb{R}^{m \times l}$ = state space matrices in discrete form; $\mathbf{z}(k) \in \mathbb{R}^{n}$ = state vector; $\mathbf{u}(k) \in \mathbb{R}^{l}$ = load vector (vector of loading functions); and $\mathbf{x}(k) \in \mathbb{R}^{m}$, a column vector of size m (= number of measured/output channels) which represents the measured system response at discrete time $t = k(\Delta t)$ along m DOFs. In practical applications, the load vector input function **u** is often unknown/unmeasured and only the response of the structure is measured. In this case, the discrete-time state-space model in equation (4.23) is extended to the following stochastic version:

$$\begin{aligned}\mathbf{z}(k+1) &= \mathbf{A}\mathbf{z}(k) + \mathbf{w}(k) \\ \mathbf{x}(k) &= \mathbf{C}\mathbf{z}(k) + \mathbf{v}(k)\end{aligned} \tag{4.24}$$

where state matrices **A** and **C** are the same as in equation (4.23): **A** = state transition matrix, which completely characterizes the dynamics of the system through its eigenproperties, and **C** = output matrix that specifies how the inner states are transformed into the measured system response/output; $\mathbf{w}(k) \in \mathbb{R}^n$ = process noise due to external disturbances, modeling inaccuracies (i.e., missing high-frequency dynamics) and unknown input excitation (undistinguishable from the external disturbances); and $\mathbf{v}(k) \in \mathbb{R}^m$ = measurement noise due to sensor inaccuracies and also unknown input excitation (feed-through term). Both noise terms $\mathbf{w}(k)$ and $\mathbf{v}(k)$ are assumed to be zero-mean, white vector sequences with the following covariance matrix:

$$E\left[\begin{pmatrix}\mathbf{w}(i)\\ \mathbf{v}(i)\end{pmatrix}\begin{pmatrix}\mathbf{w}(j)^T & \mathbf{v}(j)^T\end{pmatrix}\right] = \begin{bmatrix}\mathbf{Q} & \mathbf{S}\\ \mathbf{S}^T & \mathbf{R}\end{bmatrix}\delta_{ij} \tag{4.25}$$

where $E[\ldots]$ denotes the mathematical expectation operator; δ_{ij} = Kronecker delta; and **Q**, **R**, **S** = process and measurement noise auto/cross-covariance matrices.

The SSI-DATA procedure of extracting the state-space matrices **A** and **C** from output-only data can be summarized as follows: (1) Form an output Hankel matrix and partition it into "past" and "future" output sub-matrices. (2) Calculate the orthogonal projection matrix of the row space of the "future" output sub-matrix into the row space of the "past" output sub-matrix using QR factorization. (3) Obtain the system observability matrix and Kalman filter state estimate via SVD of the projection matrix. (4) Using the available Kalman filter state estimate, extract the discrete-time system state-space matrices as a least squares solution. In order to increase the computational efficiency of the system identification procedure, only the

reference "past" outputs (outputs from the "reference" sensors) instead of all "past" outputs are used to form the output Hankel matrix (Peeters and De Roeck, 1999). Once the system state-space matrices are determined, the modal parameters (natural frequencies and damping ratios) of the $N = n/2$ vibration modes can be obtained as

$$\omega_i = \left|\ln(\lambda_{2i})/\Delta t\right|$$

$$\xi_i = -\cos(angle(\ln(\lambda_{2i}))) \tag{4.26}$$

$$i = 1,\ 2,\ \ldots,\ N$$

where $\lambda_i = i^{th}$ eigenvalue of matrix **A** and Δt = sampling time. It should be noted that λ_{2i-1} and λ_{2i} (i = 1, 2, …, N) are complex conjugate pairs, each pair corresponding to a vibration mode, i.e., the natural frequency and damping ratio obtained from λ_{2i-1} are the same as those obtained from λ_{2i}. The vibration mode shapes are obtained as

$$\phi_i = \mathbf{C} \cdot \mathbf{T}_{2i-1} \tag{4.27}$$

where $\mathbf{T}_i$ denotes the i^{th} eigenvector of matrix **A**. Similarly, $\mathbf{T}_{2i-1}$ and $\mathbf{T}_{2i}$ (i = 1, 2, …, N) are complex conjugate pairs of eigenvectors, each pair corresponding to a vibration mode.

4.4.2 System Identification Results

A simulated array of 42 channels (21 along each side of the bridge deck) of vertical acceleration response of the bridge subjected to wind excitation is used for system identification. The simulated wind aerodynamic forces correspond to a mean wind velocity $U = 10$ m/s (36 km/h). Figure 4.9 shows the virtual accelerometer array along the bridge deck. The simulated acceleration records used in the identification process are 250 s long with a sampling rate of 20 Hz, corresponding to 5000 samples per record/channel and a Nyquist frequency $f_{Nyq} = 10$ Hz. In applying SSI-DATA, these simulated acceleration data were first

low-pass filtered using a finite impulse response (FIR) filter of order 512 with a cut-off frequency at 1.0 Hz. Then, an output Hankel matrix is formed including 100 block rows based on these low-pass filtered vibration data. The 15 channels on the east side of main span are used as reference "past" output channels.

The identified natural frequencies and damping ratios are reported in Table 4.1 together with the corresponding computed natural frequencies and specified damping ratios of the VTB FE model used in this study. Table 4.1 also provides modal parameters obtained from previous system identification studies of VTB based on actual ambient vibration data and earthquake records (Abdel-Ghaffar et al., 1992). It is observed that there is an excellent agreement between the identified natural frequencies based on the simulated wind-induced response data and those computed from the bridge FE model. The difference between identified and analytically predicted natural frequency is largest for the first mode, which could be due to the fact that the FE model of VTB used here has three very closely spaced modes with natural frequencies of 0.182, 0.226, and 0.231 Hz. The vibration mode at 0.182 Hz could not be accurately identified based on the simulated accelerometer data. The damping ratios identified based on the simulated wind-induced response data and the damping ratios specified in the FE model of VTB are in a good agreement considering that the estimation uncertainty of damping ratios is inherently larger than that of natural frequencies.

It is important to mention that the identified natural frequencies and damping ratios also include the contribution of the aerodynamic stiffness and damping induced by the wind-structure interaction, which depend on the reduced wind velocity ($2\pi U/B\omega$), the geometrical configuration of the bridge section and the approach wind flow. Due to wind-structure interaction, the identified modal parameters (especially the damping ratios) of long-span cable-supported bridges under wind loading can vary significantly with wind velocity when

approaching the flutter onset velocity. In a hybrid experimental-analytical flutter analysis of Jianyin Bridge, a suspension bridge with a main span of 1385 m and a streamlined closed box steel girder (36.8 m wide and 3 m high), modal aerodynamic damping ratios of some vibration modes reached values of approximately up to 10% (from corresponding structure modal damping ratios of 0.5%) at the flutter onset wind velocity (Ding et al., 2002). More studies about effects of wind-structure interaction on dynamic characteristics of long-span cable-supported bridges can be found in Matsumoto et al. (1996), Miyata et al. (1997), Larsen (1998), Chen et al. (2000a, b; 2001), Matsumoto et al. (2002), and Chen and Kareem (2003).

The vibration mode shapes identified using state-space model based system identification methods such as SSI-DATA are in general complex valued. Figure 4.10 represents in polar plots (i.e., rotating vectors in the complex plane) the mode shapes of VTB identified using SSI-DATA based on the simulated (wind-induced) ambient vibration data. These polar plots have the advantage to show directly the extent of the non-proportional damping characteristics of a vibration mode. If all complex valued components of a mode shape vector are collinear (i.e., in phase or 180 degrees out of phase), this vibration mode is said to be classically (or proportionally) damped. On the other hand, the more these mode shape components are scattered in the complex plane, the more the vibration mode is non-classically (or non-proportionally) damped. However, measurement noise, estimation errors and modeling errors can also cause a truly classically damped mode to be identified as non-classically damped. Figure 4.10 shows that most of the vibration modes (modes # 1, 4-8) identified in this study are either perfectly or nearly classically damped. A 3D representation of the normalized mode shapes of the bridge deck for these identified vibration modes is given in Figure 4.11. Normalization was performed by projecting all mode shape components onto their principal axis (in the complex plane) and then scaling this projected mode shape vector

for a unit value of its largest component. The identified space-discrete mode shapes were interpolated between the virtual sensor locations using cubic splines along both sides of the bridge deck and straight lines across the deck.

The modal assurance criterion (MAC) (Allmang and Brown, 1982) is used to compare the identified and computed ("exact") vibration mode shapes. The MAC value, bounded between 0 and 1, measures the degree of correlation between corresponding identified and computed mode shapes as

$$\mathrm{MAC}(\phi_{\text{identified}}, \phi_{\text{computed}}) = \frac{\left|\phi^{*}_{\text{identified}} \phi_{\text{computed}}\right|^2}{\left|\phi_{\text{identified}}\right|^2 \left|\phi_{\text{computed}}\right|^2} \tag{4.28}$$

where * denotes the complex conjugate transpose. A MAC value of 0 indicates that the corresponding identified and computed mode shapes are completely uncorrelated, while a MAC value of 1 indicates perfect correlation between them. The MAC values for all pairs of identified and computed mode shapes are also given in Table 4.1. For all vibration modes identified, except for the second one, there is a very good to excellent agreement between corresponding identified and computed mode shapes. The high degree of non-classical damping identified for the second mode (see Figure 4.10) could be the reason behind the low MAC value obtained for this mode. Such high degree of non-classical damping could be true/physical (possibly due to wind-structure interaction) or could be caused by estimation and/or modeling errors. 3D representations of the mode shapes computed from the FE model of VTB are shown in Figure 4.12, which can be compared directly with their identified counterparts in Figure 4.11.

In order to study the effects of measurement noise on the system identification results, zero-mean Gaussian white noise processes are added to the simulated bridge vibration response data. Statistical properties (mean and standard deviation) of the estimated modal

parameters are investigated for increasing level of measurement noise. For this purpose, a set of 100 identifications was performed at each of three different measurement noise levels (2%, 5% and 10%). For a given output channel, the noise level is defined as the ratio (in percent) of the root mean square (RMS) of the added noise process to the RMS of the simulated acceleration response. The added measurement noise processes are assumed statistically independent across the output channels and over the 100 realizations considered. The statistics (mean and coefficient-of-variation) over 100 trials of the identified natural frequencies and damping ratios normalized to their counterparts identified based on simulated noise-free data are reported in Table 4.2 and Table 4.3, respectively, for the three measurement noise levels considered. The coefficient-of-variation of a random variable is defined as the ratio of its standard deviation to its (absolute) expected value (mean). In addition, mean and mean +/- one standard deviation of the identified natural frequencies and damping ratios normalized to their counterparts identified based on simulated noise-free data are represented graphically in Figure 4.13 and Figure 4.14, respectively. Based on the results reported in Table 4.2 and Table 4.3 and plotted in Figure 4.13 and Figure 4.14, it is observed that both the bias and coefficient-of-variation of the identified natural frequencies and damping ratios introduced by the measurement noise increase with increasing noise level as expected. However, bias and coefficient-of-variation due to measurement noise remain very small (negligible) for the identified natural frequencies (see Table 4.2 and Figure 4.13). Although they are significantly larger for the identified damping ratios (see Table 4.3 and Figure 4.14), they remain relatively small since it is well known that the estimation uncertainty of damping ratios is inherently larger than that of natural frequencies. It was also found that the measurement noise considered has very small (negligible) effects on the identified mode shapes.

4.5 Conclusions

Wind-induced ambient vibration of Vincent Thomas Bridge (VTB), a long-span suspension bridge located in San Pedro near Los Angeles, California, is simulated using a detailed three-dimensional FE model of the bridge and a state-of-the-art stochastic wind excitation model including both buffeting and self-excited forces. Based on these simulated ambient vibration data, modal parameters of the low frequency vertical vibration modes of VTB are identified using data-driven stochastic subspace identification (SSI-DATA), a state-of-the-art output-only system identification method. The identified modal parameters are in good agreement with the computed ("exact") modal parameters obtained directly from the FE model of VTB, which themselves are in good agreement with the corresponding modal parameters of VTB identified by other researchers using actual ambient vibration data. This system identification study also provides the opportunity to investigate the accuracy of the modal identification results obtained using SSI-DATA in the case of a large and complex (virtual) structural problem for which the "exact" modal parameters (modal parameters of the FE model of VTB) are known, which is usually not the case when system identification methods are applied directly to real-world structures and data.

The effect of measurement noise on the identified modal parameters is investigated. Measurement noise is simulated by adding statistically independent zero-mean Gaussian white noise processes to the finite element simulated bridge response to wind excitation along a set of degrees of freedom (virtual output channels). The statistical properties (mean and coefficient-of-variation) of the identified modal parameters are investigated under increasing measurement noise level. Both bias and coefficient-of-variation of the identified natural frequencies and damping ratios introduced by the measurement noise increase with increasing noise level as expected. However, bias and coefficient-of-variation due to measurement noise

remain very small (negligible) for the identified natural frequencies. Although they are significantly larger for the identified damping ratios, they remain relatively small since it is well known that the estimation uncertainty of damping ratios is inherently larger than that of natural frequencies.

The methodology and study presented in this paper provide a validated framework for studying the effects of realistic damage scenarios in long-span cable-supported (suspension and cable-stayed) bridges (e.g., corrosion-induced losses in stiffness and strength of main cables and suspenders at different locations along the bridge) on modal identification results. These effects represent the basis for developing robust and reliable vibration-based structural health monitoring systems for long-span cable-supported bridges.

4.6 Acknowledgements

This Chapter is based on the manuscript submitted for possible publication (tentatively approved) in Journal of Computer-Aided Civil and Infrastructure Engineering (2007) under the title "Modal Identification Study of Vincent Thomas Bridge Using Simulated Wind-Induced Ambient Vibration Data" with authors Xianfei He, Babak Moaveni, Joel P. Conte, Ahmed Elgamal, and Sami F. Masri. The dissertation author is the primary investigator of this paper. For this part of research, I would like to express my thanks to Dr. Jon D. Raggett, President of West Wind Laboratory, Inc. and Dr. Xinzhong Chen at Texas Tech University for providing the aerodynamic parameters needed for the wind response simulation and for very useful suggestions and insightful discussions regarding the stochastic wind excitation model.

4.7 References

Abdel-Ghaffar, A. M., Masri, S. F., and Niazy, A. S. M. (1992). "Seismic performance evaluation of suspension bridges." *Proceedings of the 10th World Conference on Earthquake Engineering*, 4845- 4850.

Allemang, R. J., and Brown, D. L. (1982). "A correlation coefficient for modal vector analysis." *Proceedings of the 1st International Modal Analysis Conference*, Bethel, Connecticut, 110-116.

ADINA R&D, Inc. (2002). "Theory and modeling Guide Vol.1: ADINA", *Report ARD 02-7*, ADINA R&D, Inc., Watertown, MA, USA.

Cao, Y., Xiang, H., and Zhou, Y. (2000). "Simulation of stochastic wind velocity field on long-span bridges." *Journal of Engineering Mechanics,* ASCE, 126(1), 1-6.

Chen X., and Kareem, A. (2003). "Aeroelastic analysis of bridges: effects of turbulence and aerodynamic nonlinearities." *Journal of Engineering Mechanics*, ASCE 129(8), 885-895.

Chen, X., Kareem, A., and Matsumoto, M. (2001). "Multimode coupled flutter and buffeting analysis of long span bridges." *Journal of Wind Engineering and Industrial Aerodynamics*, 89(7), 649-664.

Chen, X., Matsumoto, M., and Kareem, A. (2000a). "Time domain flutter and buffeting response analysis of bridges." *Journal of Engineering Mechanics,* ASCE, 126(1), 7-16.

Chen, X., Matsumoto, M., and Kareem, A. (2000b). "Aerodynamic coupling effects on flutter and buffeting of bridges." *Journal of Engineering Mechanics,* ASCE, 126(1), 17-26.

Davenport, A. G. (1968). "The dependence of wind load upon meteorological parameters." *Proceedings of the International Research Seminar on Wind Effects on Buildings and Structures*, University of Toronto Press, Toronto, 19-82.

Deodatis, G. (1996). "Simulation of ergodic multivariate stochastic processes." *Journal of Engineering Mechanics,* ASCE, 122(8), 778-787.

Ding, Q., Chen, A., and Xiang, H. (2002). "Coupled flutter analysis of long-span bridges by multimode and full-order approaches." *Journal of Wind Engineering and Industrial Aerodynamics*, 90(12), 1981-1993

Doebling, S. W., Farrar, C. R., Prime, M. B., and Shevitz, D. W. (1996). "Damage identification and health monitoring of structural mechanical systems from changes in their vibration characteristics: A literature review." *Los Alamos National Laboratory Report No.LA-13070-MS,* Los Alamos National Laboratory, Los Alamos, New Mexico.

Farrar, C. R., and Jauregui, D. A. (1998). "Comparative study of damage identification algorithms applied to a bridge: I. experiment." *Smart Materials and Structures*, 7(5), 704-719.

Friswell, M. I., and Mottershead, J. E. (1995). *Finite element model updating in structural dynamics*, Kluwer Academic Publishers, Boston, USA.

James, G. H., Carne, T. G., and Lauffer, J. P. (1993). "The natural excitation technique for modal parameters extraction from operating wind turbines." *Report No. SAND92-1666, UC-261,* Sandia National Laboratories, Sandia, New Mexico.

Juang, J. N., and Pappa, R. S. (1985). "An eigensystem realization algorithm for modal parameter identification and model reduction." *Journal of Guidance, Control and Dynamics*, 8(5), 620-627.

Kaimal, J. C., Wyngaard, J. C., Izumi, Y., and Cote, O. R. (1972). "Spectral characteristics of surface-layer turbulence." *Journal of Royal Meteorological Society*, 98(417), 563-589.

Larsen, A. (1998). "Advances in aeroelastic analysis of suspension and cable-stayed bridges." *Journal of Wind Engineering and Industrial Aerodynamics*, 74, 73-90.

Lazzari, M., Vitaliani, R. V., and Saetta, A. V. (2004). "Aeroelastic forces and dynamic response of long-span bridges." *International Journal for Numerical Methods in Engineering*, 60(6), 1011-1048.

Liepmann, H. W. (1952). "On the application of statistical concepts to the buffeting problem." *Journal of Aeronautical Science*, 19(12), 793-800.

Lin, Y. K., and Yang, J. N. (1983). "Multimode bridge response to wind excitations." *Journal of Engineering Mechanics,* ASCE, 109(2), 586-603.

Lumley, J. L., and Panofsky, H. A. (1964). *The structure of atmospheric turbulence*. Wiley-Interscience, New York.

Maeck, J., and De Roeck, G. (1999). "Dynamic bending and torsion stiffness derivation from modal curvatures and torsion rates." *Journal of Sound and Vibration*, 225(1), 153-170.

Matsumoto, M., Kobayashi, Y., and Shirato, H. (1996). "The influence of aerodynamic derivatives on flutter." *Journal of Wind Engineering and Industrial Aerodynamics*, 60(1), 227-239.

Matsumoto, M., Shirato, H., Yagi, T., Shijo, R., Eguchi, A., and Tamaki, H. (2002). "Effects of aerodynamic interferences between heaving and torsional vibration of bridge decks: the case of Tacoma Narrows Bridge." *Journal of Wind Engineering and Industrial Aerodynamics*, 91(12), 1547-1557.

Miyata, T., Yamada, H., and Kazama, K. (1997). "Discussion on aeroelastic detail and control in the flutter occurrences of long-span bridges." *Journal of Wind Engineering and Industrial Aerodynamics*, 69, 839-849.

Pandey, A. K., Biswas, M., and Samman, M. M. (1991). "Damage detection from changes in curvature mode shapes." *Journal of Sound and Vibration*, 145(2), 321-332.

Pandey, A. K., and Biswas, M. (1994). "Damage detection in structures using changes in flexibility." *Journal of Sound and Vibration*, 169(1), 3-17.

Peeters, B., and De Roeck, G. (1999). "Reference-based stochastic subspace identification for output-only modal analysis." *Journal of Mechanical Systems and Signal Processing*, 13(6), 855-878.

Peeters, B., and De Roeck, G. (2001). "Stochastic system identification for operational modal analysis: A review." *Journal of Dynamic Systems, Measurement, and Control*, 123(4), 659-667.

Roger, K. L. (1977). "Airplane math modeling methods for active control design." *Tech. Report CP-228,* AGARD.

Salawu, O. S. (1997). "Detection of structural damage through changes in frequency: A review." *Engineering Structures*, 19(9), 718-723.

Scanlan, R. H. (1978a). "The action of flexible bridges under the wind. I: Flutter theory." *Journal of Sound and Vibration*, 60(2), 187-199.

Scanlan, R. H. (1978b). "The action of flexible bridges under the wind. II: Buffeting theory." *Journal of Sound and Vibration*, 60(2), 201-211.

Shi, Z.Y., Law, S. S., and Zhang, L.M. (2002). "Improved damage quantification from elemental modal strain energy change." *Journal of Engineering Mechanics*, ASCE, 128(5), 521-529.

Simiu, E., and Scanlan, R. H. (1996). *Wind effects on structures: Fundamentals and Applications to Design*. John Wiley and Sons, New York, USA.

Sohn, H., Farrar, C. R., Hemez, F. M., Shunk, D. D., Stinemates, D. W., and Nadler, B. R. (2003). "A review of structural health monitoring literature: 1996-2001." *Los Alamos National Laboratory Report No. LA-13976-MS*, Los Alamos National Laboratory, Los Alamos, New Mexico.

Teughels, A., and De Roeck, G. (2004). "Structural damage identification of the highway bridge Z24 by FE model updating." *Journal of Sound and Vibration*, 278(3), 589-610.

Van Overschee, P., and De Moor, B. (1996). *Subspace identification for linear systems.* Kluwer Academic Publishers, Norwell, Massachusetts, USA.

Table Captions

Table 4.1. System identification results

Mode No.	Natural frequency [Hz]		Damping ratio [%]		MAC	Abdel-Ghaffar et al. (1992)			
						Identified freq. [Hz]		Computed freq. [Hz]	
	Identified	Computed	Identified	Specified		A.V.	E.Q.	2D Model	3D Model
1	0.214	0.231	3.8	1.8	0.961	0.216	0.209	0.197	0.201
2	0.226	0.226	2.3	1.8	0.711	0.234	0.224	0.221	0.224
3	0.357	0.364	0.9	1.6	0.928	0.366	0.364	0.348	0.336
4	0.455	0.459	2.6	1.7	0.988	0.487	0.448	0.459	0.443
5	0.514	0.511	2.1	1.8	0.995	0.494	0.513	0.455	0.438
6	0.576	0.571	0.5	1.8	0.994	0.579	0.562	0.549	0.527
7	0.687	0.684	1.5	2.0	0.994	N/A	N/A	N/A	N/A
8	0.815	0.823	0.2	2.3	0.997	N/A	N/A	N/A	N/A

Table 4.2. Mean and coefficient-of-variation (COV) of the identified natural frequencies normalized to their counterparts identified based on noise-free data at different measurement noise levels

Mode No	2% noise		5% noise		10% noise	
	mean	COV[%]	mean	COV [%]	mean	COV [%]
1	0.9998	0.05	0.9994	0.06	0.9992	0.07
2	1.0003	0.07	1.0000	0.09	0.9998	0.10
3	1.0005	0.03	1.0006	0.03	1.0008	0.04
4	0.9998	0.04	0.9997	0.05	0.9996	0.06
5	0.9999	0.01	0.9999	0.01	0.9999	0.02
6	0.9994	0.01	0.9992	0.01	0.9991	0.02
7	1.0001	0.01	1.0001	0.01	1.0001	0.01
8	1.0006	0.01	1.0007	0.01	1.0009	0.02

Table 4.3. Mean and coefficient-of-variation (COV) of the identified damping ratios normalized to their counterparts identified based on noise-free data at different measurement noise levels

Mode No	2% noise		5% noise		10% noise	
	mean	COV[%]	mean	COV [%]	mean	COV [%]
1	0.984	1.61	0.973	1.73	0.966	1.91
2	0.993	3.01	0.976	3.92	0.979	3.74
3	1.306	3.46	1.372	4.09	1.417	4.58
4	1.018	1.53	1.016	2.07	1.012	2.83
5	1.010	0.49	1.016	0.58	1.017	0.83
6	1.097	1.83	1.122	2.14	1.186	2.93
7	1.007	0.28	1.011	0.47	1.018	0.70
8	1.275	2.21	1.308	2.92	1.375	3.53

Figure Captions

Figure 4.14. Statistics (mean, mean +/- one standard deviation) over 100 trials of the identified damping ratios normalized to their counterparts identified based on noise-free data at different noise levels

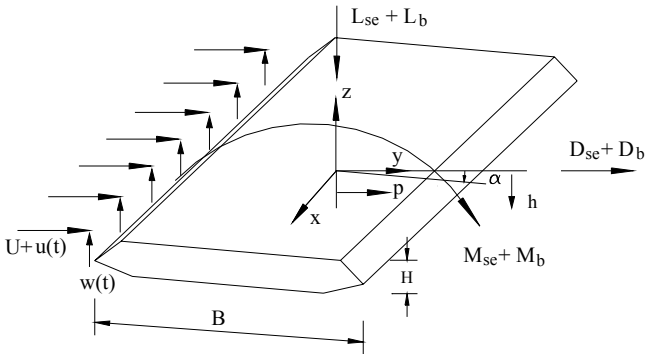

Figure 4.1. Aerodynamic forces on bridge deck section

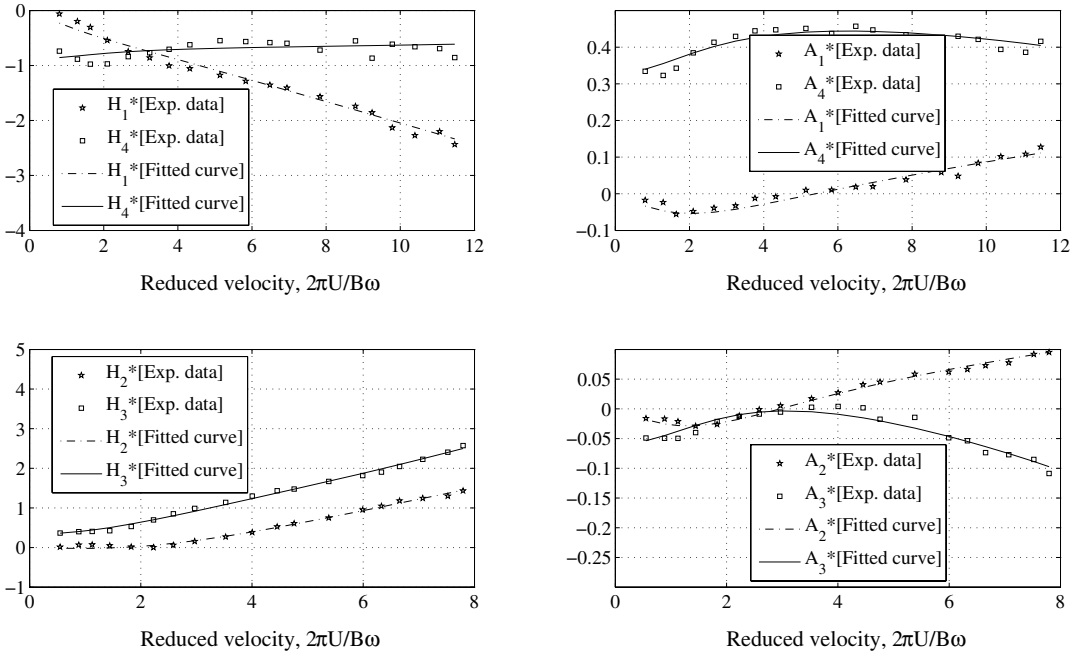

Figure 4.2. Rational function approximations of flutter derivatives for William Preston Lane Bridge (J. D. Raggett, Personal communication, 2004)

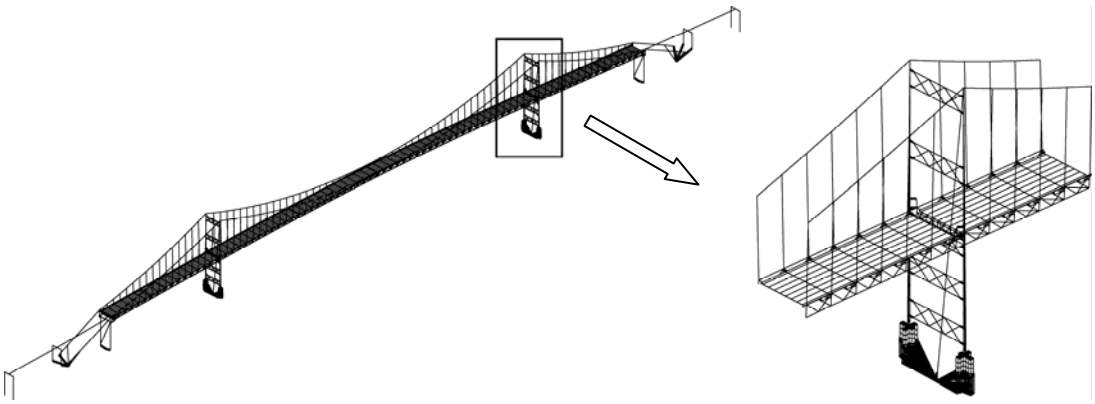

Figure 4.3. Three-dimensional finite element model of Vincent Thomas Bridge

Figure 4.4. Locations of spatially discretized aerodynamic forces ("aerodynamic" nodes) along the bridge deck

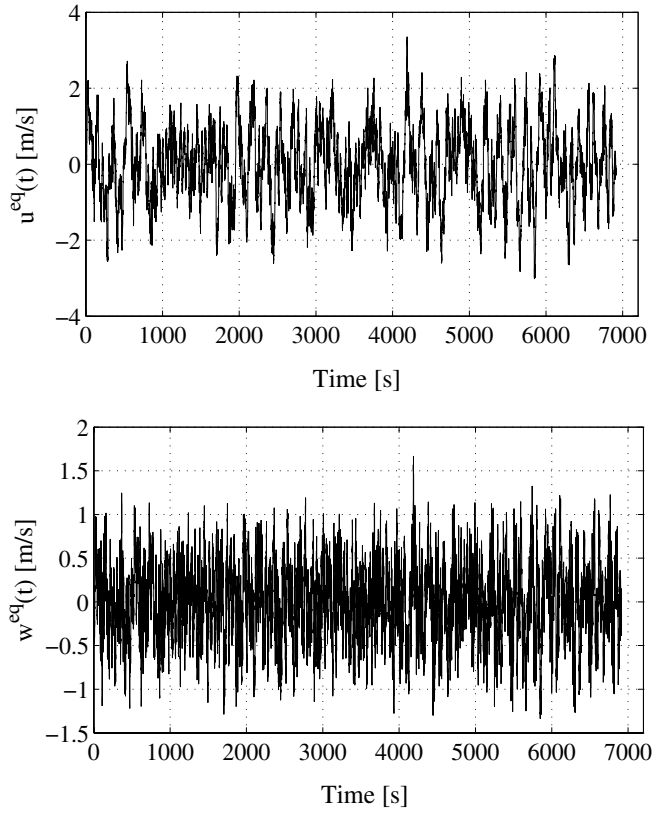

Figure 4.5. Simulated longitudinal, $u^{eq}(t)$, and vertical, $w^{eq}(t)$, wind velocity fluctuations (U = 10 m/s)

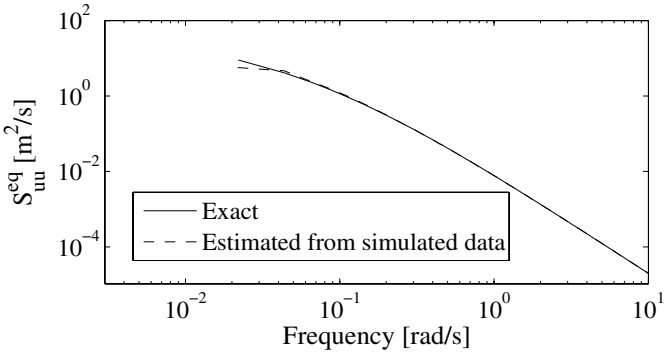

Figure 4.6. Comparison of estimated (from simulated data) and exact longitudinal wind velocity spectrum

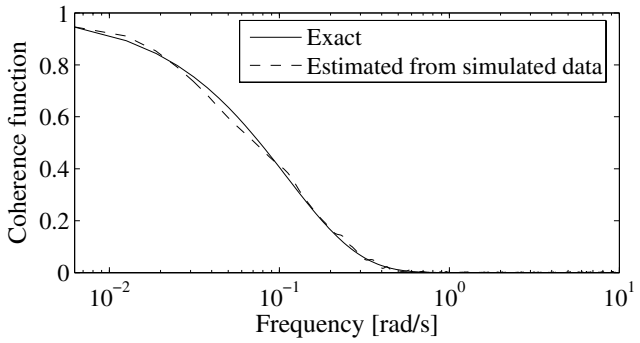

Figure 4.7. Comparison of simulated and exact coherence function of the longitudinal wind velocity fluctuation

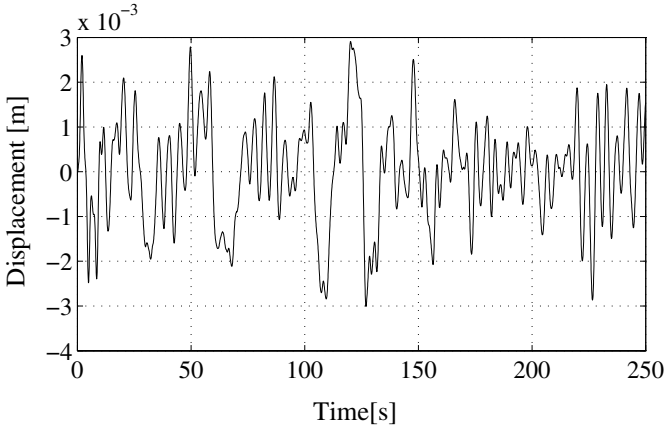

Figure 4.8. Simulated vertical displacement response of VTB at center of main span

Figure 4.9. Virtual array of accelerometers along the bridge deck

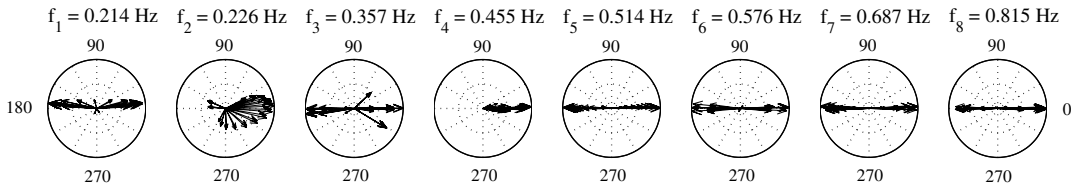

Figure 4.10. Polar plot representation of vibration mode shapes identified using SSI-DATA

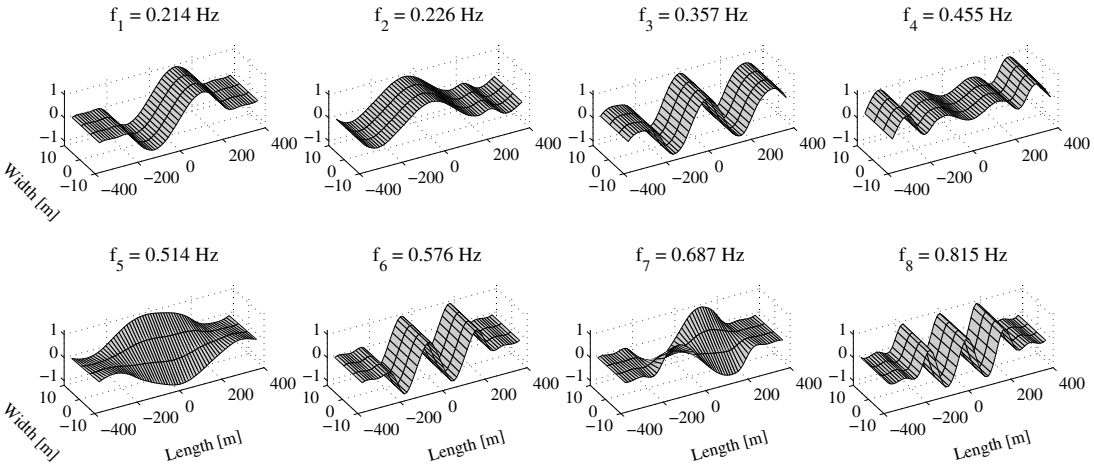

Figure 4.11. 3D representation of normalized vibration mode shapes identified using SSI-DATA

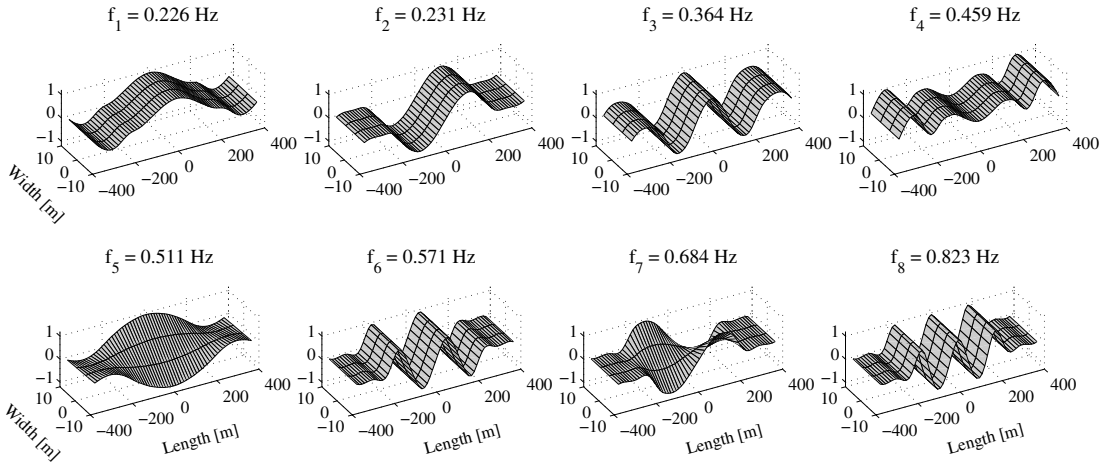

Figure 4.12. 3D representation of vibration mode shapes computed from the finite element model of VTB

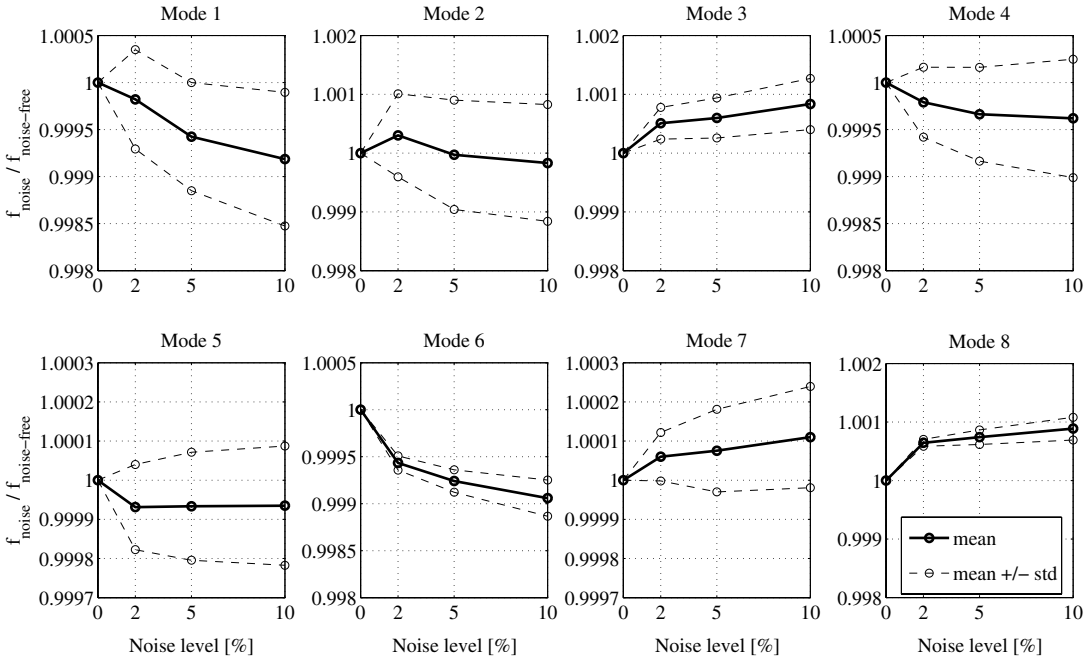

Figure 4.13. Statistics (mean, mean +/- one standard deviation) over 100 trials of the identified natural frequencies normalized to their counterparts identified based on noise-free data at different measurement noise levels

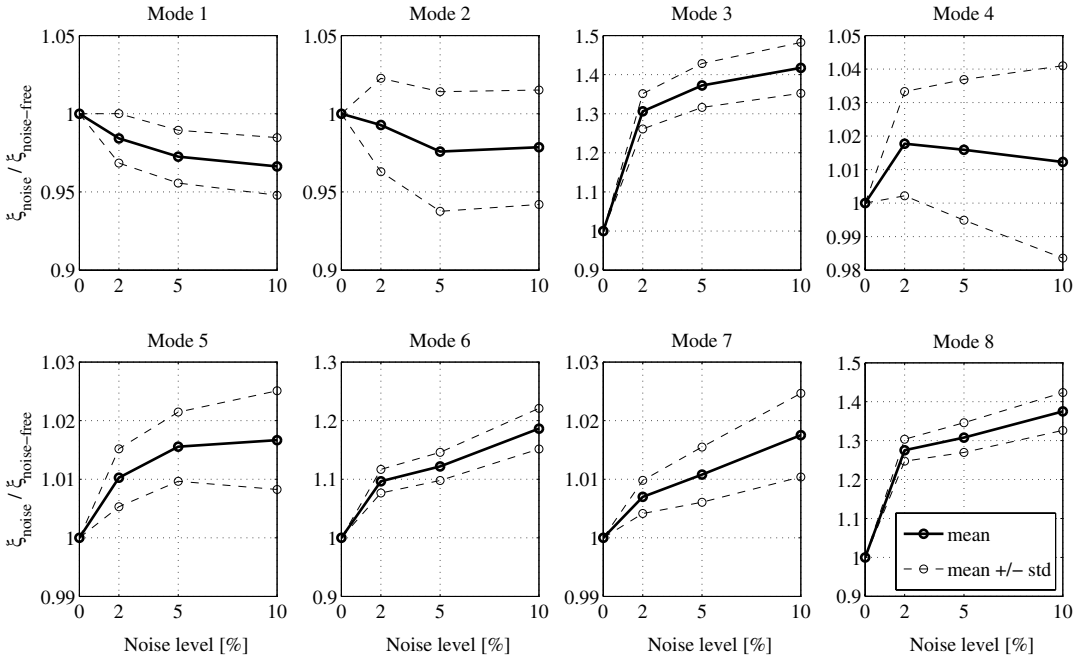

Figure 4.14. Statistics (mean, mean +/- one standard deviation) over 100 trials of the identified damping ratios normalized to their counterparts identified based on noise-free data at different noise levels

Chapter 5

Finite Element Model Updating and Damage Identification of a Seven-Story Reinforced Concrete Shear Wall Building Slice Tested on the UCSD-NEES Shake Table

5.1 Introduction

Damage identification consists of detecting the occurrence of damage, localizing the damage zones, and estimating the extent of damage. Numerous vibration-based methods have been proposed to achieve these goals. Salawu (1997) presented a review on the use of natural frequency changes for damage detection. It is however challenging to localize the damage (e.g., to obtain spatial information on the structural damage) from changes in natural frequencies only. Pandey et al. (1991) introduced the concept of mode shape curvature for damage localization. In his study, both a cantilever and a simply supported beam model were used to demonstrate the effectiveness of using changes in modal curvature as a damage indicator to detect and localize damage. As another mode shape based damage indicator, Pandey and Biswas (1994) proposed the use of changes in the dynamically measured flexibility matrix to detect and localize damage. It was shown that the flexibility matrix of a structure can be easily and accurately estimated from a few low frequency vibration modes of the structure. Recently, Bernal and Gunes (2004) have incorporated changes in modal flexibility matrices (or flexibility proportional matrices) into the damage locating vector (DLV) technique to localize damage. Methods based on changes in identified modal parameters to detect and localize damage in structures have also been further developed for the purpose of

damage quantification. Among these methods are strain-energy based methods (Shi et al., 2002) and the direct stiffness calculation method (Maeck and De Roeck, 1999).

Another class of sophisticated methods consists of applying sensitivity-based finite element (FE) model updating for damage identification. The FE model updating methodology is one of the most promising approaches to identify (i.e., detect, localize and quantify) structural damage. This class of methods updates the physical parameters of a FE model of the structure by minimizing an objective function expressing the discrepancy between analytically predicted and experimentally identified features that are sensitive to damage such as natural frequencies and mode shapes. Optimum solutions of the problem are reached through sensitivity-based optimization algorithms. In this study, a sensitivity-based FE model updating strategy is applied for damage identification of a full-scale seven-story reinforced concrete (R/C) building slice tested on the UCSD-NEES shake table. The shake table tests were designed so as to damage the building progressively through several seismic input motions reproduced on the shake table. At various levels of damage, several low amplitude white noise base excitations were applied through the shake table to the building which responded as a quasi-linear system with parameters evolving as a function of damage. In addition, ambient vibration tests were performed on the building specimen between seismic tests.

In this chapter, the sensitivity-based FE model updating methodology is described. A linear flat shell element is implemented in the element library of the MATLAB-based structural analysis software FEDEASLab (Filippou and Constantinides, 2004), which is then integrated with the FE model updating algorithms used/developed in order to perform structural damage identification. This shell element is based on the mixed discrete variational principle proposed by Hughes and Brezzi (1989) in conjunction with Allman type interpolation (Allman, 1988) for the membrane part and the discrete Kirchhoff plate element

derived by Batoz and Tahar (1982) for the plate part. The resulting finite element has six degrees of freedom (DOFs) per node, including a true (mechanics-based) drilling degree of freedom. A comparative study of the influence of different objective functions on the damage identification results is performed by using simulated data for a simply supported plate. Finally a sensitivity-based FE model updating strategy is applied for damage identification of a full-scale seven-story reinforced concrete (R/C) building slice.

5.2. Sensitivity-Based FE Model Updating

5.2.1 Objective Function

The sensitivity-based FE model updating can be posed as an optimization problem to minimize an objective function containing the discrepancies between numerical and experimental modal data by adjusting a set of physical parameters (see Figure 5.1):

$$\min_{\boldsymbol{\theta}} f(\boldsymbol{\theta}) = \frac{1}{2}\mathbf{r}(\boldsymbol{\theta})^T \mathbf{r}(\boldsymbol{\theta}) = \frac{1}{2}\sum_{j=1}^{m}[r_j(\boldsymbol{\theta})]^2 \tag{5.1}$$

in which $\mathbf{r}(\boldsymbol{\theta})$ = residual vector containing the differences between the analytically predicted and experimentally identified modal data; $\boldsymbol{\theta} \in \mathbb{R}^n$ = a set of physical parameters, also called updating parameters, which is adjusted to minimize the objective function. In order to obtain a unique solution, the number *m* of residuals should be larger than the number *n* of unknowns (i.e., updating parameters).

5.2.1.1 Eigen-Frequency Residual

Natural frequencies provide global information of a structure and are sensitive to the structural stiffness property. In addition, the natural frequencies are usually identified with a higher accuracy than other modal parameters. Therefore the natural frequencies are excellent residual candidates for setting up the objective function in the FE model updating. In order to

simplify the sensitivity formulations, the eigen-frequency residuals, instead of the natural frequency residuals, are usually used in the FE model updating, which are defined as (Teughels and De Roeck, 2004)

$$\mathbf{r}_f(\boldsymbol{\theta}) = \left[r_f(\boldsymbol{\theta}) \right] = \left[\frac{\lambda_j(\boldsymbol{\theta}) - \tilde{\lambda}_j}{\tilde{\lambda}_j} \right], \quad \lambda_j = \omega_j^2, \; j \in \{1 \quad 2 \quad \cdots \quad N_f\} \tag{5.2}$$

in which $\mathbf{r}_f(\boldsymbol{\theta}) \in \mathbb{R}^{N_f}$ = eigen-frequency residual vector; $\lambda_j(\boldsymbol{\theta})$ and $\tilde{\lambda}_j$ = numerical and corresponding experimental eigenvalues, respectively; N_f = number of identified natural frequencies which are used in the model updating.

5.2.1.2 Mode Shape Residual

In order to obtain spatial information on the structural damage, it is necessary to include mode shape residuals in the objective function. Due to the fact that only non-mass normalized mode shapes can be identified using output-only system identification methods based on structural response measurements, the mode shape residuals are usually defined as (Teughels and De Roeck, 2004)

$$\mathbf{r}_{ms}(\boldsymbol{\theta}) = \left[r_{ms}(\boldsymbol{\theta}) \right] = \left[\frac{\phi_j^l(\boldsymbol{\theta})}{\phi_j^r(\boldsymbol{\theta})} - \frac{\tilde{\phi}_j^l}{\tilde{\phi}_j^r} \right], \; j \in \{1 \quad 2 \quad \cdots \quad N_m\}, \quad l \in \{1 \quad 2 \quad \cdots \quad Ndof_j\} \tag{5.3}$$

$\boldsymbol{\phi}_j(\boldsymbol{\theta})$ and $\tilde{\boldsymbol{\phi}}_j$ = numerical and corresponding experimentally identified mode shape vectors; N_m = number of identified mode shapes used in the model updating; l, r = arbitrary and reference DOF of the mode shape $\boldsymbol{\phi}_j(\boldsymbol{\theta})$ (or $\tilde{\boldsymbol{\phi}}_j$), respectively. In the mode shape residual vector, each mode shape component l is divided by the reference component r, which is the component of largest amplitude. This way, both numerical and experimental mode shapes are normalized in the same fashion.

5.2.1.3 Pseudo Modal Flexibility Residual

Changes in the dynamically measured flexibility matrix have been shown to be useful damage indicators to detect and localize damage (Pandey and Biswas, 1994; Toksoy and Aktan, 1994; Catbas et al. 1997; Zhao and DeWolf 1999). These changes can also be used in the FE model updating for damage identification. However, due to the fact that (1) identified mode shapes are un-mass normalized in the case of output-only modal analysis, (2) identified mode shape components are available only at the sensor locations, and (3) only relative differences of flexibility matrices are required in the damage identification procedure, the pseudo modal flexibility matrix, instead of the flexibility matrix, can be used to set up the residual vector. The pseudo modal flexibility residual vector is defined as

$$\mathbf{r}_{pf}(\boldsymbol{\theta}) = \left[r_{pf}(\boldsymbol{\theta}) \right] = \left[\frac{f_{ij}(\boldsymbol{\theta}) - \tilde{f}_{ij}}{\tilde{f}_{ij}^{r}} \right], \; j \in \{1 \quad 2 \quad \cdots \quad Ndof\}, \quad i \in \{1 \quad 2 \quad \cdots \quad j\} \tag{5.4}$$

where $\tilde{f}_{ij}^{r}$ = reference component of the measured pseudo modal flexibility matrix. The numerical and experimentally identified pseudo modal flexibility matrices are defined as

$$\mathbf{F}(\boldsymbol{\theta})_{Ndof \times Ndof} = \sum_{j=1}^{N_{pf}} \frac{1}{\lambda_j} \frac{\boldsymbol{\phi}_j}{\phi_j^r} \frac{\boldsymbol{\phi}_j^T}{\phi_j^r} \tag{5.5}$$

$$\tilde{\mathbf{F}}_{Ndof \times Ndof} = \sum_{j=1}^{N_{pf}} \frac{1}{\tilde{\lambda}_j} \frac{\tilde{\boldsymbol{\phi}}_j}{\tilde{\phi}_j^r} \frac{\tilde{\boldsymbol{\phi}}_j^T}{\tilde{\phi}_j^r} \tag{5.6}$$

where N_{pf} , $Ndof$ = number of identified modes and measured DOFs, respectively, used to build the pseudo modal flexibility matrix.

Additional to aforementioned three types of residuals, other modal properties such as modal curvature, modal strains, modal strain energy, uniform load surface, etc. can also be used to set up the objective function. The selection of residuals and objective functions is dependent on the particular applications.

5.2.2 Correction Factors and Residual Sensitivity

The updating parameters are the uncertain physical properties of the numerical model. Instead of the absolute value of each uncertain variable θ, a dimensionless correction factor p_i is defined to represent the variation of θ_i relative to its reference values θ_i^{ref}

$$\mathbf{p} = [p_i] = \left[-(\theta_i - \theta_i^{ref})/\theta_i^{ref}\right] \quad \rightarrow \quad \theta_i = \theta_i^{ref}(1 - p_i) \tag{5.7}$$

The correction factor p_i can be assigned to a single element or a group of elements. The FE model updating problem defined in equation (5.1) is then to find the values of **p** to minimize the differences between the numerical (analytical) and measured modal data

$$\min_{\mathbf{p}} f(\mathbf{p}) = \frac{1}{2}\mathbf{r}(\mathbf{p})^T \mathbf{r}(\mathbf{p}) = \frac{1}{2}\sum_{j=1}^{m}[r_j(\mathbf{p})]^2 \tag{5.8}$$

In the case that Young's modulus is considered as the model updating parameter, the correction factor for element (group) i becomes $p_i = -(E_i - E_i^{ref})/E_i^{ref}$. Thus the correction factor indicates directly the level of damage when the finite element model updating is applied for structural damage identification purposes.

The optimum solutions of the minimization problem defined in equation (5.7) will be solved through an iterative sensitivity based optimization methods, in which the gradient and the Hessian of the objective function $f(\mathbf{p})$ are needed

$$\nabla f(\mathbf{p}) = \sum_{j=1}^{m} r_j(\mathbf{p})\nabla r_j(\mathbf{p}) = \mathbf{J}(\mathbf{p})^T \mathbf{r}(\mathbf{p}) \tag{5.9}$$

$$\nabla^2 f(\mathbf{p}) = \mathbf{J}(\mathbf{p})^T \mathbf{J}(\mathbf{p}) + \sum_{j=1}^{m} r_j(\mathbf{p})\nabla^2 r_j(\mathbf{p}) \approx \mathbf{J}(\mathbf{p})^T \mathbf{J}(\mathbf{p}) \tag{5.10}$$

in which $\mathbf{J}(\mathbf{p})$ = Jacobian matrix (sensitivity matrix) containing the first partial derivatives of the residuals with respect to **p**. The Hessian matrix $\nabla^2 f(\mathbf{p})$ is approximated with the first

order term in equation (5.10), which is known as the Gauss-Newton approximation, most often used in nonlinear least squares problems. In this case, the nonlinear least squares problem is solved by a sequence of approximating linearized least squares problems, at each iteration *k*

$$\min_{\mathbf{z}} q_k(\mathbf{z}_k) = \frac{1}{2}[\mathbf{r}(\mathbf{p}_k) + \mathbf{J}(\mathbf{p}_k)\mathbf{z}_k]^T[\mathbf{r}(\mathbf{p}_k) + \mathbf{J}(\mathbf{p}_k)\mathbf{z}_k], \text{ with } \mathbf{p}_{k+1} = \mathbf{p}_k + \mathbf{z}_k \tag{5.11}$$

$q_k(\mathbf{z})$ = quadratic model function that approximates $f(\mathbf{p})$ at the current vector $\mathbf{p}_k$; $\mathbf{z}$ = the step vector from $\mathbf{p}_k$.

The sensitivity of the residuals defined in equations (5.2), (5.3), and (5.4) with respect to the correction factor p_i can be obtained through the modal parameter sensitivities as

$$\frac{\partial \mathbf{r}_f}{\partial p_i} = \left[\frac{1}{\tilde{\lambda}_j}\frac{\partial \lambda_j}{\partial p_i}\right] \tag{5.12}$$

$$\frac{\partial \mathbf{r}_{ms}}{\partial p_i} = \left[\frac{1}{\phi_j^r}\frac{\partial \phi_j^l}{\partial p_i} - \frac{\phi_j^l}{(\phi_j^r)^2}\frac{\partial \phi_j^r}{\partial p_i}\right] \tag{5.13}$$

$$\frac{\partial \mathbf{r}^{pf}}{\partial p_i} = \left[\frac{1}{\tilde{f}_{kj}^r}\frac{\partial f_{kj}}{\partial p_i}\right] \tag{5.14}$$

where $\frac{\partial f_{kj}}{\partial p_i} = \left[\sum_{j=1}^{N_{pf}}\{\frac{1}{\lambda_j(\phi_j^r)^2}(\frac{\partial \boldsymbol{\phi}_j}{\partial p_i}\boldsymbol{\phi}_j^T + \boldsymbol{\phi}_j\frac{\partial \boldsymbol{\phi}_j^T}{\partial p_i}) - \boldsymbol{\phi}_j\boldsymbol{\phi}_j^T(\frac{1}{\lambda_j^2(\phi_j^r)^2}\frac{\partial \lambda_j}{\partial p_i} + \frac{2}{\lambda_j(\phi_j^r)^3}\frac{\partial \phi_j^r}{\partial p_i})\}\right]_{kj}$; the modal sensitivities $\partial\lambda_j/\partial p_i$ and $\partial\boldsymbol{\phi}_j/\partial p_i$ can be obtained by the work of Fox and Kapoor (1968). In the case of updating Young's modulus only, these formulas are simplified to

$$\frac{\partial \lambda_j}{\partial p_i} = \boldsymbol{\phi}_j^T\frac{\partial \mathbf{K}}{\partial p_i}\boldsymbol{\phi}_j = -\boldsymbol{\phi}_j^T\frac{\partial \mathbf{K}}{\partial E_i}\boldsymbol{\phi}E_i^{ref} \tag{5.15}$$

$$\frac{\partial \boldsymbol{\phi}_j}{\partial p_i} = \sum_{q=1;q\neq j}^{d}\frac{\boldsymbol{\phi}_q}{\lambda_j - \lambda_q}(\boldsymbol{\phi}_q^T\frac{\partial \mathbf{K}}{\partial p_i}\boldsymbol{\phi}_j) = -\sum_{q=1;q\neq j}^{d}\frac{\boldsymbol{\phi}_q}{\lambda_j - \lambda_q}(\boldsymbol{\phi}_q^T\frac{\partial \mathbf{K}}{\partial E_i}\boldsymbol{\phi}_j)E_i^{ref} \tag{5.16}$$

in which d = number of analytical vibration mode shapes used to calculate $\frac{\partial \boldsymbol{\phi}_j}{\partial p_i}$. It should be noted that the analytical mode shapes used in above sensitivity equations are mass normalized. Based on the residual sensitivity described above, the sensitivity matrix $\mathbf{J}(\mathbf{p})$ is finally obtained as

$$\mathbf{J}(\mathbf{p}) = \left[\frac{\partial r_j}{\partial p_i}\right] = \begin{bmatrix} \frac{\partial r_1}{\partial p_1} & \frac{\partial r_1}{\partial p_2} & \cdots & \frac{\partial r_1}{\partial p_n} \\ \frac{\partial r_2}{\partial p_1} & \frac{\partial r_2}{\partial p_2} & \cdots & \frac{\partial r_2}{\partial p_n} \\ \vdots & \vdots & \cdots & \vdots \\ \frac{\partial r_m}{\partial p_1} & \frac{\partial r_m}{\partial p_2} & \cdots & \frac{\partial r_m}{\partial p_n} \end{bmatrix} \tag{5.17}$$

It can be seen that in the application of the sensitivity-based FE model updating techniques, the fundamental properties of the original model such as the symmetry, positivity and sparse pattern in the stiffness and mass matrices are retained because the updating is carried out at the element level.

5.2.3 Weighting and Optimization Algorithm

Considering the importance and the identification accuracy of the different modal parameters (i.e., statistical uncertainty of identified parameters), the weighted nonlinear least squares problem can be used in FE model updating instead of the normal least squares problem given in equation (5.1), i.e.,

$$\min_{\mathbf{p}} f(\mathbf{p}) = \sum_{j=1}^{m} [w_j r_j(\mathbf{p})]^2 + \sum_{i=n}^{n} [w_i^p p_i]^2 \tag{5.18}$$

where w_j = weight factor of residual component $r_j(\mathbf{p})$ and w_i^p = weight factor of damage factors p_i. Depending on each particular FE model updating problem, weight factors w_j

applied to the various modal residuals can be selected so as to account for the different levels of identification accuracy of the different modal parameters. In practice, the values of w_j can be selected as inversely proportional to the coefficient-of-variation of the corresponding measured components. Weight factors w_i^p are penalizing the larger values of damage factors in order to limit the perturbation of updating parameters to which the considered residuals are little sensitive. In the weighted nonlinear least squares problem, only the relative proportion of the weight factors is important rather than their absolute values. The ability to weight the different data sets gives the method its power and versatility, but at the same time requires engineering insight to provide the correct weights.

The optimization algorithm used to minimize the objective function defined in equation (5.1) and (5.18) is a standard Trust Region Newton method, which is a sensitivity-based iterative method available in MATLAB optimization Toolbox (e.g., fmincon, fminunc, and lsqnonlin). The gradient and Hessian of the objective function can be obtained analytically from equations (5.9) and (5.10).

5.3 Linear Flat Shell Element

In this study, the MATLAB-based structural analysis software FEDEASLab (Filippou and Constantinides, 2004) is integrated with the FE model updating algorithms described above in order to perform structural damage identification. FEDEASLab was developed as an instruction tool for linear and nonlinear matrix structural analysis. This software is extended herein by implementing a four-node linear flat shell element borrowed from the FE literature.

Considering a linear flat shell element (See Figure 5.2), deformations of the element due to the membrane and bending forces will be uncoupled under the assumptions: (1) the middle surface (corresponding to z = 0) is chosen in representing displacement, rotations and

stress resultants; (2) the material properties are constant across the thickness, and (3) the displacement are small. This section briefly reviews the implemented linear flat shell element based on the previous research work performed by Kamal (1998). The shell element is based on the discrete Kirchhoff plate element derived by Batoz and Tahar (1982) for the plate part and the mixed discrete variational principle proposed by Hughes and Brezzi (1989) in conjunction with Allman type interpolation (Allman, 1988) for the membrane part. The resulting finite element has six DOFs per node.

5.3.1 Strain-Displacement Relationship

The in-plan displacement at any point in the shell can be expressed (assuming that the plane sections remain plane):

$$\mathbf{u} = \mathbf{u}_0 + z\boldsymbol{\beta} \tag{5.19}$$

in which

$$\mathbf{u} = \begin{bmatrix} u \\ v \end{bmatrix}; \quad \mathbf{u}_0 = \begin{bmatrix} u_0 \\ v_0 \end{bmatrix}; \quad \boldsymbol{\beta} = \begin{bmatrix} \beta_x \\ \beta_y \end{bmatrix} \tag{5.20}$$

where u_0 and v_0 are the in-plane displacements of the middle surface of the shell; $\beta_x = \theta_y$ is y-rotation of the shell cross-section perpendicular to x-axis and $\beta_y = -\theta_x$ is x-rotation of the shell cross-section perpendicular to y-axis. Then the strain vector at any point in the shell element due to these displacements are given by

$$\boldsymbol{\varepsilon} = \boldsymbol{\varepsilon}_0 + z\boldsymbol{\chi} \tag{5.21}$$

where

$$\boldsymbol{\varepsilon}_0 = \begin{bmatrix} \dfrac{\partial u_0}{\partial x} \\ \dfrac{\partial v_0}{\partial y} \\ \dfrac{\partial v_0}{\partial x} + \dfrac{\partial u_0}{\partial y} \end{bmatrix} \tag{5.22}$$

and

$$\boldsymbol{\chi} = \begin{bmatrix} \dfrac{\partial \beta_x}{\partial x} \\ \dfrac{\partial \beta_y}{\partial y} \\ \dfrac{\partial \beta_y}{\partial x} + \dfrac{\partial \beta_x}{\partial y} \end{bmatrix} \tag{5.23}$$

The principal of virtual work requires a virtual strain vector which can be expressed as

$$\delta\boldsymbol{\varepsilon} = \delta\boldsymbol{\varepsilon}_0 + z\delta\boldsymbol{\chi} \tag{5.24}$$

5.3.2 Stress-Strain Relationship

The linear stress-strain relationship at any depth *z* of the shell is given by

$$\boldsymbol{\sigma} = \mathbf{D}\boldsymbol{\varepsilon} = \mathbf{D}(\boldsymbol{\varepsilon}_0 + z\boldsymbol{\chi}) \tag{5.25}$$

where **D** is the constitutive matrix for plane stress condition at any depth *z*

$$\mathbf{D} = \frac{E}{(1-v)^2}\begin{bmatrix} 1 & v & 0 \\ v & 1 & 0 \\ 0 & 0 & (1-v)/2 \end{bmatrix} \tag{5.26}$$

in which *E* and *v* = represent the Young's modulus and the Poisson ratio, respectively. The stress vector $\boldsymbol{\sigma}$ at any depth *z* is given as

$$\boldsymbol{\sigma} = \begin{bmatrix} \sigma_{xx} \\ \sigma_{yy} \\ \sigma_{xy} \end{bmatrix} \tag{5.27}$$

By integrating equation (5.25) through the thickness of the shell, *t*, the stress resultants are obtained as

$$\mathbf{N} = \int \boldsymbol{\sigma} dz = \int \mathbf{D}(\boldsymbol{\varepsilon}_0 + z\boldsymbol{\chi}) dz = (\int \mathbf{D} dz)\boldsymbol{\varepsilon}_0 + (\int \mathbf{D} z dz)\boldsymbol{\chi} = \mathbf{D}_m \boldsymbol{\varepsilon}_0 + \mathbf{D}_{mb} \boldsymbol{\chi} \tag{5.28}$$

$$\mathbf{M} = \int \boldsymbol{\sigma} z dz = \int \mathbf{D} z(\boldsymbol{\varepsilon}_0 + z\boldsymbol{\chi}) dz = (\int \mathbf{D} z dz)\boldsymbol{\varepsilon}_0 + (\int \mathbf{D} z^2 dz)\boldsymbol{\chi} = \mathbf{D}_{mb} \boldsymbol{\varepsilon}_0 + \mathbf{D}_b \boldsymbol{\chi} \tag{5.29}$$

where $\mathbf{N} = \begin{bmatrix} N_{xx} & N_{yy} & N_{xy} \end{bmatrix}^T$ are the internal in-plane normal and shear forces per unit length of the shell and $\mathbf{M} = \begin{bmatrix} M_{xx} & M_{yy} & M_{xy} \end{bmatrix}^T$ are the internal moment per unit length of the shell. The integrated constitute matrices $\mathbf{D}_m$, $\mathbf{D}_b$, and $\mathbf{D}_{mb}$ are known respectively as membrane, bending and membrane-bending coupling constitutive matrices. Based on the assumption that the middle surface corresponds to $z = 0$ and the material properties are constant across the thickness, then

$$\mathbf{D}_m = \frac{Et}{(1-\nu^2)} \begin{bmatrix} 1 & \nu & 0 \\ \nu & 1 & 0 \\ 0 & 0 & (1-\nu)/2 \end{bmatrix}; \quad \mathbf{D}_{mb} = 0; \quad \mathbf{D}_b = \frac{Et^3}{12(1-\nu^2)} \begin{bmatrix} 1 & \nu & 0 \\ \nu & 1 & 0 \\ 0 & 0 & (1-\nu)/2 \end{bmatrix} \tag{5.30}$$

This shows that the deformations due to the membrane and bending forces are uncoupled in the case of aforementioned assumptions.

5.3.3 Principle of Virtual Work

The principle of virtual work for shell can be written as

$$\delta W = \int_V \boldsymbol{\sigma}^T \delta\boldsymbol{\varepsilon} dV - \int_V \mathbf{f}_m{}^T \delta \mathbf{u} dV - \int_V f_p \delta w dV \tag{5.31}$$

where $\boldsymbol{\sigma}$ and $\delta\boldsymbol{\varepsilon}$ are defined in equations (5.27) and (5.24), respectively; $\mathbf{f}_m$ and f_p are the in-plane and out-of-plane body forces; $\mathbf{u}$ is the displacement field vector defined in equation (5.19) and *w* is the out-of-plane displacement field. Using the definition of the stress resultant vectors defined in equations (5.28) and (5.29), the above equation can be expressed as

$$\begin{aligned}\delta W &= \int_V \boldsymbol{\sigma}^T(\delta\boldsymbol{\varepsilon}_0 + z\delta\boldsymbol{\chi})dzdA - \int_V \mathbf{f}_m{}^T(\delta\mathbf{u}_0 + z\delta\boldsymbol{\beta})dzdA - \int_V f_p\delta w dzdA \\ &= \int_A \mathbf{N}^T\delta\boldsymbol{\varepsilon}_0 dA + \int_A \mathbf{M}^T\delta\boldsymbol{\chi}dA - \int_A \mathbf{n}^T\delta\mathbf{u}_0 dA - \int_A \mathbf{m}^T\delta\boldsymbol{\beta}dA - \int_A f_p t\delta w dA\end{aligned} \tag{5.32}$$

where **n** and **m** represent the external forces resultants defined as

$$\mathbf{n} = \int \mathbf{f}_m dz; \quad \mathbf{m} = \int \mathbf{f}_m z dz \tag{5.33}$$

Based on the principle of virtual work, the total inertial virtual work δW_I and total external virtual work δW_E are equal to each other, thus,

$$\begin{aligned}&\delta W_I = \delta W_E \\ &\delta W_I = \int_A \mathbf{N}^T\delta\boldsymbol{\varepsilon}_0 dA + \int_A \mathbf{M}^T\delta\boldsymbol{\chi}dA \\ &\delta W_E = \int_A \mathbf{n}^T\delta\mathbf{u}_0 dA + \int_A \mathbf{m}^T\delta\boldsymbol{\beta}dA + \int_A f_p t\delta w dA\end{aligned} \tag{5.34}$$

In the above, **N** and **M** are the internal stress resultants in equilibrium with external body force resultants **n** and **m** and out-of-plane body forces f_p. The principle of virtual work expressed in equation (5.34) is an integral form of equilibrium.

5.3.4 Finite Element Approximation

The interpolation for the in-plane displacement field can be written as

$$\mathbf{u}_0 = \mathbf{N}^m\mathbf{P}_m + \mathbf{N}^\psi\mathbf{P}_\psi \tag{5.35}$$

where the nodal displacement vectors $\mathbf{P}_m$ and $\mathbf{P}_\psi$ are given by (see Figure 5.3):

$$\mathbf{P}_m = \begin{bmatrix} u_1 & v_1 & u_2 & v_2 & u_3 & v_3 & u_4 & v_4 \end{bmatrix}^T; \quad \mathbf{P}_\psi = \begin{bmatrix} \psi_1 & \psi_2 & \psi_3 & \psi_4 \end{bmatrix} \tag{5.36}$$

The shape function matrix $\mathbf{N}^m$ is defined as

$$\mathbf{N}^m = \begin{bmatrix} N_1 & 0 & N_2 & 0 & N_3 & 0 & N_4 & 0 \\ 0 & N_1 & 0 & N_2 & 0 & N_3 & 0 & N_4 \end{bmatrix} \tag{5.37}$$

where the bilinear shape functions N_I are defined as

$$
\begin{aligned}
N_1 &= \frac{1}{4}(1-\xi)(1-\eta) \\
N_2 &= \frac{1}{4}(1+\xi)(1-\eta) \\
N_3 &= \frac{1}{4}(1+\xi)(1+\eta) \\
N_4 &= \frac{1}{4}(1-\xi)(1+\eta)
\end{aligned}
\tag{5.38}
$$

In the above, ξ and η are the natural coordinates defined in the interval {-1, 1}. The shape function $\mathbf{N}^{\psi}$ is defined as

$$
\mathbf{N}^{\psi} = \begin{bmatrix} N_1^{\psi} & N_2^{\psi} & N_3^{\psi} & N_4^{\psi} \end{bmatrix} \tag{5.39}
$$

where

$$
N_I^{\psi} = N_L \frac{l_{JI}}{8} \mathbf{n}_{JI} + N_M \frac{l_{KI}}{8} \mathbf{n}_{KI} \tag{5.40}
$$

The indices in the above equation are defined in Table 5.1. The l_{JI} denotes the length of the element side associated with the corner nodes *J* and *I*, i.e.,

$$
\begin{aligned}
& x_{JI} = x_I - x_J; \quad y_{JI} = y_I - y_J \\
& l_{JI} = (x_{JI}{}^2 + y_{JI}{}^2)^{1/2} \\
& \cos\alpha_{JI} = \frac{y_{JI}}{l_{JI}}; \quad \sin\alpha_{JI} = -\frac{x_{JI}}{l_{JI}}; \\
& \mathbf{n}_{JI} = \begin{bmatrix} \cos\alpha_{JI} \\ \sin\alpha_{JI} \end{bmatrix}
\end{aligned}
\tag{5.41}
$$

The serendipity shape functions used in equation (5.40) are

$$
\begin{aligned}
N_5 &= \frac{1}{4}(1-\xi^2)(1-\eta) \\
N_6 &= \frac{1}{4}(1+\xi)(1-\eta^2) \\
N_7 &= \frac{1}{4}(1-\xi^2)(1+\eta) \\
N_8 &= \frac{1}{4}(1-\xi)(1-\eta^2)
\end{aligned}
\tag{5.42}
$$

The interpolation for the out-of-plane displacement field *w* and rotation field θ_x and θ_y were given, respectively, as

$$w = \mathbf{N}^w \mathbf{P}_p \tag{5.43}$$

and

$$\theta_x = \mathbf{N}_x^\theta \mathbf{P}_p; \quad \theta_y = \mathbf{N}_y^\theta \mathbf{P}_p \tag{5.44}$$

The nodal displacement vector $\mathbf{P}_p$ is defined as (see Figure 5.4)

$$\mathbf{P}_p = \begin{bmatrix} w_1 & \theta_{x1} & \theta_{y1} & w_2 & \theta_{x2} & \theta_{y2} & w_3 & \theta_{x3} & \theta_{y3} & w_4 & \theta_{x4} & \theta_{y4} \end{bmatrix}^T \tag{5.45}$$

The shape function $\mathbf{N}^w$ is given as

$$\mathbf{N}^w = \begin{bmatrix} \mathbf{N}_1^w & \mathbf{N}_2^w & \mathbf{N}_3^w & \mathbf{N}_4^w \end{bmatrix} \tag{5.46}$$

where

$$\mathbf{N}_I^w = \left[\left\{ N_I + \frac{1}{4}(M_L - M_M) \right\} \quad \left\{ (N_M - M_M)\frac{l_{JI}}{8}\mathbf{n}_{IJ}^T - (N_L + M_L)\frac{l_{KI}}{8}\mathbf{n}_{KI}^T \right\} \right]_{1\times 3} \tag{5.47}$$

The indices in the above equation are defined in Table 5.2. The bilinear shape functions (N_1, N_2, N_3, and N_4) and serendipity shape functions (N_5, N_6, N_7, and N_8) are defined in (5.38) and (5.42), respectively. The definition of l_{JI} and $\mathbf{n}_{IJ}$ can be found in (5.41). The shape functions M_5, M_6, M_7, and M_8 are defined as

$$\begin{aligned} M_5 &= \frac{1}{2}(1-\xi^2)\xi(1-\eta) \\ M_6 &= \frac{1}{2}(1+\xi)\eta(1-\eta^2) \\ M_7 &= \frac{1}{2}(1-\xi^2)\xi(1+\eta) \\ M_8 &= \frac{1}{2}(1-\xi)\eta(1-\eta^2) \end{aligned} \tag{5.48}$$

The shape functions $\mathbf{N}_x^\theta$ and $\mathbf{N}_y^\theta$ are defined as

$$\begin{aligned}\mathbf{N}_x^\theta &= \begin{bmatrix}\widehat{\mathbf{N}}_{x1}^\theta & \widehat{\mathbf{N}}_{x2}^\theta & \widehat{\mathbf{N}}_{x3}^\theta & \widehat{\mathbf{N}}_{x4}^\theta\end{bmatrix} \\ \mathbf{N}_y^\theta &= \begin{bmatrix}\widehat{\mathbf{N}}_{y1}^\theta & \widehat{\mathbf{N}}_{y2}^\theta & \widehat{\mathbf{N}}_{y3}^\theta & \widehat{\mathbf{N}}_{y4}^\theta\end{bmatrix}\end{aligned} \tag{5.49}$$

where

$$\begin{aligned}\widehat{\mathbf{N}}_{xI}^\theta &= \begin{bmatrix}\hat{\mathbf{e}}_x^T\widehat{\mathbf{M}}_I & N_I - \hat{\mathbf{e}}_x^T N_I \hat{e}_x & -\hat{\mathbf{e}}_x^T N_I \hat{\mathbf{e}}_y\end{bmatrix}_{1\times 3} \\ \widehat{\mathbf{N}}_{yI}^\theta &= \begin{bmatrix}\hat{\mathbf{e}}_y^T\widehat{\mathbf{M}}_I & -\hat{\mathbf{e}}_y^T N_I \hat{\mathbf{e}}_x & N_I - \hat{\mathbf{e}}_y^T N_I \hat{\mathbf{e}}_y\end{bmatrix}_{1\times 3}\end{aligned} \tag{5.50}$$

The unit vector $\hat{\mathbf{e}}_x$ and $\hat{\mathbf{e}}_y$ are defined as

$$\hat{\mathbf{e}}_x = \begin{bmatrix}1\\0\end{bmatrix}; \quad \hat{\mathbf{e}}_y = \begin{bmatrix}0\\1\end{bmatrix} \tag{5.51}$$

The shape functions $\widehat{M}_1, \widehat{M}_2, \widehat{M}_3$, and $\widehat{M}_4$ are defined as

$$\widehat{\mathbf{M}}_I = \frac{3}{2}(N_L \frac{\mathbf{n}_{KI}}{l_{KI}} - N_M \frac{\mathbf{n}_{IJ}}{l_{IJ}}) \tag{5.52}$$

The indices *I, J, K, L, M*, the shape functions N_1, N_2, N_3, N_4 and the definition of l_{JI} and $\mathbf{n}_{IJ}$ are the same as those defined in equation (5.47). The interpolations for rotation fields β_x and β_y are written in a form similar to equation (5.44) as

$$\beta_x = \mathbf{N}_x^\beta \mathbf{P}_p; \quad \beta_y = \mathbf{N}_y^\beta \mathbf{P}_p \tag{5.53}$$

in which matrices $\mathbf{N}_x^\beta$ and $\mathbf{N}_y^\beta$ can be written in terms of $\mathbf{N}_x^\theta$ and $\mathbf{N}_y^\theta$ using the relationship as

$$\mathbf{N}_x^\beta = \mathbf{N}_y^\theta; \quad \mathbf{N}_y^\beta = -\mathbf{N}_x^\theta \tag{5.54}$$

It is worth noting that the interpolation of the initial geometry (assumed to be flat) is give by bilinear map (see Figure 5.3 and Figure 5.4)

$$\begin{bmatrix} x \\ y \end{bmatrix} = \begin{bmatrix} N_1 & 0 & N_2 & 0 & N_3 & 0 & N_4 & 0 \\ 0 & N_1 & 0 & N_2 & 0 & N_3 & 0 & N_4 \end{bmatrix} \begin{bmatrix} x_1 \\ y_1 \\ x_2 \\ y_2 \\ x_3 \\ y_3 \\ x_4 \\ y_4 \end{bmatrix} \tag{5.55}$$

Based on the form of strain-displacement relationship used by Jetteur and Frey (1986) and Taylor (1988), the membrane strain-displacement relationship can be written

$$\boldsymbol{\varepsilon}_0(x,y) = \mathbf{B}_m(x,y)\mathbf{P}_m + \mathbf{G}^{\psi}(x,y)\mathbf{P}_{\psi} \tag{5.56}$$

The matrices $\mathbf{B}_m$ and $\mathbf{G}^{\psi}$ are defined as

$$\begin{aligned} \mathbf{B}_m &= \begin{bmatrix} \mathbf{B}_1^m & \mathbf{B}_2^m & \mathbf{B}_3^m & \mathbf{B}_4^m \end{bmatrix} \\ \mathbf{G}_{\psi} &= \begin{bmatrix} \widehat{\mathbf{G}}_1 & \widehat{\mathbf{G}}_2 & \widehat{\mathbf{G}}_3 & \widehat{\mathbf{G}}_4 \end{bmatrix} \end{aligned} \tag{5.57}$$

where

$$\mathbf{B}_I^m = \begin{bmatrix} \dfrac{\partial N_I}{\partial x} & 0 \\ 0 & \dfrac{\partial N_I}{\partial y} \\ \dfrac{\partial N_I}{\partial y} & \dfrac{\partial N_I}{\partial x} \end{bmatrix} \tag{5.58}$$

and

$$\begin{aligned} \mathbf{G}_I &= \frac{1}{8}[l_{JI}\mathbf{B}_L^m\mathbf{n}_{JI} + l_{KI}\mathbf{B}_M^m\mathbf{n}_{KI}] \\ \widehat{\mathbf{G}}_I &= \mathbf{G}_I - \frac{1}{\Omega^e}\int_{\Omega^e}\mathbf{G}_I\,d\Omega \end{aligned} \tag{5.59}$$

The indices *I, J, K, L, M,* the bilinear shape functions N_1, N_2, N_3, N_4, the serendipity shape functions N_5, N_6, N_7, N_8 and the definition of l_{JI} and $\mathbf{n}_{IJ}$ are the same as those defined in

equation (5.40). The Ω^e denotes the domain of the element. Similarly, the plate strain-displacement relationship can be written as

$$\boldsymbol{\chi}(x,y) = \mathbf{B}_p(x,y)\mathbf{P}_p \tag{5.60}$$

in which

$$\mathbf{B}_p = \begin{bmatrix} B_1^p & B_2^p & B_3^p & B_4^p \end{bmatrix} \tag{5.61}$$

and

$$B_I^p = \begin{bmatrix} \dfrac{\partial \widehat{\mathbf{N}}_{yI}^{\theta}}{\partial x} \\ -\dfrac{\partial \widehat{\mathbf{N}}_{xI}^{\theta}}{\partial y} \\ \dfrac{\partial \widehat{\mathbf{N}}_{yI}^{\theta}}{\partial y} - \dfrac{\partial \widehat{\mathbf{N}}_{xI}^{\theta}}{\partial x} \end{bmatrix}_{3\times 3} \tag{5.62}$$

The shape functions $\widehat{\mathbf{N}}_{xI}^{\theta}$ and $\widehat{\mathbf{N}}_{yI}^{\theta}$ can be found in equation (5.50).

By discretizing the shell region into *Nel* finite elements, the virtual work equation, i.e., equation (5.34), can be written as the following form:

$$\sum_{e=1}^{Nel}\left[\int_{A^e} \delta\boldsymbol{\varepsilon}_0{}^T \mathbf{N} dA + \int_{A^e} \delta\boldsymbol{\chi}^T \mathbf{M} dA\right]^e = \sum_{e=1}^{Nel}\left[\int_{A^e} \delta\mathbf{u}_0{}^T \mathbf{n} dA + \int_{A^e} \delta\boldsymbol{\beta}^T \mathbf{m} dA + \int_{A^e} \delta w^T f_p t dA\right]^e \tag{5.63}$$

Substitute equations (5.28) and (5.29) into above equation, it can be obtained

$$\begin{aligned} &\sum_{e=1}^{Nel}\left[\int_{A^e} \delta\boldsymbol{\varepsilon}_0{}^T (\mathbf{D}_m\boldsymbol{\varepsilon}_0 + \mathbf{D}_{mb}\boldsymbol{\chi}) dA + \int_{A^e} \delta\boldsymbol{\chi}^T (\mathbf{D}_{mb}\boldsymbol{\varepsilon}_0 + \mathbf{D}_b\boldsymbol{\chi}) dA\right]^e \\ &= \sum_{e=1}^{Nel}\left[\int_{A^e} \delta\mathbf{u}_0{}^T \mathbf{n} dA + \int_{A^e} \delta\boldsymbol{\beta}^T \mathbf{m} dA + \int_{A^e} \delta w^T f_p t dA\right]^e \end{aligned} \tag{5.64}$$

Using the displacement interpolations in equations (5.35) and (5.43), the cross-section rotations interpolations in equation (5.53), the strain-displacement relationship in equations (5.56)and (5.60), equation (5.64) becomes

$$\sum_{e=1}^{Nel}\left\{\begin{bmatrix}\delta\mathbf{P}_m^T & \delta\mathbf{P}_\psi^T & \delta\mathbf{P}_p^T\end{bmatrix}\begin{bmatrix}\int_{A^e}\mathbf{B}_m^T\mathbf{D}_m\mathbf{B}_m dA & \int_{A^e}\mathbf{B}_m^T\mathbf{D}_m\mathbf{G}_\psi dA & \int_{A^e}\mathbf{B}_m^T\mathbf{D}_{mb}\mathbf{B}_p dA\\ \int_{A^e}\mathbf{G}_\psi^T\mathbf{D}_m\mathbf{B}_m dA & \int_{A^e}\mathbf{G}_\psi^T\mathbf{D}_m\mathbf{G}_\psi dA & \int_{A^e}\mathbf{G}_\psi^T\mathbf{D}_{mb}\mathbf{B}_p dA\\ \int_{A^e}\mathbf{B}_p^T\mathbf{D}_{mb}\mathbf{B}_m dA & \int_{A^e}\mathbf{B}_p^T\mathbf{D}_{mb}\mathbf{G}_\psi dA & \int_{A^e}\mathbf{B}_p^T\mathbf{D}_b\mathbf{B}_p dA\end{bmatrix}\begin{bmatrix}\mathbf{P}_m\\ \mathbf{P}_\psi\\ \mathbf{P}_p\end{bmatrix}\right\}^e$$
$$=\sum_{e=1}^{Nel}\left\{\begin{bmatrix}\delta\mathbf{P}_m^T & \delta\mathbf{P}_\psi^T & \delta\mathbf{P}_p^T\end{bmatrix}\begin{bmatrix}\int_{A^e}\mathbf{N}^{m^T}\mathbf{n}dA\\ \int_{A^e}\mathbf{N}^{\psi^T}\mathbf{n}dA\\ \int_{A^e}\begin{bmatrix}\mathbf{N}_x^{\beta^T} & \mathbf{N}_y^{\beta^T}\end{bmatrix}\mathbf{m}dA+\int_{A^e}\mathbf{N}^{w^T}tf_p dA\end{bmatrix}\right\}^e \tag{5.65}$$

Finally the integral equilibrium equation for linear analysis of shells using flat element can be written

$$\sum_{e=1}^{Nel}\left\{(\delta\mathbf{P}_L)^T\mathbf{K}_L\mathbf{P}_L\right\}^e=\sum_{e=1}^{Nel}\left\{(\delta\mathbf{P}_L)^T\mathbf{F}_L\right\}^e \tag{5.66}$$

in which matrices $\mathbf{K}_L$, $\mathbf{F}_L$, and $\mathbf{P}_L$ are well known as the stiffness matrix, the equivalent consistent nodal load vector, and the nodal displacement vector for a linear flat shell element in its local coordinate system. They are defined as following:

$$\mathbf{K}_L=\begin{bmatrix}\mathbf{K}_{mm} & \mathbf{K}_{m\psi} & \mathbf{K}_{mp}\\ \mathbf{K}_{\psi m} & \mathbf{K}_{\psi\psi} & \mathbf{K}_{\psi p}\\ \mathbf{K}_{pm} & \mathbf{K}_{p\psi} & \mathbf{K}_{pp}\end{bmatrix};\quad \mathbf{F}_L=\begin{bmatrix}\mathbf{F}_m\\ \mathbf{F}_\psi\\ \mathbf{F}_p\end{bmatrix};\quad \mathbf{P}_L=\begin{bmatrix}\mathbf{P}_m\\ \mathbf{P}_\psi\\ \mathbf{P}_p\end{bmatrix} \tag{5.67}$$

Based on the equation (5.65), it can be seen that

$$
\begin{aligned}
\mathbf{K}_{mm} &= \int_{A^e} \mathbf{B}_m^T \mathbf{D}_m \mathbf{B}_m dA \\
\mathbf{K}_{m\psi} &= \int_{A^e} \mathbf{B}_m^T \mathbf{D}_m \mathbf{G}_\psi dA \\
\mathbf{K}_{mp} &= \int_{A^e} \mathbf{B}_m^T \mathbf{D}_{mb} \mathbf{B}_p dA \\
\mathbf{K}_{\psi m} &= \int_{A^e} \mathbf{G}_\psi^T \mathbf{D}_m \mathbf{B}_m dA \\
\mathbf{K}_{\psi\psi} &= \int_{A^e} \mathbf{G}_\psi^T \mathbf{D}_m \mathbf{G}_\psi dA \\
\mathbf{K}_{\psi p} &= \int_{A^e} \mathbf{G}_\psi^T \mathbf{D}_{mb} \mathbf{B}_p dA \\
\mathbf{K}_{pm} &= \int_{A^e} \mathbf{B}_p^T \mathbf{D}_{mb} \mathbf{B}_m dA \\
\mathbf{K}_{p\psi} &= \int_{A^e} \mathbf{B}_p^T \mathbf{D}_{mb} \mathbf{G}_\psi dA \\
\mathbf{K}_{pp} &= \int_{A^e} \mathbf{B}_p^T \mathbf{D}_b \mathbf{B}_p dA
\end{aligned}
\tag{5.68}
$$

and

$$
\begin{aligned}
\mathbf{F}_m &= \int_{A^e} \mathbf{N}^{m^T} \mathbf{n} dA \\
\mathbf{F}_\psi &= \int_{A^e} \mathbf{N}^{\psi^T} \mathbf{n} dA \\
\mathbf{F}_p &= \int_{A^e} \begin{bmatrix} \mathbf{N}_x^{\beta^T} & \mathbf{N}_y^{\beta^T} \end{bmatrix} \mathbf{m} dA + \int_{A^e} \mathbf{N}^{w^T} t f_p dA
\end{aligned}
\tag{5.69}
$$

It is evident, from the definitions of its sub-matrices in equation (5.68), that the stiffness matrix $\mathbf{K}_L$ satisfies symmetry owing to the symmetry of constitutive matrices $\mathbf{D}_m$, $\mathbf{D}_b$, and $\mathbf{D}_{mb}$. In addition, since the $\mathbf{D}_{mb} = \mathbf{0}$ under the condition that the middle surface corresponds to z = 0 and the material properties are constant across the thickness, see equation (5.30), the sub-matrices $\mathbf{K}_{mp}$, $\mathbf{K}_{pm}$, $\mathbf{K}_{p\psi}$, and $\mathbf{K}_{\psi p}$ become

$$
\mathbf{K}_{mp} = \mathbf{K}_{pm} = \mathbf{K}_{p\psi} = \mathbf{K}_{\psi p} = \mathbf{0} \tag{5.70}
$$

and imply that the membrane and bending behaviors are uncoupled at the element level. Therefore the stiffness for a linear flat shell element can be written as

$$\mathbf{K}_L = \begin{bmatrix} \mathbf{K}_{membrane} & \mathbf{0} \\ \mathbf{0} & \mathbf{K}_{bending} \end{bmatrix}; \quad \mathbf{K}_{membrane} = \begin{bmatrix} \mathbf{K}_{mm} & \mathbf{K}_{m\psi} \\ \mathbf{K}_{\psi m} & \mathbf{K}_{\psi\psi} \end{bmatrix}; \quad \mathbf{K}_{bending} = \mathbf{K}_{pp} \tag{5.71}$$

The Allman type (Allman 1988) membrane interpolations are used in above derivations and there are three parameters at each node for the membrane element (see Figure 5.3). Among these, two are in-plane nodal displacements and the third one ψ is used for a higher order interpolation of the in-plane displacement field. This nodal parameter can be interpreted as an in-plane rotation (i.e., drilling degree of freedom) for the membrane element (Jetteur and Frey, 1986; Kamal, 1998). The meaning of this nodal kinematics parameter ψ can also be tied to true in-plane rotation if the mixed variational formulation (Kamal, 1998) is employed for the membrane part, which requires modifying the virtual work equation (5.66)

$$\sum_{e=1}^{Nel} \left\{ (\delta \mathbf{P}_L)^T \mathbf{K}_L \mathbf{P}_L + \begin{bmatrix} \delta \mathbf{P}_m & \delta \mathbf{P}_\psi \end{bmatrix} \frac{\gamma}{\Omega_e} \mathbf{h}^e \mathbf{h}^{eT} \begin{bmatrix} \mathbf{P}_m \\ \mathbf{P}_\psi \end{bmatrix} \right\}^e = \sum_{e=1}^{Nel} \left\{ (\delta \mathbf{P}_L)^T \mathbf{F}_L \right\}^e \tag{5.72}$$

in which γ is the regularization parameter. The element matrix $\mathbf{h}^e$ is defined as

$$\mathbf{h}^e = \begin{bmatrix} \mathbf{h}_m^e \\ \mathbf{h}_\psi^e \end{bmatrix}; \quad \mathbf{h}_m^e = \int_{\Omega^e} \mathbf{b}_m^T d\Omega; \quad \mathbf{h}_\psi^e = \int_{\Omega^e} \mathbf{g}_\psi d\Omega \tag{5.73}$$

where

$$\mathbf{b}_m = \begin{bmatrix} \mathbf{b}_1 & \mathbf{b}_2 & \mathbf{b}_3 & \mathbf{b}_4 \end{bmatrix}; \quad \mathbf{g}_\psi = \begin{bmatrix} g_1 & g_2 & g_3 & g_4 \end{bmatrix} \tag{5.74}$$

and

$$\mathbf{b}_I = \frac{1}{2} \begin{bmatrix} -\dfrac{\partial N_I}{\partial y} & \dfrac{\partial N_I}{\partial x} \end{bmatrix}; \quad g_I = \frac{1}{8} \left[l_{JI} \mathbf{b}_L \mathbf{n}_{JI} - l_{KI} \mathbf{b}_M \mathbf{n}_{KI} \right] - N_I \tag{5.75}$$

In the above equation, the indices *I, J, K, L, M,* the bilinear shape functions N_1, N_2, N_3, N_4, the serendipity shape functions N_5, N_6, N_7, N_8, and the definition of l_{JI} and $\mathbf{n}_{IJ}$ are the same as those defined in equation (5.40).

Based on equation (5.72), the stiffness for a linear flat shell element in equation (5.71) can be modified as

$$\widehat{\mathbf{K}}_L = \begin{bmatrix} \widehat{\mathbf{K}}_{membrane} & \mathbf{0} \\ \mathbf{0} & \mathbf{K}_{bending} \end{bmatrix}; \quad \widehat{\mathbf{K}}_{membrane} = \begin{bmatrix} \mathbf{K}_{mm} & \mathbf{K}_{m\psi} \\ \mathbf{K}_{\psi m} & \mathbf{K}_{\psi\psi} \end{bmatrix} + \frac{\gamma}{\Omega_e} \mathbf{h}^e \mathbf{h}^{e^T} \tag{5.76}$$

The stiffness matrix obtained from equation (5.76) is implemented in study. As aforementioned, this brief review about the linear flat shell element is based on the work performed by Kamal (1998), from which more detail can be found.

5.4 Damage Identification of a Simply Supported Plate Based on Numerical Data

A comparative study of the influence of different objective functions on the damage identification results is performed in this section by using simulated data for a simply supported plate. The simply supported plate with a size of $180 \times 120 \times 8$ in ($4.57 \times 3.05 \times 0.2$ m) is discretized into 36 shell elements with 49 nodes (see Figure 5.5). The density and modulus of elasticity of the plate are 2.6098×10^{-7} kip$\cdot$s^2/in^4 (2.79×10^3 kg/m^3) and 3600 ksi (2.48×10^{10} Pa), respectively. These 36 elements are divided into 9 groups / substructures as seen in Figure 5.6. In order to simulate structural damage, the elastic moduli of group 1, 2, 5, and 7 are assumed to be reduced by 45, 40, 35 and 30 percent, respectively. Natural frequencies of the first 6 vibration modes considered in this study are listed in Table 5.3 for both undamaged and damaged plate. Table 5.3 also reports the modal assurance criterion (MAC) (Allemang and Brown, 1982) values between mode shapes computed from the undamaged plate with their counterparts computed from the damaged plate. From Table 5.3, it can be seen that due to the simulated damage, the maximum difference in natural frequency is on the order of 12% and the minimum MAC value is about 0.906. As an illustration, Figure 5.7 shows mode shapes of these six vibration modes computed from undamaged state.

Three different objective functions are considered in this numerical example based on the natural frequency residuals, mode shape residuals, and pseudo modal flexibility residuals

$$\min_{\mathbf{p}} f_I(\mathbf{p}) = \frac{1}{2}\mathbf{r}_I(\mathbf{p})^T \mathbf{r}_I(\mathbf{p}) = \frac{1}{2}\sum_{j=1}^{N_f}[r_j^f(\mathbf{p})]^2 + \frac{1}{2}\frac{N_f}{N_s}\sum_{j=1}^{N_s}[r_j^{ms}(\mathbf{p})]^2 \tag{5.77}$$

$$\min_{\mathbf{p}} f_{II}(\mathbf{p}) = \frac{1}{2}\mathbf{r}_{II}(\mathbf{p})^T \mathbf{r}_{II}(\mathbf{p}) = \frac{1}{2}\sum_{j=1}^{N_f}[r_j^f(\mathbf{p})]^2 + \frac{1}{2}\frac{N_f}{N_{pf}}\sum_{j=1}^{N_{pf}}[r_j^{pf}(\mathbf{p})]^2 \tag{5.78}$$

$$\min_{\mathbf{p}} f_{III}(\mathbf{p}) = \frac{1}{2}\mathbf{r}_{III}(\mathbf{p})^T \mathbf{r}_{III}(\mathbf{p}) = \frac{1}{2}\sum_{j=1}^{N_f}[r_j^f(\mathbf{p})]^2 + \frac{1}{2}\frac{N_f}{N_s}\sum_{j=1}^{N_s}[r_j^{ms}(\mathbf{p})]^2 + \frac{1}{2}\frac{N_f}{N_{pf}}\sum_{j=1}^{N_{pf}}[r_j^{pf}(\mathbf{p})]^2 \tag{5.79}$$

In the above definitions, $r_j^f(\mathbf{p})$, $r_j^{ms}(\mathbf{p})$, $r_j^{pf}(\mathbf{p})$, are the component of frequency residual vector , mode shape residual vector, and pseudo modal flexibility residual vector, respectively [see equations (5.2), (5.3), and (5.4)]; $\mathbf{p}$ is the vector of correction factor [see equation (5.7)]; N_f, N_s, and N_{pf} are the number of frequency residual components, mode shape residual components, and pseudo modal flexibility residual components, respectively, used in the objective functions. In this example, Young's moduli of the nine groups of elements are selected as model updating parameters (i.e., nine unknown parameters). Thus the locations and levels of the simulated damage are identified by the correction factors directly.

In the implementation of the first objective function, six different cases are considered depending on the number of vibration modes used in the FE model updating, namely: Case 1, only the natural frequency and mode shape of the first vibration mode is used; Case 2, the natural frequencies and mode shapes of the first two vibration modes are used; Case 3, the natural frequencies and mode shapes of the first three vibration modes are used; Case 4, the natural frequencies and mode shapes of the first four vibration modes are used; Case 5, the natural frequencies and mode shapes of the first five vibration modes are used; and Case 6, the natural frequencies and mode shapes of all the first six vibration modes are used. The standard

optimization algorithm *lsqnonlin* available in MATLAB optimization Toolbox is applied for all six cases. In this example, the maximum number of iterations (*MaxIter*) is defined as 400. The termination tolerance on the function value (*TolFun*) and termination tolerance on updating parameters *(TolX*) are defined as 10^{-10}. The damage identification results of these six cases are reported in Table 5.4. It should be noted that the optimization programs are not converged within 400 iterations for Case 1 and Case 2. The correction factors provided in Table 5.4 are the results at the 400^{th} step iteration for these two cases. For the Cases 3, 4, 5, and 6, the exact correction factors are obtained. In other words, the locations and levels of the simulated damage are exactly identified using the first objective function in the case that frequencies and mode shapes of more than two vibration modes are used to set up the objective function. Thus, in the application FE model updating for damage identification, enough modal properties are needed. Figure 5.8 shows the history of the correction factors in the model updating process for Case 3. It is clearly observed that the correction factors assigned to the undamaged elements (substructures) approach zeros during the model updating and those assigned to the damaged elements (substructures) reach their corresponding exact levels of the simulated damage at the end of model updating.

In the implementation of the other two objective functions for damage identification of the simulated plate, the natural frequencies and mode shapes of the first three vibration modes are used to define these functions. Table 5.5 presented the damage identification results obtained using all three different objective functions. It is found that the locations and levels of the simulated damage can be exactly (or almost exactly) identified using any of these three objective functions. However, based on this example, it is found that the locations and levels of the damage can be exactly identified with high computation efficiency using the first and third objective functions. The first objective function is defined by the combination of natural

frequency residuals and mode shapes residuals whereas the third objective function is defined by combination of natural frequency residuals, mode shapes residuals, and pseudo modal flexibility residuals. Considering the propagation of the identification errors of the natural frequencies and mode shapes to the pseudo modal flexibility matrix, the objective function defined by the combination of natural frequency and mode shape residuals is applied for damage identification of a seven-story shear wall building tested on the UCSD-NEES shake table.

5.5 Damage Identification a Seven-Story Shear Wall Building Slice Tested on the UCSD-NEES Shake Table

The UCSD-NEES shake table is located at the Englekirk Structural Engineering Center at the Camp Elliott Field Station, 15 km east of the main UCSD campus. This unique facility allows to perform landmark seismic experiments on large- or full-scale structural and soil-foundation-structure interaction systems. A full-scale seven-story reinforced concrete (R/C) shear wall building slice was tested on the UCSD-NEES shake table in the period October 2005 - January 2006. The objective of this test program was to verify the seismic performance of a reinforced concrete wall system designed for lateral forces obtained from a displacement-based design methodology, which are significantly smaller than those dictated by current seismic design provisions. The shake table tests were designed so as to damage the building progressively through several historical seismic motions reproduced on the shake table. At various levels of damage, several low amplitude white noise base excitations were applied through the shake table to the building slice which responded as a quasi-linear system with dynamic parameters depending on the level of structural damage. In addition to white noise base excitation tests, ambient vibration tests were also performed on the building specimen at different damage levels. Different state-of-the-art system identification methods

were applied to dynamic response measurements to estimate modal parameters (natural frequencies, damping rations and mode shapes) of the test building in its undamaged (baseline) and various damage states (Moaveni et al., 2007). In this section, modal parameters identified using the data-driven stochastic subspace identification (SSI-DATA) method (Van Overschee and De Moor, 1996) based on ambient vibration data are used for damage identification. First, changes of the identified modal parameters with increasing level of damage are investigated. Then, a FE model updating strategy is applied to identify the damage existed in the building at various damage states, in which the objective function is defined as a combination of residuals in natural frequencies and mode shape components. Finally, the damage identification results are compared to the actual damage observed in the test building.

5.5.1 Seven-Story Reinforced Concrete Shear Wall Building Slice

The full-scale seven-story R/C building slice tested on the UCSD-NEES shake table consists of a main wall (web wall), a back wall perpendicular to the main wall (flange wall) for lateral stability, concrete slabs at each floor level, an auxiliary post-tensioned column to provide torsional stability, and four gravity columns to transfer the weight of the slabs to the shake table. A picture of the building slice is shown in Figure 5.9. Figure 5.10 presents an elevation dimensions of the test building and Figure 5.11 shows a plan view of the structure with wall and slab dimensions at different levels. More details about the test structure can be found elsewhere (http://nees.ucsd.edu/7Story.html).

In order to perform damage identification of this test building based on FE model updating techniques, a three dimensional (3D) linear elastic FE model of the building is developed using the general-purpose FE structural analysis program, FEDEASLab. A four-node linear flat shell element presented in section 5.3 borrowed from the FE literature is

implemented in FEDEASLab in order to model the web wall, back wall, and concrete slabs. As aforementioned, this shell element is based on the mixed discrete variational principle in conjunction with Allman type interpolation for the membrane part and the discrete Kirchhoff plate element for the plate part. In the FE model of the test building, the gravity columns and braces are modeled using truss elements. Overall, the FE building model is defined by 423 nodes and 398 elements. Figure 5.12 shows the FE model of the shear wall building developed and Table 5.6 provides measured values of Young's moduli of various concrete components of the building structure (referred to as initial values). The location of the various concrete components is defined in Figure 5.10.

5.5.2 Dynamic Tests and Identified Modal Parameters

The test structure was instrumented with an array of accelerometers, strain gages, and linear variable displacement transducers (LVDTs). In addition, the displacement response of selected points on the structure was measured in 3D using global positioning system (GPS) sensors. Table 5.7 provides a summary of the sensor array installed on the test structure. In this study, measured response data from 28 longitudinal accelerometers (three on each floor slab as shown in Figure 5.11) and one on the web wall at mid-height of each story are used to identify the modal parameters of the test structure.

A sequence of dynamic tests (68 tests in total) were performed including ambient vibration, free vibration, and forced vibration tests (white noise and seismic base excitations) using the UCSD-NEES shake table. The test structure was damaged progressively through four historical earthquake records consisting of (http://peer.berkeley.edu/smcat): (1) longitudinal component of the 1971 San Fernando earthquake recorded at the Van Nuys station (EQ1); (2) transversal component of the 1971 San Fernando earthquake recorded at the

Van Nuys station (EQ2); (3) longitudinal component of the 1994 Northridge earthquake recorded at the Oxnard Boulevard station in Woodland Hill (EQ3); and (4) 360 degree component of the 1994 Northridge earthquake recorded at the Sylmar station (EQ4). The acceleration time histories of these four earthquake records are shown in Figure 5.13.

Based on these seismic tests, five different damage states (S0, S1, S2, S3 and S4) of the building are defined. Damage state S0 is defined as the undamaged state of the structure or state of the structure before experiencing the first seismic excitation (EQ1), while damage states S1, S2, S3, and S4 correspond to the state of the structure after it was subjected to the first (EQ1), second (EQ2), third (EQ3), and fourth (EQ4) seismic excitation, respectively. Damage state S0 does not correspond to the uncracked state of the structure, since the structure had already been subjected to low-amplitude white noise base excitations (0.02-0.03g RMS) for the purposes of checking the instrumentation and data acquisition system as well as tuning the shaking table controller. It should be noted that the bracing system between the slabs and the post-tensioned column was modified after the third seismic excitation (EQ3). Table 5.8 describes a reduced set of the dynamic tests used in this study together with the corresponding damage states.

SSI-DATA is applied herein for modal parameters identification using ambient vibration data. SSI-DATA determines the system model in state-space using output-only measurements directly. The procedure of extracting the modal parameters using SSI-DATA can be summarized as follows: (1) Form the output Hankel matrix and partition it into “past” and “future” output sub-matrices; (2) Calculate the orthogonal projection of the row space of the “future” output sub-matrix into the row space of the “past” output sub-matrix using QR factorization; (3) Obtain the observability matrix and Kalman filter state estimate via SVD of the projection matrix; and (4) Using the available Kalman filter state estimate, extract the

discrete-time system state-space matrices based on a least squares solution. Once the system state-space matrices are determined, the modal parameters are ready to be obtained (see Chapter 2 for detail).

The measured acceleration response was sampled at a rate of 240 Hz resulting in a Nyquist frequency of 120 Hz, which is much higher than the modal frequencies of interest in this study (< 25 Hz). In the implementation of SSI-DATA, the acceleration response is first filtered between 0.5 Hz and 25 Hz using a high order (1024) band-pass finite impulse response (FIR) filter. Then the filtered acceleration data are down-sampled to 80 Hz in order to improve the computational efficiency of system identification. For each dynamic test, an output Hankel matrix is formed including 45 block rows with 28 rows in each block (28 longitudinal channels). Figure 5.14 represents in polar plots (i.e., rotating vectors in the complex plane) three longitudinal mode shapes associated with natural frequencies and damping ratios identified at the undamaged state of the structure. These polar plots have the advantage to show directly the extent of the non-proportional damping characteristics of a vibration mode. If all complex valued components of a mode shape vector are collinear (i.e., in phase or 180 degrees out of phase), this vibration mode is said to be classically (or proportionally) damped. On the other hand, the more these mode shape components are scattered in the complex plane, the more the vibration mode is non-classically (or non-proportionally) damped. However, measurement noise, estimation errors, and modeling errors could also cause a “true” classically damped mode to be identified as non-classically damped. Figure 5.14 shows that the first two identified modes are nearly perfectly classically damped, while the third mode is non-classically damped. A 3D representation of the normalized mode shapes for these identified vibration modes is given in Figure 5.15. Normalization was performed by projecting all mode shape components onto their principal axis (in the complex plane).

The identified natural frequencies and damping ratios of the first three longitudinal vibration modes at different damage states are reported in Table 5.9 and Table 5.10, respectively. The identified natural frequencies and damping ratios are also represented in bar plots (see Figure 5.16 and Figure 5.17). From these tables and figures, it is observed that: (1) with increasing level of damage, the identified natural frequencies decrease monotonically due to loss of stiffness in the building; (2) although the identified damping ratios vary from damage state to damage state, there is no clear trend between the level of damage and changes in the damping ratios. Figure 5.18 shows in bar plots of the MAC values between the corresponding mode shapes identified at various damaged states and undamaged state. For each mode, the MAC values generally decrease with increasing level of damage. From this figure, it is found that mode shapes of the second and third vibration modes are more sensitive to the level of damage.

5.5.3 Damage Identification

The first step to identify damage in the test structure using the FE model updating algorithm described earlier is to obtain a reference (calibrated) FE model based on the modal parameters identified at the undamaged (or baseline) state of the building (S0). In this step, Young's moduli of the main wall at all seven stories (two parameters per story at the first three levels and one parameter per story for levels 4-7) and Young's moduli of the slab at each story are taken as updating (or calibrating) parameters, which results in 17 calibrating parameters in this step. Once the reference model is determined, Young's moduli of the main wall at all seven stories (two parameters per story at the first three levels and one parameter per story for levels 4-7) are updated at the four damage states S1, S2, S3, and S4. In all model updating performed, the natural frequencies and mode shapes of the first three longitudinal modes identified using SSI-DATA are used in the objective function [see equation (5.18)], resulting

in a residual vector with 42 components (i.e., 3 natural frequencies and 3 vibration mode shapes of 13 components each). At each damage state, a specific set of weight factors is assigned to the residuals based on their statistical uncertainty (coefficient-of-variation). It should be mentioned that the optimal weights at each damage state are obtained through a trial-and-error process, observing the match between the numerically predicted and experimentally identified modal parameters (Teughels and De Roeck, 2004).

The Young's moduli of the different concrete components of the main (web) wall updated based on the modal parameters identified at the undamaged state S0, referred to as reference values, are reported in Table 5.11 together with the corresponding measured values (at the day of the test) used in the initial FE model. From these results, it is observed that the reference (calibrated) Young's moduli of the main wall differ from their initial/measured values. This is due to the fact that the updating parameters (Young's moduli) act as effective Young's moduli reflecting the overall stiffness of the test structure, including the contributions of other structural components such as back wall and steel braces for which the parameters are not calibrated / updated. The correction factors / damage factors (relative to the reference state) obtained at different damage states are presented in bar plot Figure 5.19. These results indicate that: (1) the severity of structural damage increases as the structure is exposed to stronger earthquake excitations; and (2) the extent of damage decreases rapidly along the height of the structure (damage concentrated in the two bottom stories), except for a false alarm in the fourth story at damage state S4. The large identified damage factor in the fourth story could be due to large identification errors in the identified modal parameters at damage state S4. Table 5.12 presents the natural frequencies computed from the updated FE model at each damage state together with their counterparts identified from ambient vibration data as well as the MAC values between the corresponding analytical (FE computed) and experimental mode

shapes. It should be noted that the analytical (FE computed) mode shapes are truncated at the locations of the accelerometers in order to match the size of the experimental mode shapes. The natural frequencies computed from the updated FE model at each damage state are also given in bar plot in Figure 5.20 together with their counterparts identified from vibration data. From Table 5.12 and Figure 5.20, it is observed that: (1) Generally speaking, there is a very good agreement between the identified natural frequencies and their analytical counterparts computed from the updated FE model at each damaged state. However, the discrepancies between analytical and identified natural frequencies are larger for the second and third modes than those for the first mode. This is due to the fact that the identified modal parameters of the second and third modes are not as accurate as (i.e., have a larger estimation uncertainty than) those of the first mode, resulting in smaller weight factors being assigned to their corresponding residuals. (2) The MAC values between analytical and identified mode shapes are very close to one for all damage states except damage state S4, in which the MAC values for the second and third modes are lower. This indicates a lower level of confidence for identified damage at damage state S4. Pictures of the actual damage in the bottom two stories of the main wall at damage state S4 are shown Figure 5.21 and Figure 5.22. During the seismic test EQ4, a lap-splice failure (i.e., debonding between longitudinal steel reinforcement bars and the surrounding concrete) occurred in the web wall at the bottom of the second story on the west side as shown in Figure 5.22. Figure 5.23 shows the envelope of absolute strains along the shear wall height for the first two stories measured from LVDTs during the four seismic tests. Figure 5.24 shows the envelope of absolute strains along the vertical steel reinforcement bars measured from strain gages during the four seismic tests. All these figures provide a physical observation/measure of the damage in the wall. The damage identification

results in the bottom two stories are consistent with the actual damage observed in the test structure.

5.6 Summary and Conclusions

In this chapter, the sensitivity-based finite element (FE) model updating methodology is described. A four-node linear flat shell element borrowed from the FE literature is implemented in the element library of the MATLAB-based structural analysis software FEDEASLab, which is then integrated with the FE model updating algorithms used/developed in order to perform structural damage identification. The implemented linear flat shell element is based on the mixed discrete variational principle proposed by Hughes and Brezzi in conjunction with Allman type interpolation for the membrane part and the discrete Kirchhoff plate element derived by Batoz and Tahar for the plate part. The resulting finite element has six degrees of freedom per node, including a true (mechanics-based) drilling degree of freedom.

A comparative study of the influence of different objective functions on the damage identification results is performed by using simulated data for a simply supported plate. From this numerical example, it is found that the objective function defined by a combination of natural frequency residuals and mode shapes residuals and the objective function defined by a combination of natural frequency residuals, mode shapes residuals, and pseudo modal flexibility residuals are good candidates for structural damage identification using sensitivity-based FE model updating techniques.

Finally, a sensitivity-based FE model updating strategy is applied for damage identification of a full-scale seven-story R/C building slice tested on the UCSD-NEES shake table. The shake table tests were designed so as to damage the building progressively through

a sequence of historical earthquake records reproduced on the shake table. The natural frequencies and mode shapes of the first three longitudinal modes identified using the data-driven stochastic subspace identification based on the ambient vibration data are used in the damage identification. In the application of the FE model updating strategy to identify the damage in the building at various damage states, the objective function is defined as a combination of residuals in natural frequencies and mode shape components. The damage identification results are consistent with the actual damage observed (visually) in the building and inferred from LVDT and strain gages data.

5.7 Acknowledgements

This Chapter is an extended version of the paper published in the proceedings of the 4th Word Conference on Structural Control and Monitoring (2006) under the title “Damage identification of a seven-story reinforced concrete shear wall building tested on the UCSD-NEES shake table” with authors Xianfei He, Babak Moaveni, Joel P. Conte, Jose I Restrepo, and Ahmed Elgamal. This Chapter is also an extended version of the manuscript in final stage of preparation for possible publication in the Journal of Structural Engineering, ASCE (2008) under the title “Damage identification of a seven-story reinforced concrete shear wall building sliced tested on the UCSD-NEES shake table” with authors Babak Moaveni, Xianfei He, and Joel P. Conte. The dissertation author is primary investigator of these two papers.

5.8 References

Allemang, R. J., and Brown, D. L. (1982). “A correlation coefficient for modal vector analysis.” *Proceedings of 1st International Modal Analysis Conference*, Bethel, Connecticut, 110-116.

Allman, D. J. (1988). “A quadrilateral finite element including vertex rotations for plane elasticity analysis.” *International Journal for Numerical Methods in Engineering*, 26(3), 717-730.

Batoz, J. L. and Tahar, M. B. (1982). "Evaluation of a new quadrilateral thin plate bending element." *International Journal for Numerical Methods in Engineering*, 18(11), 1655-1677.

Bernal, D., and Gunes, B. (2004). "Flexibility based approach for damage characterization: Benchmark application." *Journal of Engineering Mechanics*, ASCE, 130(1), 61-70.

Catabas, F., Lenett, M., Brown, D., Doebling, S., Farrar, C., and Turer, A. (1997). "Modal analysis of multi-reference impact test data for steel stringer bridges." *Proceedings of 15th International Modal Analysis Conference*, Orlando, Fl.

Filippou, F. C. and Constantinides, M. (2004). "FEDEASLab Getting started guide and simulation examples." *Technical Report NEESgrid-2004-22, August 31, <http://fedeaslab.berkeley.edu/>*.

Fox, R., and M. Kapoor (1968), "The Location of Defects in Structures - A Comparison of the Use of Natural Frequency and Mode Shape Data," *Proceedings of 10th International Modal Analysis Conference*, San Diego, USA.

Hughes, T. J. R. and Brezzi, F. (1989). "On drilling degrees of freedom." *Computer Methods in Applied Mechanics and Engineering*, 72(1), 105-121.

Jetteur, P., and Frey, F. (1986)." A four node Marguerre element for non-linear shell analysis." *Engineering Computations*, 3(4), 276-282.

Kamal, R. (1998). "Nonlinear geometric and material analysis of shell structures with particular emphasis on tubular joints." *PhD Dissertation*, Department of Civil Engineering, Rice University, Houston, Texas.

Maeck, J., and De Roeck, G. (1999). "Dynamic bending and torsion stiffness derivation from modal curvatures and torsion rates." *Journal of Sound and Vibration*, 225(1), 153-170.

Moaveni, B., He, X., Conte, J. P., and Restrepo, J. I. (2007). "System identification of a seven-story reinforced concrete shear wall building tested on the UCSD-NEES shake table." *Under final stage of preparation.*

Pandey, A. K., Biswas, M., and Samman, M. M. (1991). "Damage detection from changes in curvature mode shapes." *Journal of Sound and Vibration*, 145(2), 321-332.

Pandey, A. K., and Biswas, M. (1994). "Damage detection in structures using changes in flexibility." *Journal of Sound and Vibration*, 169 (1), 3-17.

Shi, Z.Y., Law, S. S., and Zhang, L.M. (2002). "Improved damage quantification from elemental modal strain energy change." *Journal of Engineering Mechanics*, ASCE, 128(5), 521-529.

Salawu, O. S. (1997). "Detection of structural damage through changes in frequency: A review." *Engineering Structures*, 19(9), 718-723.

Taylor, R. L. (1988). “Finite element analysis of linear shell problems.” *The Mathematics of Finite Elements and Applications (ed. J. R. Whiteman)*, 6, 191-205.

Teughels, A., and De Roeck, G. (2004). “Structural damage identification of the highway bridge Z24 by FE model updating.” *Journal of Sound and Vibration*, 278(3), 589-610.

Toksoy, T., and Aktan, A. E. (1994). “Bridge-condition assessment by modal flexibility.” *Experimental Mechanics*, 34(3), 271-278.

Zhao, J., DeWolf, J. T. (1999). “Sensitivity study for vibration parameters used in damage detection.” *Journal of Structural Engineering*, ASCE, 125(4), 410-417.

Van Overschee, P., and De Moor, B. (1996). *Subspace Identification for Linear Systems: Theory-Implementation-Applications*, Kluwer Academic Publishers, Norwell, Massachusetts, USA.

Table Captions

Table 5.1 Indices in Equation (5.40)

I	*J*	*K*	*L*	*M*
1	4	2	8	5
2	1	3	5	6
3	2	4	6	7
4	3	1	7	8

Table 5.2 Indices in Equation (5.47)

I	*J*	*K*	*L*	*M*
1	2	4	8	5
2	3	1	5	6
3	4	2	6	7
4	1	3	7	8

Table 5.3 Modal parameters of the simulated plate at both undamaged and damaged states

Mode No	Natural frequencies (Hz)		Difference in frequencies (%)	MAC values
	Undamaged state	Damaged state		
1	42.71	37.74	11.64	0.996
2	80.39	73.35	8.76	0.991
3	130.44	114.82	11.97	0.952
4	142.74	129.42	9.34	0.966
5	160.33	144.44	9.91	0.919
6	210.91	189.40	10.20	0.906

Table 5.4 Damage identification results of the simulated plate using the first objective function

		Exact values	Case No.					
			1	2	3	4	5	6
Correction factors	p_1	0.45	0.446	0.450	0.450	0.450	0.450	0.450
	p_2	0.40	0.402	0.397	0.400	0.400	0.400	0.400
	p_3	0.00	0.002	0.002	0.000	0.000	0.000	0.000
	p_4	0.00	0.040	0.004	0.000	0.000	0.000	0.000
	p_5	0.35	0.348	0.351	0.350	0.350	0.350	0.350
	p_6	0.00	0.000	0.000	0.000	0.000	0.000	0.000
	p_7	0.30	0.266	0.297	0.300	0.300	0.300	0.300
	p_8	0.00	0.026	0.000	0.000	0.000	0.000	0.000
	p_9	0.00	0.000	0.000	0.000	0.000	0.000	0.000
No. of iterations		N/A	> 400	> 400	23	108	65	57

Table 5.5 Damage identification results of the simulated plate using different objective functions

		Exact values	Objective function		
			1	2	3
Correction factors	p_1	0.45	0.450	0.449	0.450
	p_2	0.40	0.400	0.399	0.400
	p_3	0.00	0.000	0.001	0.000
	p_4	0.00	0.000	0.000	0.000
	p_5	0.35	0.350	0.350	0.350
	p_6	0.00	0.000	0.000	0.000
	p_7	0.30	0.300	0.298	0.300
	p_8	0.00	0.000	0.005	0.000
	p_9	0.00	0.000	0.000	0.000
No. of iterations		N/A	23	37	21

Table 5.6 Measured values of Young's moduli of various concrete components

Components	C1	C2	C3	C4	C5	C6	C7	C8	C9
E (GPa)	24.47	26.00	34.84	30.20	28.90	32.14	33.54	28.91	30.32

Table 5.7 Summary of instrumentations

Sensor Type	Location	Quantity
Accelerometer (113)	Foundation	14
	Slabs	89
	Reaction block	9
	Soil	1 (tri-axial)
LVDT (54)	Web wall (levels 1-2)	34
	Web wall (levels 3-7)	20
Potentiometer (8)	Web wall (levels 1-2)	8
Strain Gage (231)	Web wall	143
	Flange wall	64
	Gravity columns	16
	Braces connecting slabs to post-tensioned column	8

Table 5.8 Dynamic tests used in this study (WN: white noise test, AV: ambient vibration test)

Test No.	Test Date	Test Description	Damage State
39	Nov. 21, 05	8 min WN + 3 min AV	S0
40	Nov. 21, 05	EQ1	
41	Nov. 21, 05	8 min WN + 3 min AV	S1
43	Nov. 21, 05	EQ2	
46	Nov. 22, 05	8 min WN + 3 min AV	S2
48	Nov. 22, 05	EQ3	
49	Nov. 22, 05	8 min WN + 3 min AV	S3
62	Jan. 14, 06	EQ4	
64	Jan. 14, 06	8 min WN + 3 min AV	S4

Table 5.9 Identified natural frequencies using SSI-DATA based on ambient vibration data

Mode No	S0	S1	S2	S3	S4
1	1.91	1.88	1.67	1.44	1.02
2	10.51	10.21	10.16	9.23	5.67
3	24.51	24.31	22.60	21.82	15.09

Table 5.10 Identified damping ratios using SSI-DATA based on ambient vibration data

Mode No	S0	S1	S2	S3	S4
1	2.32	2.93	1.31	2.70	1.02
2	2.38	2.68	1.42	1.32	1.73
3	0.45	0.64	0.92	1.43	0.95

Table 5.11 Young's moduli of various concrete components in the main wall

Story	Measured/Initial values (GPa)	Ref. values (GPa)
First bottom	24.47	17.13
First top	24.47	21.61
Second bottom	26.00	27.40
Second top	26.00	25.89
Third bottom	34.84	35.24
Third top	34.84	37.52
Fourth	30.20	33.86
Fifth	28.90	28.35
Sixth	32.14	34.40
Seventh	33.54	34.57

Table 5.12 Comparison of experimentally identified modal parameters with their FE computed counterparts

Damage State	Experimentally Identified Natural Frequencies [Hz]			FE Computed Natural Frequencies [Hz]			MAC		
	Mode 1	Mode 2	Mode 3	Mode 1	Mode 2	Mode 3	Mode 1	Mode 2	Mode 3
S0	1.91	10.51	24.51	1.89	10.37	25.03	1.00	0.99	0.96
S1	1.88	10.21	24.31	1.86	10.25	24.91	1.00	0.99	0.97
S2	1.67	10.16	22.60	1.69	9.82	22.43	1.00	0.98	0.98
S3	1.44	9.23	21.82	1.46	9.06	21.36	1.00	0.97	0.96
S4	1.02	5.67	15.09	1.01	5.82	15.59	1.00	0.90	0.88

Figure Captions

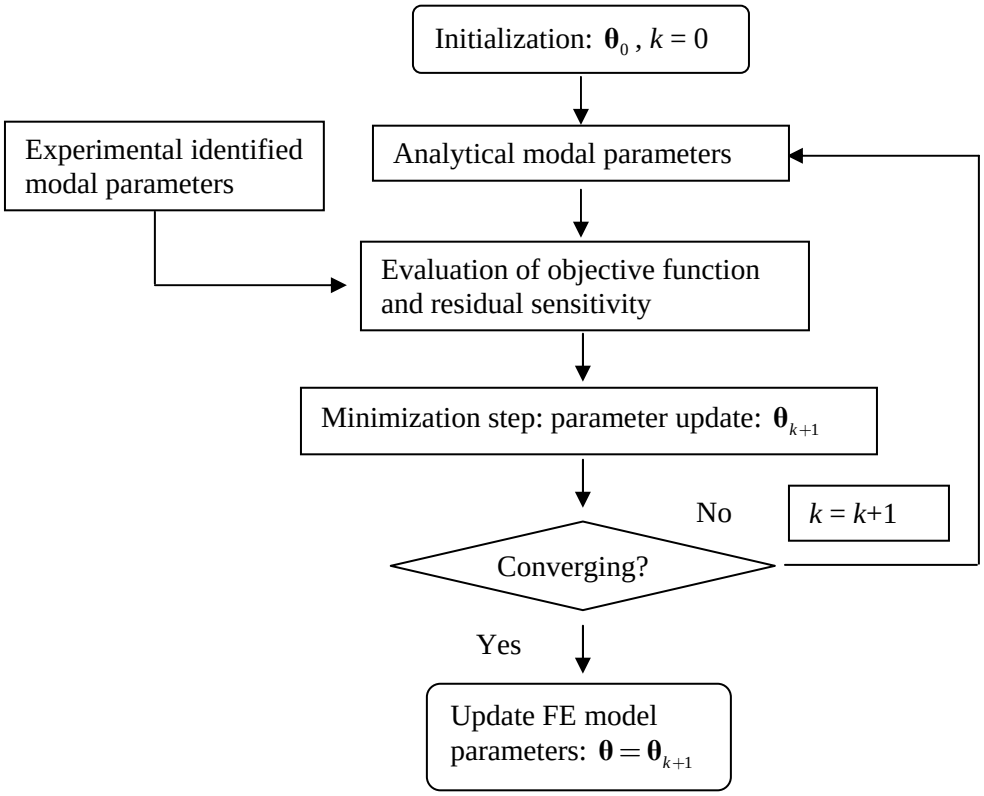

Figure 5.1. Flowchart of FE model updating procedure with physical parameters $\boldsymbol{\theta}$

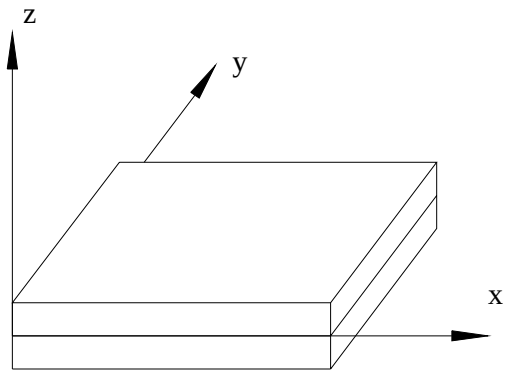

Figure 5.2. Local reference coordinate system of the flat shell element

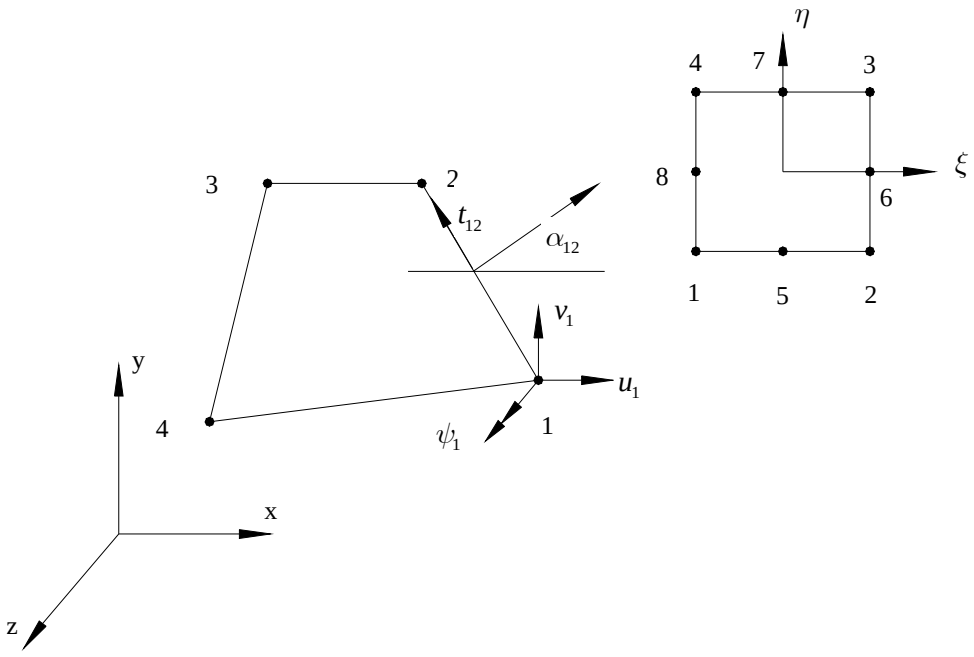

Figure 5.3. Membrane element with drilling degrees of freedom

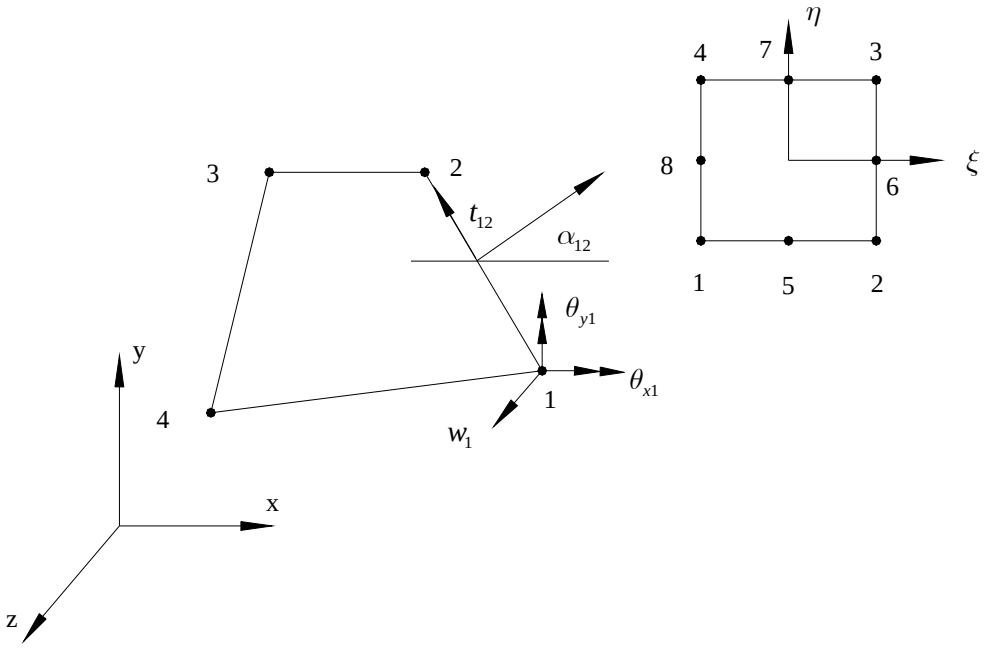

Figure 5.4. Bending plate element

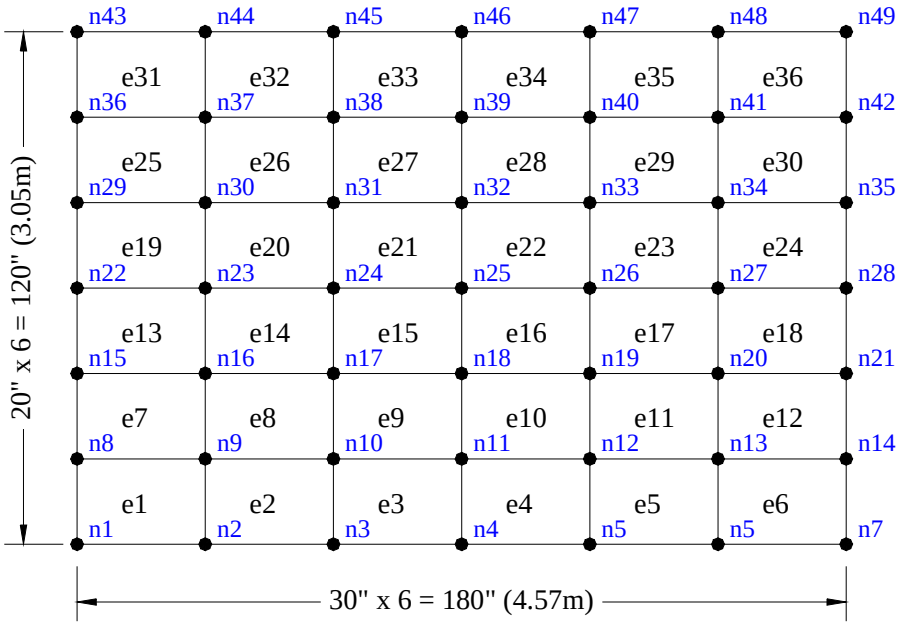

Figure 5.5. Simulated simply supported plate

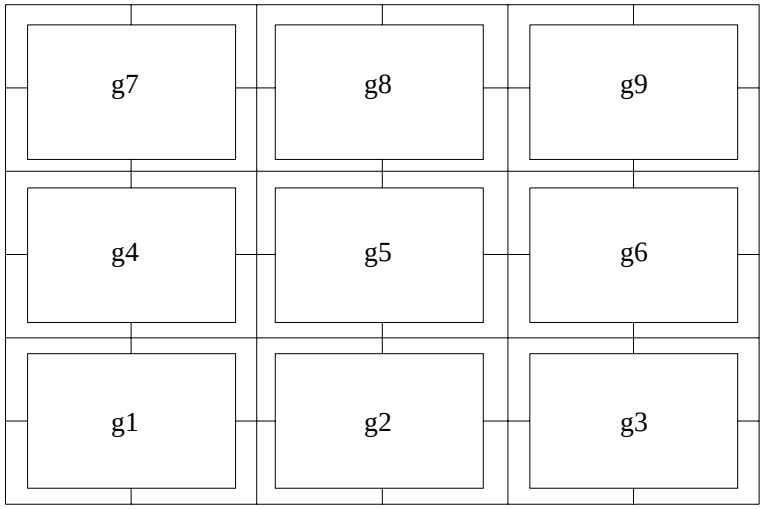

Figure 5.6. Substructures of the simulated plate

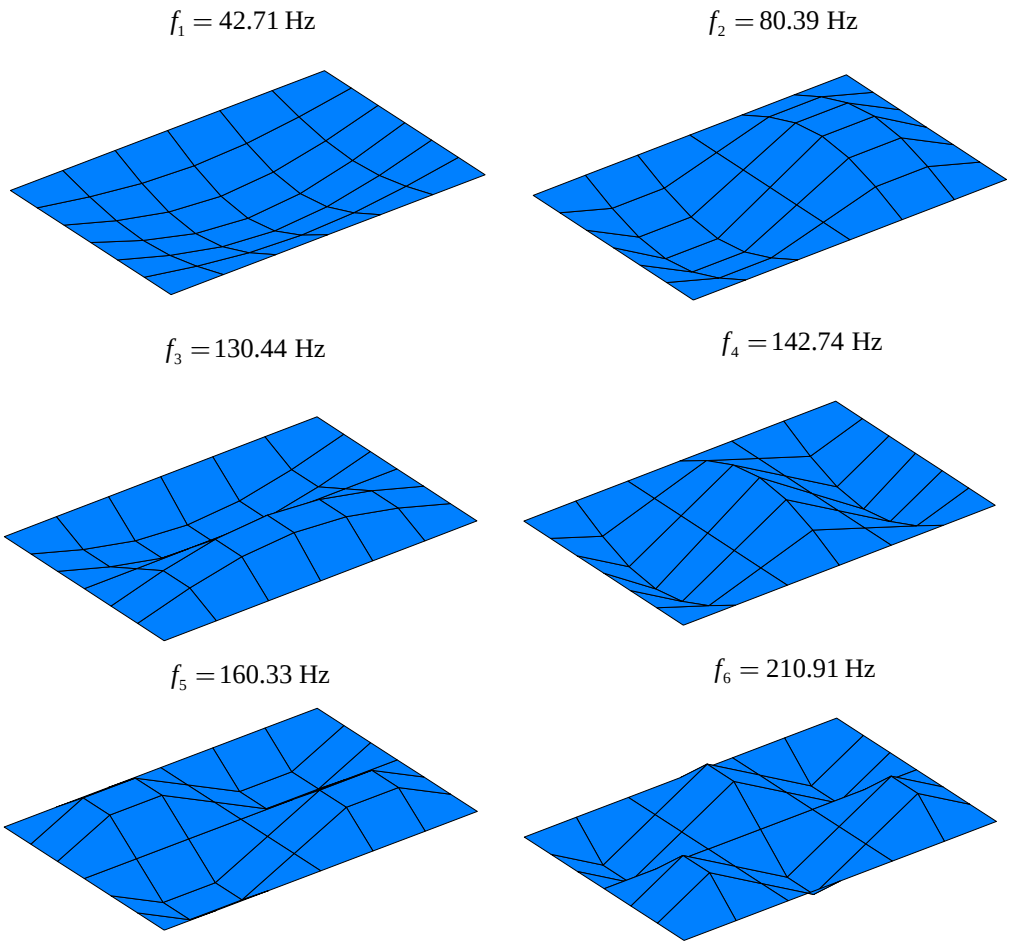

Figure 5.7. Mode shapes of the first six vibration modes computed from the undamaged plate

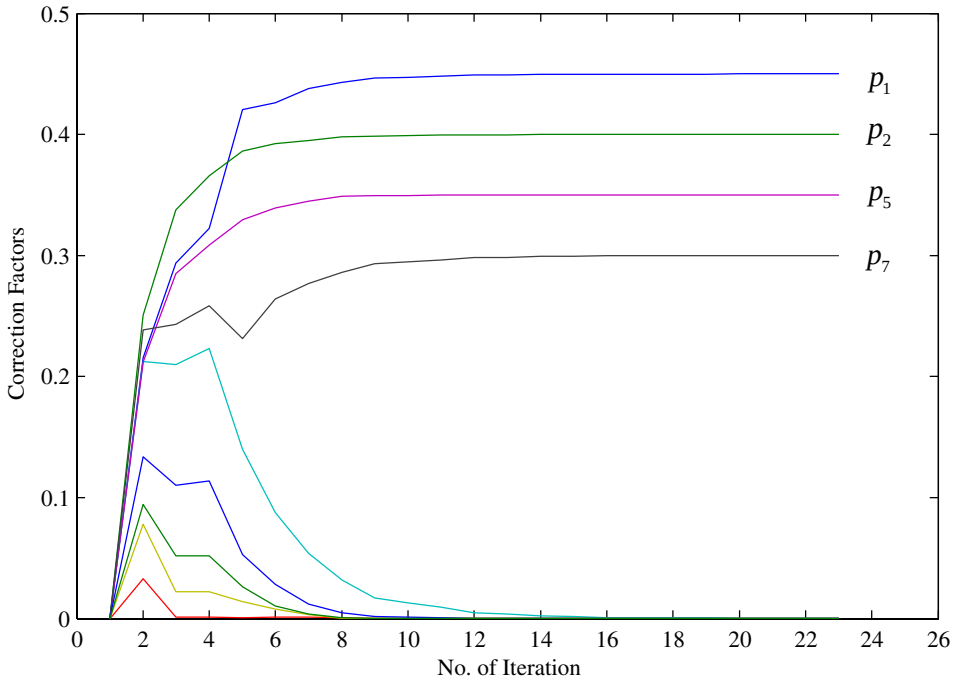

Figure 5.8. Updating history of correction factors

Figure 5.9. Picture of the seven-story shear wall building slice

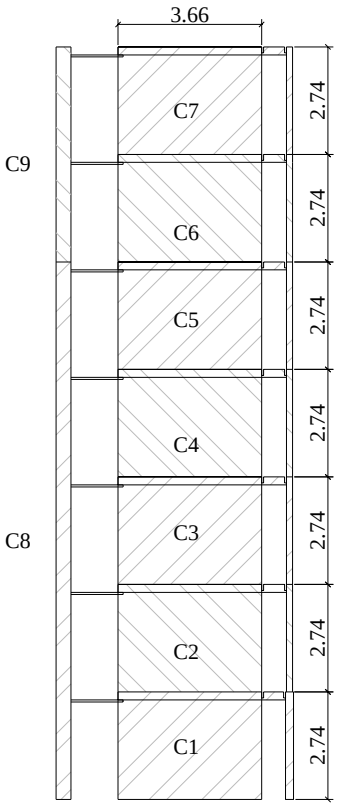

Figure 5.10. Elevation dimensions (unit: m) of the shear wall building slice

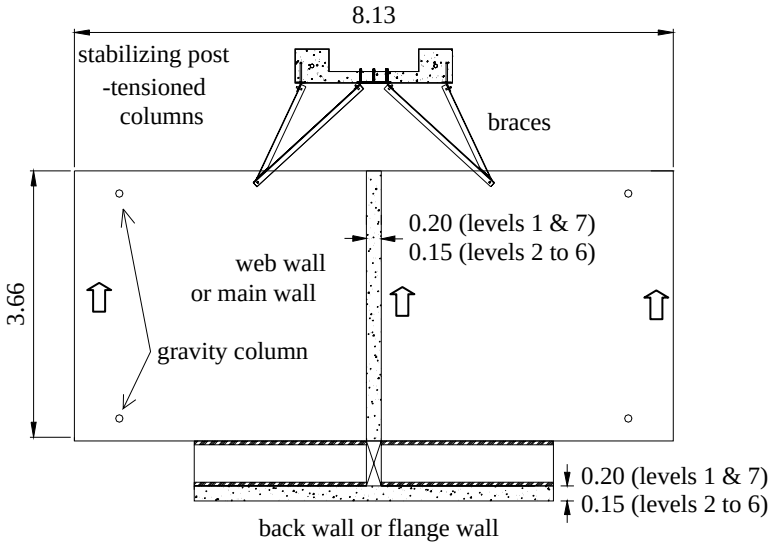

Figure 5.11. Plan view (unit: m) of the shear wall building slice

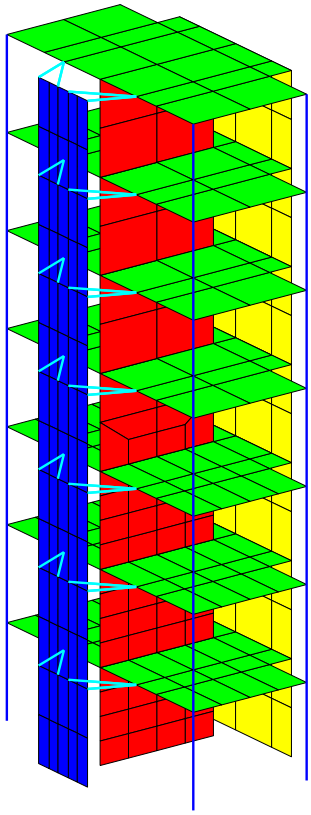

Figure 5.12. Finite element model of the shear wall building slice

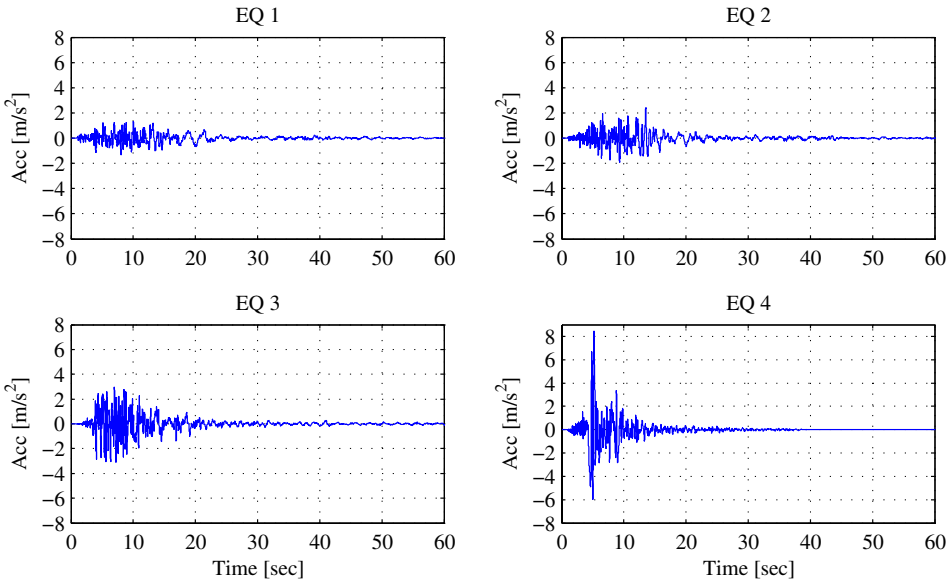

Figure 5.13. Acceleration time history of the input earthquake records

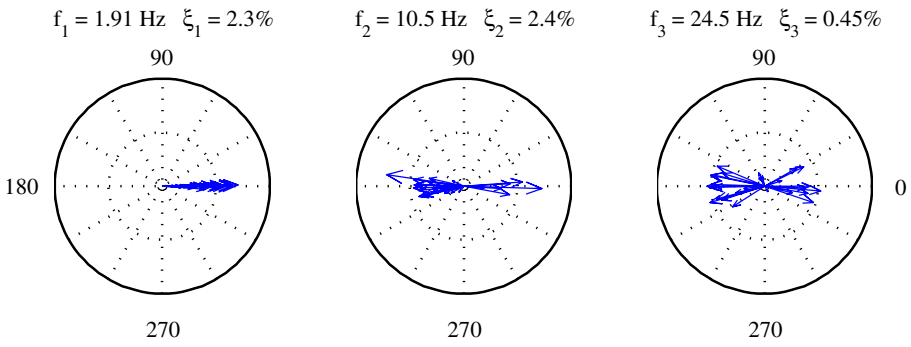

Figure 5.14. Polar plot representation of vibration mode shapes identified using SSI-DATA based on ambient vibration data at undamaged state

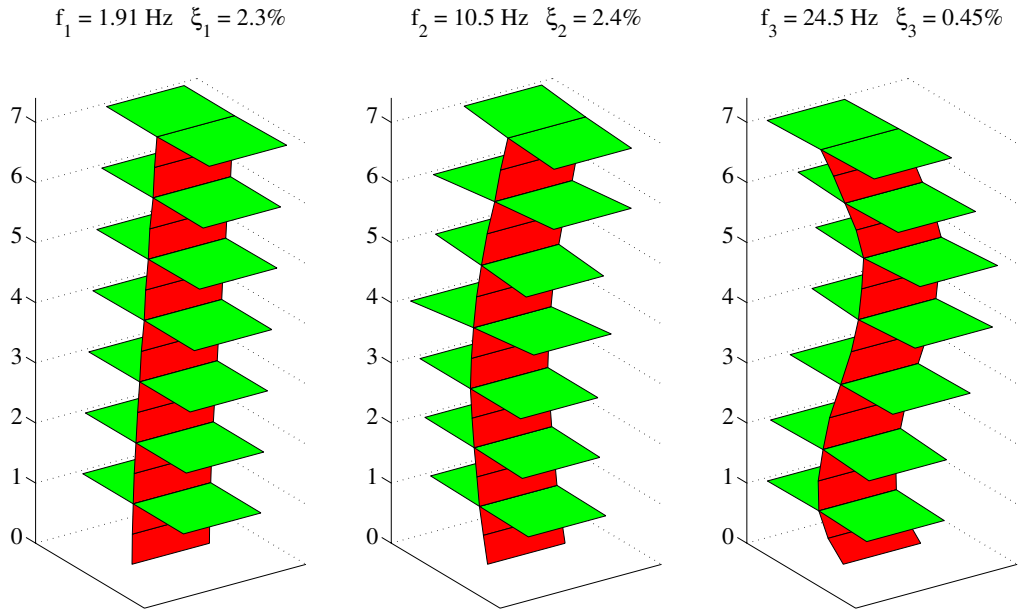

Figure 5.15. 3D representation of normalized vibration mode shapes identified using SSI-DATA based on ambient vibration data at undamaged state

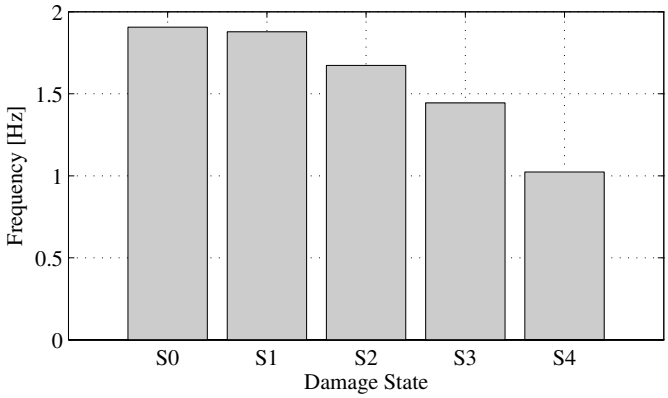

(a) Mode 1

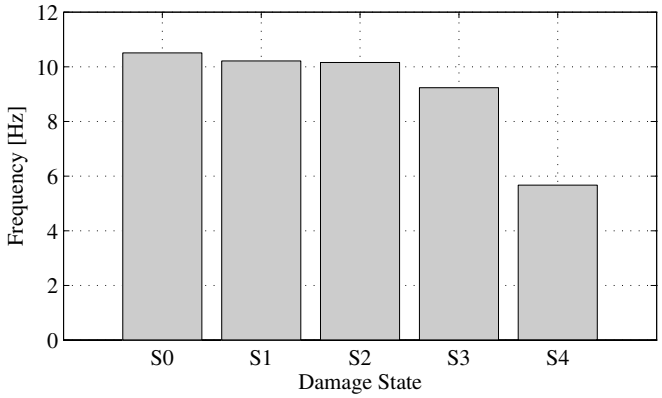

(b) Mode 2

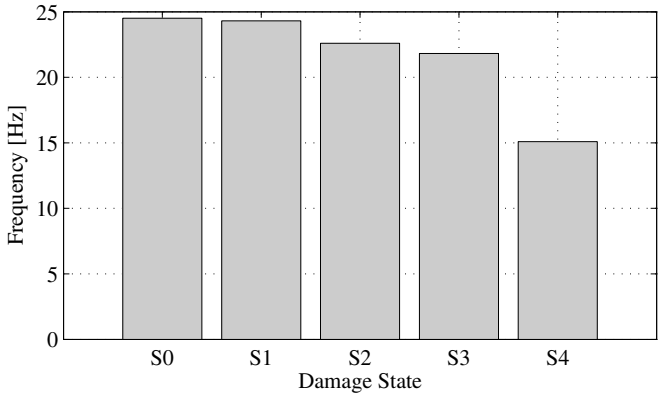

(c) Mode 3

Figure 5.16. Natural frequencies identified using SSI-DATA at different damaged states

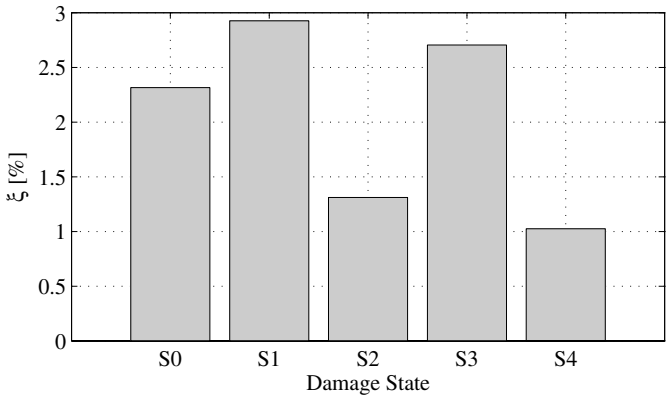

(a) Mode 1

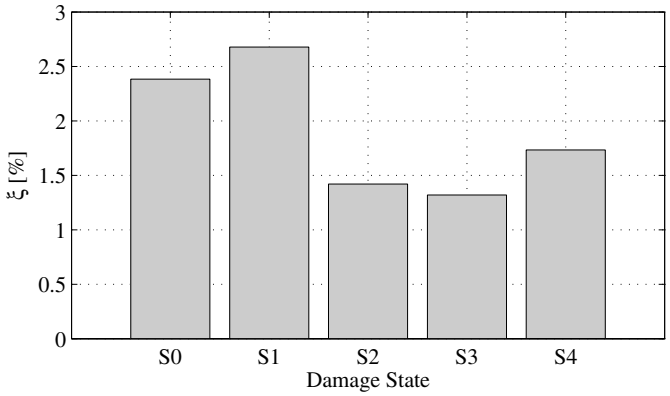

(b) Mode 2

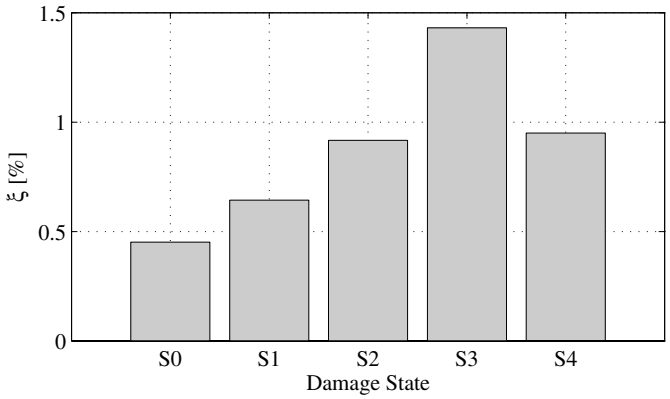

(c) Mode 3

Figure 5.17. Damping ratios identified using SSI-DATA at different damaged states

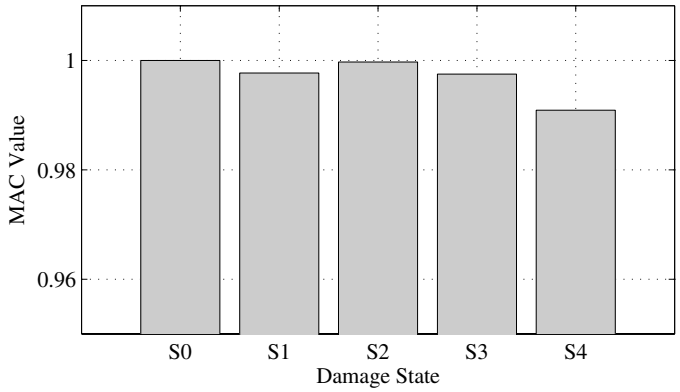

(a) Mode 1

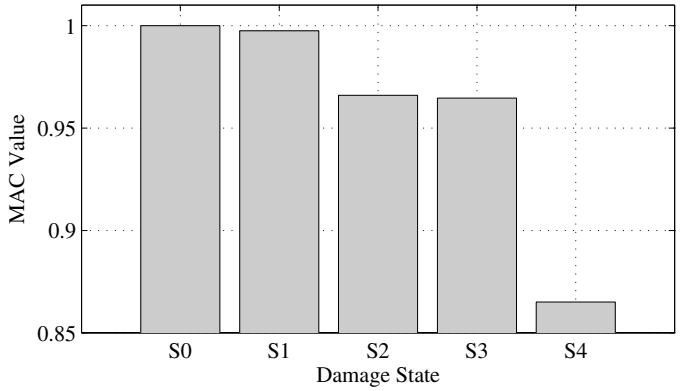

(b) Mode 2

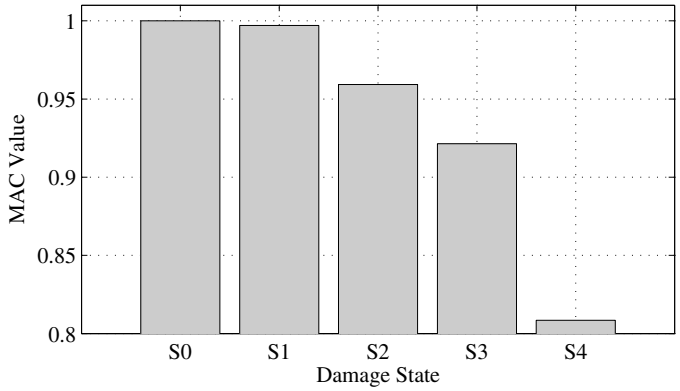

(c) Mode 3

Figure 5.18. MAC values between corresponding mode shapes identified at various damaged states and undamaged state

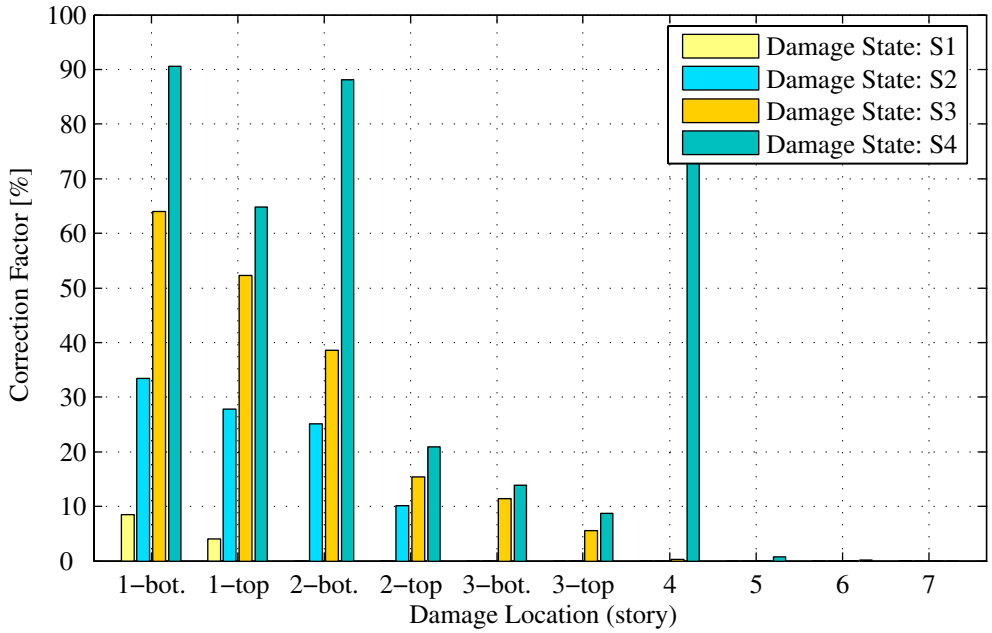

Figure 5.19. Identified correction factors/damage factors

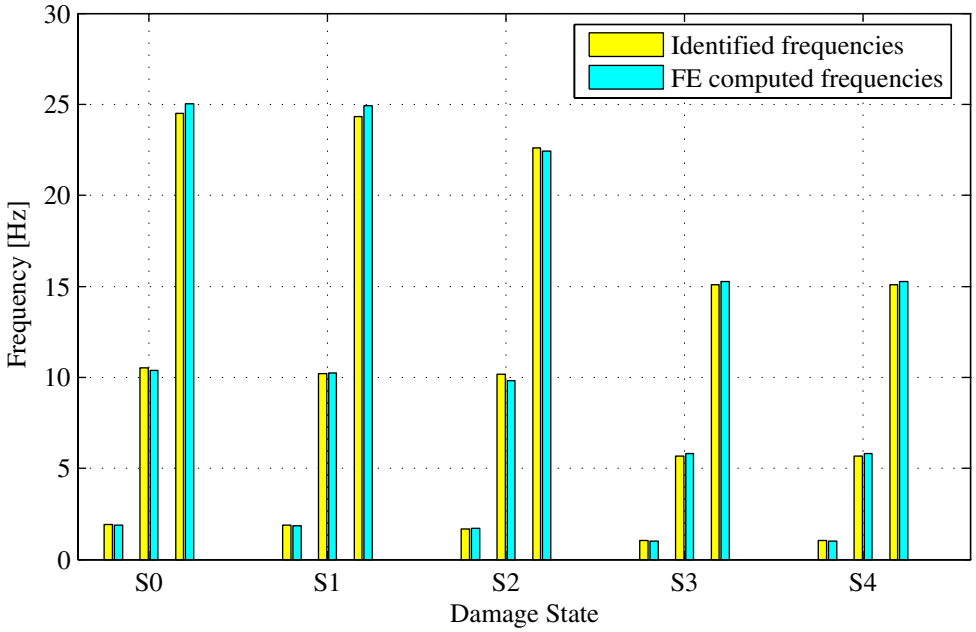

Figure 5.20. Comparison of the identified natural frequencies and their analytical counterparts computed from the updated FE model at each damage state

Figure 5.21. Observed damage at bottom of the first story at damage state 4

Figure 5.22. Lap-splice failure at bottom of the second story at damage state 4

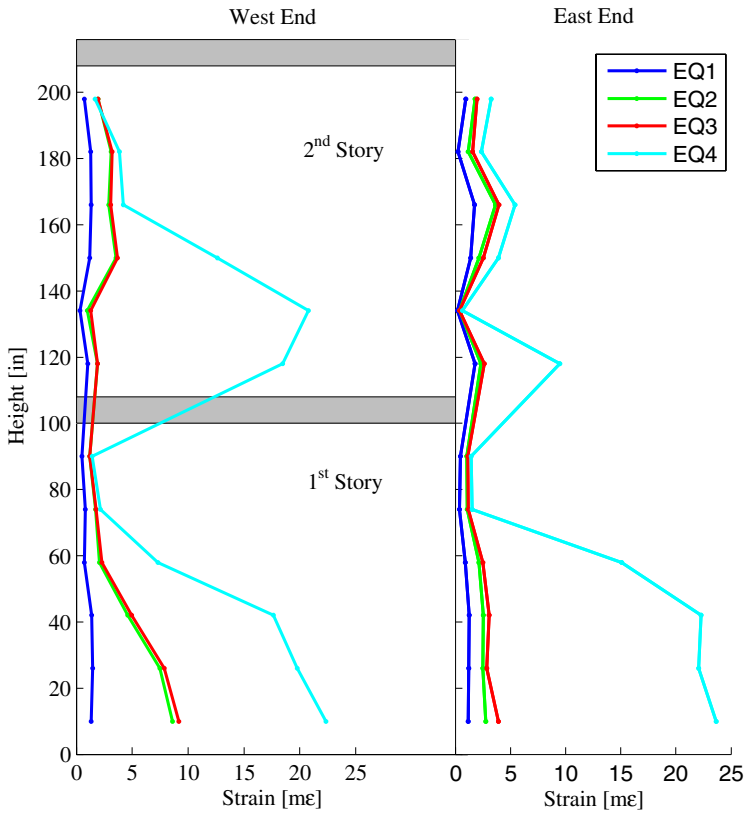

Figure 5.23. Envelope of absolute strains along the shear wall height for the first two stories measured from LVDTs during the four seismic tests

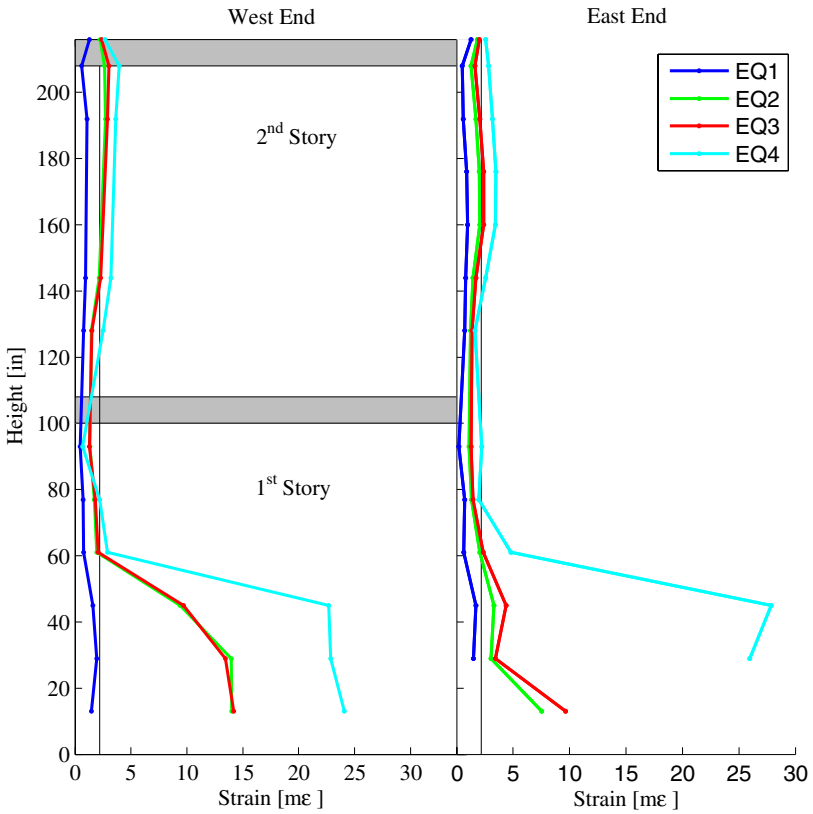

Figure 5.24. Envelope of absolute strains along the vertical steel reinforcement bars for the first two stories measured from strain gages during the four seismic tests

Chapter 6

Deployment of Long-Term Continuous Structural Monitoring System on Voigt Bridge Testbed

6.1 Introduction

Long-term continuous health monitoring and condition assessment of highways and bridges is necessary to allow for the early identification of possible damages existing in structures and to enable maintenance and repair works at the initial damage phase, to maximize the lifespan of these structures at minimum life-cycle costs, while guaranteeing structural safety and reliability. In addition, a long-term monitoring system makes it possible to study the effects of varying environmental conditions such as temperature, wind characteristics, and relative humidity on the identified modal properties (e.g., natural frequencies, damping ratios, and mode shapes) of bridges. Variations in modal properties due to changes in environmental conditions have been shown to be very significant in previous studies; they may even induce changes larger than those caused by structural damage (e.g., Abdel Wahab and De Roeck, 1997; Cornwell et al., 1999; Peeters and De Roeck, 2001; He et al., 2007).

In this study, a state-of-the-art long-term continuous monitoring system is developed and deployed on the Voigt Bridge. In this monitoring system, thirty piezoelectric accelerometers and a video camera are deployed for traffic induced vibration monitoring and fifteen capacitive accelerometers are installed for seismic monitoring. In addition, twenty-four thermocouples, and eight thermistor & relative humidity (RH) sensors are installed inside the

bridge to measure the concrete temperature and temperature / relative humidity (RH) of the air inside the bridge box girders. Another two thermocouples are installed outside the bridge to measure the temperature of the air surrounding the bridge. A wind monitor and a thermistor & RH sensor are installed at the weather monitoring station to measure the wind characteristics, temperature and relative humidity of the air outside the bridge. This monitoring system makes it possible to: (1) study the effects of varying environmental conditions such as temperature, wind characteristics, and humidity on the identified modal properties of the bridge; (2) allow for the early identification of possible damages in the bridge structure and enable maintenance and repair works at the initial damage phase; and (3) evaluate the health condition of this structure shortly after a major catastrophic event such as an earthquake.

In this chapter, details of the monitoring system are presented, including sensor instrumentation, data acquisition, data synchronization and data transmission. In next Chapter, an automated system identification procedure will be developed and applied to identify the modal parameters of the Voigt Bridge, as a function of time, based on response measurements from this long-term monitoring system. Then the correlation between the identified natural frequencies and different measured environmental parameters will be studied.

6.2 Voigt Bridge Testbed

The Interstate-5 / Voigt Drive overcrossing, i.e., referred to as Voigt Bridge (Figure 6.1), is located on the eastern edge of the University of California at San Diego (UCSD) campus. This two-lane two-way bridge was built in 1964 to connect UCSD west and east campus facilities and carries traffic over Interstate-5. It is about 90 m in length, with two middle spans 29 m each and two side spans of 15 m and 16 m, respectively. This single-column bent, 4-span, reinforced concrete box girder structure has a skew angle of

approximately 32 degrees. Cap beams (lateral diaphragms), 1.8 m in thickness, are situated over each of the columns and provide additional stiffness to the girders. It is worth noting that the Voigt Bridge represents a construction style typical of a large number of highway overpasses in California.

It is envisioned that this densely instrumented bridge testbed will serve as a live laboratory for the development of vibration-based structural health monitoring technologies. This particular bridge is selected due to its proximity to the campus, an important consideration for convenient long-term maintenance and accessibility. Secure access to the bridge-deck cells is provided through manhole arrays. This access to the interior of the bridge makes it possible to place all of the sensors and data acquisition hardware inside the bridge girder structure, thereby providing security and protection from weather conditions. Figure 6.2 shows the cross section and plan view of the bridge and Figure 6.3 shows two interiors of the box cells through which the instruments are installed on the bridge. As an illustration, Figure 6.4 shows the access to interior of the north side of the bridge through a manhole.

6.3 Instrumentation Component of Long-Term Monitoring System

The long-term monitoring system developed on the Voigt Bridge includes thirty piezoelectric accelerometers, fifteen capacitive accelerometers, a video camera, twenty six thermocouples, nine thermistor & RH sensors, and a wind monitor.

6.3.1 Sensor Instrumentation for Bridge Vibration Monitoring

6.3.1.1 Piezoelectric Accelerometers

Thirty PCB model 393B04 piezoelectric accelerometers (http://www.pcb.com) are deployed along both sides of the bridge (i.e., the northern-most cell and next to the southern-most cell) to measure the vertical acceleration response of the bridge (Figure 6.5). This class

of accelerometers makes use of the piezoelectric effect discovered in 1880 by Pierre and Jacques Curie (http://www.encyclopedia.com, Fraser, 2006), whereby certain crystals exhibit electrical charges under mechanical loading. Piezoelectric accelerometers incorporate a crystal sensing element which has the property of emitting a charge when subjected to a force. As these are active electrical systems, the crystals produce an electrical output only when they experience a change in load, they cannot perform true static measurements. Typical piezoelectric accelerometers offer higher measurement and frequency ranges than force balance accelerometers at the expense of resolution and inability to measure down to 0 Hz (http://www.pcb.com). Lower costs are another advantage of piezoelectric accelerometers over force balance accelerometers. The piezoelectric accelerometers used here have a large measurement range: ± 5 g, a wide frequency range ($\pm 5\%$) from 0.06 to 450 Hz, and a highly accurate broadband resolution of $3\,\mu g$ RMS. Table 6.1 present the calibration coefficients of 30 accelerometers used in this system.

At each station, the accelerometer is attached with machine screws to an L-shaped aluminum bracket, cut to length with a threaded hole. The bracket is then glued to the stem wall using high-strength Epoxy. Figure 6.6 shows a picture of a piezoelectric accelerometer installed on the stem wall.

6.3.1.2 Capacitive Accelerometers

Fifteen PCB model 3801 accelerometers (http://www.pcb.com) are deployed along the north side of the bridge to measure the bridge's horizontal response (Figure 6.7). Capacitive accelerometers measure acceleration by monitoring a change in electrical capacitance. Within these sensors, the sensing element consists of two parallel plate capacitors acting in a differential mode. These capacitors operate in a bridge circuit, along with two fixed capacitors,

and alter the peak voltage generated by an oscillator when the structure undergoes acceleration (http://www.sensorland.com). The capacitive accelerometers typically operate in a low frequency range. Unlike piezoelectric accelerometers, these sensors can measure down to 0 Hz. The principal advantage of capacitive accelerometers is their low cost, making them attractive for dense sensor arrays. However, the resolution of these sensors is typically less than either force balance or piezoelectric accelerometers. In this system, these sensors primary purpose is seismic monitoring as traffic loads mainly induce vertical vibration of the bridge. The frequency range ($\pm 5\%$) of the employed PCB model 3801 accelerometer is from 0 to 80 Hz and the broadband resolution is $60\,\mu g$. Table 6.2 provides the calibration coefficients of these accelerometers.

At each station, the accelerometer is attached with hot glues to an L-shaped aluminum bracket that is used to attach the piezoelectric accelerometer to the stem wall. Figure 6.8 shows a picture of a capacitive accelerometer mounted on the stem wall.

6.3.1.3 Video Camera

A Sony XCD-X710CR digital color camera (http://bssc.sel.sony.com) is installed on a light post on the southwestern end of the bridge (Figure 6.9). Sony´s XCD-X710CR digital camera incorporates a progressive scan 1/3" CCD with square pixels and offers excellent sensitivity (1024 (H) x 768 (V) XGA. This digital camera satisfies the demand for high speed, color, progressive scan cameras and is ideally suited for (a) achieving 30 frames/sec in color; (b) high resolution of 1024 x 768; and (c) access to the raw pixel values allowing a user to perform their own color processing. The "CR" in its model number stands for "Color Raw". This “CR” model uses a CCD with a color mask (commonly called a "Bayer filter") and outputs the "raw color" pixel values in 8 or 10 bit to be converted later to a color image on a

computer (http://www.goelectronic.com).

In the monitoring system deployed in this study, this camera is positioned so as to monitor traffic crossing over the bridge, in order to correlate the bridge's measured dynamic response with the corresponding vehicles.

6.3.2 Sensor Instrumentation for Environmental Monitoring

6.3.2.1 Temperature and Humidity Sensors

Twenty four thermocouples are installed at eight stations along both south and north sides of the bridge superstructure (Figure 6.10). The thermocouple provides a simple and efficient means of measuring temperature. A thermocouple works because there is voltage drop across dissimilar metals placed in contact and subjected to a change in temperature. In principle, a thermocouple can be made from almost any two metals. In practice, several thermocouple types have become standard because of desirable qualities such as linearity of the voltage drop as a function of temperature and large voltage to temperature ratio (http://www.iotech.com). The four most common types are designated as J (Iron & Constantan), K (Chromel, Nickel - Chromium Alloy & Alumel, Nickel - Aluminium Alloy), T (Copper & Constantan) and E (Chromega & Constantan).

In this study, the Omega wire type K TT-K-24 is used to make the sensing point (or probe part) of the thermocouple. The type K is the most commonly used general purpose thermocouple and the temperature range is approximately between -200 ^{o}C and 1200 ^{o}C . Extension wire EXPP-K-20 and Connectors (pair) SMPW-K-MF are used to extend a thermocouple signal from a probe back to the conditioning module and A/D convector. From Figure 6.10, it can be seen that twenty four thermocouples are deployed at eight stations. At each section, two thermocouples are inserted into the top and bottom of the stem wall to

measure the concrete temperature. 6.35mm holes are drilled 80 mm deep into the concrete and then filled using silicone heat sink grease. A thermocouple is then inserted into the center of each of the holes. The heat sink grease serves as an electronic isolator to prevent the thermocouples from accidentally grounding out on any metal in the holes (i.e., rebar) and also functions as a thermal conductor to transfer heat from the concrete to the sensor. Finally, a silicone caulk is placed over the drilled hole to prevent water from seeping into the hole and to keep the heat sink grease from drying. A third thermocouple is attached at midheight to the exterior of the stem wall to measure air temperature inside the bridge. The deployment of thermocouples makes it possible to study the effects of temperature and its gradients (if needed) in longitudinal, transversal, and vertical directions on the bridge dynamic properties. Another two thermocouples (EXPP-K-20) are employed to measure the temperature of the air surrounding the bridge. One of them is used to measure the air temperature above the bridge (see Figure 6.11) and the other one is used to measure the air temperature underneath the bridge (see Figure 6.12).

Eight Precon HS-2000V (http://www.preconusa.com) thermistor & RH sensors are also installed at each midspan along both south and north sides of the bridge superstructure to measure the relative humidity and temperature of the air inside the bridge. The HS-2000V humidity sensor combines capacitive-polymer sensing technology with a novel measurement method, eliminating the need for temperature correction and calibration by the user (http://www.preconusa.com). The sensor, which was calibrated by the manufacturer prior to shipment, includes a thermistor and circuitry to correct for temperature and calculate the true relative humidity. The sensor provides both humidity and temperature outputs and is accurate to $\pm 2\%$. The output of the HS-200V is ratiometric, with output voltage varying from zero to the supply voltage as the measured parameter varies from zero to full-scale. Figure 6.13 shows

a picture of a Precon HS-2000V thermistor & RH sensor and thermocouples installed along the stem wall at a typical station.

6.3.2.2 Weather Monitoring Station

In order to measure the wind characteristics, a model 05103V wind monitor from R. M. Young Company (http://www.youngusa.com) is installed to measure both wind speed and wind direction. The wind speed sensor is a four blade helicoid propeller. Propeller rotation produces an AC voltage with frequency directly proportional to wind speed. The wind direction sensor is a rugged yet lightweight vane with a sufficiently low aspect ratio to assure good fidelity in fluctuating wind conditions (http://www.youngusa.com). Vane angle is sensed by a precision potentiometer housed in a sealed chamber. With a known excitation voltage applied to the potentiometer, the output voltage is directly proportional to the vane angle. A mounting orientation ring assures correct realignment of the wind direction reference when the instrument is removed for maintenance. The instrument is made of UV stabilized plastic with stainless steel and anodized aluminum fittings. Transient protection and cable terminations are in a convenient junction box. The model 05103V used in this study offers calibrated 0-5 VDC outputs, which is convenient for data collection. The operational temperature for this model is between -50 ^{o}C to 50 ^{o}C. The output range of this mode is 0-100 m/s for wind speed and 360^{o} (mechanical) for Azimuth. The model is mounted at the top of the light post on which the camera is mounted (Figure 6.14).

In order to measure the temperature and relative humidity of the air outside the bridge, another Precon HS-2000V thermistor & RH sensor is installed together with the wind monitor (Figure 6.14) at the top of the light post. Within this study, this station is referred to as a weather monitoring station since the air temperature, relative humidity and wind

characteristics can be measured from instruments installed at this station. In order to protect the thermistor & RH sensor from error-producing solar radiation and precipitation, a multi-plate radiation shield is used (see Figure 6.14). The multiple plates have a unique profile that blocks direct and reflected solar radiation, yet permits easy passage of air. Enlarged top plate and steep edge profile minimize moisture accumulation from precipitation and dew. The plate material is especially formulated for high reflectivity, low thermal conductivity, and maximum weather resistance (http://www.youngusa.com).

6.4 Data Acquisition System

Data from all the sensors are collected on the bridge, using a local data acquisition system, housed within the northwest corner of the bridge. The current data acquisition system (Figure 6.15) is built around a National Instruments (NI) PXI/SCXI combination chassis with an embedded PXI-8186 real-time controller (http://ni.com).

Four NI PXI-4472B boards (http://ni.com) are being used for acquiring signals from thirty piezoelectric accelerometers. Each PXI-4472B board has eight analog inputs with 24-bit resolution delta-sigma modulating analog-to-digital converters (ADCs) that are simultaneously sampled at a programmable rate from 0 to 45 kHz (http://ni.com). In addition to acquiring data, the PXI-4472B incorporates for each channel integrated electronic piezoelectric (IEPE) signal conditioning and anti-aliasing filters. The analog inputs have both analog and real-time digital filters implemented in the hardware to prevent aliasing.

In order to acquire the temperature using thermocouples, a SCXI-1303, 32-channel isothermal terminal block (a shielded device with screw terminals) is used to connect thermocouples and signals to SCXI-1102 modules (http://ni.com). The SCXI-1303 has a high-accuracy thermistor cold-junction temperature sensor, and an isothermal copper plane to

minimize the temperature gradients across the screw terminals when taking measurements with thermocouples. The SCXI-1102 module is used for signal conditioning of the thermocouples, which has a two-pole low-pass filter with a 2 Hz cutoff frequency to reject 60 Hz noise.

A NI PXI-6031E (16-bit A/D, 32 differential inputs, 100 kS/s maximum multiplexed sampling rate) board is currently being used for acquiring signals from the capacitive accelerometers, thermistor & RH sensors, and the wind monitor. A SCB-100 is used to connect all these sensors and signals to the PXI-6031E board. The SCB-100 is a shielded I/O connector block for interfacing I/O signals to plug-in DAQ devices with 100-pin connectors. Combined with the shielded cables, the SCB-100 provides rugged, very low-noise signal termination.

6.5 Data Acquisition and Synchronization

For this monitoring system, a data acquisition program is developed using NI LabVIEW program to sample the analog signals from the accelerometers and environmental sensors at a rate of 1000 Hz. Once digitized, the signals are placed into a ring buffer. After a predetermined number of samples are collected in the buffer, the data is written to disk as a text file in ASCII format and the buffer is cleared (Fraser, 2006). The concrete temperature, the temperature and relative humidity of the air (both inside and outside the bridge) are collected during the first two minutes of each hour. Then during the following five minutes, the acceleration responses of the bridge and wind characteristics are collected.

Synchronization of the data from all of the sensors is accomplished through the National instruments PXI hardware. PXI modular instrumentation makes use of the technology advancements of the mainstream PC industry and by using the standard PCI bus,

PXI modular instrumentation systems can benefit from widely available software and hardware components (http://zone.ni.com/devzone/cda/tut/p/id/4811). Further PXI provides advanced timing and triggering capabilities allowing for the synchronized acquisition of data from all of the sensors through the various A/D boards.

6.6 Image Acquisition and Synchronization

As aforementioned, a Sony XCD-X710CR digital color camera is positioned to monitor traffic crossing over the bridge. Using LabVIEW (http://ni.com), images are acquired from the camera at a programmable sampling rate, and time stamped using the system clock on the data / image acquisition computer. By building the image acquisition directly into the data acquisition program, highly accurate synchronization between the dynamic sensors and the camera is achieved.

The firewire output from the Sony camera is connected to the data acquisition computer through an IEEE 1394 interface board. A “while loop” is embedded within the LabVIEW data acquisition code which configures the camera (image resolution and size), controls the acquisition sampling rate, decodes the acquired Bayer image, and saves the picture in a compressed color jpeg format. In its current state, the camera and image acquisition code are configured to sample and archive 640x480 pixel color images at 3 frames / second (FPS). Within LabVIEW, a compression ratio of 70% is utilized. While higher sampling rates and image sizes with no compression are feasible, these are deemed unnecessary in accurately identifying and tracking traffic on the bridge. As an illustration, Figure 6.16 shows the streaming images measured from the camera, which can be used to monitor the traffic flow crossing the bridge.

6.7 Internet Connectivity and Data Transmission

For controlling the data acquisition system and streaming data from the bridge, a wireless cloud is created to access the wired UCSD Internet network located in a nearby UCSD building (Figure 6.17). A high bandwidth Internet connection is established on the bridge by installing a wireless router on the southeast corner of this building (approximately 60 meters from the bridge). Using a wireless Ethernet bridge with an external antenna mounted on the bridge guard rail (Figure 6.17), this wireless cloud is converted to a standard wired Internet connection and connected to the data acquisition system through an Ethernet cable.

Remote access to the data acquisition computer is provided using Windows Remote Desktop Connection. Through the Windows Remote Desktop Connection, changes can be made to the data acquisition parameters (e.g., sample rates, sensor calibration constants, buffer size, etc.) and the measured data are transferred to archiving server located on the campus network. Figure 6.18 shows data streaming path from the bridge to the archiving server located inside the SERF building on UCSD campus. On-going work is underway for the development of an automated java-based data transmission program, capable of compressing the data files and streaming the zipped data using File Transfer Protocols (FTP) to an archiving server located on the campus network.

6.8 Summary

A state-of-the-art long-term continuous monitoring system has been developed and deployed on the Voigt Bridge. In this chapter, details of this structural monitoring system are described, including sensor instrumentation, data acquisition system, data synchronization and transmission. The monitoring system consists of video camera, thirty piezoelectric

accelerometers (in the bridge vertical direction), and fifteen capacitive accelerometers (in the bridge lateral direction) for bridge vibration monitoring. The primary purpose of the fifteen capacitive accelerometers is seismic monitoring, while the piezoelectric accelerometers measure the traffic induced mainly vertical vibrations of the bridge. Twenty six thermocouples, nine thermistor & relative humidity sensors, and a wind monitor are also employed to measure concrete temperature, temperature and relative humidity of the air (both inside and outside the bridge), and wind characteristics. This monitoring system makes it possible to: (1) study the effects of varying environmental conditions such as temperature, wind characteristics, and humidity on the identified modal properties of the bridge; (2) allow for the early identification of possible damages in the bridge structure and enable maintenance and repair works at the initial damage phase; and (3) evaluate the health condition of this structure shortly after a major catastrophic event such as an earthquake.

It is envisioned that this densely instrumented bridge testbed will serve as a live laboratory for the development of vibration-based structural health monitoring technologies.

6.9 Acknowledgements

This chapter is an extended version of the manuscript published in the proceedings of the International Conference on Experimental Vibration Analysis for Civil Engineering Structures (2007) under the title “Structural monitoring of the I-5 / Voigt Drive Bridge, San Diego County, California” with authors Michael Fraser, Xianfei He, Ahmed Elgamal, and Joel P. Conte. The dissertation author is the primary investigator of this paper.

6.10 References

Abdel Wahab, M. and De Roeck, G. (1997). “Effect of temperature on dynamic system parameters of a highway bridge.” *Structural Engineering International*, 7(4), 266-270.

Cornwell, P., Farrar, C.R., Doebling, S.W. and SOhn, H. (1999). “Environmental variability of modal properties.” *Experimental Techniques*, 23(6), 45-48.

Fraser, M. (2006). “Development and implementation of an integrated framework for structural health monitoring.” *PhD Dissertation*, Department of Structural Engineering, University of California, San Diego, La Jolla, CA.

He, X., Fraser, M., Conte J.P. and Elgamal, A. (2007). “Investigation of environmental effects on identified modal parameters of the Voigt Bridge.” *Proceedings of 18th Engineering Mechanics Division Conference of the ASCE*, Blacksburg, VA.

Peeters, B. and De Roeck, G. (2001). “One-year monitoring of the Z24-Bridge: environmental effects versus damage events.” *Earthquake Engineering and Structural Dynamics*, 30(2), 149-171.

Table Captions

Table 6.1 Calibration coefficients of the piezoelectric accelerometers

Channel No.	Serial No.	Calibration Coefficient [mV/g]	Channel No.	Serial No.	Calibration Coefficient [mV/g]
1	21641	1001	16	21622	1015
2	21621	1023	17	21730	1017
3	21745	1010	18	21733	1027
4	21620	1006	19	21729	1015
5	21743	1062	20	21851	1024
6	21742	997	21	21853	1014
7	21746	1005	22	21854	1032
8	21855	1028	23	21857	998
9	21613	994	24	21616	1056
10	21615	1007	25	21619	1024
11	21744	1013	26	21852	1005
12	21747	1017	27	21856	1006
13	21748	971	28	21617	996
14	21618	1005	29	21749	1010
15	21741	1024	30	21750	1026

Table 6.2 Calibration coefficients of the capacitive accelerometers

Channel No.	Serial No.	Calibration Coefficient [mV/g]
1	209	1001
2	214	1001
3	205	1000
4	216	1003
5	206	1003
6	210	1003
7	218	1000
8	207	998
9	217	984
10	211	1009
11	204	1006
12	208	998
13	215	1005
14	213	1006
15	203	1002

Figure Captions

Figure 6.1. Picture of Voigt Bridge (Photo on the bottom is from http://maps.google.com)

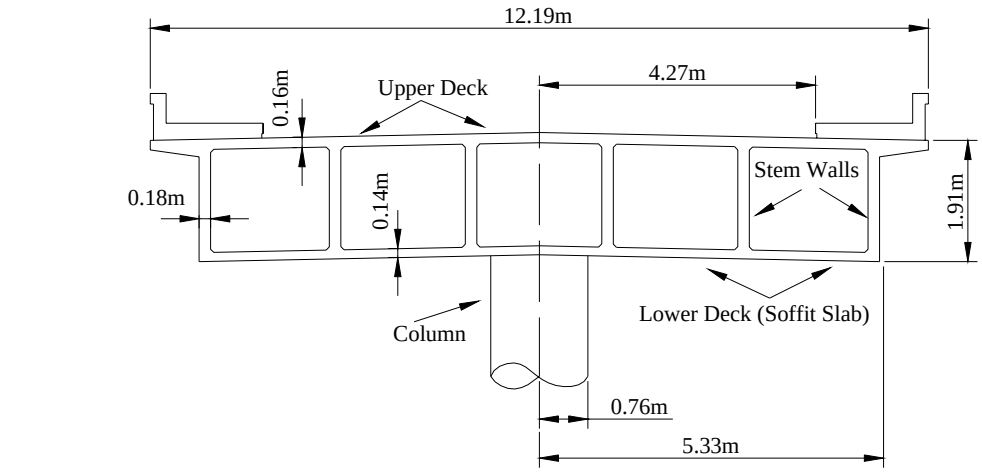

(a)

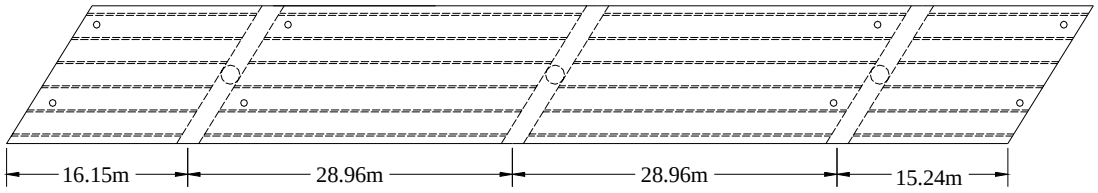

(b)

Figure 6.2. (a) Cross section of Voigt Bridge; (b) Plan view of Voigt Bridge

(a)

(b)

Figure 6.3. (a) Interior of the northern-most cell, and (b) Interior of next to the southern-most cell

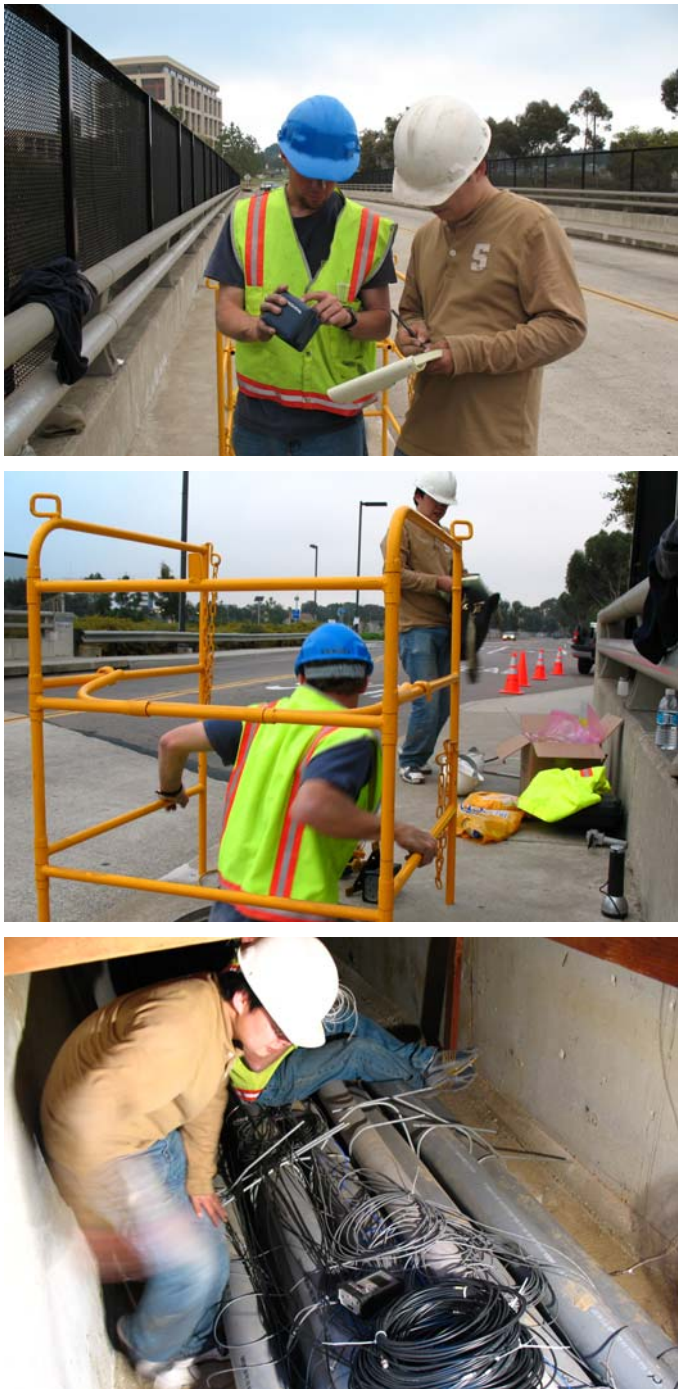

Figure 6.4. Access to the interior of the bridge box-girder through a manhole

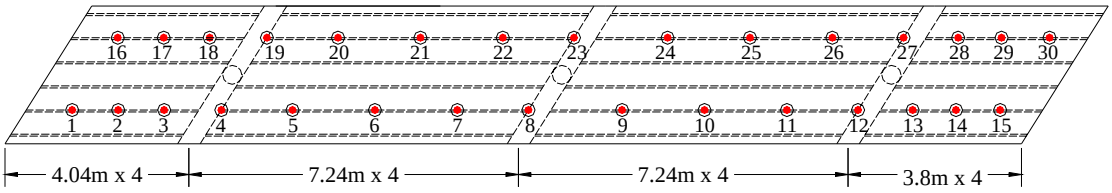

Figure 6.5. Deployment of piezoelectric accelerometers shown on plan view of bridge superstructure

Figure 6.6. Picture of a piezoelectric accelerometer installed on the stem wall

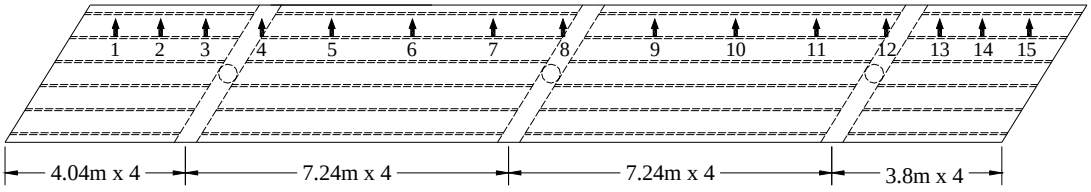

Figure 6.7. Deployment of capacitive accelerometers shown on plan view of bridge superstructure

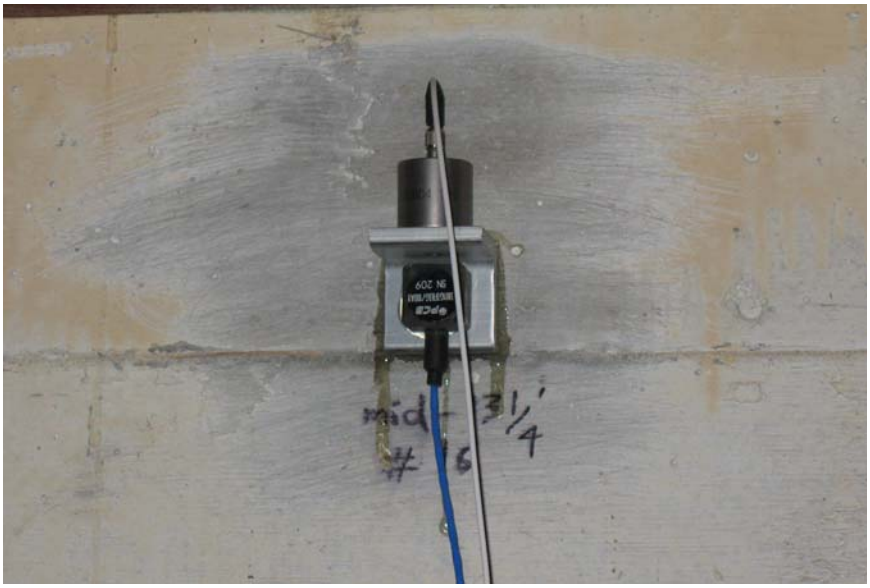

Figure 6.8. Picture of a capacitive accelerometer installed on the stem wall

Figure 6.9. Sony XCD-X710CR digital color camera installed in the monitoring system

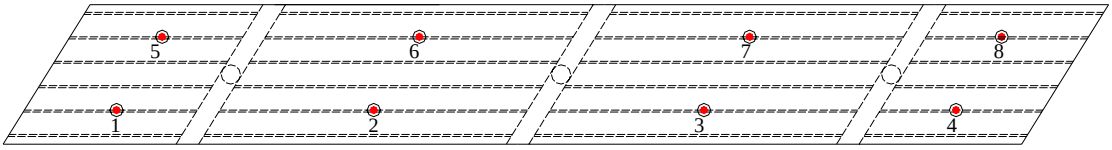

(a) Locations of thermocouples along the bridge deck

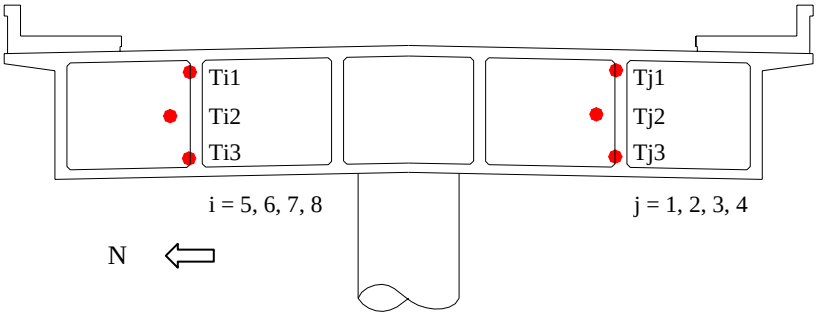

(b) Locations of thermocouples along the stem walls

Figure 6.10. Deployment of thermocouples inside the bridge

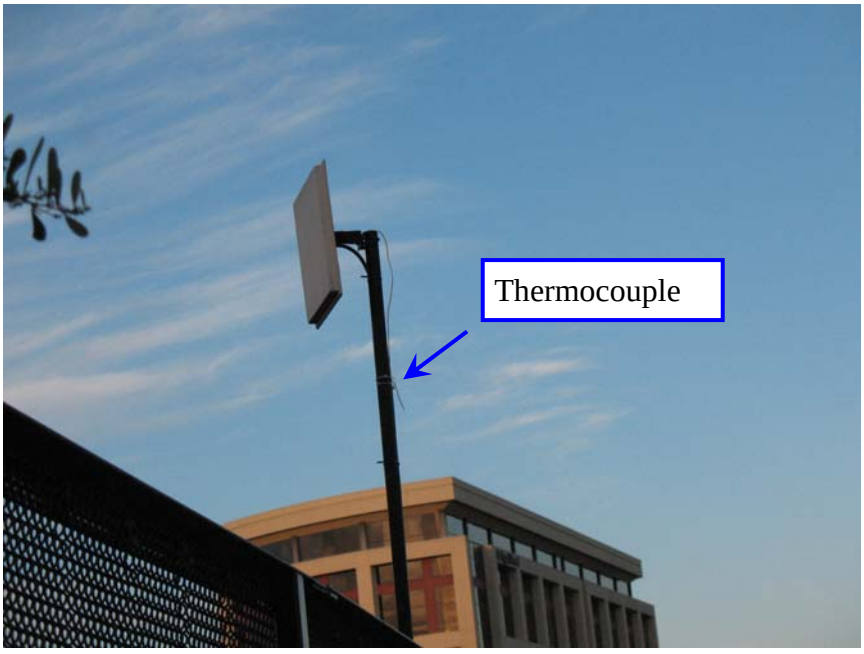

Figure 6.11. Thermocouple used to measure the air temperature above the bridge

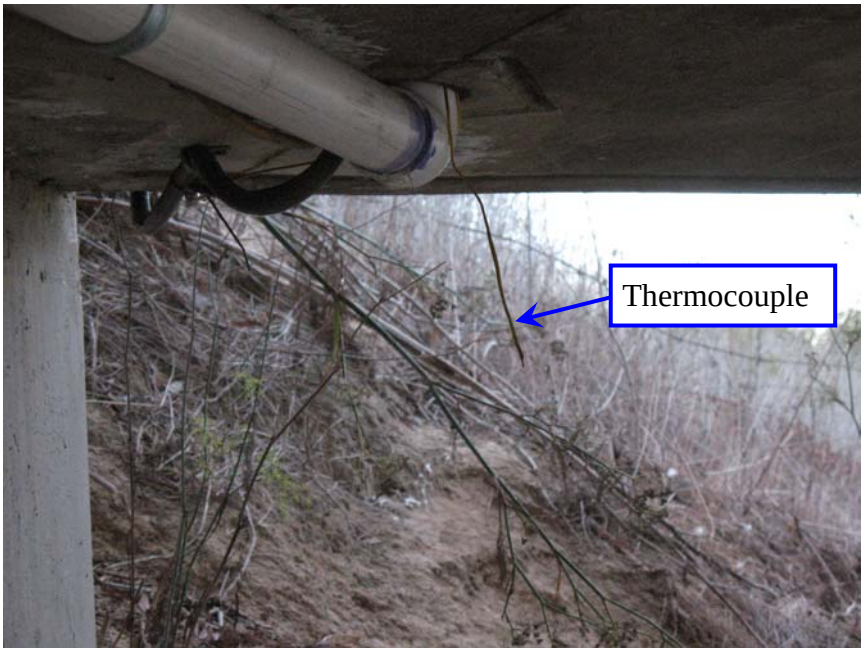

Figure 6.12. Thermocouple used to measure the air temperature underneath the bridge

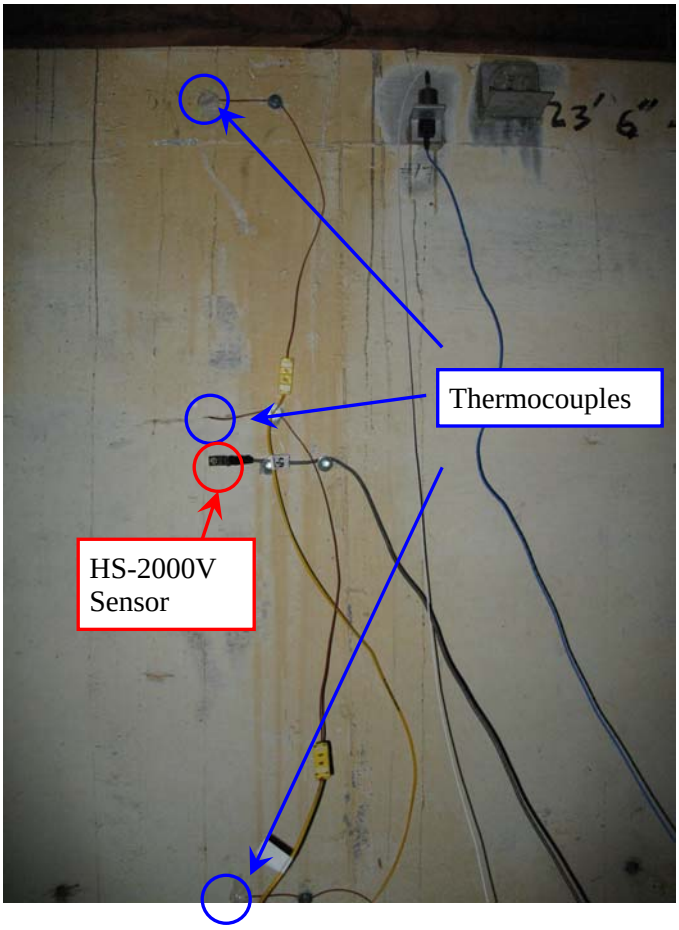

Figure 6.13. HS-2000V sensor and thermocouples installed along the stem wall at a typical station

Figure 6.14. Weather monitoring station

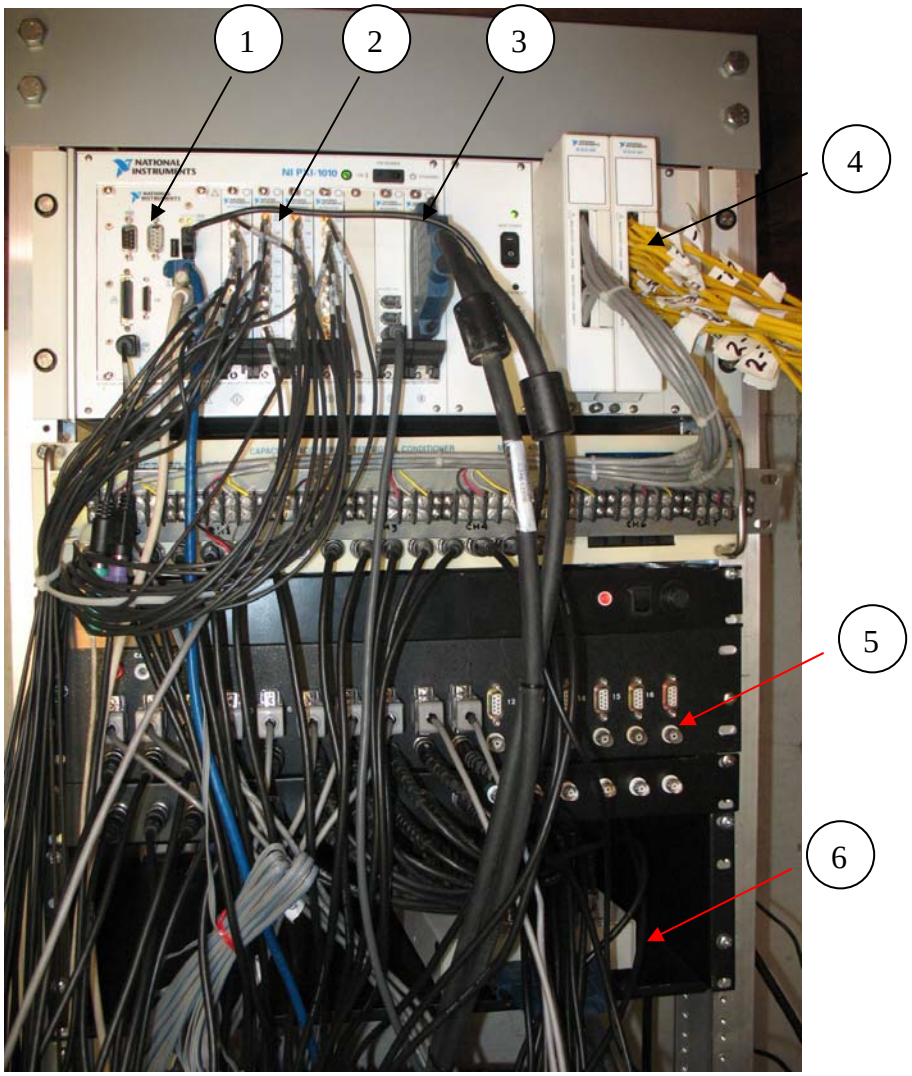

Figure 6.15. Data acquisition system: 1. PXI/SCXI combination chassis, 2. PXI 4472B DAQ boards, 3. PXI-6031E DAQ board, 4. SCXI-1303 terminal block, 5. DC power supplies for thermistor & relative humidity sensors and wind monitor, 6. SCB-100 connector block

Figure 6.16. Traffic flow crossing over the bridge

Figure 6.17. Locations of antennas deployed in the monitoring system (Original photo is from http://maps.google.com)

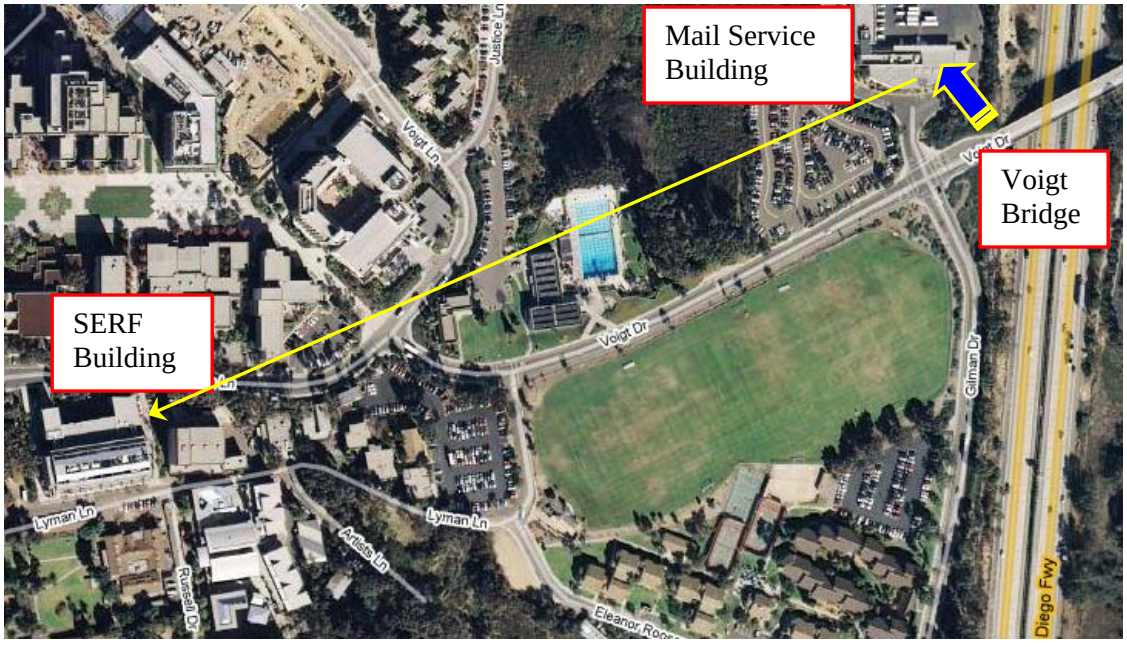

Figure 6.18. Data streaming path from Voigt Bridge to SERF Building (Original photo is from http://maps.google.com)

Chapter 7

Environmental Effects on Identified Modal Parameters of Voigt Bridge Testbed

7.1 Introduction

Variations in modal properties due to changes in environmental conditions have been shown to be very significant in previous studies; they may even induce changes larger than those caused by structural damage (e.g., Abdel Wahab and De Roeck 1997, Cornwell et al. 1999, Peeters and De Roeck 2001, He et al. 2007).

Abdel Wahab and De Roeck (1997) investigated the effect of temperature variation on modal parameters of a pre-stressed concrete highway bridge by performing two sets of dynamic tests at different times. It was observed that a decrease in temperature from 15 ˚C to 0 ˚C caused some natural frequencies to increase by about 4-5%. Cornwell et al. (1999) studied the variability of modal frequencies of the Alamosa Canyon Bridge caused by varying temperature conditions. In their studies, two sets of vibration tests were performed in August 1996 and July 1997, respectively. In each of them, the tests were performed every two hours over a 24-hour time period. It was shown that the measured frequency of the first mode varied by approximately 5% during the first 24-hour period. The frequencies of the first, second and third modes varied by 4.7%, 6.6%, and 5.0%, respectively, over the second 24-hour period.

Peeters and De Roeck (2001a) reported their studies about the effects of environmental conditions on modal frequencies of Z24-Bridge through nearly one-year continuous monitoring of this four-span classical post-tensioned concrete box girder bridge. It

was found that natural frequencies of the first four vibration modes changed by 14-18% during the monitoring period. A bilinear behavior was observed between temperature and frequency with the knee situated around $0^{\circ}C$. The frequencies of all the modes presented, except the second mode, decreased with the temperature increase. As for the second mode, its frequency increased with increasing temperature when the temperature was above $0^{\circ}C$. The reason for the bilinear behavior between temperature and frequency was the asphalt layer (wearing surface), which contributed significantly to the stiffness of the structure during the cold period. However, during the warm period, the asphalt did not play any role in the structural stiffness. Finally, black-box models were built in their studies to describe the identified natural frequencies as a function of environmental temperature.

More recently, studying environmental effects on structural modal properties has received more attention in the structural health monitoring research community (e.g., Ni et al., 2005; Xia et al., 2006; He et al., 2007). The study presented in this Chapter is based on the state-of-the-art long-term continuous monitoring system deployed on the Voigt Bridge, which is described in detail in Chapter 6. In this state-of-the-art monitoring system, thirty piezoelectric accelerometers and a video camera are deployed for traffic induced vibration monitoring and fifteen capacitive accelerometers are installed for seismic monitoring. In addition, twenty four thermocouples, and eight thermistor & relative humidity (RH) sensors are installed inside the bridge to measure the concrete temperature and temperature / relative humidity of the air inside the bridge box girder. A wind monitor, a thermistor & RH sensor, and two thermocouples are employed to measure the wind characteristics, temperature and relative humidity of the air outside the bridge.

In this chapter, the acceleration response of the bridge collected over a period of 50 days (from August to September, 2007) are used to identify the modal parameters of the Voigt

Bridge as a function of time. An automated system identification procedure is developed based on the data-driven stochastic subspace identification method (Van Overschee and De Moor, 1996). Various environmental parameters (e.g., temperature, humidity, wind characteristics) measured during this period are investigated. Finally, based on the research work performed by Peeters and De Roeck (2001a), black-box models are constructed to correlate the identified time-varying natural frequencies with the measured environmental parameters. An objective criterion for damage detection under varying environmental conditions is also provided based on the estimated black-box models.

7.2 Automated System Identification of the Voigt Bridge

7.2.1 Automated System Identification Procedure

As described in Chapter 6, the Voigt Bridge is located on the eastern edge of the University of California at San Diego (UCSD) campus. This two-lane two-way bridge was built in 1964 to connect UCSD west and east campus facilities and carries traffic over Interstate-5. It is about 90 m in length, with two middle spans 29 m each and two side spans of 15 m and 16 m, respectively. This single-column bent, 4-span, reinforced concrete box girder structure has a skew angle of approximately 32 degrees. The Voigt Bridge represents a construction style typical of a large number of highway overpasses in California.

Since only the response of the bridge is measured (i.e., un-measured input) from the long-term monitoring system during the monitoring period, the system identification procedure developed herein is based on output-only measurements. The data-driven stochastic subspace identification (SSI-DATA) method is applied to extract the modal properties of the bridge (Van Overschee and De Moor, 1996; Peeters and De Roeck, 2001b). The SSI-DATA algorithm extracts a system model in state-space using output-only measurement data directly.

Compared to two-stage time-domain system identification methods such as covariance-driven stochastic subspace identification (SSI-COV) (Van Overschee and De Moor, 1996) and the natural excitation technique (NExT) (James et al., 1993) combined with the eigensystem realization algorithm (ERA) (Juang and Pappa, 1985), SSI-DATA does not require any pre-processing of the data to calculate auto / cross-correlation functions or auto / cross-spectra of output data. In addition, robust numerical techniques such as QR factorization, singular value decomposition (SVD) and least squares are involved in this method. A brief review of this method is presented below.

The discrete-time state-space representation of a finite dimensional, linear time invariant system of order *n* is given by

$$\begin{aligned} \mathbf{z}(k+1) &= \mathbf{A}\mathbf{z}(k) + \mathbf{B}\mathbf{u}(k) \\ \mathbf{x}(k) &= \mathbf{C}\mathbf{z}(k) + \mathbf{D}\mathbf{u}(k) \end{aligned} \tag{7.1}$$

where $\mathbf{A} \in \mathbb{R}^{n \times n}$, $\mathbf{B} \in \mathbb{R}^{n \times l}$, $\mathbf{C} \in \mathbb{R}^{m \times n}$, $\mathbf{D} \in \mathbb{R}^{m \times l}$ = state space matrices in discrete form; $\mathbf{z}(k) \in \mathbb{R}^{n}$ = state vector; $\mathbf{u}(k) \in \mathbb{R}^{l}$ = load vector (vector of loading functions); and $\mathbf{x}(k) \in \mathbb{R}^{m} = \begin{bmatrix} x_1(k) & x_2(k) & \cdots & x_m(k) \end{bmatrix}^T$, a column vector of size *m* (= number of measured / output channels) which represents the system response at discrete time $t = k(\Delta t)$ along the m measured degrees of freedom (DOFs).

In practice, the input function $\mathbf{u}$ is often unknown / unmeasured and only the response of the structure is measured. Thus, the discrete-time state-space model in equation (7.1) can be extended to the following stochastic version:

$$\begin{aligned} \mathbf{z}(k+1) &= \mathbf{A}\mathbf{z}(k) + \mathbf{w}(k) \\ \mathbf{x}(k) &= \mathbf{C}\mathbf{z}(k) + \mathbf{v}(k) \end{aligned} \tag{7.2}$$

where state-space matrices **A** and **C** are the same as in equation (7.1): **A** = state transition matrix, which completely characterizes the dynamics of the system through its eigenproperties, and **C** = output matrix that specifies how the inner states are transformed into the measured system response / output; $\mathbf{w}(k) \in \mathbb{R}^n$ = process noise due to external disturbances and modeling inaccuracies (i.e, missing high-frequency dynamics) and unknown input excitation (undistinguishable from the external disturbances); and $\mathbf{v}(k) \in \mathbb{R}^m$ = measurement noise due to sensor inaccuracies and also unknown input excitation (feed-through term). Both noise terms $\mathbf{w}(k)$ and $\mathbf{v}(k)$ are assumed to be zero-mean, white vector sequences with the following covariance matrix:

$$E\left[\begin{pmatrix}\mathbf{w}(i)\\ \mathbf{v}(i)\end{pmatrix}\begin{pmatrix}\mathbf{w}(j)^T & \mathbf{v}(j)^T\end{pmatrix}\right]=\begin{bmatrix}\mathbf{Q} & \mathbf{S}\\ \mathbf{S}^T & \mathbf{R}\end{bmatrix}\delta_{ij} \tag{7.3}$$

where E[…] is the mathematical expectation operator; δ_{ij} = Kronecker delta; and **Q, R, S** = process and measurement noise auto / cross-covariance matrices.

The SSI-DATA procedure of extracting the state-space matrices **A** and **C** from output-only data can be summarized as follows: (1) Form an output Hankel matrix and partition it into “past” and “future” output sub-matrices. (2) Calculate the orthogonal projection matrix of the row space of the “future” output sub-matrix into the row space of the “past” output sub-matrix using QR factorization. (3) Obtain the system observability matrix and Kalman filter state estimate via SVD of the projection matrix. (4) Using the available Kalman filter state estimate, extract the discrete-time system state-space matrices as a least squares solution. Once the system state-space matrices are determined, the modal parameters (natural frequencies and damping ratios) of the $N = n/2$ vibration modes can be obtained as

$$\omega_i = \left|\ln(\lambda_{2i})/\Delta t\right|$$

$$\xi_i = -\cos(angle(\ln(\lambda_{2i}))) \tag{7.4}$$

$$i = 1,\ 2,\ \ldots,\ N$$

where $\lambda_i = i^{th}$ eigenvalue of matrix **A** and Δt = sampling time. It should be noted that λ_{2i-1} and λ_{2i} (i = 1, 2, …, N) are complex conjugate pairs, each pair corresponding to a vibration mode (i.e., the natural frequency and damping ratio obtained from λ_{2i-1} are the same as those obtained from λ_{2i}). The vibration mode shapes are obtained as

$$\phi_i = \mathbf{C} \cdot \mathbf{T}_{2i-1} \tag{7.5}$$

where $\mathbf{T}_i$ denotes the i^{th} eigenvector of matrix **A**. Similarly, $\mathbf{T}_{2i-1}$ and $\mathbf{T}_{2i}$ (i = 1, 2, …, N) are complex conjugate pairs of eigenvectors, each pair corresponding to a vibration mode.

An automated modal analysis procedure has been developed to apply SSI-DATA for continuous health monitoring of the Voigt Bridge. In this implementation of SSI-DATA, first a stabilization diagram is constructed for system order $n = 2, 4, \cdots, 60$ [see equation (7.1) or equation (7.2)]. An example of stabilization diagram is given in Figure 7.1. For a realized state-space model of a given order *n*, an identified mode is considered as a physical vibration mode of the bridge if its identified modal parameters satisfy each of the following four conditions: (1) The deviation of its natural frequency from the average value of the corresponding frequencies obtained from models of order less than *n* is less than 1%. (2) The modal assurance criterion (MAC) value (Allemang and Brown, 1982) between the mode shape and the average of the corresponding mode shapes identified from models of order less than *n* is higher than 95%. (3) Its identified damping ratio is nonnegative and less than 20%. The relative change of damping ratio with respect to the average value of the corresponding damping ratios obtained from models of order less than *n* is not considered herein due to the

relatively high estimation uncertainty characterizing damping ratios. (4) Increasing progressively the model order n (starting from $n = 2$), the identified modal parameters corresponding to this mode satisfy the first three conditions defined above at least 10 times. The system order is then determined by the minimum order which contains all the physical modes identified using criteria 1 through 4. Finally, the bridge modal parameters are extracted from the realized state space model with the determined minimum order.

7.2.2 Automated System Identification Results

In this study, the acceleration data collected over a period of 50 days (from August to September, 2007) is used in the identification process. It should be noted that the accelerometers measuring the vertical response at stations 4, 5, 14, and 15 are not functioning properly (at periods of time). Thus acceleration response measured form these stations are not used in the automated system identification. Typical acceleration data in time and frequency domain are shown in Figure 7.2 and Figure 7.3, respectively. The measured bridge acceleration responses are sampled at the rate of 1000 samples-per-second resulting in a Nyquist frequency of 500 Hz, which is much higher than the bridge's natural frequencies of interest (< 20 Hz in this study). In the aforementioned implementation of SSI-DATA at each time period, the measured data are first filtered by a band-pass finite impulse response (FIR) filter of order 1024 with lower and upper cut-off frequencies of 2 Hz and 25 Hz, respectively. The filtered data is down-sampled to 100 Hz in order to improve the computational efficiency. After re-sampling, the Nyquist frequency (50 Hz) is still higher than the natural frequencies of interest (< 20 Hz). The down-sampled filtered data is then used to form the output Hankel matrix composed of 100 block rows with 23 rows in each block (23 vertical channels) for identifying the modal parameters of the bridge. Acceleration measured from stations 16, 17

and 18 are not used either in order to improve the system identification results for the monitoring period considered in this study.

The natural frequencies of three identified vibration modes of the Voigt Bridge are plotted as a function of time in Figure 7.4. The monitoring system was not operating at the beginning of September so the response measurement is not available during this short period. A 3D representation of the normalized identified mode shape for each of these three vibration modes is given in Figure 7.5 obtained using traditional SSI-DATA based on acceleration response measurements from all 30 channels. It is worth noting that different physical vibration modes are identified at different time periods due to varying excitation sources and environmental conditions. Table 7.1 summarizes the natural frequency identification results obtained from the automated system identification procedure. For each identified mode, the frequency change is defined as $\Delta f = (f_{\max} - f_{\min}) / f_{\min}$. It is seen that the relative changes in the bridge identified natural frequencies are on the order of 10-15% for the three modes considered. These changes are primarily caused by the varying environmental conditions since the bridge did not undergo any change in damage / deterioration during the monitoring period. From Figure 7.4, some temporal variation patterns of the identified natural frequencies of these modes are observed.

The identified damping ratios of these three vibration modes of the Voigt Bridge are plotted as a function of time in Figure 7.6. No clear temporal variation patterns of the identified damping ratios are observed, and the damping ratios identified during the monitoring period are consistent (considering the relatively high estimation uncertainty in characterizing damping ratios). The average damping ratios for these three modes are respectively 1.3%, 2.2% and 1.6%. In order to illustrate the identified mode shapes as a function of time, the identified mode shapes along the south side of the bridge are plotted in

Figure 7.7, Figure 7.8, and Figure 7.9, for the first, second, and third vibration mode, respectively. Generally speaking, no clear patterns in the temporal variation of these mode shapes are observed.

7.3 Measurement of Environmental Parameters

7.3.1 Temperature Measurements

Two thermocouples (EXPP-K-20) are employed to measure the air temperature surrounding the bridge. One of them is used to measure the air temperature above the bridge and the other to measure air temperature underneath the bridge (see Chapter 6). Figure 7.10 shows the temperature of the air surrounding the bridge measured using these two thermocouples during the period of 50 days. Figure 7.11 shows the temperature measured during the period of August 7 through August 14 in order to illustrate the typical temporal variation patterns of the temperature measurements. It should be noted that the temperature shown in these figures at each hour is the averaged temperature based on 2 minutes of recorded data. From these figures, it is observed that: (1) the temperature of the air surrounding the bridge reaches its maximum in the early afternoon every day; (2) the temperature of the air above the bridge is generally higher than its counterpart underneath the bridge during the daytime while the air temperature underneath the bridge is higher than its counterpart above the bridge during the night. This is due to the fact that the thermocouple used to measure the air temperature above the bridge is exposed to direct sunlight and the thermocouple used to measure the air temperature underneath the bridge is installed under the shadow and very close to the ground.

In order to measure the concrete temperature and the air temperature inside the bridge, twenty four thermocouples are installed at eight stations along both south and north sides of

the bridge superstructure (see chapter 6). At each section, two thermocouples are inserted into the top and bottom of the stem wall to measure the concrete temperature and the third thermocouple is attached at mid-height to the exterior of the stem wall to measure the air temperature inside the bridge. Figure 7.12 and Figure 7.13 show the air and concrete temperatures measured inside the bridge along south and north sides of the bridge, respectively. In order to illustrate the typical temporal variation patterns of the measured temperatures, Figure 7.14 depicts the temperature measured along the north side of the bridge during the period of August 7 through August 14. Based on these figures, it is found that: (1) the temperature measurements inside the bridge are much smoother than the temperature measurements outside the bridge; (2) at each station, the concrete temperatures measured at the top and bottom of the stem wall, typically lags behind the air temperature by approximately 2-3 hours; (3) the temperature measured during night is higher than that measured during the day time; (4) the concrete temperature and the air temperature inside the bridge typically lag several hours behind the air temperature outside the bridge.

Besides these thermocouples, nine thermistor & RH sensors (HS-2000V) are also installed to measure the air temperature both inside and outside the bridge. Eight of them are installed at each midspan along both south and north sides of the bridge superstructure to measure the air temperature inside the bridge. Another one is installed together with the wind monitor at the weather monitoring station. Figure 7.15 shows the air temperature measured at the weather monitoring station during the monitoring period. Figure 7.16 shows the air temperature measured during the period of August 7 through August 14 so as to investigate the typical variation patterns of the temperature measurements. The variation patterns of the air temperature measured at the weather monitoring station are similar to those of the air temperature surrounding the bridge (see Figure 7.10 and Figure 7.11). It should be noted that

the air temperature measured at the weather monitoring station is different from the air temperature surrounding the bridge because the thermistor installed at the weather monitoring station is protected by a multi-plate radiation shield. The multiple plates have a unique profile that blocks direct and reflected solar radiation, yet permits easy passage of air (see Chapter 6). For the sake of brevity, the air temperature measurements inside the bridge using thermistor & RH sensors are not shown here; however, the data measured by these sensors are consistent with those obtained from the thermocouples.

7.3.2. Wind Characteristics and Air Humidity Measurements

In the state-of-the art monitoring system developed and implemented in this study, a model 05103V wind monitor from R. M. Young Company is used to measure wind speed and wind direction. The measured data is first filtered by a low-pass FIR filter of order 1024 with cut-off frequency of 100 Hz. Then the averaged wind speed and wind direction over a period of 5 minutes are obtained at each hour. Figure 7.17 and Figure 7.18 present the wind speed and direction, respectively, measured at the weather monitoring station during the monitoring period. Figure 7.19 shows the wind speed measured during the period of August 7 through August 14 so as to investigate the typical variation patterns of the wind speed. It is observed that: (1) the wind speed measured during day time is usually higher than that measured during night; and (2) the wind speed reaches the maximum in the early afternoon every day.

The air humidity both inside and outside bridge is also measured using the installed nine thermistor & RH sensors mentioned earlier. The measured data is first filtered by a low-pass FIR filter of order 1024 with cut-off frequency of 10 Hz. Then the averaged relative humidity over 2-minute measurements is obtained for each hour. Figure 7.20 and Figure 7.21 present the air relative humidity measured inside the bridge along south and north sides of the

bridge, respectively. Figure 7.22 shows the relative humidity of the air measured at the weather monitoring station. Variation patterns of the air humidity measured at various stations are not consistent except at stations 6, 7, and 8. It is also observed that air relative humidity measured at the weather monitoring station is much higher than that measured inside the bridge.

7.4 Correlation between Identified Natural Frequencies and Measured Environmental Parameters

The bridge did not undergo any damage / deterioration during the monitoring period considered in this study. Therefore, experimental black-box models can be built to correlate the time varying natural frequencies identified during this period with the measured environmental parameters. The environmental parameters considered herein include the temperature of the air surrounding the bridge, the temperature measurements inside the bridge, the wind speed measured at the weather monitoring station and the averaged relative humidity measurements over eight stations inside the bridge.

Based on the correlation coefficients computed for twenty four temperature measurements taken inside the bridge, these measured temperatures are divided into four groups: (1) the concrete temperature measured at the top of stem walls; (2) the air temperature; (3) the concrete temperature measured at the bottom of the stem wall along the south side of the bridge; and (4) the concrete temperature measured at the bottom of the stem wall along the north side of the bridge. The correlation coefficient ρ_{xy} between two variables x and y is defined as (Peeters and De Roeck, 2001a)

$$\rho_{xy} = \frac{s_{xy}}{s_x s_y}, \quad s_{xy} = \frac{1}{N-1}\sum_{k=1}^{N}(x_k - \overline{x})(y_k - \overline{y}), \quad \overline{x} = \frac{1}{N}\sum_{k=1}^{N} x_k \tag{7.6}$$

where s_{xy} is the sample covariance; $s_x = \sqrt{s_{xx}}$, $s_y = \sqrt{s_{yy}}$ are the sample standard deviation; N is the number of data points and k is the discrete time index. An absolute value of correlation coefficient close to 1 indicates a high linear correlation between the two variables. For each of these four groups of the temperature measurements inside the bridge, the correlation coefficient between any two station measurements exceeds 99%. In other words, temperature measurements from different stations within the same group provide nearly the same information. The averaged temperature measurement of each group is reated as representative of the whole group.

Therefore, a total of eight different environmental parameters are considered in this study, namely, (1) T1: air temperature measured above the bridge; (2) T2: air temperature measured underneath the bridge; (3) T3: space-averaged temperature measured in the concrete at the top of the stem walls; (4) T4: space-averaged air temperature measured inside the bridge; (5) T5: space-averaged temperature measured in the concrete at the bottom of the stem wall along the south side of the bridge; (6) T6: space-averaged temperature measured in the concrete at the bottom of the stem wall along the north side of the bridge; (7) WS: wind speed measured at the weather monitoring station; and (8) RH: air relative humidity measured inside the bridge. As an illustration, Figure 7.23 through Figure 7.26 present plots of identified natural frequencies as a function of T1, T3, WS, and RH, respectively. It should be noted that the variations of the identified natural frequencies are influenced by combination of various environmental parameters. Thus, in the following section, ARX models with multiple inputs are used to correlate the identified natural frequencies with different measured environmental parameters based on the data collected over the 50 day period.

7.4.1 Modeling Natural Frequencies as a Function of Measured Environmental Parameters

7.4.1.1 Brief Review of ARX Models

In this section, black-box models are constructed to represent the relationship between an identified natural frequency (output) and the measured environmental parameters (inputs). For a single-input-single-output (SISO) linear, time-invariant system, probably the simplest input-output relationship is obtained by describing it as a linear difference equation (Ljung, 1999)

$$\begin{aligned} & y(t)+a_1 y(t-1)+\cdots+a_{na} y(t-na) \\ & =b_1 u(t-nk)+b_2 u(t-1-nk)+\cdots+b_{nb} u(t-nb-nk+1)+e(t) \end{aligned} \tag{7.7}$$

where $y(t)$ is the output (e.g., an identified natural frequency in our case); $u(t)$ is the input (e.g., a measured environmental parameter in our case); and $e(t)$ is the equation error term which is assumed to be zero-mean Gaussian distributed white noise with covariance

$$E[e(t)e(t-\tau)]=\lambda\delta(\tau) \tag{7.8}$$

where $\delta(\tau)$ is the Kronecker delta and $E[\bullet]$ is the expected value operator. This well known, model (7.7) is called an ARX model, where AR refers to the autoregressive part and X to the extra input (called the exogeneous variable in econometrics). In the above definition, na, nb, and nk are the auto-regressive order, the exogeneous order, and the pure time delay between input and output, respectively. The orders na and nb determine the number of model parameters: a_i $(i=1,\cdots,na)$ and b_j $(j=1,\cdots,nb)$. By introducing the backward shift operator q^{-1}: $q^{-1}y(t)=y(t-1)$, the model (7.7) is rewritten as

$$A(q)y(t)=B(q)u(t)+e(t) \tag{7.9}$$

where

$$A(q) = 1 + a_1 q^{-1} + \cdots + a_{na} q^{-na}$$
$$B(q) = b_1 q^{-nk} + b_2 q^{-nk-1} + \cdots + b_{nb} q^{-nk-nb+1} \tag{7.10}$$

In general, the parametrized linear input-output models are written as (Ljung, 1999)

$$y(t) = G(q, \boldsymbol{\theta}) u(t) + H(q, \boldsymbol{\theta}) e(t) \tag{7.11}$$

where $\boldsymbol{\theta}$ contains the model parameters; G is the transfer function and H is the noise model. In the case of ARX model, $\boldsymbol{\theta}$, G, and H are give as

$$\boldsymbol{\theta}^T = [a_1 \quad \cdots \quad a_{na} \quad b_1 \quad \cdots \quad b_{nb}]$$
$$G(q, \boldsymbol{\theta}) = \frac{B(q)}{A(q)}, \quad H(q, \boldsymbol{\theta}) = \frac{1}{A(q)} \tag{7.12}$$

The model parameters $\boldsymbol{\theta}$ of an ARX model can be estimated by a linear least squares method, which makes the ARX model popular in practical application. With different choice of na, nb, and nk, different ARX models can be identified based on the input and output data. The loss function is usually used as a criterion to assess the quality of these different identified ARX models. The loss function is defined as (Ljung, 1999; Peeters and De Roeck, 2001a)

$$\hat{\lambda} = \frac{1}{N} \sum_{t=1}^{N} \varepsilon^2(t, \hat{\boldsymbol{\theta}}) \tag{7.13}$$

with the prediction errors (the residuals) defined as

$$\varepsilon(t, \hat{\boldsymbol{\theta}}) = \hat{A}(q) y(t) - \hat{B}(q) u(t) \tag{7.14}$$

The loss function is also an estimate of the noise covariance λ. In practical applications, the loss function usually keeps decreasing as the model order increases. Therefore some other criteria such as Akaike's information criterion (AIC) and Rissanen's minimum description length (MDL) criterion are necessary to estimate the system orders (Ljung, 1999).

In our application, for each vibration mode, a multiple-input single-output ARX model is needed to correlate the identified natural frequency with different measured

environmental parameters. Based on the definition in equations (7.7) and (7.9), the ARX model with multiple inputs is defined as

$$A(q)y(t) = B_1(q)u_1(t) + \cdots + B_{nu}(q)u_{nu}(t) + e(t) \tag{7.15}$$

where nu is the number of input variables and

$$\begin{aligned} A(q) &= 1 + a_1 q^{-1} + \cdots + a_{na} q^{-na} \\ B_1(q) &= b_{1,1} q^{-nk_1} + b_{1,2} q^{-nk_1-1} + \cdots + b_{1,nb_1} q^{-nk_1-nb_1+1} \\ &\vdots \\ B_{nu}(q) &= b_{nu,1} q^{-nk_{nu}} + b_{nu,2} q^{-nk_{nu}-1} + \cdots + b_{nu,nb_{nu}} q^{-nk_{nu}-nb_{nu}+1} \end{aligned} \tag{7.16}$$

In the above equation, a_k $(k = 1, \cdots, na)$ and $b_{i,j}$ $(i = 1, \cdots, nu;\ j = 1, \cdots, nb_i)$ are the ARX model parameters.

7.4.1.2 Identification of ARX Models Based on Identified Natural Frequencies and Measured Environmental Parameters

For a typical concrete bridge, such as the bridge testbed developed in this study, the effects of wind and relative humidity on the identified natural frequencies are usually negligible (Peeters and De Roeck, 2001a). In this study, for each vibration mode, three different cases are considered to identify the ARX model representing the identified natural frequency as a function of measured environmental parameters, namely: (1) only six temperature measurements are used as input variables (i.e., T1, T2, T3, T4, T5, T6); (2) six temperature measurements and the wind speed measurement are consider as input variables (i.e., T1, T2, T3, T4, T5, T6, WS); (3) all eight environmental parameters are considered as input variables (i.e., T1, T2, T3, T4, T5, T6, WS, RH). Table 7.2 presents the loss functions [see equation (7.13)] of ARX models for these three cases. It is observed that the influence of

the relative humidity and the wind speed on the variations of natural frequencies based on the ARX model is very small. The contribution of the wind speed to natural frequencies based on the ARX model is slightly higher than that of relative humidity. In this study, for each identified vibration mode, the ARX model with seven inputs (i.e., temperature measurements and wind speed measurement) is finally used to correlate the identified natural frequency with the measured environmental parameters. Table 7.3, Table 7.4, and Table 7.5 present the model parameters of each identified ARX model. For each identified ARX model, the system order is estimated based on the AIC criterion. In addition, the measured data is divided into two subsets for estimating the system order. The first subset includes the data measured in August and the second subset includes the data measured in September. Another quality criterion to assess the quality of the identified ARX model is to investigate the auto-correlation function of its prediction error due to the fact that the prediction error should be zero-mean white noise in the case that a good ARX model is obtained. The auto-correlation function of the prediction error is estimated as

$$\hat{R}_e(\tau) = \frac{1}{N}\sum_{k=1}^{N} \varepsilon(t, \hat{\boldsymbol{\theta}})\varepsilon(t-\tau, \hat{\boldsymbol{\theta}}) \tag{7.17}$$

The auto-correlation functions of prediction errors for three ARX models corresponding to natural frequencies of three identified vibration modes are plotted, respectively, in Figure 7.27, Figure 7.28, and Figure 7.29 together with the 99% confidence intervals. From these figures, it can be concluded that the identified ARX models with multiple inputs fit the measured data very well.

Based on previous research work performed by Peeters and De Roeck (2001a), the ARX models are identified using the following dimensionless normalized data:

$$y(t) = \frac{y^m(t) - \overline{y}}{s_y},\ u_i(t) = \frac{u_i{}^m(t) - \overline{u}_i}{s_{u_i}},\ i = 1,\ 2,\ \cdots nu \tag{7.18}$$

where the superscript *m* denotes a measured / identified quantity with the engineering units; $\overline{y}$, $\overline{u}_i$ are the sample mean of output and input data, respectively and s_y, s_{u_i} are the sample standard deviations defined in equation (7.6). By substituting equation (7.18) into (7.15), the ARX models identified from the dimensionless normalized data can be converted to engineering units ARX models:

$$A(q)y^m(t) = B_1(q)\frac{s_y}{s_{u_1}}u_1^m(t) + \ \cdots + B_{nu}(q)\frac{s_y}{s_{u_{nu}}}u_{nu}^m(t) + s_y e(t) + C \tag{7.19}$$

in which the offset *C* is computed as

$$C = A(1)\overline{y} - B_1(1)\frac{s_y}{s_{u_1}}\overline{u}_1 - \ \cdots - \ B_{nu}(1)\frac{s_y}{s_{u_{nu}}}\overline{u}_{nu} \tag{7.20}$$

The estimated value of *C* for each ARX model is given in Table 7.3, Table 7.4, and Table 7.5 together with the corresponding estimated model parameters. Based on equation (7.15) or (7.19), the identified natural frequency can be described as a function of measured temperatures and wind speed. As an illustration, Figure 7.30 shows the simulated natural frequencies of three vibration modes considered in this study using the corresponding ARX models based on the measured environmental parameters. Figure 7.31 shows the differences / deviations between the corresponding simulated and identified natural frequencies. It should be noted that these differences are actually the variations of the identified natural frequencies after removing the environmental effects.

7.4.2 Objective Criterion for Damage Detection under Varying Environmental Conditions

Once good models representing the identified natural frequencies as a function of measured environmental parameters are obtained using the data collected from the undamaged state (or baseline state) of the bridge, they can be used to simulate the natural frequencies based on the new measured environmental parameters (fresh data). From the comparison of these simulated natural frequencies and their identified counterparts, the changes in identified natural frequencies caused by structural damage can be distinguished from those caused by varying environmental conditions. This section will provide an objective criterion for damage detection under the varying environmental conditions.

Considering an ARX model representation of a linear SISO system

$$y(t) = G(q,\boldsymbol{\theta})u(t) + H(q,\boldsymbol{\theta})e(t) \tag{7.21}$$

It is assumed that the "true" system can be described by the model structure of the above equation

$$y(t) = G(q,\boldsymbol{\theta}_0)u(t) + H(q,\boldsymbol{\theta}_0)e^0(t) \tag{7.22}$$

where $\boldsymbol{\theta}_0$ are the "true" model parameters and $e^0(t)$ is zero-mean Gaussian distributed white noise with covariance λ^0. Based on the input-output data, the model parameters are estimated by the linear least squares method. Then, the noise-free simulated output from the estimated model is written as

$$\hat{y}(t) = G(q,\hat{\boldsymbol{\theta}})u(t) \tag{7.23}$$

The simulation error is defined as the difference between the true output and its simulated counterpart

$$\begin{aligned}\hat{d}(t) &= y(t) - \hat{y}(t) = G(q,\boldsymbol{\theta}_0)u(t) + H(q,\boldsymbol{\theta}_0)e^0(t) - G(q,\hat{\boldsymbol{\theta}})u(t) \\ &= [G(q,\boldsymbol{\theta}_0) - G(q,\hat{\boldsymbol{\theta}})]u(t) + v^0(t)\end{aligned} \tag{7.24}$$

where $v^0(t) = H(q,\boldsymbol{\theta}_0)e^0(t)$. The term between the brackets can be expanded by a Taylor series. If only the first-order term is retained (Peeters and De Roeck, 2001a)

$$\hat{d}(t) = J(q,\boldsymbol{\theta}_0)u(t)(\boldsymbol{\theta}_0 - \hat{\boldsymbol{\theta}}) + v^0(t) \tag{7.25}$$

in which

$$J(q,\boldsymbol{\theta}_0) = \left.\frac{\partial G(q,\boldsymbol{\theta})}{\partial \boldsymbol{\theta}}\right|_{\boldsymbol{\theta}=\boldsymbol{\theta}_0} \tag{7.26}$$

Since when $N \to \infty$, $\hat{\boldsymbol{\theta}} \to \boldsymbol{\theta}_0$ and $e^0(t)$ is zero-mean Gaussian distributed white noise, the simulation error $\hat{d}(t)$ is asymptotically Gaussian distributed with zero-mean (i.e., $E[\hat{d}(t)] = 0$), and a certain covariance $E[\hat{d}^2(t)] = P_{\hat{d}(t)}$, which is denoted as

$$\hat{d}(t) \sim N(0,\ P_{\hat{d}(t)}) \tag{7.27}$$

By introducing the asymptotic covariance matrix of the model parameters $P_{\hat{\boldsymbol{\theta}}}$, the covariance $P_{\hat{d}(t)}$ can be derived as (Peeters and De Roeck, 2001a)

$$\begin{aligned}P_{\hat{d}(t)} &= [J(q,\boldsymbol{\theta}_0)u(t)]\ P_{\hat{\boldsymbol{\theta}}}\ [J(q,\boldsymbol{\theta}_0)u(t)]^T + R_v^0(0) \\ &= [\left.\frac{\partial G(q,\boldsymbol{\theta})}{\partial \boldsymbol{\theta}}\right|_{\boldsymbol{\theta}=\boldsymbol{\theta}_0} u(t)]\ P_{\hat{\boldsymbol{\theta}}}\ [\left.\frac{\partial G(q,\boldsymbol{\theta})}{\partial \boldsymbol{\theta}}\right|_{\boldsymbol{\theta}=\boldsymbol{\theta}_0} u(t)]^T + R_v^0(0)\end{aligned} \tag{7.28}$$

where $R_v^0(0) = E[(v^0(t))^2]$.

Similarly, in the case of an ARX model with multiple inputs, the covariance $P_{\hat{d}(t)}$ can be derived as

$$P_{\hat{d}(t)} = [\sum_{i=1}^{nu} \frac{\partial G_i(q,\boldsymbol{\theta})}{\partial \boldsymbol{\theta}}\bigg|_{\boldsymbol{\theta}=\boldsymbol{\theta}_0} u_i(t)]\, P_{\hat{\boldsymbol{\theta}}}\, [\sum_{i=1}^{nu} \frac{\partial G_i(q,\boldsymbol{\theta})}{\partial \boldsymbol{\theta}}\bigg|_{\boldsymbol{\theta}=\boldsymbol{\theta}_0} u_i(t)]^T + R_v^0(0) \tag{7.29}$$

in which nu is the number of input variables and

$$G_i(q,\boldsymbol{\theta}) = \frac{B_i(q)}{A(q)}$$
$$\boldsymbol{\theta} = [a_1 \quad \cdots \quad a_{na} \quad b_{1,1} \quad \cdots \quad b_{1,nb_1} \quad \cdots \quad b_{nu,1} \quad \cdots \quad b_{nu,nb_{nu}}] \tag{7.30}$$

In the above equation, $A(q)$ and $B_i(q)$, $i = 1, \cdots, nu$, is defined in equations (7.15) and (7.16). Since none of the expressions at the right-hand side of the equation (7.29), namely, $\sum_{i=1}^{nu} \frac{\partial G_i(q,\boldsymbol{\theta})}{\partial \boldsymbol{\theta}}\Big|_{\boldsymbol{\theta}=\boldsymbol{\theta}_0} u_i(t)$, $P_{\hat{\boldsymbol{\theta}}}$, and $R_v^0(0)$ are known, the asymptotic covariance of the simulation error can only be estimated by these three terms estimates. As discussed earlier, the model parameters of the ARX model are estimated using least squares method. The least squares method not only provides estimates of the model parameters ($\hat{\boldsymbol{\theta}}$), but also an estimate of the asymptotic covariance matrix of these parameters ($\hat{P}_{\hat{\boldsymbol{\theta}}}$). The estimates of $\hat{\boldsymbol{\theta}}$ and $\hat{P}_{\hat{\boldsymbol{\theta}}}$ can be obtained using MATLAB system identification toolbox.

Base on equations (7.15) and (7.16), we can get

$$\frac{\partial G_i(q,\boldsymbol{\theta})}{\partial \boldsymbol{\theta}} = \left[\frac{\partial G_i(q,\boldsymbol{\theta})}{\partial a_k} \quad \mathbf{0} \quad \cdots \quad \mathbf{0} \quad \frac{\partial G_i(q,\boldsymbol{\theta})}{\partial b_{ij}} \quad \mathbf{0} \quad \cdots \quad \mathbf{0}\right] \tag{7.31}$$

The partial derivatives can be written as

$$\frac{\partial G_i(q,\boldsymbol{\theta})}{\partial a_k} = -\frac{B_i(q)}{A^2(q)} q^{-i} \quad (k = 1, \cdots na)$$
$$\frac{\partial G_i(q,\boldsymbol{\theta})}{\partial b_{ij}} = -\frac{1}{A(q)} q^{-j+1-nk_i} \quad (j = 1, \cdots, nb_i) \tag{7.32}$$

These expressions are defining time domain filtering operations on the inputs. An estimate of

$\sum_{i=1}^{nu} \left.\frac{\partial G_i(q,\boldsymbol{\theta})}{\partial \boldsymbol{\theta}}\right|_{\boldsymbol{\theta}=\boldsymbol{\theta}_0} u_i(t)$ is obtained by replacing the true but unknown parameters $\boldsymbol{\theta}_0$ by their estimate: $\sum_{i=1}^{nu} \left.\frac{\partial G_i(q,\boldsymbol{\theta})}{\partial \boldsymbol{\theta}}\right|_{\boldsymbol{\theta}=\hat{\boldsymbol{\theta}}} u_i(t)$.

Since $v^0(t)$ is obtained by filtering the white noise sequence $e^0(t)$ through an auto-regressive filter

$$v^0(t) = \frac{1}{A(q)} e^0(t) \tag{7.33}$$

The computation of $R_v^0(0)$ can be obtained through the following procedure (Ljung, 1999; Peeters and De Roeck, 2001a). The vectors $\mathbf{x}(t)$, $\mathbf{w}(t)$ and the matrix $\mathbf{A}$ are defined as

$$\mathbf{x}(t) = \begin{bmatrix} v^0(t-1) & v^0(t-2) & \cdots & v^0(t-na) \end{bmatrix}^T$$

$$\mathbf{w}(t) = \begin{bmatrix} e^0(t) & 0 & \cdots & 0 \end{bmatrix}^T$$

$$\mathbf{A} = \begin{bmatrix} -a_1^0 & -a_2^0 & \cdots & -a_{na-1}^0 & -a_{na}^0 \\ 1 & 0 & \cdots & 0 & 0 \\ 0 & 1 & \cdots & 0 & 0 \\ \cdots & \cdots & \cdots & \cdots & \cdots \\ 0 & 0 & \cdots & 1 & 0 \end{bmatrix} \tag{7.34}$$

in which $\mathbf{x}(t) \in \mathbb{R}^{na\times 1}$ is the state vector; $\mathbf{A} \in \mathbb{R}^{na\times na}$ is the state transition matrix and $\mathbf{w}(t) \in \mathbb{R}^{na\times 1}$ is the process noise vector. Equation (7.33) is now written as

$$\mathbf{x}(t+1) = \mathbf{A}x(t) + \mathbf{w}(t) \tag{7.35}$$

The state covariance matrix is defined as $\boldsymbol{\Sigma} = E[\mathbf{x}(t)\mathbf{x}(t)^T]$ and the noise covariance matrix is defined as $\mathbf{Q} = E[\mathbf{w}(t)\mathbf{w}(t)^T]$. Since $e^0(t)$ is independent of any of the previous outputs, thus we have

$$\mathbf{\Sigma} = A\mathbf{\Sigma}A^T + \mathbf{Q} \tag{7.36}$$

The above equation is known as Lyapunov equation. Any of the diagonal elements of $\mathbf{\Sigma}$ is equal to $R_v^0(0)$. An estimate $\hat{R}_v^0(0)$ of $R_v^0(0)$ is obtained by replacing λ_0 by $\hat{\lambda}$ in $\mathbf{Q}$ and $A_0(q)$ by $\hat{A}(q)$ in $\mathbf{A}$.

Based on all these estimates described above, the asymptotic covariance estimate of the simulation error $\hat{P}_{\hat{d}(t)}$ is obtained.

From equation (7.27), we can get

$$\frac{y(t) - \hat{y}(t)}{\sqrt{P_{\hat{d}_k}}} \sim N(0,\ 1) \tag{7.37}$$

Since the true asymptotic covariance of the simulation error is unknown and only its estimate $\hat{P}_{\hat{d}(t)}$ is available, the 100(1-α) percent confidence interval on $y(t)$ (the true value) is given by

$$\left[\hat{y}(t) - t_{\alpha/2,v}\sqrt{\hat{P}_{\hat{d}_k}}\ ,\ \ \hat{y}(t) + t_{\alpha/2,v}\sqrt{\hat{P}_{\hat{d}_k}}\right] \tag{7.38}$$

in which $t_{\alpha/2,v}$ can be found from a statistical table of the Student's t – distribution. The symbol v is the number of degrees of freedom of the data, $v = N - d$, where d is the number of model parameters.

The confidence interval defined in equation (7.38) can be used as an objective criterion to detect damage under the varying environmental conditions. In the case that the natural frequency (identified from the bridge vibration data) is lower than its ARX simulated counterpart and lies outside the confidence interval of a specified level (e.g., 95% confidence interval), then the variation of the identified natural frequency is caused not only by variations in environmental conditions, but also by a statistically significant loss of stiffness (i.e.,

damage) in the bridge structure. In this study, the data collected in the period of 50 days which are used to identify the ARX models and the new data measured over the first 10 days of October are fed the models to yield the simulated natural frequencies and the 95% confidence intervals. The identified natural frequencies and the differences between the corresponding identified and simulated natural frequencies (variations of the identified natural frequencies after removing environmental effects) during the period from September 10th to October 10th are shown in Figure 7.32 and Figure 7.33, respectively, together with the corresponding 95% intervals. It is worth noting that these two figures provide the same information for damage detection under varying environmental conditions. Based on these two figures, it is observed the identified natural frequencies are in general within the confidence intervals, which is consistent with the fact that the bridge did not undergo any damage during this period. However, it is also observed that the identified natural frequencies during some short periods move out of the lower bounds of the confidence intervals (especially for the second mode). This could be due to the fact that in general the temperature during the validation period (the first 10 days of October) is lower than those used to estimate the ARX models. Therefore these ARX models are not capable of correlating well the natural frequencies with the measured environmental parameters. The ARX models identified in this study need to be improved and validated using vibration and environmental data recorded over a longer time period (e.g., one year) from the long-term monitoring system developed in this study.

7.5 Summary and Conclusions

In this chapter, an automated system identification procedure is developed based on the data-driven stochastic subspace identification. This automated system identification procedure is successfully applied to identify the modal parameters of the Voigt Bridge as a function of time. Data collected over a period of 50 days from the state-of-the-art structural

monitoring system deployed on the bridge (see Chapter 6) is used in the identification process. It is found that changes in the identified natural frequencies due to varying environmental conditions are significant, on the order of 10-15 percent. It is worth noting that variations of the identified natural frequencies are caused mainly by changes in environmental conditions since the bridge did not suffer any damage during the monitoring period. The identified modal damping ratios and mode shapes are also investigated as a function of time in this study. No clear temporal variation patterns of the identified damping ratios and mode shapes are observed.

Different measured environmental parameters are investigated during the monitoring period considered in this study (i.e., period of 50 days from August to September, 2007). For each vibration mode, a multiple-input single-output ARX model is successfully identified to represent the identified natural frequency of this mode (output variable) as a function of seven measured environmental parameters (input variables), namely, (1) T1 = air temperature measured above the bridge; (2) T2 = air temperature measured underneath the bridge; (3) T3 = space-averaged temperature measured in the concrete at the top of the stem walls; (4) T4 = space-averaged air temperature measured inside the bridge; (5) T5 = space-averaged temperature measured in the concrete at the bottom of the stem wall along the south side of the bridge; (6) T6 = space-averaged temperature measured in the concrete at the bottom of the stem wall along the north side of the bridge; and (7) WS = wind speed measured at the weather monitoring station. Based on the estimated parameters of each ARX model, the confidence interval of the natural frequency is obtained and used as an objective criterion for damage detection under varying environmental conditions. In the case that the natural frequency (identified from the bridge vibration data) is lower than its ARX simulated counterpart and lies outside the confidence interval of a specified level (e.g., 95% confidence

interval), then the variation of the identified natural frequency is caused not only by variations in environmental conditions, but also by a statistically significant loss of stiffness (i.e., damage) in the bridge structure.

It should be noted that the effects of changing environmental conditions on the identified modal parameters need further investigation using vibration and environmental data recorded over a longer time period (e.g., one year) from the long-term monitoring system developed in this study. In addition, other types of methods such as statistical learning techniques should be applied to explain/correlate the identified natural frequencies to the measured environmental conditions.

7.6 References

Abdel Wahab, M. and De Roeck, G. (1997). "Effect of temperature on dynamic system parameters of a highway bridge." *Structural Engineering International*, 7(4), 266-270.

Allemang, R. J., and Brown, D. L. (1982). "A correlation coefficient for modal vector analysis." *Proc. of 1st International Modal Analysis Conference*, Society for Experimental Mechanics, Bethel, Connecticut, 110-116.

Cornwell, P., Farrar, C.R., Doebling, S.W. and SOhn, H. (1999). "Environmental variability of modal properties." *Experimental Techniques*, 23(6), 45-48.

He, X., Fraser, M., Conte J. P., and Elgamal, A. (2007). "Investigation of environmental effects on identified modal parameters of the Voigt Bridge." *Proceedings of 18th Engineering Mechanics Division Conference of the ASCE*, Blacksburg, VA.

James, G. H., Carne, T. G., and Lauffer, J. P. (1993). "The natural excitation technique for modal parameters extraction from operating wind turbines." *Report No. SAND92-1666, UC-261*, Sandia National Laboratories, Sandia, NM, USA.

Juang, J. N., and Pappa, R. S. (1985). "An eigensystem realization Algorithm for modal parameters identification and model reduction." *Journal of Guidance, Control and Dynamics*, 8(5), 620-627.

Ljung, L. (1999). *System Identification: Theory for the User (Second Edition*). Upper Saddle River, NJ, USA.

Ni, Y.Q., Hua, X. G., Fan, K. Q., and Ko, J. M. (2005). "Correlating modal properties with temperature using long term monitoring data and support vector machine technique," *Engineering Structures*, 27(12), 1762-1773.

Peeters, B. and De Roeck, G. (2001a). "One-year monitoring of the Z24-Bridge: environmental effects versus damage events." *Earthquake Engineering and Structural Dynamics*, 30(2): 149-171.

Peeters, B., and De Roeck, G. (2001b). "Stochastic system identification for operational modal analysis: A review." *Journal of Dynamic Systems, Measurement, and Control*, 123(4), 659-667.

Van Overschee, P., and De Moor, B. (1996). *Subspace Identification for Linear Systems*, Kluwer Academic Publishers, Boston.

Xia, Y., Hao, H., Zanardo, G., and Deeks, A. (2006). "Long term vibration monitoring of an RC slab: Temperature and humidity effect," *Engineering Structures*, 28(3), 441-452.

Table Captions

Table 7.1. Summary of natural frequency identification results obtained during the monitoring period

Mode No	Minimum (Hz) f_{min}	Average (Hz) f_{avg}	Maximum (Hz) f_{max}	Frequency change (%) $(f_{max} - f_{min})/f_{min}$
1	4.31	4.74	4.92	14.3%
2	9.77	10.60	11.28	15.5%
3	12.62	13.07	13.83	9.6%

Table 7.2. Loss functions of the identified ARX models with different input parameters

Mode	ARX model with 6 input parameters	ARX model with 7 input parameters	ARX model with 8 input parameters
1	0.5391	0.5352	0.5336
2	0.4067	0.3961	0.3944
3	0.4201	0.4148	0.4136

Table 7.3. ARX model parameters identified for the natural frequency of the first mode

	$\hat{a}_0$	$\hat{a}_1$	$\hat{a}_2$			
$\hat{a}_i$	1	-0.4299	-0.1575			
	$\hat{b}_{11}$	$\hat{b}_{12}$	$\hat{b}_{13}$	$\hat{b}_{14}$	$\hat{b}_{15}$	
$\hat{b}_{1i}$	0.0265	-0.1655	0.0073	0.1688	-0.012	
	$\hat{b}_{21}$	$\hat{b}_{22}$	$\hat{b}_{23}$	$\hat{b}_{24}$	$\hat{b}_{25}$	$\hat{b}_{26}$
$\hat{b}_{2i}$	0.0807	-0.3054	0.1797	-0.1538	-0.085	0.0698
	$\hat{b}_{31}$	$\hat{b}_{32}$				
$\hat{b}_{3i}$	-0.3001	-0.1784				
	$\hat{b}_{41}$	$\hat{b}_{42}$	$\hat{b}_{43}$	$\hat{b}_{44}$		
$\hat{b}_{4i}$	1.588	-1.0393	2.7157	-3.8781		
	$\hat{b}_{51}$	$\hat{b}_{52}$	$\hat{b}_{53}$			
$\hat{b}_{5i}$	-5.1709	5.6823	-0.3488			
	$\hat{b}_{61}$	$\hat{b}_{62}$				
$\hat{b}_{6i}$	2.8011	-1.6623				
	$\hat{b}_{71}$	$\hat{b}_{72}$				
$\hat{b}_{7i}$	-0.0403	-0.0876				
$\hat{C}$	1.9254					

Table 7.4. ARX model parameters identified for the natural frequency of the second mode

	$\hat{a}_0$	$\hat{a}_1$	$\hat{a}_2$	
$\hat{a}_i$	1	-0.2639	-0.2352	
	$\hat{b}_{11}$	$\hat{b}_{12}$	$\hat{b}_{13}$	
$\hat{b}_{1i}$	-0.114	-0.0534	0.2238	
	$\hat{b}_{21}$			
$\hat{b}_{2i}$	0.2915			
	$\hat{b}_{31}$	$\hat{b}_{32}$		
$\hat{b}_{3i}$	-4.0032	3.9551		
	$\hat{b}_{41}$	$\hat{b}_{42}$	$\hat{b}_{43}$	$\hat{b}_{44}$
$\hat{b}_{4i}$	0.9968	1.1921	-2.0157	-1.6793
	$\hat{b}_{51}$	$\hat{b}_{52}$		
$\hat{b}_{5i}$	4.8792	-4.9224		
	$\hat{b}_{61}$	$\hat{b}_{62}$	$\hat{b}_{63}$	
$\hat{b}_{6i}$	-2.2781	3.2761	0.5388	
	$\hat{b}_{71}$	$\hat{b}_{72}$	$\hat{b}_{73}$	
$\hat{b}_{7i}$	-0.1447	0.0016	-0.0666	
$\hat{C}$	5.0414			

Table 7.5. ARX model parameters identified for the natural frequency of the third mode

	$\hat{a}_0$	$\hat{a}_1$	$\hat{a}_2$	
$\hat{a}_i$	1	-0.4687	-0.1613	
	$\hat{b}_{11}$	$\hat{b}_{12}$	$\hat{b}_{13}$	$\hat{b}_{14}$
$\hat{b}_{1i}$	0.1119	-0.0629	0.002	0.1848
	$\hat{b}_{21}$			
$\hat{b}_{2i}$	0.2248			
	$\hat{b}_{31}$	$\hat{b}_{32}$		
$\hat{b}_{3i}$	-3.305	3.498		
	$\hat{b}_{41}$			
$\hat{b}_{4i}$	-1.6624			
	$\hat{b}_{51}$	$\hat{b}_{52}$		
$\hat{b}_{5i}$	3.2168	-3.1146		
	$\hat{b}_{61}$			
$\hat{b}_{6i}$	1.1605			
	$\hat{b}_{71}$			
$\hat{b}_{7i}$	-0.1236			
$\hat{C}$	4.7430			

Figure Captions

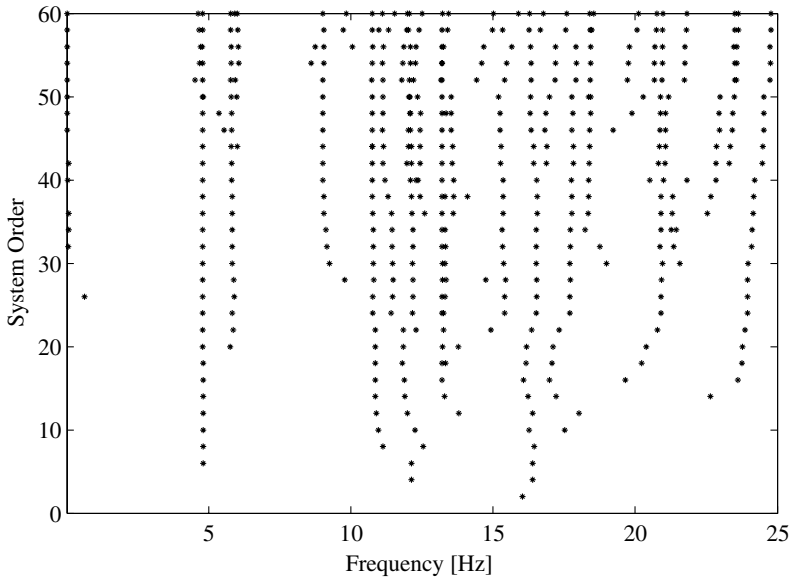

Figure 7.1. Stabilization diagram obtained using SSI-DATA

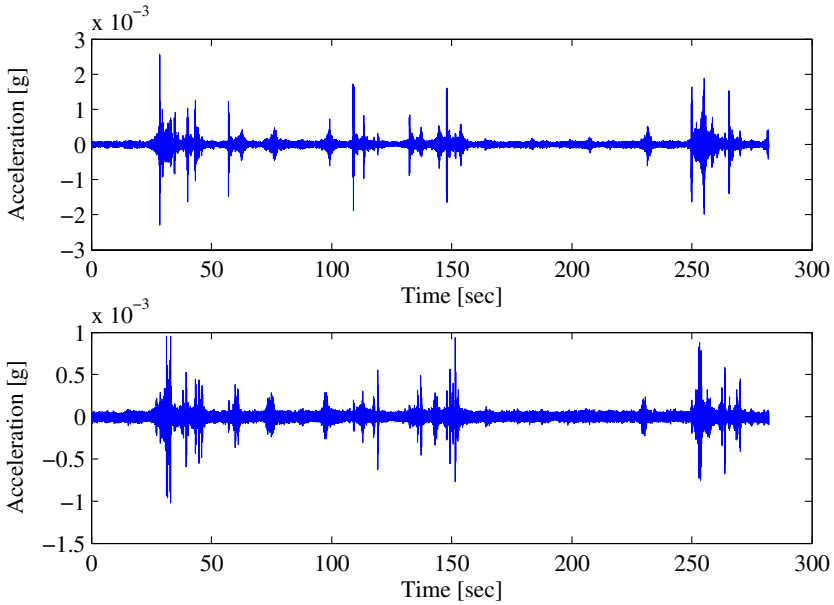

Figure 7.2. Typical acceleration response measurements: (Top) acceleration response measured at mid-point of the west middle span along north side of the bridge; (Bottom) acceleration response measured at mid-point of the east middle span along north side of the bridge

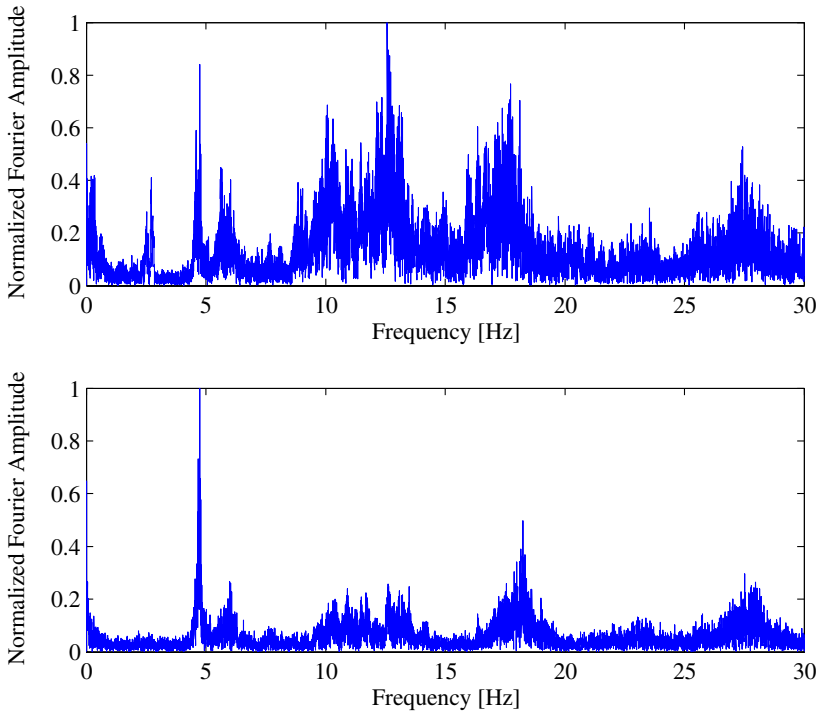

Figure 7.3. Fourier amplitude spectra of typical acceleration response measurements: (Top) acceleration response measured at mid-point of the west middle span along north side of the bridge; (Bottom) acceleration response measured at mid-point of the east middle span along north side of the bridge

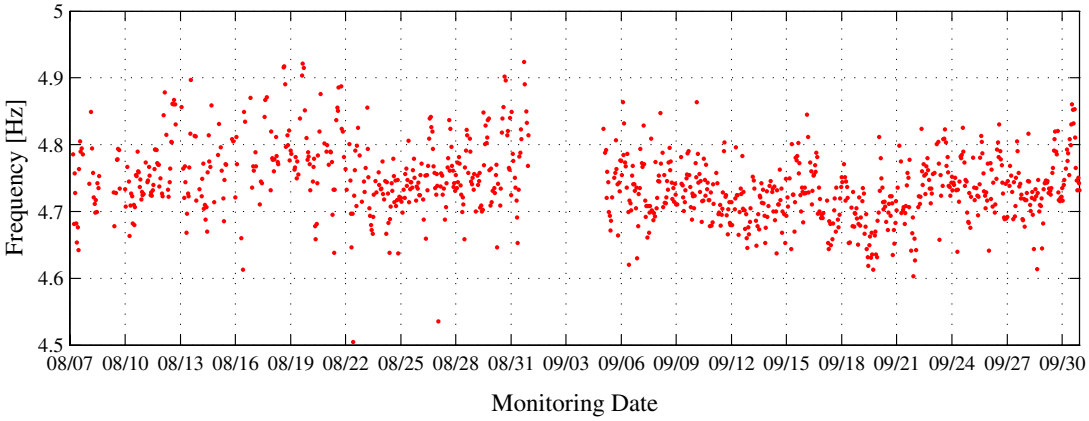

(a) Mode 1

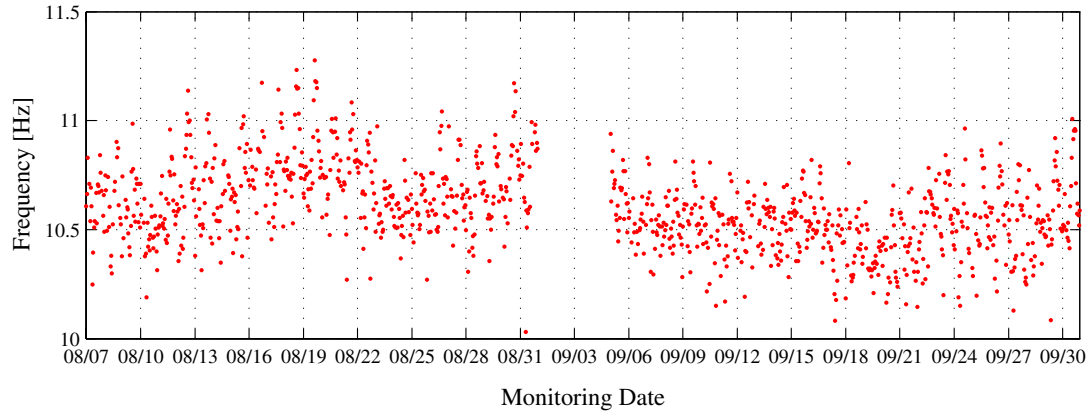

(b) Mode 2

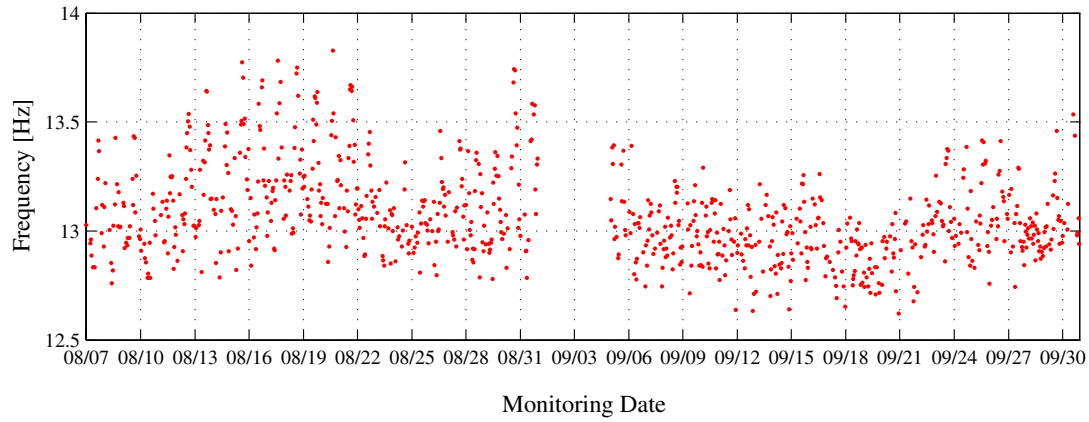

(c) Mode 3

Figure 7.4. Natural frequencies identified during the monitoring period

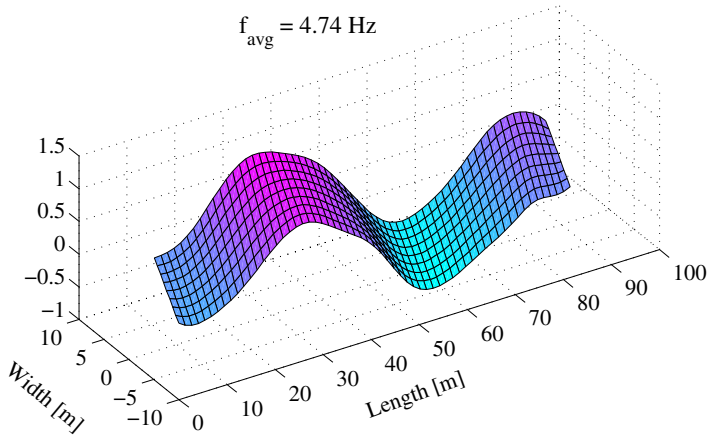

(a) Mode 1

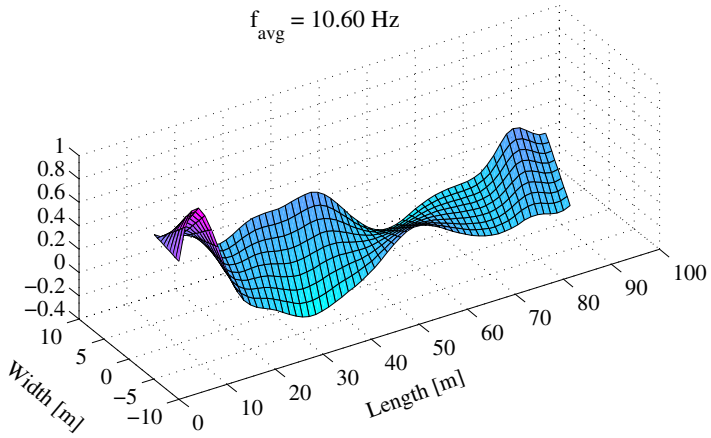

(b) Mode 2

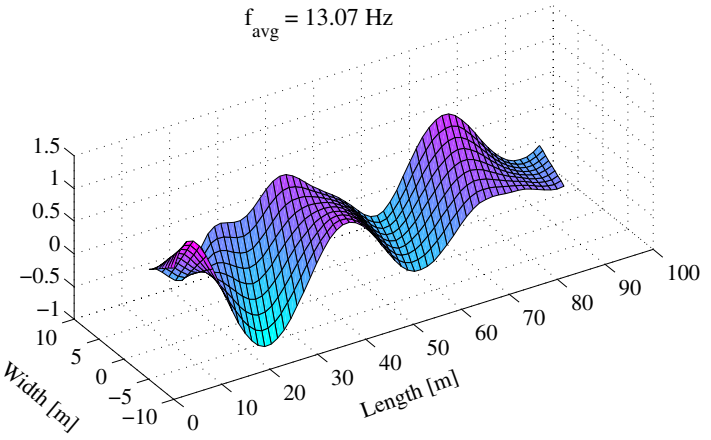

(c) Mode 3

Figure 7.5. 3D representation of normalized identified mode shapes

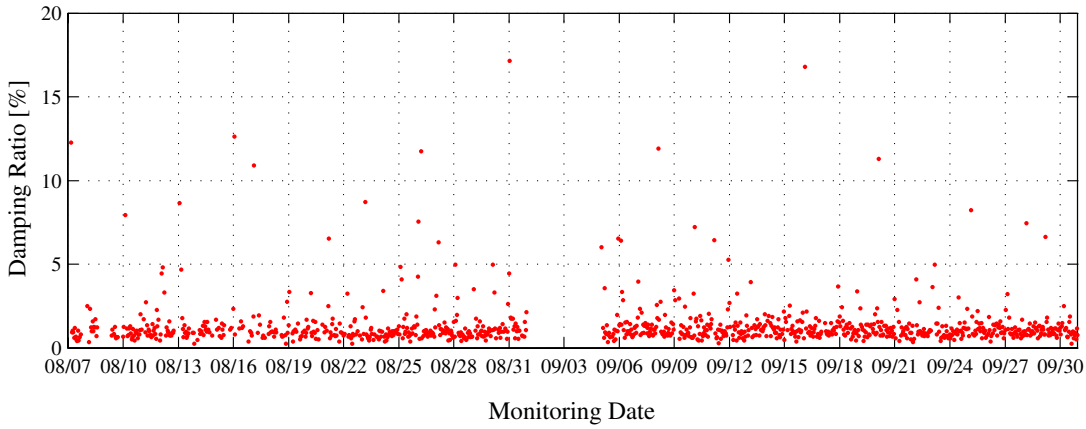

(a) Mode 1

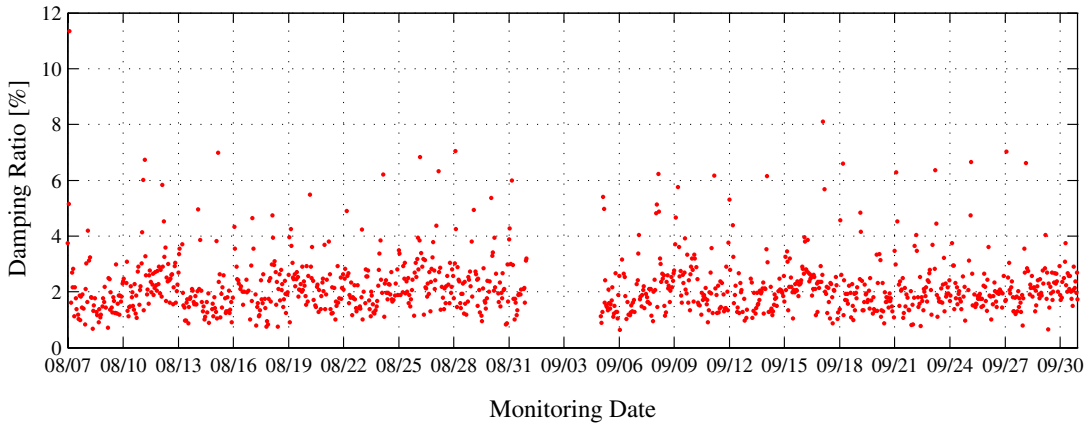

(b) Mode 2

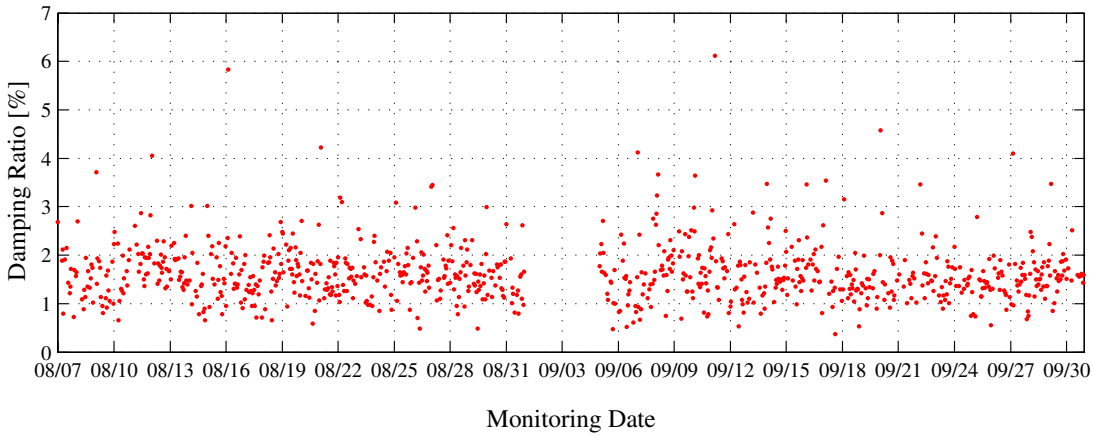

(c) Mode 3

Figure 7.6. Damping ratios identified during the monitoring period

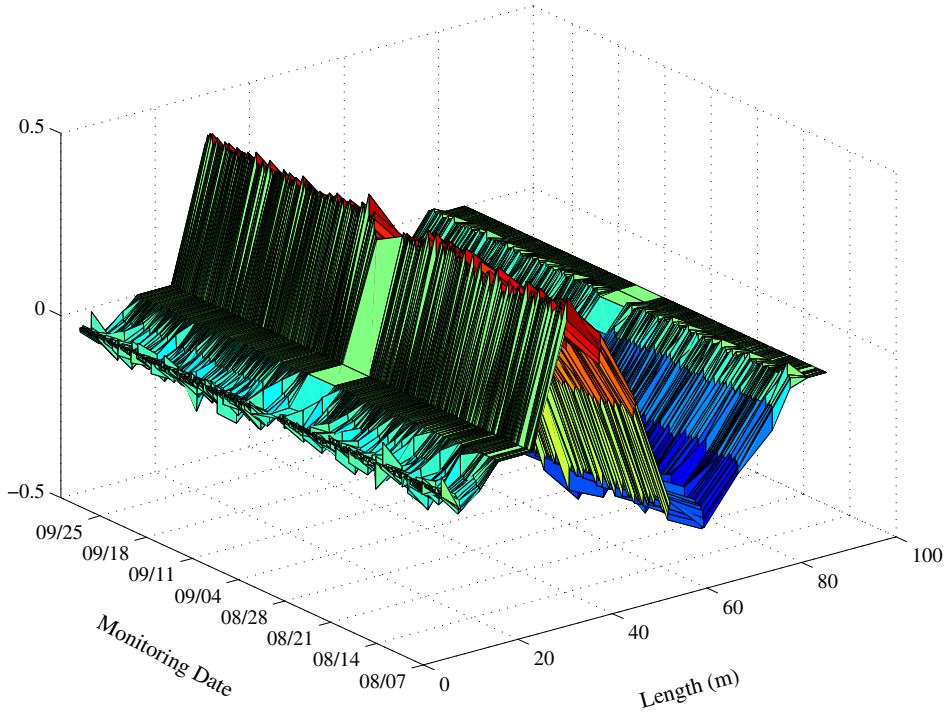

Figure 7.7. Normalized mode shape of the first vibration mode identified during the monitoring period along south side of the bridge

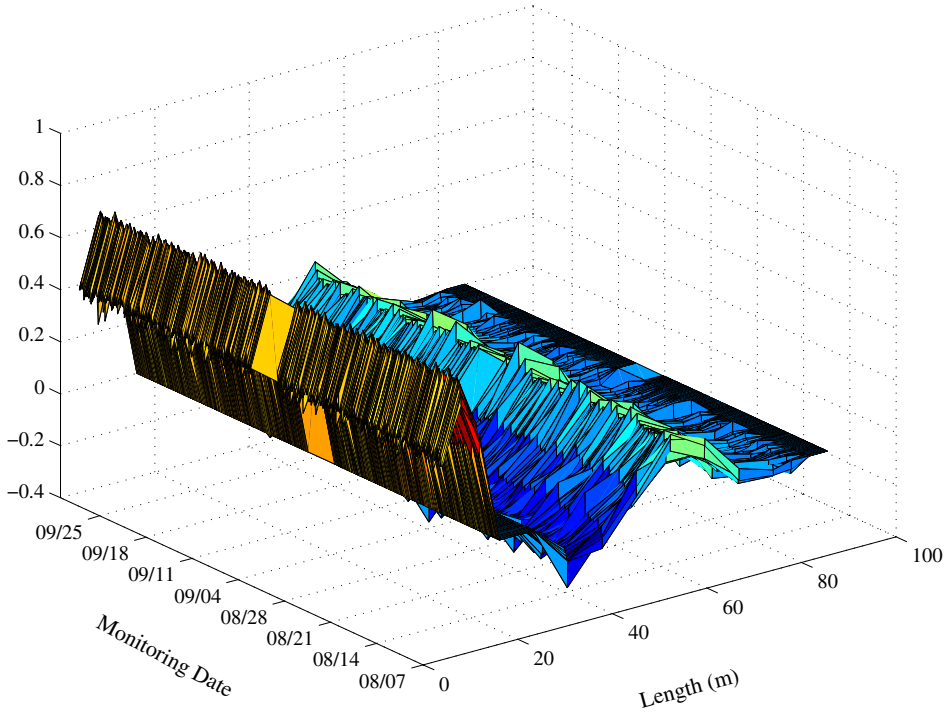

Figure 7.8. Normalized mode shape of the second vibration mode identified during the monitoring period along south side of the bridge

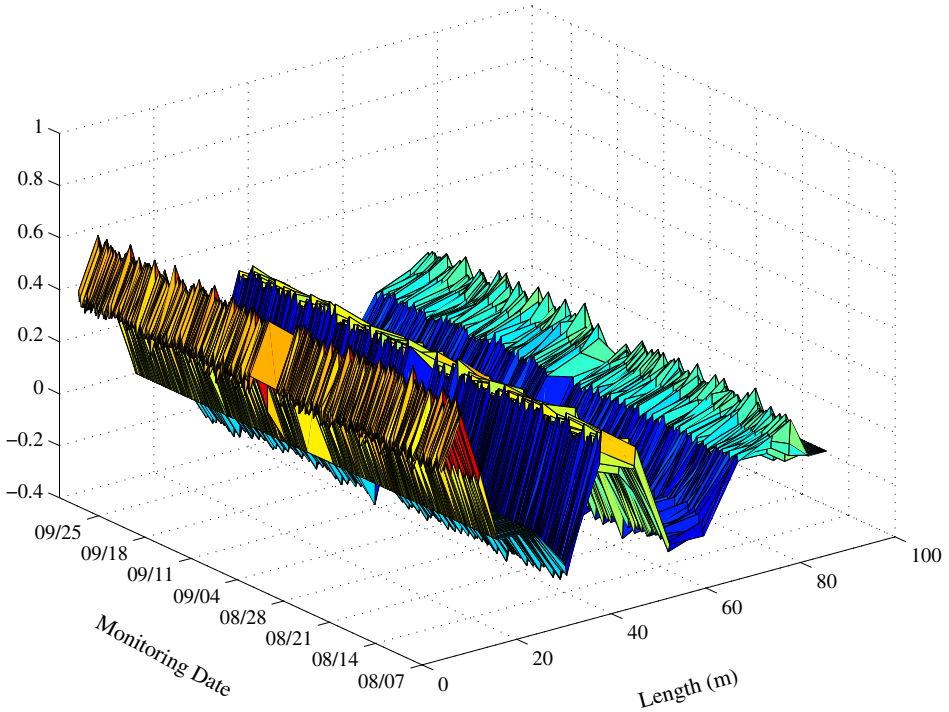

Figure 7.9. Normalized mode shape of the third vibration mode identified during the monitoring period along south side of the bridge

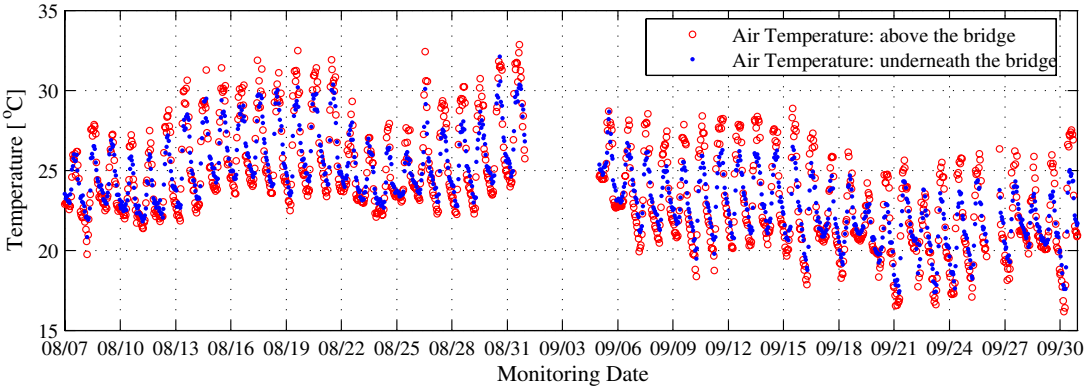

Figure 7.10. Air temperature surrounding the bridge measured during the monitoring period

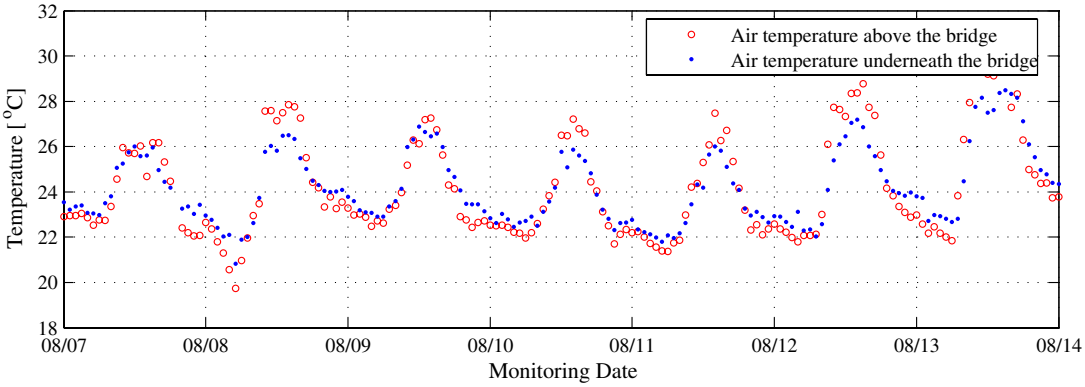

Figure 7.11. Air temperature surrounding the bridge measured during the period of Aug. 7 through Aug. 14

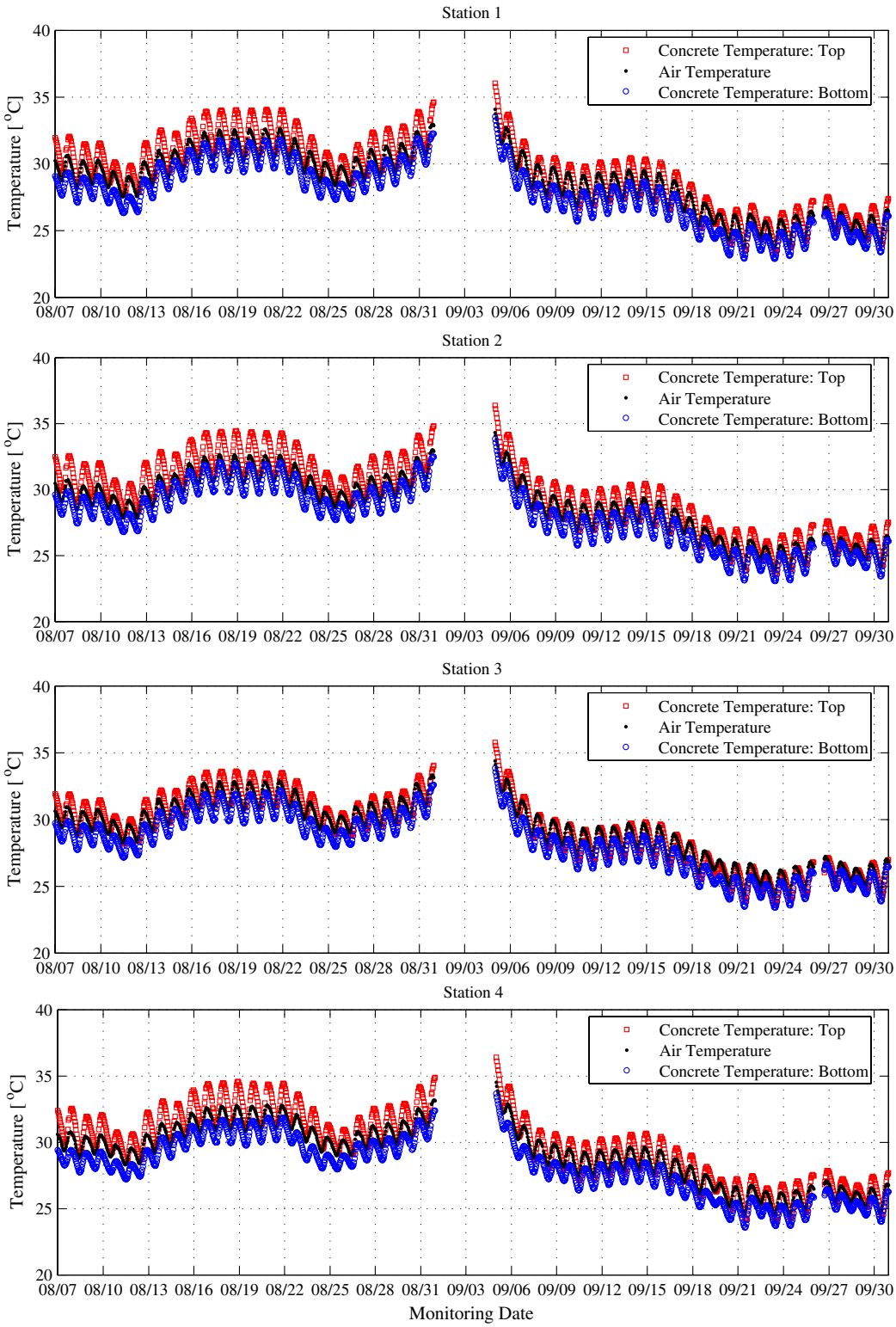

Figure 7.12. Temperature measurements inside the bridge (along south side of the bridge) during the monitoring period

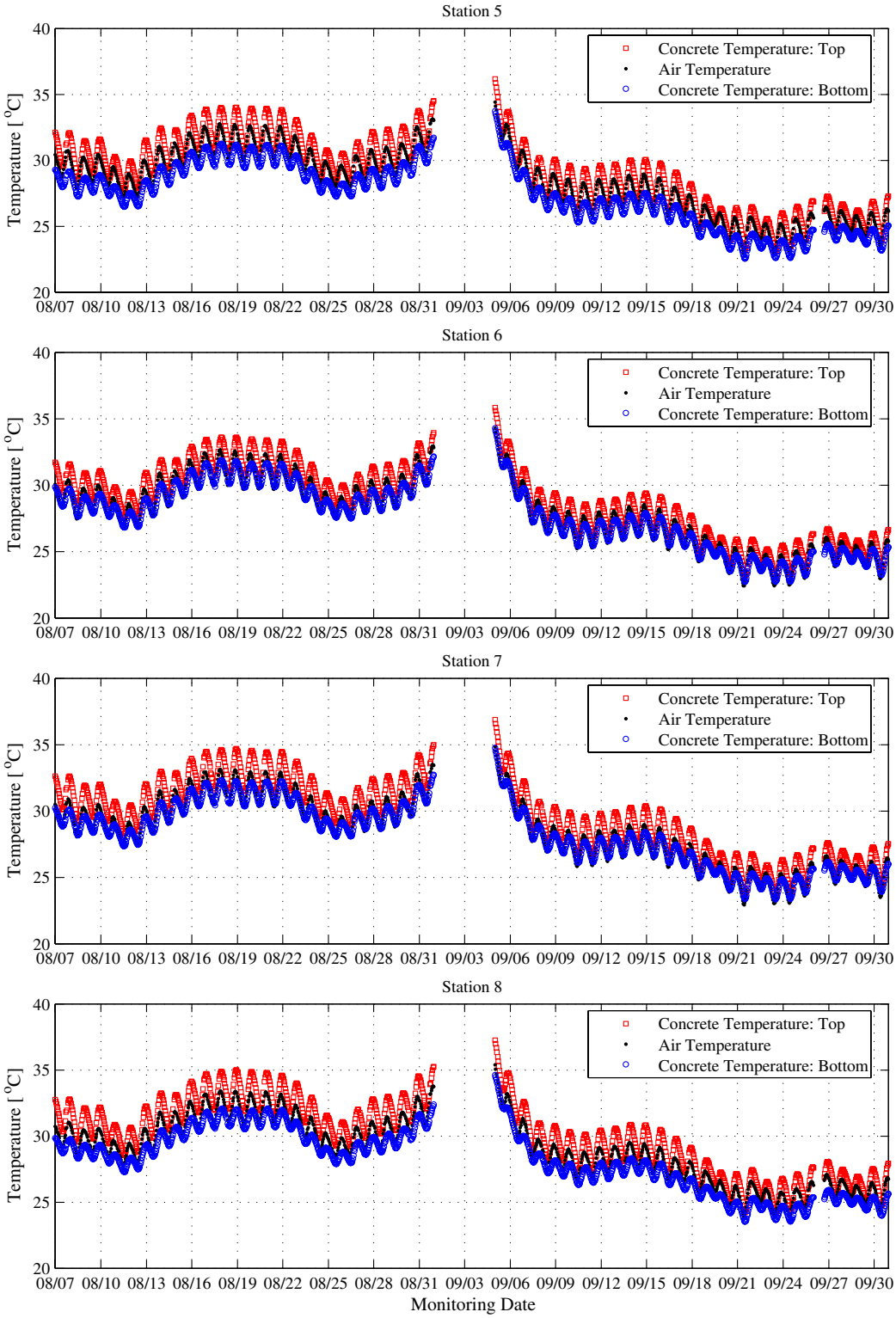

Figure 7.13. Temperature measurements inside the bridge (along north side of the bridge) during the monitoring period

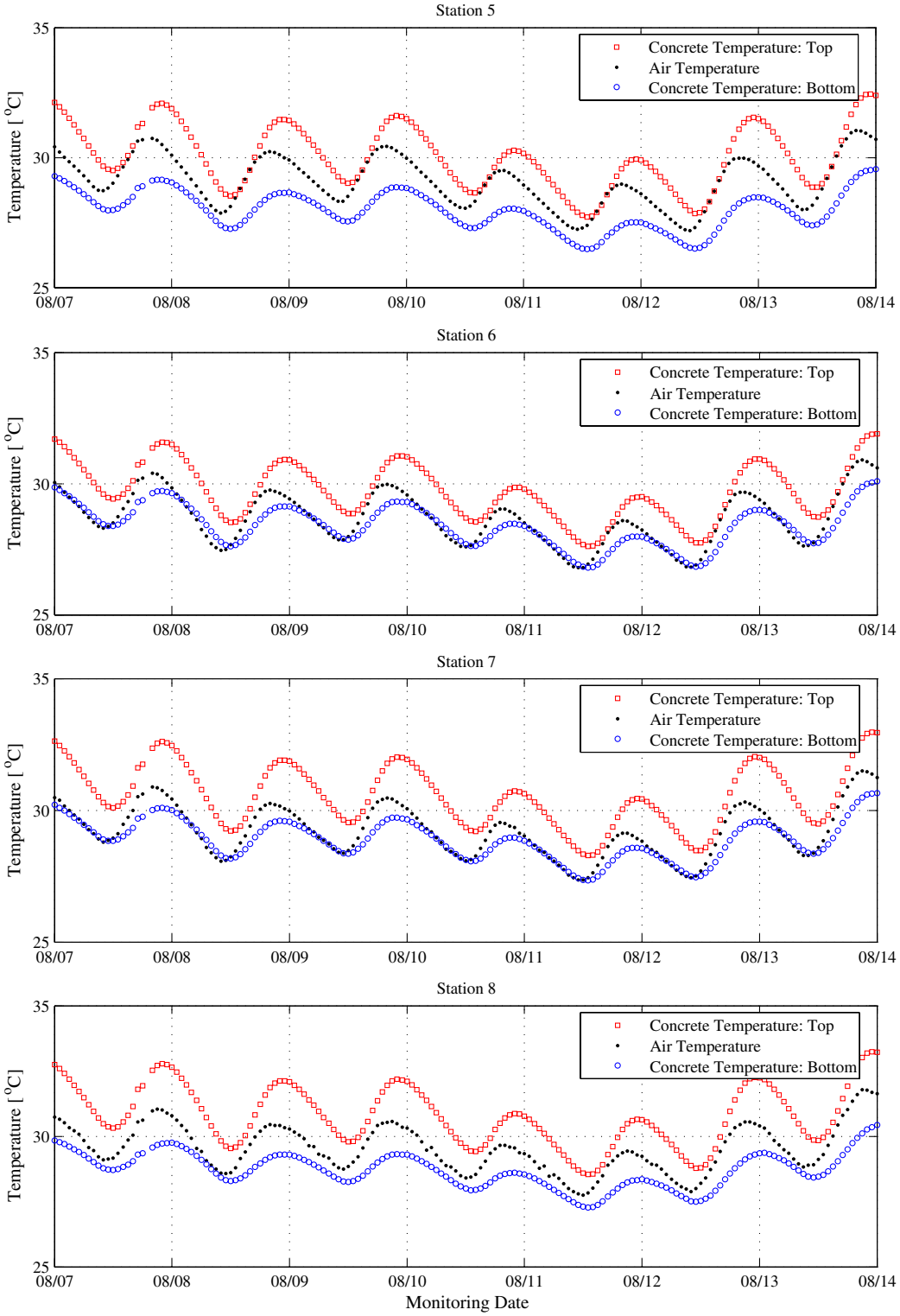

Figure 7.14. Temperature measurements inside the bridge (along north side of the bridge) during the period of Aug. 7 through Aug. 14

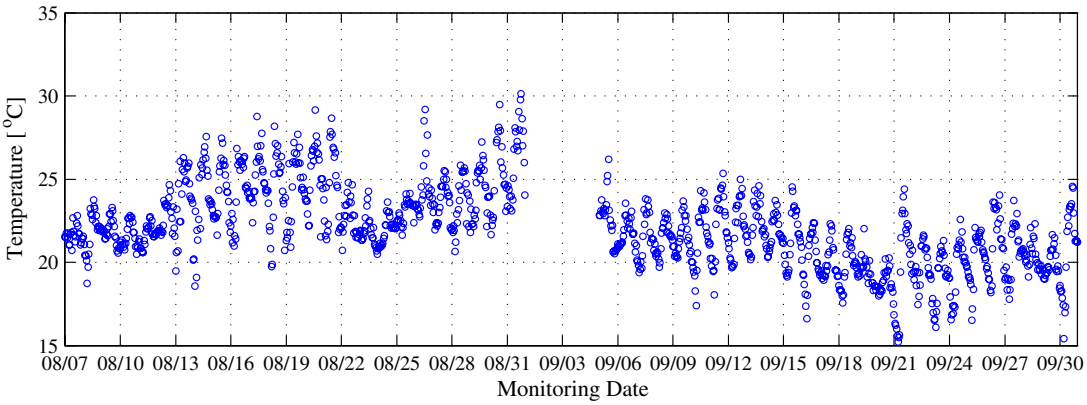

Figure 7.15. Air temperature measured at the weather monitoring station during the monitoring period

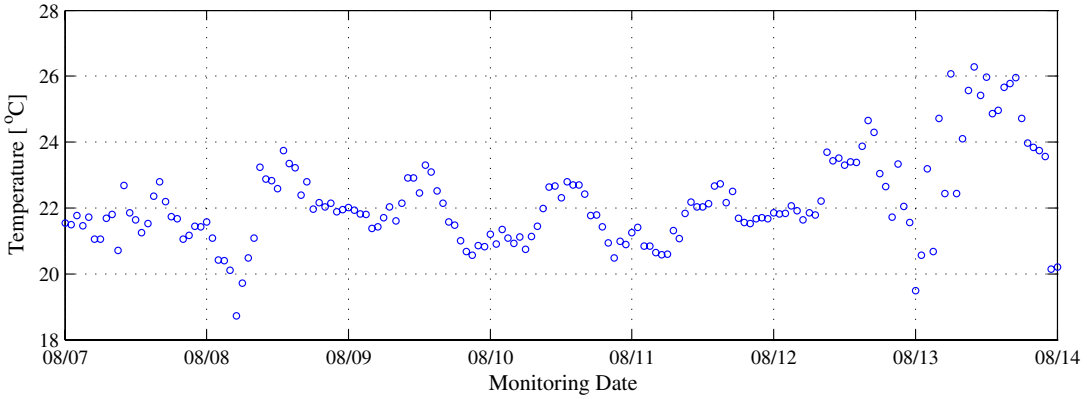

Figure 7.16. Air temperature measured at the weather monitoring station during the period of Aug. 7 through Aug. 14

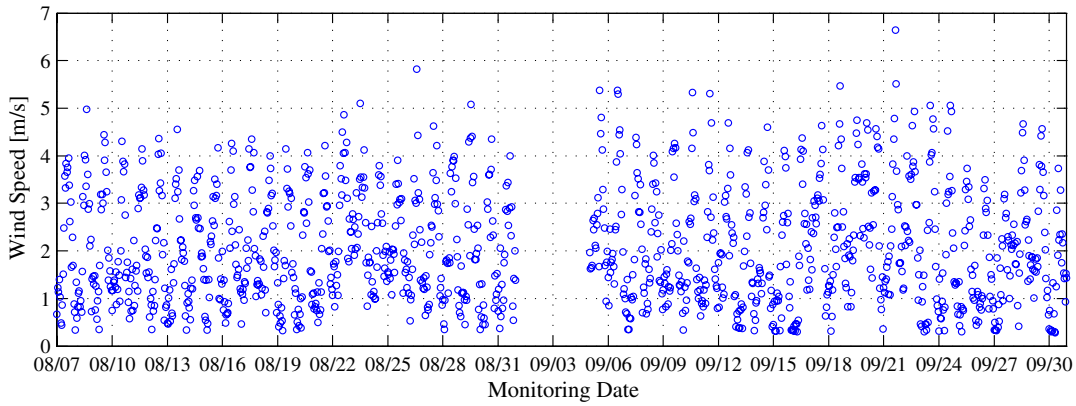

Figure 7.17. Wind speed measured at the weather monitoring station during the monitoring period

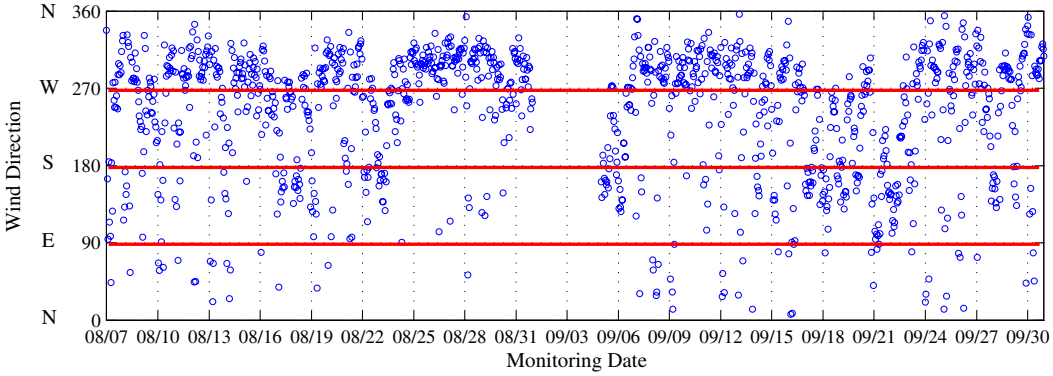

Figure 7.18. Wind direction measured at the weather monitoring station during the monitoring period

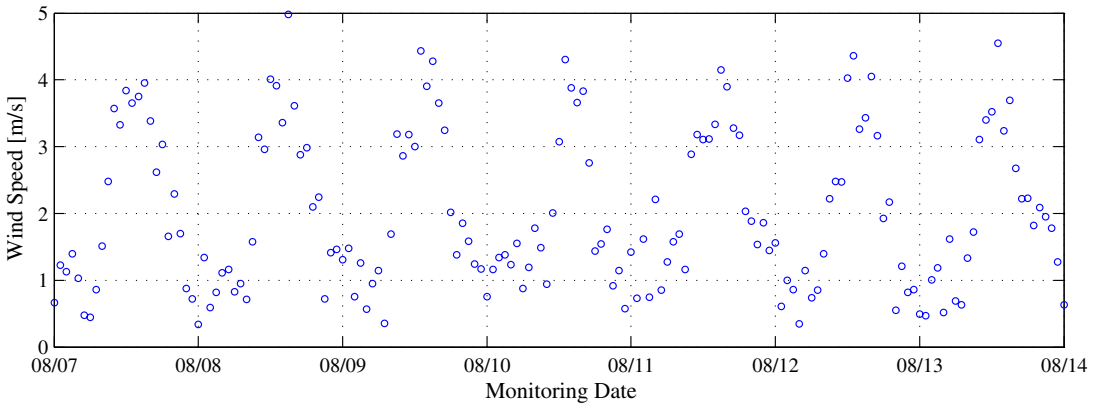

Figure 7.19. Wind speed measured at the weather monitoring station during the period of Aug. 7 through Aug. 14

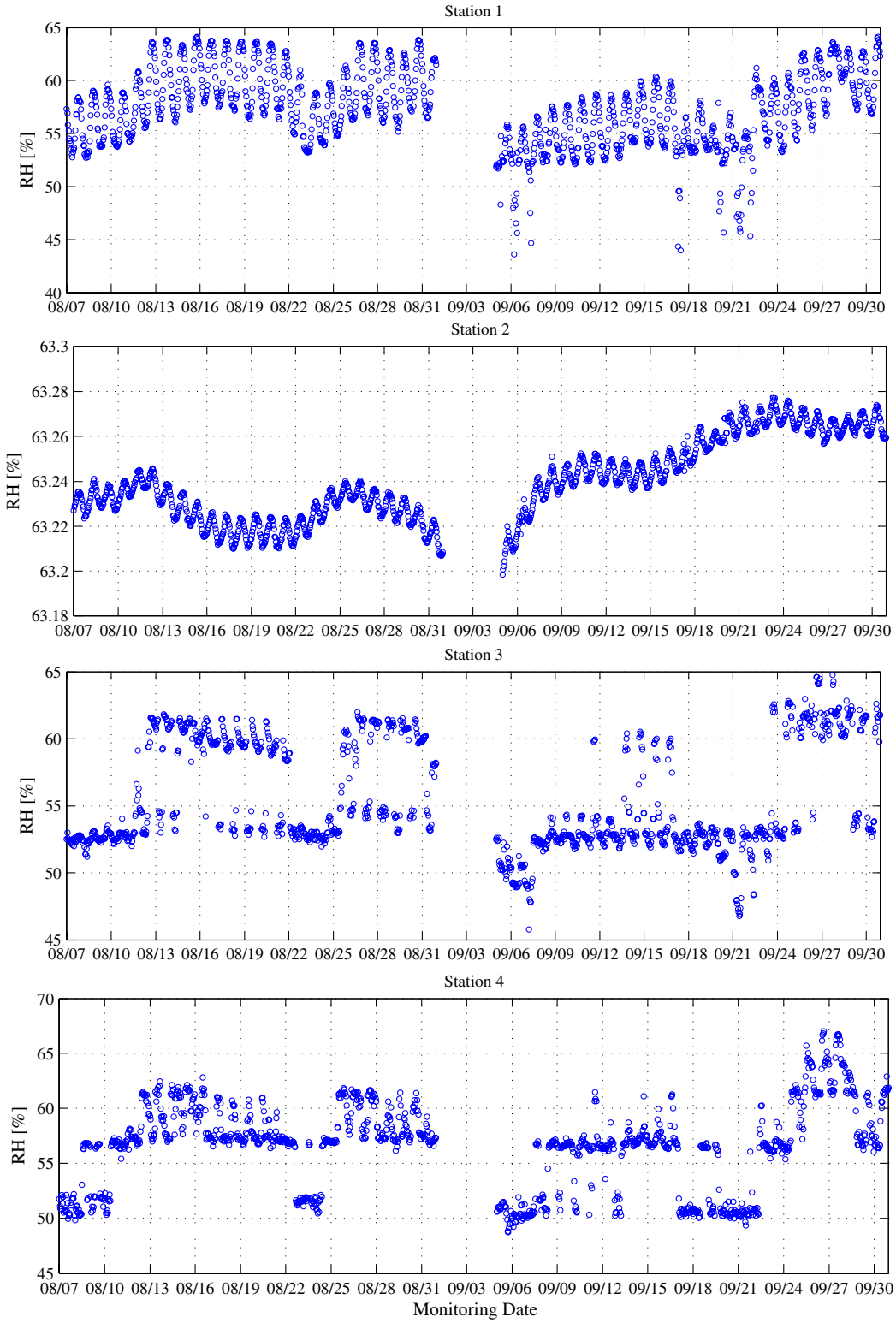

Figure 7.20. Air relative humidity inside the bridge (along south side of the bridge) measured during the monitoring period

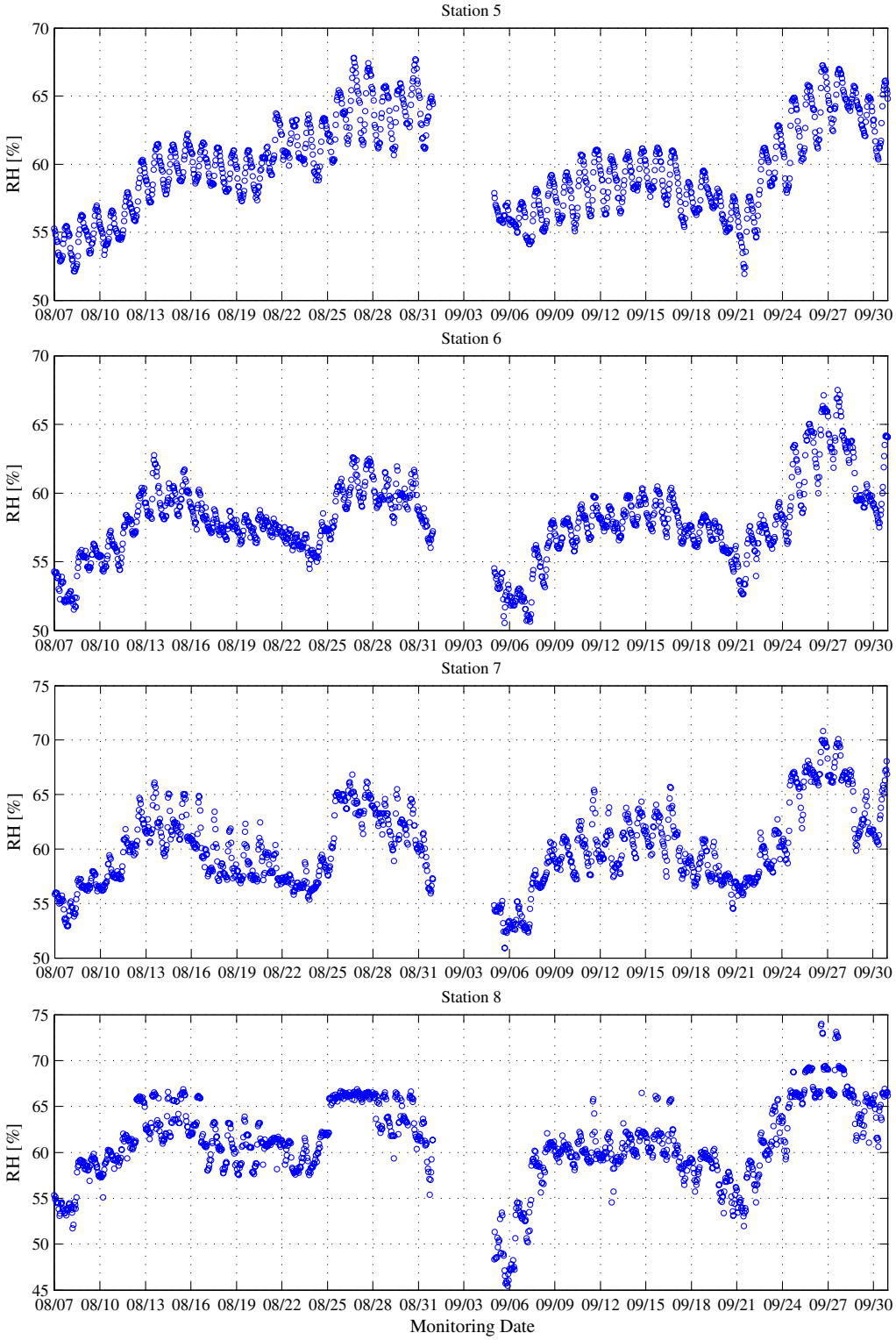

Figure 7.21. Air relative humidity inside the bridge (along north side of the bridge) measured during the monitoring period

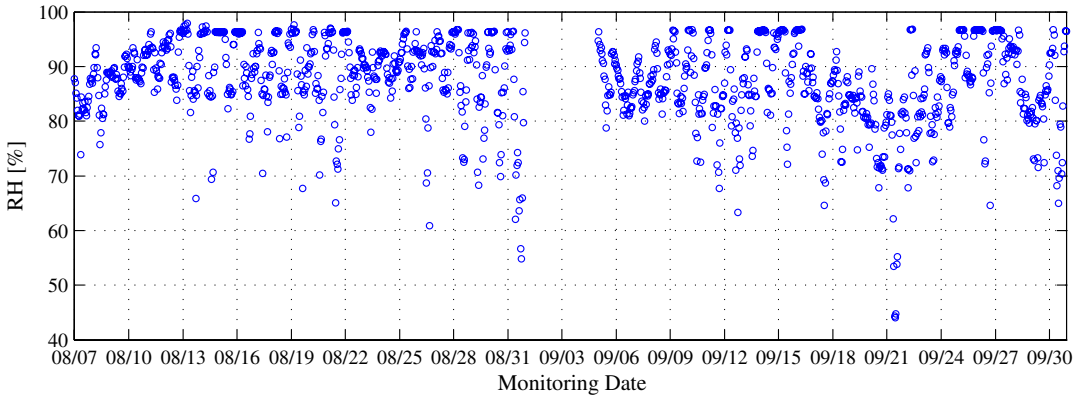

Figure 7.22. Air relative humidity measured at the weather monitoring station during the monitoring period

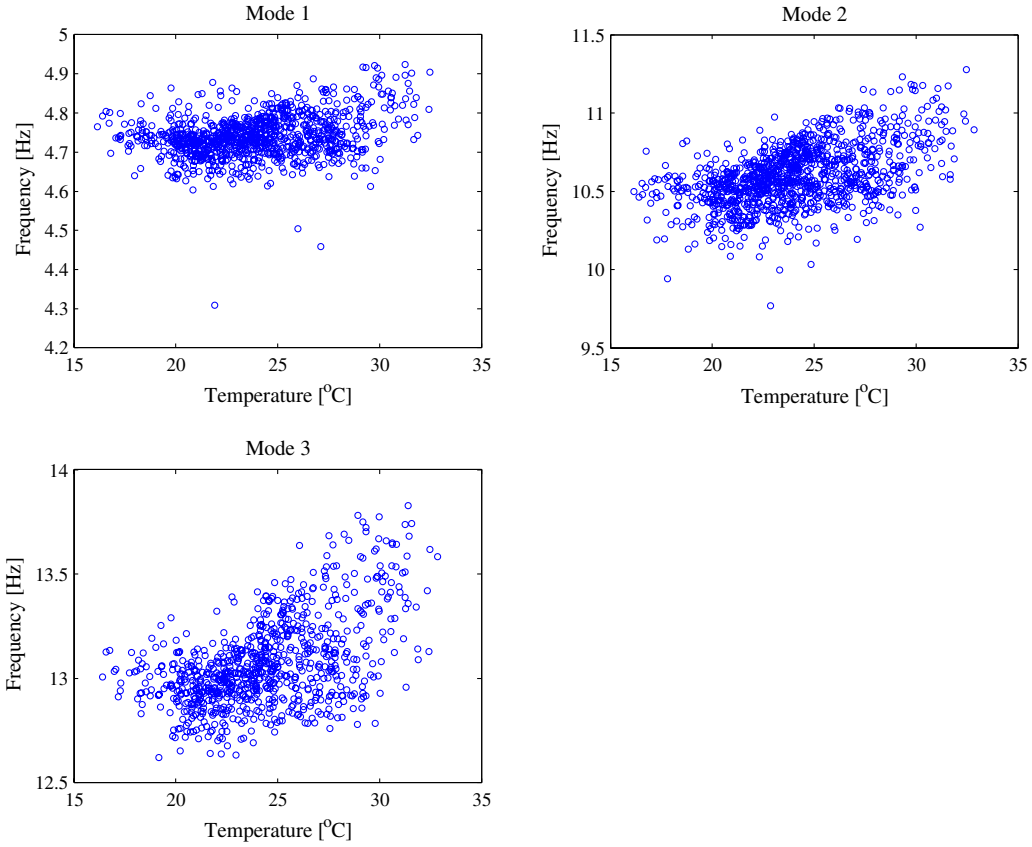

Figure 7.23. Identified natural frequencies vs. air temperature measured above the bridge (T1)

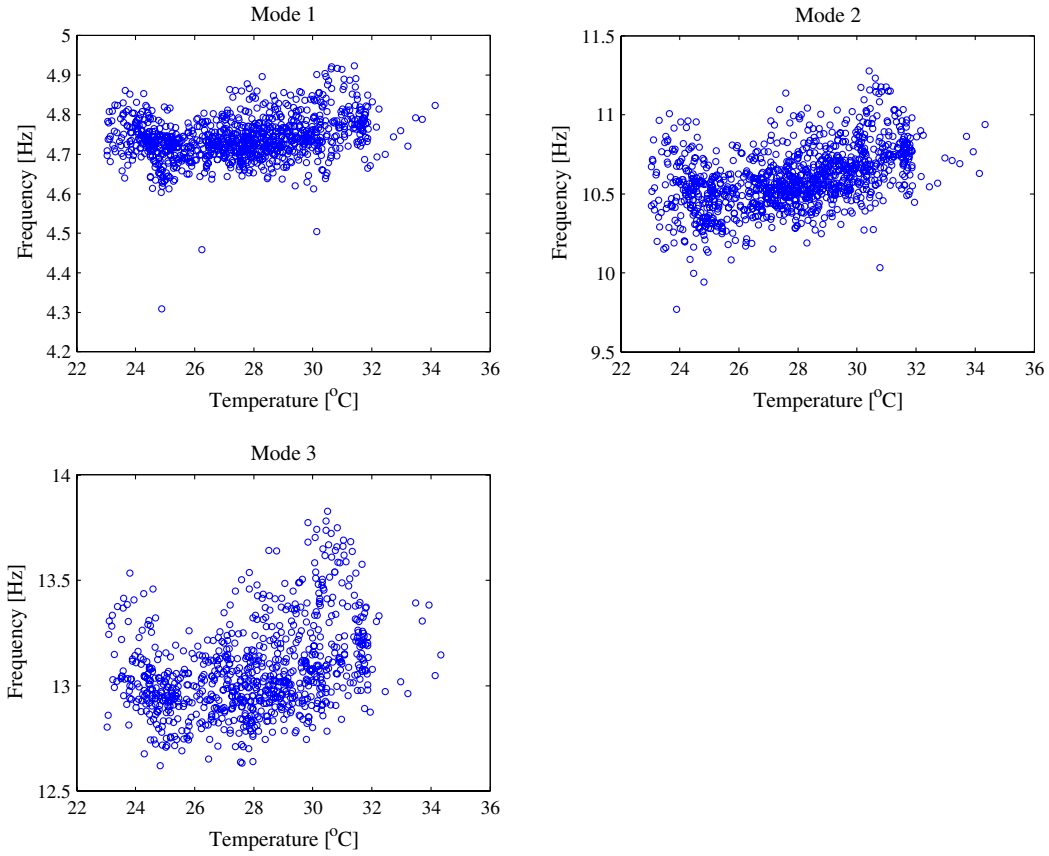

Figure 7.24. Identified natural frequencies vs. concrete temperature measured at the top of the stem walls (T3)

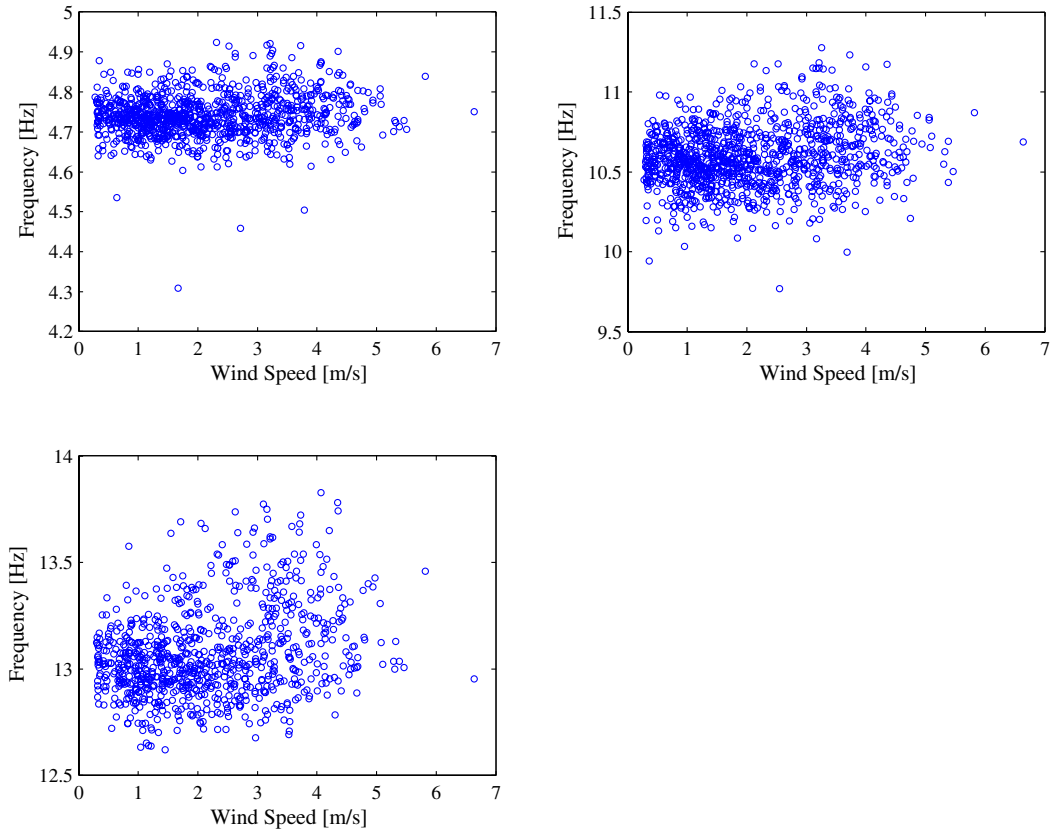

Figure 7.25. Identified natural frequencies vs. wind speed

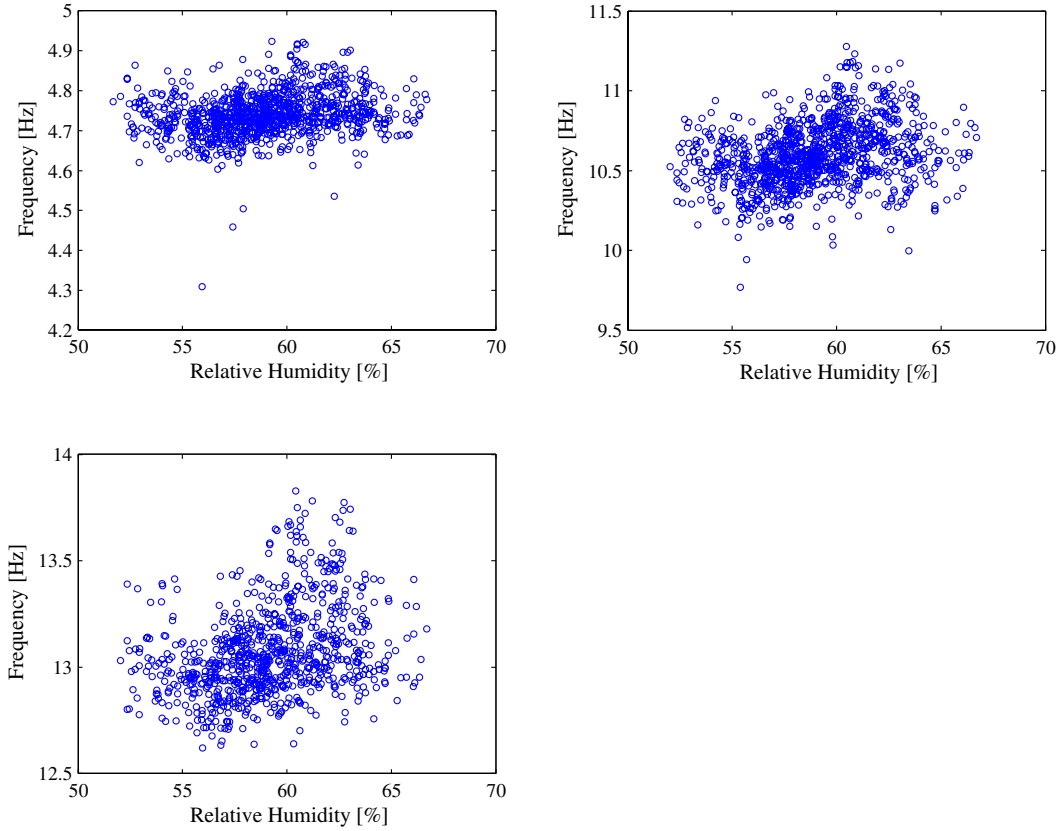

Figure 7.26. Identified natural frequencies vs. air relative humidity measured inside the bridge

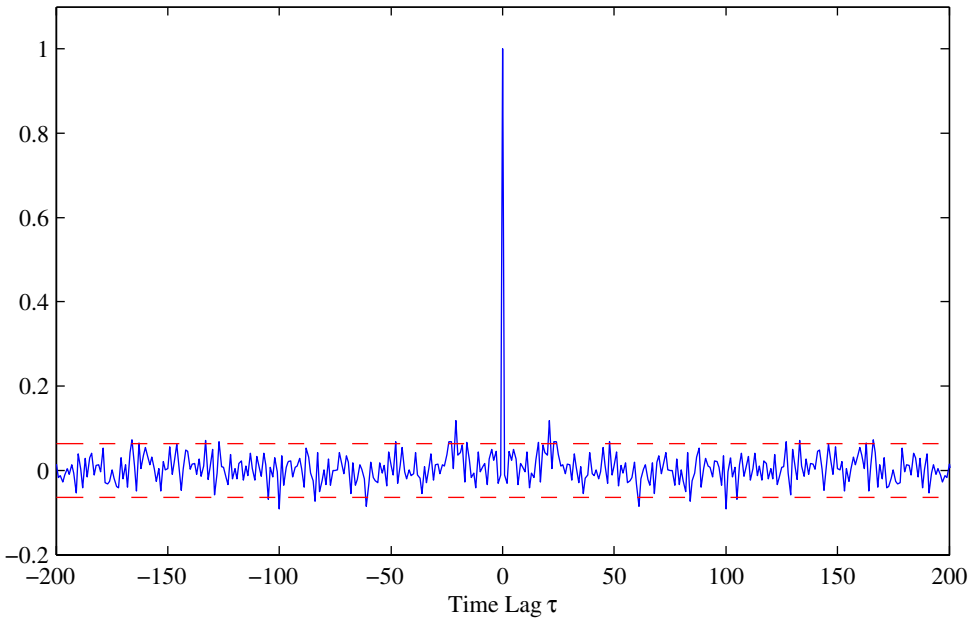

Figure 7.27. Normalized auto-correlation of the prediction errors of the ARX model identified for the first vibration mode natural frequency

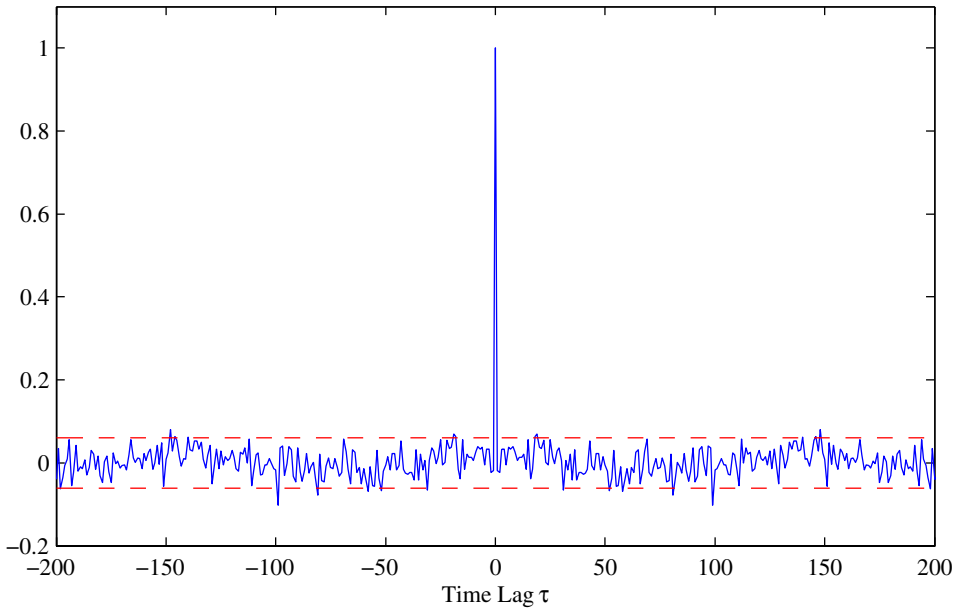

Figure 7.28. Normalized auto-correlation of the prediction errors of the ARX model identified for the second vibration mode natural frequency

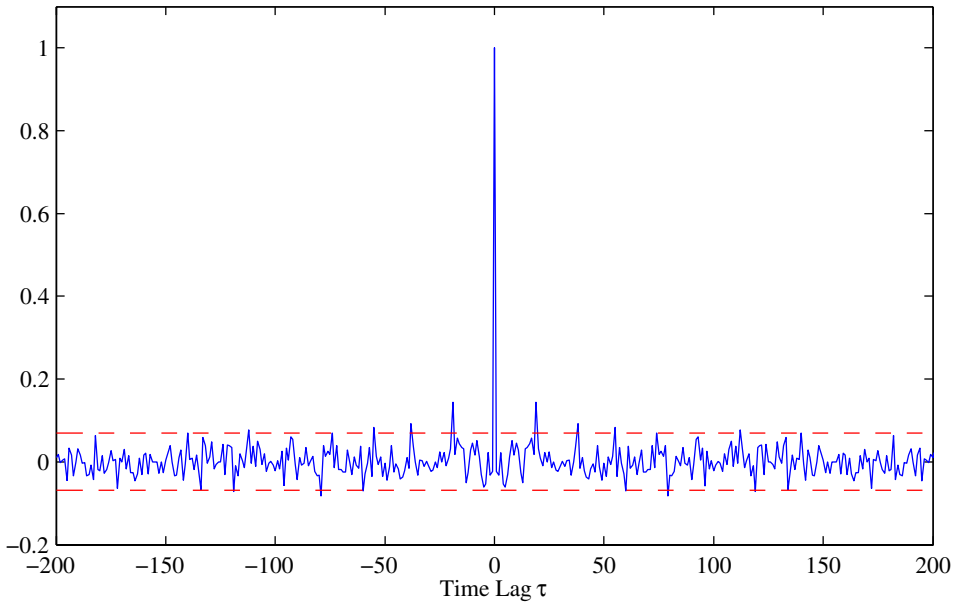

Figure 7.29. Normalized auto-correlation of the prediction errors of the ARX model identified for the third vibration mode natural frequency

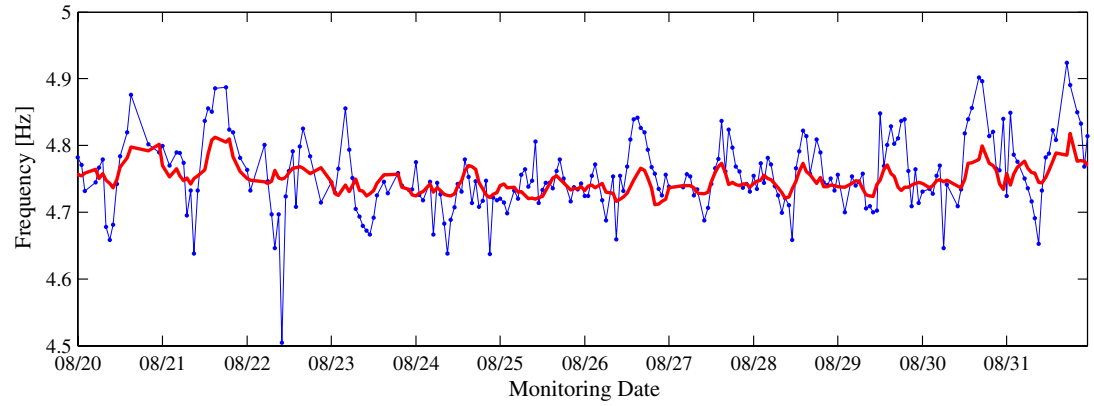

(a) Mode 1

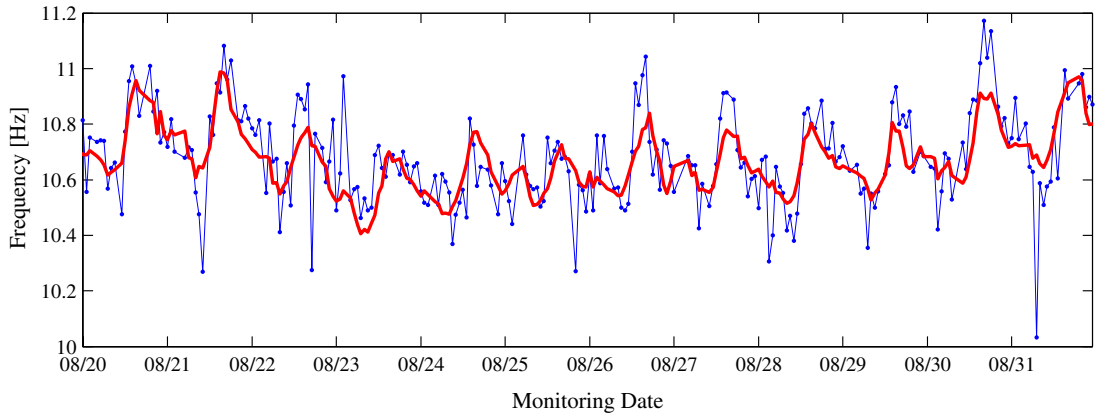

(b) Mode 2

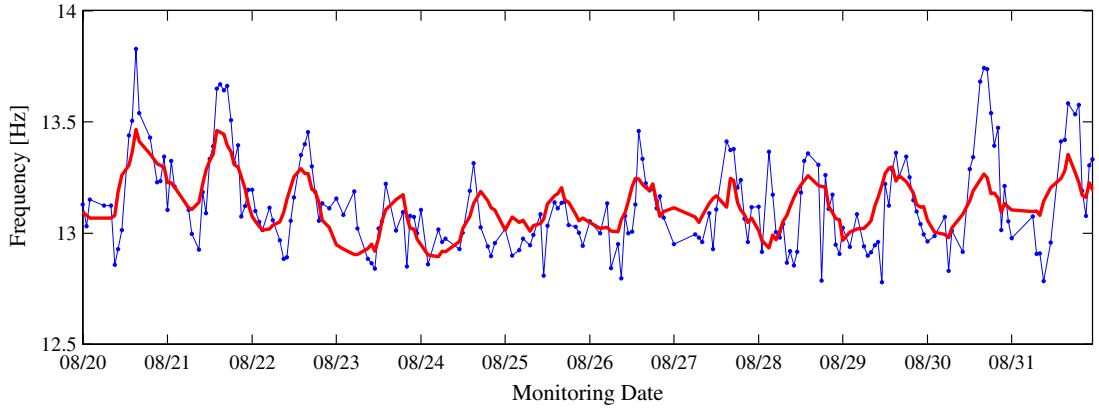

(c) Mode 3

Figure 7.30. Comparison of the simulated natural frequencies and their identified counterparts: red thick line, simulated natural frequency based on measured environmental parameters; blue thin line, identified natural frequency

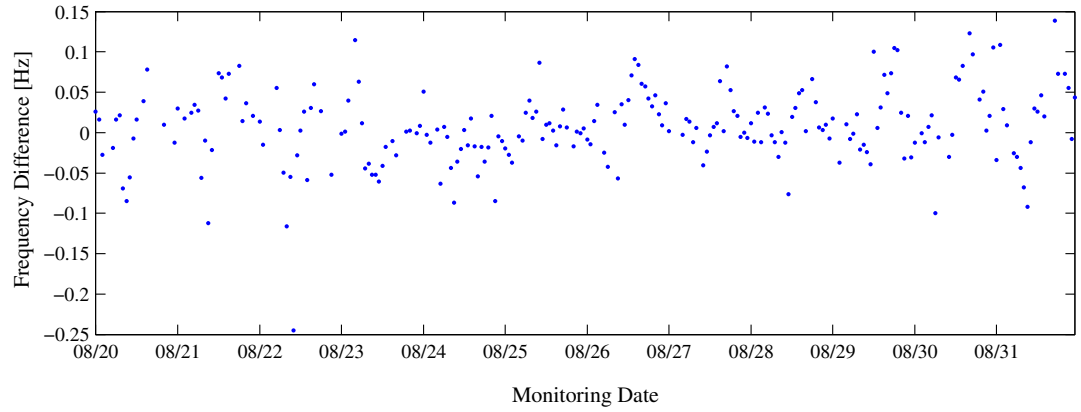

(a) Mode 1

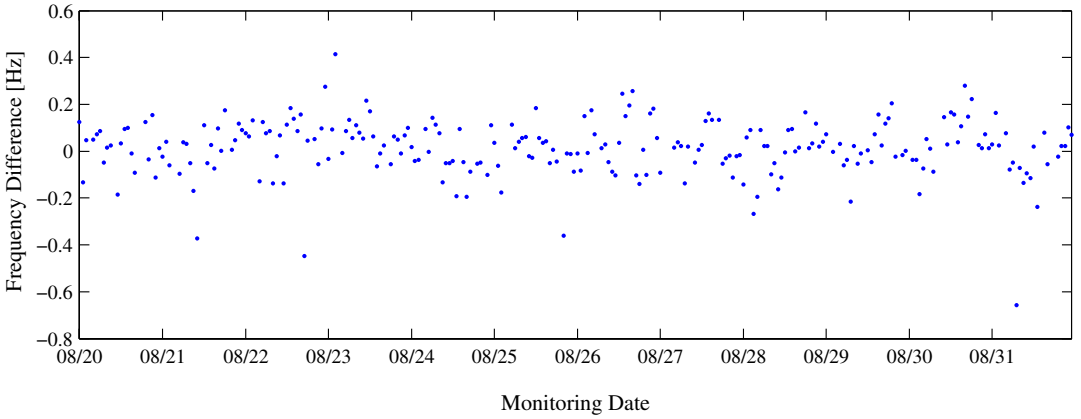

(b) Mode 2

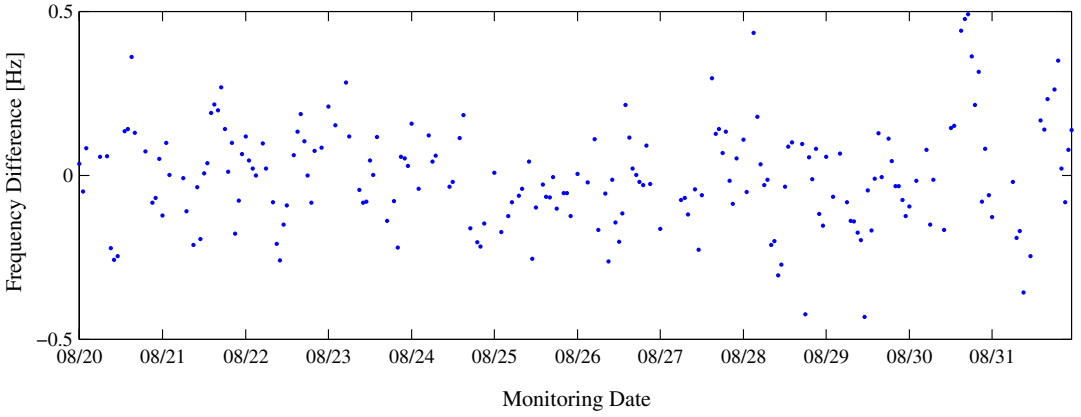

(c) Mode 3

Figure 7.31. Differences between the corresponding simulated and identified natural frequencies (variations of identified natural frequencies after removing the environmental effects)

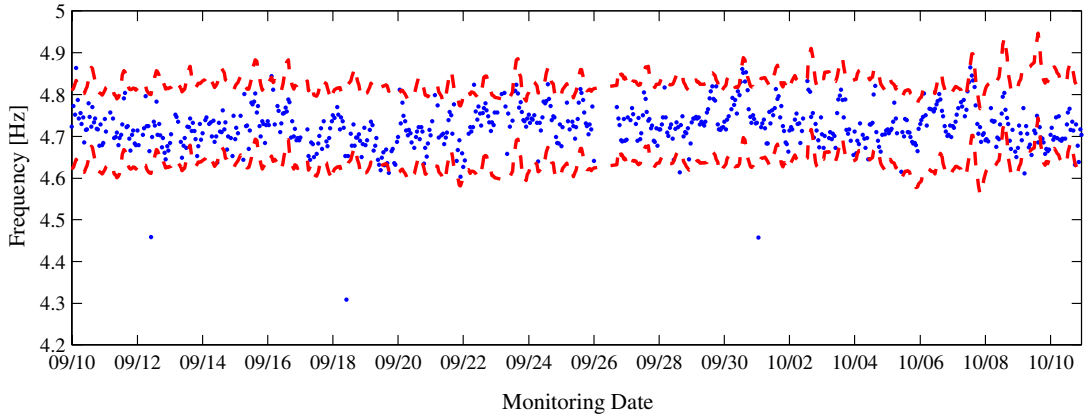

(a) Mode 1

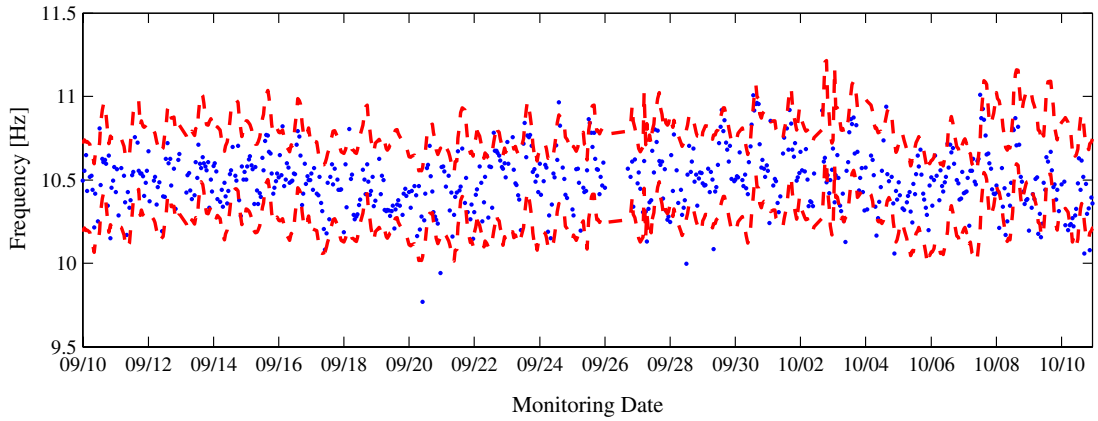

(b) Mode 2

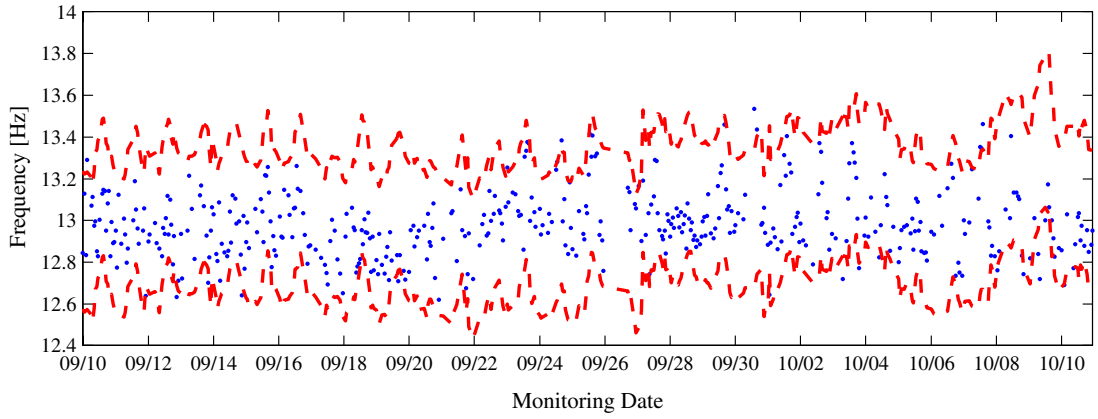

(c) Mode 3

Figure 7.32. Identified natural frequencies together with their 95% confidence intervals

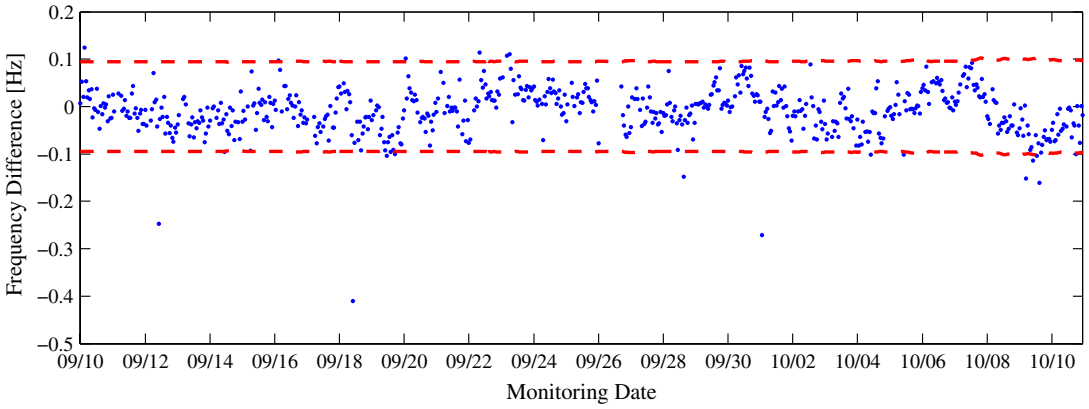

(a) Mode 1

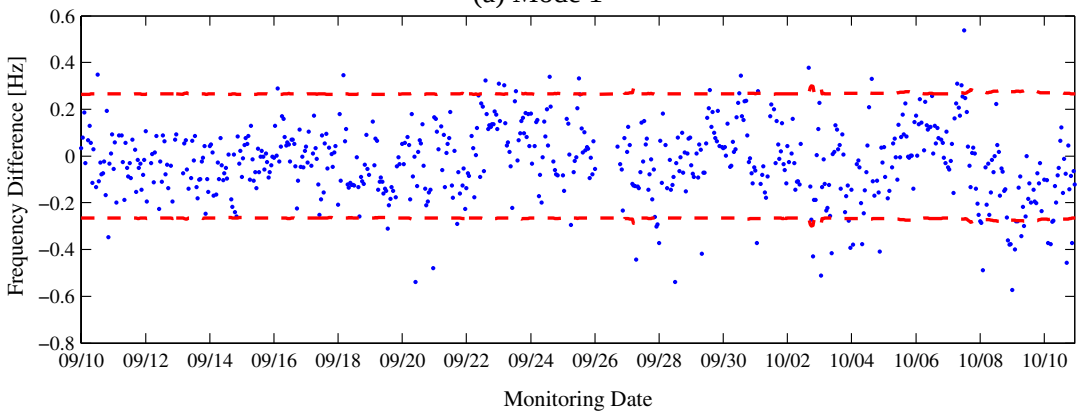

(b) Mode 2

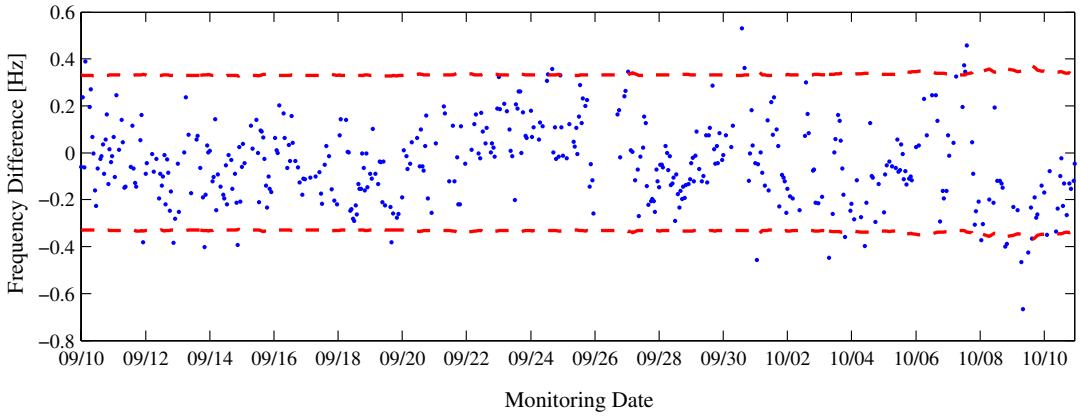

(c) Mode 3

Figure 7.33. Differences between the corresponding identified and simulated natural frequencies together with their 95% confidence intervals

Chapter 8

Concluding Remarks

8.1 Summary of Contributions and Highlight of Findings

The research work presented in this dissertation contributes to the development of a robust and reliable vibration-based structural health monitoring system in the following areas: (1) system identification of real-word structures with real-world complexities using output-only system identification methods based on dynamic field test data; (2) damage identification of real-word structures based on the modal parameters identified from dynamic field test data; (3) simulation of wind-induced ambient vibration response of long-span suspension bridges using detailed three-dimensional (3D) bridge finite element (FE) models and state-of-the-art stochastic wind excitation model; (4) development and deployment of state-of-the-art long-term continuous structural monitoring system; (5) investigation of the effects of changing environmental conditions on identified modal parameters.

The principal contributions and major findings of this research work are summarized below:

1. Dynamic field tests were conducted on the Alfred Zampa Memorial Bridge (AZMB), just before its opening to traffic in November 2003. These tests provided a unique opportunity to obtain modal parameters of the bridge in its as-built condition with no previous traffic loads or seismic excitation. The AZMB is the first major suspension bridge built in the United States since the 1960s.

A comparative study of output-only system identification techniques applied to the AZMB is performed based on bridge vibration data from two types of tests: ambient vibration test and forced vibration tests based on controlled-traffic loads. These methods consist of: (1) the multiple-reference natural excitation technique combined with the eigensystem realization algorithm (MNExT-ERA), a two-stage time-domain system identification method; (2) the data-driven stochastic subspace identification (SSI-DATA) method, a one-stage time-domain system identification method; and (3) the enhanced frequency domain decomposition (EFDD) technique (Brincker et al., 2001), a non-parametric frequency domain system identification method. Modal parameters identified using different methods and different types of test data are compared for cross-validation purposes and also to investigate the performance of different output-only system identification methods applied to bridge vibration data for different excitation sources.

From the modal identification results obtained, the following conclusions can be made: (1) The natural frequencies identified using the three different methods are in excellent agreement for each type of test. (2) The natural frequencies identified based on data from the two different types of test are also in excellent agreement, except for the 1-AS-V (first anti-symmetric vertical) mode. The significant difference in the identified natural frequency for this mode reflects the difficulty in identifying it due to its very low relative contribution to the measured bridge vibration in both the ambient and forced vibration tests. In addition, the order (in terms of natural frequency) of vibration modes 1-S-V and 1-AS-V identified based on ambient vibration data is swapped over when these modes are identified based on forced vibration data. (3) Considering that the estimation (or statistical) uncertainty of modal damping ratios is inherently significantly higher than that of natural frequencies, the modal damping ratios identified are in reasonable agreement across the different identification

methods used. (4) The identified modal damping ratios are response amplitude dependent. For most vibration modes, especially for the lower vibration modes, the modal damping ratios identified using forced vibration data are higher than those identified using ambient vibration data. (5) For most vibration modes, the mode shapes identified using different methods and different test data are in excellent agreement.

Overall, all three system identification methods applied in this study perform very well in both types of tests. However, in order to avoid missing modes in the identification process, use of several system identification methods is recommended for cross-validation purposes, as different methods have different estimation variability with respect to input factors such as measurement noise level, frequency content of input excitation, and excitation amplitude. It is found that the EFDD method is not as robust as the other two methods, since it requires user (subjective) intervention for peak picking in the identification process.

Finally, the identified natural frequencies and mode shapes are compared with their analytically predicted counterparts obtained from a 3D FE model used in the design phase of the AZMB. The identified (experimental) and analytical modal properties are found to be in good agreement for the modes contributing significantly to the measured bridge vibration.

The system identification results obtained from this study provide benchmark modal properties of the AZMB, which can be used as baseline in future health monitoring studies of this bridge.

2. The wind-induced ambient vibration of Vincent Thomas Bridge (VTB), a long-span suspension bridge located in San Pedro near Los Angeles, California, is simulated using a detailed 3D FE model of the bridge and a state-of-the-art stochastic wind excitation model including both buffeting and self-excited forces. Based on these simulated ambient vibration data, modal parameters of the low frequency vertical vibration modes of VTB are identified

using SSI-DATA. The identified modal parameters are in good agreement with the computed ("exact") modal parameters obtained directly from the FE model of VTB, which in turn are in good agreement with the corresponding modal parameters of VTB identified by other researchers using actual ambient vibration data. This system identification study also provides the opportunity to investigate the accuracy of the modal identification results obtained using SSI-DATA in the case of a large and complex (virtual) structural problem for which the "exact" modal parameters (modal parameters of the FE model of VTB) are known. This opportunity does not exist when system identification methods are applied directly to real-world structures and data.

The methodology and study presented in this part of the research provide a validated framework for studying the effects of realistic damage scenarios in long-span cable-supported (suspension and cable-stayed) bridges (e.g., corrosion-induced losses in stiffness and strength of main cables and suspenders at different locations along the bridge) on modal identification results. These effects represent the basis for developing robust and reliable vibration-based structural health monitoring systems for long-span cable-supported bridges.

3. A linear flat shell element is implemented in the element library of the MATLAB-based structural analysis software FEDEASLab, which is then integrated with the FE model updating algorithms used/developed in order to perform structural damage identification. This shell element is based on the mixed discrete variational principle proposed by Hughes and Brezzi in conjunction with Allman type interpolation for the membrane part and the discrete Kirchhoff plate element derived by Batoz and Tahar for the plate part. The resulting finite element has six degrees of freedom (DOFs) per node, including a true (mechanics-based) drilling degree of freedom.

Using the extended version of FEDEASLab, a comparative study of the influence of different objective functions on the damage identification results is performed by using simulated data for a simply supported plate. From this numerical example, it is found that the objective function defined by a combination of natural frequency residuals and mode shapes residuals and the objective function defined by a combination of natural frequency residuals, mode shapes residuals, and pseudo modal flexibility residuals are good candidates for structural damage identification using sensitivity-based FE model updating techniques.

4. A sensitivity-based FE model updating strategy is applied for damage identification of a full-scale seven-story R/C building slice tested on the UCSD-NEES shake table. The shake table tests were designed so as to damage the building progressively through a sequence of historical earthquake records reproduced on the shake table. The natural frequencies and mode shapes of the first three longitudinal modes identified using SSI-DATA based on the ambient vibration data are used in the damage identification process. In the application of the FE model updating strategy to identify the damage in the building at various damage states, the objective function is defined as a combination of residuals in natural frequencies and mode shape components. The damage identification results are consistent with the actual damage observed (visually) in the building and inferred from LVDT and strain gages data.

5. A state-of-the-art long-term continuous monitoring system is developed and deployed on the Voigt Bridge Testbed. The monitoring system consists of high-resolution video camera, thirty piezoelectric accelerometers (in the bridge vertical direction), and fifteen capacitive accelerometers (in the bridge lateral direction) for bridge vibration monitoring. The primary purpose of the fifteen capacitive accelerometers is seismic monitoring, while the piezoelectric accelerometers measure the traffic induced mainly vertical vibrations of the bridge. Twenty six thermocouples, nine thermistor & relative humidity sensors, and a wind

monitor are also employed to measure concrete temperature, temperature and relative humidity of the air (both inside and outside the bridge), and wind characteristics. This monitoring system makes it possible to: (1) study the effects of varying environmental conditions such as temperature, wind characteristics, and humidity on the identified modal properties of the bridge; (2) allow for the early identification of possible damages in the bridge structure and enable maintenance and repair works at the initial damage phase; and (3) evaluate the health condition of this structure shortly after a major catastrophic event such as an earthquake.

It is envisioned that this densely instrumented bridge testbed will serve as a live laboratory for the development of vibration-based structural health monitoring technologies.

6. An automated system identification procedure is developed based on SSI-DATA. This automated system identification procedure is successfully applied to identify the modal parameters of the Voigt Bridge as a function of time based on the data collected over a period of 50 days (from August to September, 2007) using the state-of-the-art structural monitoring system deployed. It is found that changes in natural frequencies due to varying environmental conditions are significant, on the order of 10-15 percent. It is worth mentioning that variations of these identified natural frequencies are caused mainly by changes in environmental conditions, since the bridge did not suffer any damage during the monitoring period. The identified modal damping ratios and mode shapes are also investigated as a function of time in this study. No clear temporal variation patterns of the identified damping ratios and mode shapes are observed.

7. Different measured environmental parameters are investigated during the monitoring period considered in this study (i.e., period of 50 days from August to September, 2007). For each vibration mode, a multiple-input single-output ARX model is successfully

identified to represent the identified natural frequency of this mode (output variable) as a function of seven measured environmental parameters (input variables), namely, (1) T1 = air temperature measured above the bridge; (2) T2 = air temperature measured underneath the bridge; (3) T3 = space-averaged temperature measured in the concrete at the top of the stem walls; (4) T4 = space-averaged air temperature measured inside the bridge; (5) T5 = space-averaged temperature measured in the concrete at the bottom of the stem wall along the south side of the bridge; (6) T6 = space-averaged temperature measured in the concrete at the bottom of the stem wall along the north side of the bridge; and (7) WS = wind speed measured at the weather monitoring station. Based on the estimated parameters of each ARX model, the confidence interval of the natural frequency is obtained and used as an objective criterion for damage detection under varying environmental conditions. In the case that the natural frequency (identified from the bridge vibration data) is lower than its ARX simulated counterpart and lies outside the confidence interval of a specified level (e.g., 95% confidence interval), then the variation of the identified natural frequency is caused not only by variations in environmental conditions, but also by a statistically significant loss of stiffness (i.e., damage) in the bridge structure.

8.2 Recommendations for Future Work

Based on the research work performed and presented herein, several research areas have been identified as open to and in need of future work.

1. The effects of changing environmental conditions on the identified modal parameters need further investigation using vibration and environmental data recorded over a longer time period (e.g., one year) from the long-term monitoring system developed in this study. In addition, other types of methods such as statistical learning techniques should be

applied to explain/correlate the identified natural frequencies to the measured environmental conditions.

2. Investigation of the effects of (dynamic) traffic loading on the identified bridge modal parameters is also needed for developing robust and reliable long-term health monitoring systems for highway bridges. This can be achieved by leveraging the long-term monitoring system deployed on the Voigt Bridge Testbed.

3. An important issue not addressed in this research is the propagation of uncertainty from estimation errors in statistical properties of output data (e.g., auto/cross-correlation and auto-cross spectra of output channels) to the identified modal parameters and then to the damage identification results. An interesting topic of future research is to study analytically the uncertainty in damage identification results due to the uncertainty of the identified modal parameters.

4. The simulation platform for wind-induced vibration response of long-span suspension bridges developed in this research should be exercised to study the effects of various realistic damage scenarios on system identification results of long-span cable-supported bridges, and how these effects can be used to identify the damage.

5. The discipline of structural damage identification should be extended for the purpose of damage prognosis, which consists of predicting in probabilistic terms the remaining life of a structure (e.g., buildings, bridges) from the probabilistic characterization of its current state and future loads (both service and extreme).